Public University of Navarra

Technical High School of Industrial and Telecommunications Engineers

Electric and Electronical Engineering Department

Study and design of thin-film-deposited optical biosensing devices based on wavelength detection of resonances

PhD dissertation by

Abián Bentor Socorro Leránoz

Advisors

Dr. Ignacio Del Villar Fernández

Dr. Jesús María Corres Sanz

Pamplona, Navarra, Spain
January 2015

Universidad Pública de Navarra

Escuela Técnica Superior de Ingenieros Industriales y de Telecomunicación

Departamento de Ingeniería Eléctrica y Electrónica

Estudio y diseño de dispositivos ópticos biosensores depositados con películas delgadas basados en detección de longitud de onda de resonancias

Memoria de tesis redactada por

Abián Bentor Socorro Leránoz

Directores de tesis

Dr. Ignacio Del Villar Fernández

Dr. Jesús María Corres Sanz

Pamplona, Navarra, España
Enero 2015

TESIS DOCTORAL: **"STUDY AND DESIGN OF THIN-FILM-DEPOSITED OPTICAL BIOSENSING DEVICES BASED ON WAVELENGTH DETECTION OF RESONANCES"**

Autor:　　　　Abián Bentor Socorro Leránoz

Directores:　　Dr. Ignacio Del Villar Fernández

　　　　　　　Dr. Jesús María Corres Sanz

Tribunal nombrado para evaluar la citada Tesis Doctoral:

Presidente:　　_____

Secretario:　　_____

Vocal:　　　　_____

Revisores externos:

　　　　　　　_____

　　　　　　　_____

Acuerda otorgar la calificación de:

　　　　　　　_____

En Pamplona, a _____ de _____ de 20___

"But go your way till the end. And you shall rest and shall stand in your allotted place at the End of the Days."

"Mas tú, sigue hasta el fin. Descansarás y te levantarás para recibir tu heredad al Fin de los Días."

The Holy Bible / La Sagrada Biblia, Dn 12:13

"The only limit is the one you set yourself"

"El único límite es el que tú mismo/a te pones"

Felix Baumgartner

ACKNOWLEDGEMENTS

AGRADECIMIENTOS

PREFACIO

Tras una carrera como ingeniero de telecomunicación y máster en ingeniería biomédica, no se me ocurre mejor idea que hacer un doctorado que relacione ambas cosas. Afortunadamente, creo que estoy satisfecho con la experiencia, ya que he podido aprender muchas cosas sobre cómo va la investigación.

Comencé con la idea de conseguir un tipo de biosensor bueno, bonito y barato, patentable y con el cual, ¿por qué no?, vivir de las rentas de por vida. Quizás una mentalidad ingenieril excesiva. A día de hoy, tras 4 años de trabajo, la rentabilidad ha pasado a segundo plano y ha pesado mucho más el conseguir mejorar una tecnología nueva, adquirir más conocimientos sobre nuevas técnicas y formas de detección y toda la experiencia de trabajar en un laboratorio de investigación. El objetivo de diseñar sensores para ayudar a detectar enfermedades ha sido el colofón a la mayoría de los desarrollos que hemos realizado, y ese ha sido el elemento motivador. Pero meterse en el meollo del asunto, tratar de optimizar, de mejorar… El no ser conformista, en definitiva, es lo que ha hecho que esta tesis sea un buen colofón a mi carrera como estudiante de doctorado. Espero, a pesar de todo, haber contribuido al desarrollo de tecnologías para la mejora del diagnóstico médico.

En la tesis aprendes que se pasan malos momentos cuando las cosas no salen bien. Sin embargo, es muchísimo más reconfortante saber que cuando las cosas salen bien y puedes argumentarlas y defenderlas, te son reconocidas. Así que los malos momentos pasan rápido. Como científico, que el resto de la comunidad reconozca tu esfuerzo y te publiquen, es un verdadero halago al trabajo diario.

Llegados a este punto, no queda más que mostrar gratitud. Por ello, quiero agradecer a mis tutores, Ignacio y Jesús, por igual. Uno en la parte puramente óptica y otro en la parte de biofuncionalización y caracterización de los biosensores. Hemos tenido muchas charlas a lo largo de toda la tesis. Nos hemos metido por campos que no teníamos ni idea de por dónde íbamos a salir. Pero gracias a su guía es como esto ha salido adelante. También me gustaría agradecer a Nacho y Patxi su apoyo y las enseñanzas como personas y como encargados del grupo. Es gracias a ellos que el ambiente en el grupo es tan bueno para hacer investigación.

Muchas gracias al grupo "UPNA Sensors", en general, por compartir tantos momentos, todos finalmente positivos, a pesar de que todos hayamos tenido que lidiar en no precisamente las mejores plazas en nuestras respectivas investigaciones. Especialmente a Goico, Carlos, Miguel y César, por darnos su experiencia más reciente, y a los Pedros y a Aitor, por compartir tantos momentos

de laboratorio y vida científica en estos años. Espero que en el futuro, pase lo que pase, podamos seguir en contacto y sacar adelante proyectos en común.

No quiero extenderme con nombres específicos, porque me dejaría alguno seguro. Pero no me olvido de aquellos que, de alguna manera, contribuyen o han contribuido al buen ambiente del grupo y a que las investigaciones y docencia puedan realizarse en las mejores condiciones posibles dentro de la actual coyuntura. Desde los técnicos y profesores a la gente que nos juntamos en los almuerzos, pasando por aquellos que están ahora "proyectando", "masteriando" o investigando con nosotros, así como a aquellos que decidieron o tuvieron que tomar otros rumbos. Sois parte de la historia del grupo y con vuestra presencia y trabajo ha sido un placer contar siempre. Como también es un placer contar con la predisposición y trabajo de los chicos de Nadetech. Gracias a vosotros se están acabando las largas horas de deposición de sustancias con el método manual.

Un agradecimiento especial también a Andrea y a su Armani Research Lab en la University of Southern California, en Los Ángeles – EE.UU. Ellos me enseñaron otra manera de ser, de vivir y de trabajar. Diferente a la que puedo estar acostumbrado, pero igualmente admirable y exitosa. Gracias a esa experiencia aprendí mucho en muy poco tiempo, sobre todo a nivel personal. Y espero que profesionalmente también haya podido dejar un legado que pueda aprovecharse en el futuro en ambos grupos de investigación.

Desde el punto de vista biomédico de la tesis, sería una ofensa no acordarme de la gente que he conocido a partir de los estudios del máster y que han sido y son cruciales, a día de hoy, para los planes que puedan surgir. Gracias a los consejos de Tomás Belzunegui, director adjunto de urgencias del Hospital de Navarra, por acercarme un poco más a los conceptos básicos de medicina. Y también gracias a los "proteómicos" de Navarrabiomed, Quique y Joaquín, por introducirme en el funcionamiento y tratamiento con anticuerpos. Espero que podamos seguir colaborando en un futuro muy próximo.

Y como dice el refrán, *"los últimos serán los primeros"*. Mi familia. Esa mezcla de cariño, educación y amistad que durante 30 años ha estado conmigo siempre, y nunca mejor dicho. Mis padres: los fabricantes de esa fibra óptica por la que cada día se propaga mi luz. Mis abuelos y también mi familia canaria, que son mi cargador de pilas tras los desgastes en los momentos cruciales. Espero poder seguir disfrutando de vosotros el resto de nuestras vidas.

Hagamos, pues, que haya un nuevo Dr. Socorro en la familia ;)

Abián.

ABSTRACT

Along this thesis, the study and design of several optical waveguide platforms is presented, in order to check their viability when used as biosensors based on either optical fiber or other photonic substrates. In this work, some fiber-optic-based structures such as cladding removed multimode structures, tapered single-mode fibers and single-mode – multimode – single-mode fibers are deposited with thin-films of materials, using nanotechnology-based methods such as layer-by-layer assembly (LbL-assembly) or sputtering. Moreover, a brief chapter is focused on the study of toroidal microring resonators deposited by spin-coating. The final objective is to generate or enhance the parameters of the resonant phenomena obtained in these structures, in terms of resolution and sensitivity. Then, a biological detection is addressed and characterized, to see if they are able to perform a future early diagnosis for illnesses.

RESUMEN

A lo largo de esta tesis se presenta el estudio y diseño de varias plataformas de guía-ondas ópticas, con el fin de ver su viabilidad a la hora de usarlas como biosensores sobre fibra óptica u otros sustratos fotónicos. En este trabajo se depositan estructuras ópticas como una fibra monomodo desnuda, un estrechamiento en fibra óptica o una fusión de fibras mono – multi – monomodo (SMS) con películas delgadas de materiales usando técnicas nanotecnológicas como el ensamblado capa a capa (LbL-assembly) o el sputtering. Además, se dedica un capítulo al estudio de microresonadores toroidales depositados por rotación (spin-coating). El objetivo es generar o mejorar las prestaciones en resolución y sensibilidad de los fenómenos resonantes que se pueden obtener en estas estructuras ópticas, para luego detectar reacciones biológicas que den lugar a un futuro diagnóstico precoz de enfermedades.

CONTENTS

CHAPTER 1. Introduction

1.1. Motivation. Technology for medicine

It is even more evident that we live in a society quite influenced by the information and communication technologies (ICTs). The information is generated around us and it is closely related to the knowledge and the human being development. Once acquired, the information is digitalized and prepared to be transmitted in optimal conditions, in order to generate knowledge there where it goes. Knowledge is learnt and applied in every situation and it provides data to generate information at the same time. This kind of feedback is the motor of the society. Something that makes the humanity be able to evolve conceptually and personally. Something that, in spite of some skeptics, has allowed forgetting the already former Contemporary Age to face the **Technological Age** or the ICTs Age.

Nowadays, information is crucial for all life purposes. However, when the **"health"** topic is addressed, nobody hesitates about the actual importance of information. In these times, thanks to technology possibilities and the great medical goals achieved it is possible to diagnose most of the human body diseases, treat quite many of them and obtain information from those affections that research is still working in. Patients demand even more information and knowledge about their illnesses, how to avoid and treat them or how to cure themselves. This is a human right and, therefore, something that must be always satisfied.

In this sense, both physicians and engineers have to be ready for the upcoming demand of patients who expect to be informed about their affections and to be cured. However, this should not be an issue to address unilaterally. It is true that physicians have to play the role of pioneers and, therefore, proceed based on the diagnosis they do but there is also a need for taking engineers into account, in order to develop the upcoming technological challenges.

Thus, it seems logical to think that, in a near future, the staff of the hospitals will consist of nurses, physicians, researchers and engineers, apart from the rest of general services. The formers will arrange the clinical performance and the latters will manage, renew, research and develop the existing equipment, to satisfy the hospital needs. Here it is where engineering professionals have to offer the most practical and less cost-effective technology, with the main goal of being able to afford the generated demand.

That is why **biomedical engineering** is one of the most globally valuable careers so far. Its applications cover from the molecular treatment of the illnesses

to hospital management, patient tracking and data security. In the middle, medical instrumentation, patient diagnosis and therapy are challenging objectives to pursue. Hence, there is a need for people interested in enforcing the current and future technology possibilities, in order to inform both physicians and patients about their needs. In the end, they are the clients for these applications.

Now that this thesis is finished, it is obvious that much work is still necessary to do, in order to achieve a final application. As a biomedical/telecom engineering master, the main goal at the beginning of this stage was to achieve a good biomedical application. The final product has not been possible to achieve. However, by walking this path, a novel technology has proved to be competitive and several research lines have been opened in order to continue improving the desired features. The final result is positive, so it is worth being shared with the scientific community.

1.2. State of the art in biosensors

Giving the physicians the important information they need when trying to solve a patient's problem, involves to extract some data from the patients' body and then translate it into electric domain and try to make it understandable.

Now, the question is: "how is it possible to extract the information from the inside human body?" Medicine has been trying to address this issue by the auscultation and diagnosis directly on the patient. However, in order to obtain clarifying information about the actual body condition it is not enough with the auscultation. Human body owns some well-known variables that can be studied and they permit to detect anomalies related to its bad condition.

Technology can help obtain this important information. Once extracted, the corresponding values/signals from the inside human body are transformed into electric signals (1s and 0s) and then processed, being thus converted into legible information to be interpreted by physicians. Sensors normally make the extraction.

A sensor to detect biological substances or variables, in general, is called a "biosensor". Technically, a **biosensor** could be defined as "a device capable of detecting substances called analytes with high sensitivity and using a rapid, direct and specific biomolecular recognition".

Biosensors own many advantages, apart from their high sensitivity and selectivity. Some of them are based on organic molecules that can act as receptors. However, most of biosensors are made by substances that are always specific and selective by nature, such as antibodies, enzymes, DNA chains and aptamers, mainly.

Another advantage is that the substrate can be gently reduced in size, since the biological reaction is going to occur anyway with independence on the substrate size. This leads to a higher detection resolution, less cost of resources and, therefore, less cost for the final device [1]. Besides, if adequately treated, they can be used for in situ and continuous monitoring and sometimes with reversibility in the measurements, something that will give the possibility of being reutilized.

Every biosensor is composed of three well-differentiated parts, as shown in Fig. 1.1. First of all, the **substrate**. Based on this, sensors can be classified as electrochemical [2], piezoelectric [3], thermal [4], mechanical [5] or optical sensors [6]. How to distinguish among them will depend on the transduction phenomena from the biological world to the electric world. Nevertheless, there is also a strong demand in optical sensors based on optical fibers, what permits to detect biological reactions using optical phenomena such as evanescent field, fluorescence or interferometry among others. The next subsection will show a brief review on this topic, since fiber-optic based biosensors is the focus of this thesis.

On top of the sensor, the **biodetection layer** is in charge of detecting the analytes based on the corresponding bioreactions. According to what type of biomolecule is necessary to detect, biosensors can be classified as enzyme/protein-based sensors, immunosensors, cell/tissue sensors, aptasensors or sensors based on DNA chains or even on microorganisms.

Finally, to make the biological layer attach the substrate, there is another important layer known as the **immobilization interface**. This is probably the most important step to do when fabricating a biosensor [7]. The attachment of the bioreceptors to the substrate must be done in such way that the environmental conditions are similar to their natural state or at least in not an aggressive atmosphere. The objective is to maintain the bioreceptors in good conditions so that they can work efficiently and without degrading their structures. Otherwise, this may induce mistakes in the measurements. In this sense, a wide variety of immobilization techniques has been developed during the last times [8]. For instance, those based on direct adsorption, cross-linking with other substances, membrane embedding, entrapment in a polymeric structure, or covalent attachment to the substrate. The goal of these methods is to deposit bioreceptors in an oriented way, so that a homogeneous and more sensitive effective surface is deposited.

When fabricating biosensors, some factors have to be taken into account. Some of them are reflected in Table 1.1. The right column analyzes the easiness of achievement of the properties commented in the left column. As it can be observed, most of them can be easily achieved.
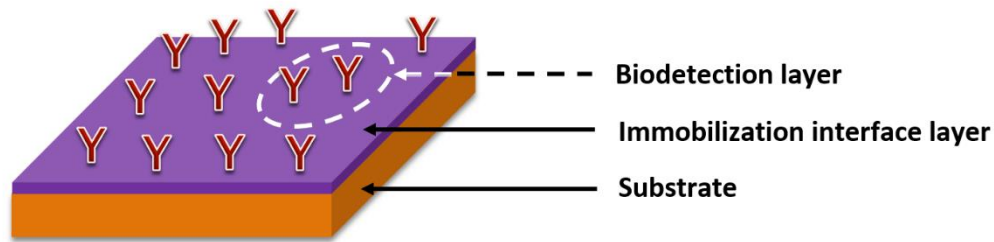
Fig. 1.1. *Schematic showing the different layers of a generic biosensor.*

In the last years, research and development have focused on one of the most fundamental aspects of biosensors fabrication, which is the miniaturization [9]. This permits to create smaller devices with better sensitive properties, as has noticeable occurred in the development of glucose biosensors. Moreover, in spite of the emerging non-invasive technologies, micro and nanotechnology are breaking up strongly lately. Consequently, companies have adopted microelectronics as the best way to integrate this biomedical tests. In this sense, cholesterol and, overall, diabetes diagnosis are on top of the most researched topics. Particularly, 31.5% of the biosensing applications are focused on glucose monitoring (see Fig. 1.2a).

Finally, the growth of novel technologies applied in biomedical detection and, therefore, in diagnosis is considerable. However, they have to compete in an aggressive and closed market where the multinationals that patent their own devices do not permit their inclusion. Nevertheless, the amount of money moved around the biosensors market is expected to increase from 12000 to 16000 million dollars between 2014 and 2016, according to what has been reported 5 years ago [10] (see Fig. 1.2b).

1.3. Fiber-optic-based biosensors

Optical fibers are cylindrical optical waveguides with an internal material (core) of refractive index higher than the refractive index of the cladding or external part of the waveguide. The difference in the refractive indices between core and cladding makes possible the phenomenon of total internal reflection derived from the Snell's Law, thus optimizing the transmission of light in the core.

The development in telecommunications industry has led to many kinds of flexible and low-loss optical fibers. The most common are silica-silica fibers (both core and cladding are made of silica with different dopants) although there are also

other types, such as plastic-clad silica-core fibers, plastic fibers, hollow-core fibers and photonic crystal fibers, among many others.

DESIRED PROPERTY	EASINESS OF ACHIEVEMENT
Specific and discriminant	Yes, given the specificity of the bioreceptor
Reproducible and accurate	Yes, since the fabrication is always the same
Safe and exact	Yes, as long as the sensor is calibrated
Adequate sensitivity	Yes, whenever the sensing method is appropriate
Fast response and reliability	Yes, although it is conditioned by the biological process to detect
Small size	Yes, as long as it is possible
Use of low measuring volumes	Yes, since the applications should imitate the actual concentrations used in medicine results
Temperature-independent	Yes, electronically compensable
Low –cost in manufacturing	Yes, since they are going to be produced in industries
Saleable	Difficult. Market dependent
Without/minimum maintenance	Difficult but affordable. There is a need for undo the bonds between biomolecules
Robust	Complicated. It requires a careful handling
Stable	Yes, as long as it is stored in well conditions or is used for short-term periods
Sterilizable	Only in the original packaging

Table 1.1. *Capability of achieving the desired properties in a biosensor.*

Fiber-optic sensors (FOS) take advantage of fiber-optics properties for light delivery or alternatively to be detected with minimal distortion or signal loss. In contrast to their utilization in telecommunications, FOS are designed to modify the

light travelling through the core as a function of the external medium properties (measurand). In many texts the optical head of these sensors is called "optode" or "optrode". The first term comes from a Greek expression that means "the optical way"; the second term comes from "optical electrode". These terms, very well received today, were coined by Lübbers and Optiz in the first CO_2 optical fiber sensor reported in the literature [11]. From then on, different optrode configurations have been proposed and some of them will be described in subsection 1.3.2.
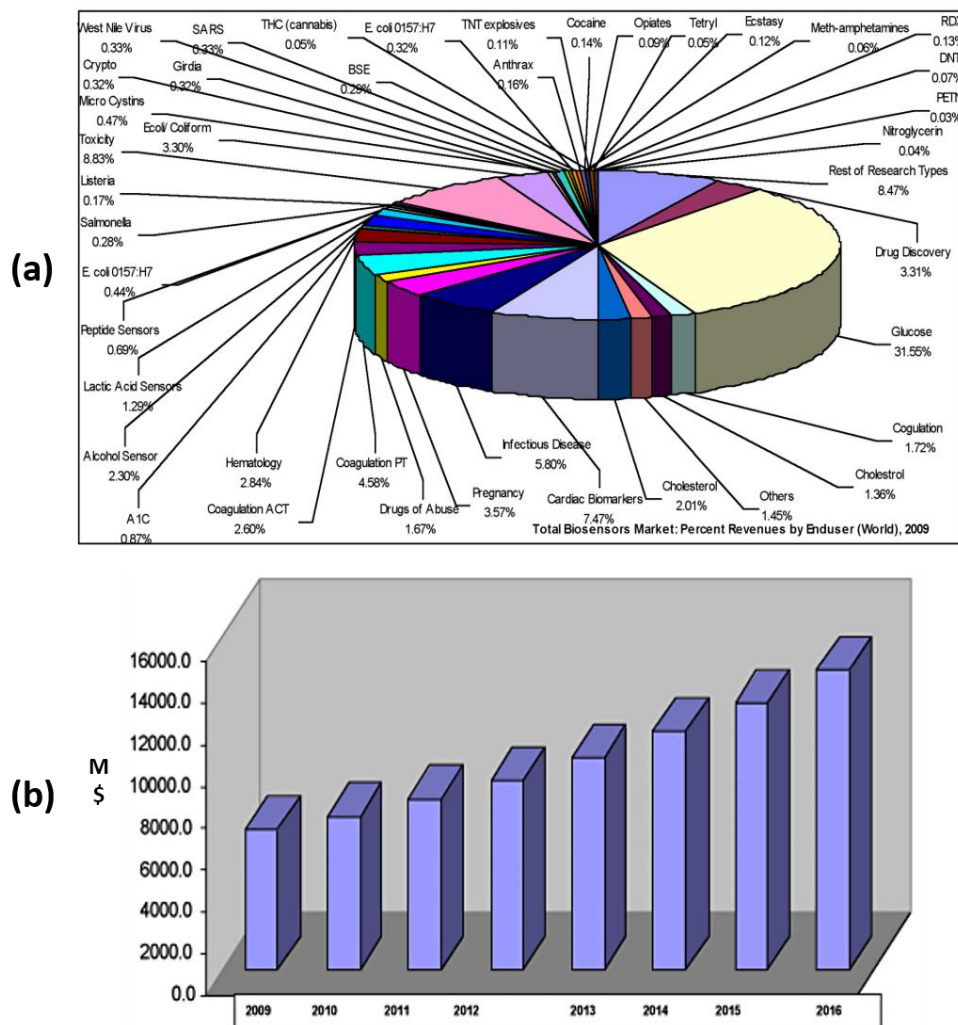

Fig. 1.2. *(a) Global demand in the use of biosensors in 2009. (b) Estimation of the incomes generated by the biosensors market until 2016 [10].*

FOS systems basically consist of an optical transducer, a communication channel and an associated subsystem for generating and/or detecting, processing, and conditioning the signal. It is usually distinguished between intrinsic FOS, when the fiber acts both as transducer and communication channel, and extrinsic FOS, when the fiber simply operates as a communication channel.

Among the wide variety of existing FOS, the main focus of this chapter will be the development of fiber-optic biosensors (FOBs). Extensive research has been dedicated in the past to this kind of FOS, with the main goal of detecting food-borne and water-borne contaminants as well as infectious disease pathogens that have paved the way for the development of FOBs [12]. In particular, the scheme of a FOB is the same as shown in Fig. 1.1 but using the optical fiber as substrate.

In the last years, the integration of optical fibers in reduced and more robust structures has led to a new generation of FOBs with lower detection limits, increased sensitivity, higher selectivity, reduced response time and, in some cases, reversibility, as well as long-term stability. In particular, FOBs have been found extremely useful for dynamic analysis of interactions inside single cells as a complement to conventional bulk cell assays, studies with a reduced number of samples that cannot be easily propagated and applications where a minimally invasive procedure is required [13]. The next subsections will begin with a more detailed description of the FOBs components, using the highest specific biorecognition elements and biosensing methods utilized and with the main focus on the fiber-optic detection techniques.

1.3.1. Biological receptors. Antibodies

As it has been mentioned, the biosensing systems are characterized by a high specificity to the substance they are designed for. Moreover, the adequate immobilization of the bioreceptor usually determines the accessibility of the biologically active component in order to provide high specific interactions with the target molecules as well as an intimate contact with the transducer component in order to provide a realistic output signal. That is why there is a need for immobilizing them in good conditions, as has been previously indicated.

A first group of bioreceptors to be considered is that formed by **enzymes**. Enzymes are complex and large macromolecules (molecular weight from 10 to 1000 kDal) that catalyze reactions of biochemical substances called "substrates". Enzymes have a reversible response and thus, they are regenerated after the chemical reaction. The Michaelis-Menten expression describes the reaction that involves the consumption of the named substrate (or analyte) "S" in presence of

the enzyme "E", giving some products "P", as described in Fig. 1.3a. For instance, the reaction where the glucose (substrate) consumes oxygen in the presence of the glucose oxidase (enzyme) and produces gluconolactone (product 1) and hydrogen peroxide (product 2), is a good example of an enzymatic reaction.

A second group to take into account is the formed by deoxyribonucleic acid-based chains (DNA). Nucleic acids are long-chain polymers built from nucleotide units. The **DNA** molecule is present in the nucleus of the biological cell and controls the production of proteins. The specific base-pairing between the two strands of the nucleic acids gives rise to the genetic code. This nucleic acids are the carriers of the essential genetic information of the living cells and each individual member of any species. DNA probes can be used to detect genetic diseases due to their specificity. The field of biosensors based on nucleic acids is one of the most promising techniques to investigate.

Probably, the most common molecule utilized for selective biorecognition is the **antibody** (Ab). In fact, antibodies are commonly used in labs around the world to perform biorecognition experiments called "Enzyme-Linked ImmunoSorbent Assays" or ELISAs. Therefore, and due to their availability in the chemical compounds market, they will be used through this thesis to fabricate and characterize all the biosensors designed.

Antibodies are proteins (about 10x10x10 nm in diameter) of high molecular weight, ranging from 100 to 1000 kDal. They are designed to protect the living beings against bacterial and viral infections through their immune system. They are closely related to the antigens (Ag) or foreign substances that invade the host organism and stimulate the synthesis and the production of antibodies for the organism's self-defense. This means that antibodies are generated by the immune system in order to eliminate these antigens. This elimination is accomplished when the reaction of antigen and antibody is completed, thus creating the Ag-Ab complex. This simple reaction is schematically depicted in Fig. 1.3b.

The Ag-Ab complex is achieved by non-covalent binding forces, sometimes allowing a certain reversibility of the Ab-Ag interaction. Unfortunately it is not so easy to undo this interaction due to its strength and stability, so the reversibility and regeneration of these devices is still an issue [14]. In fact, it is almost impossible to recover an immunosensor (a sensor based on Ag-Ab complexes detection) once it has done its job, because this reaction occurs only once and it is difficult to dissociate the biological compounds unless a powerful enzyme dissociates them. Nevertheless, as long as the Abs are proved to work properly, they are the most reliable way to detect target biomolecules.

There are several types or antibodies and antibody-based complexes with different characteristics: A, D, E, G and M. Each one is designed for a specific function in the host organisms. These complexes are all formed by repetitions of a single monomer. In particular, type G antibodies or immunoglobulins (IgGs) could serve as a good example of monomers and they are widely utilized. Two different parts can be distinguished in an IgG (see Fig. 1.3b). The first one (known as F_c) is similar in every of them, and takes part in the own structure of the biomolecule. Normally this part is used to attach the IgGs when designing a biosensor. The second part (known as F_{ab}) is specifically designed for each analyte (i.e. antigens or secondary antibodies), so that the IgG can bind it. Therefore, to take advantage of this, IgGs should be deposited in order to have most of their functional parts available, because this will increase the sensing efficiency of the biosensor [15].
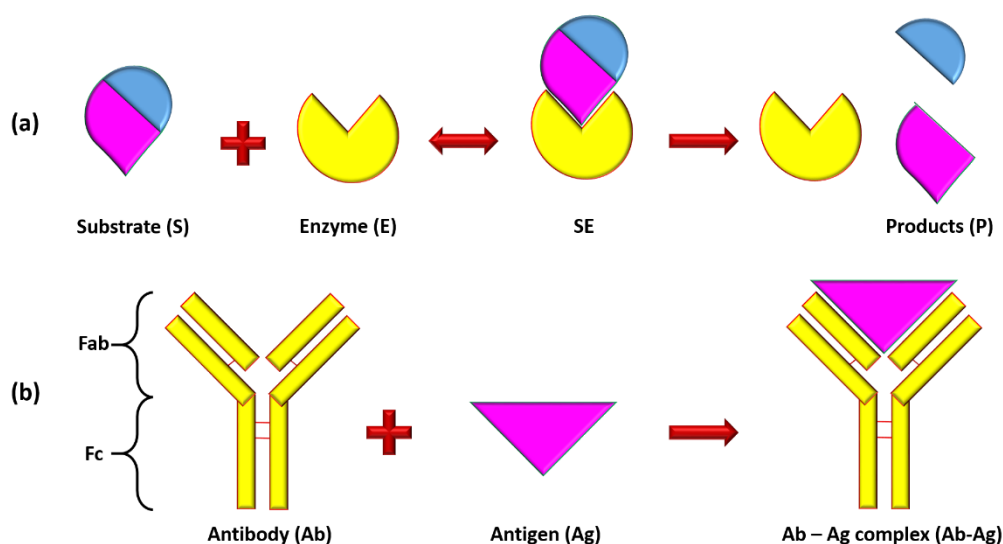
Fig. 1.3. *Schematic of the biological reactions that take place when using enzymes (a) and antibodies (b). In the former, the analytes are the products of the bioreaction, whereas in the latter, what is detected is the attachment of the antigen to the antibody.*

Apart from these widely common techniques of biorecognition, there are novel methods that are proliferating in the last decades. Among them, those based on the use of **aptamers** and molecular imprinted polymers (**MIP**s) are being extensively studied. In this sense, aptamers are synthetic short single-stranded oligomers (ssDNA or RNA) that own the capability to bind tightly and specifically to a wide range of targets [16]. Among their advantages, the possibility of reversibility and their ability to form 2D and 3D complex structures, which confers a high degree

of specificity for their target molecules. Similarly to aptamers, MIPs are synthetic receptors in a stable and reusable form by means of the fabrication of artificial recognition sites in synthetic polymers. These sites are tailor-made in situ by copolymerization of functional groups and cross-linkers. Then, the template molecules are removed from the polymer, leaving accessible binding sites in the polymeric network [17].

1.3.2. Common strategies to design FOBs

An introduction to some of the main fiber-optic sensing techniques based on the light modulation mentioned before is given in the next sub-sections, together with some reference applications.

FLUORESCENCE-BASED FOBS

Among the different optical techniques related to FOBs, fluorescence is perhaps the most commonly utilized, since it is the more extended tool in analytical chemistry, biochemistry, cell biology, photochemistry or medical diagnosis. This technique is based on the spontaneous light emission of a fluorophore or a label when it is excited with light at a wavelength (excitation wavelength) located in the absorption spectral region of such fluorophore. Different sensing schemes have been proposed attending to the fluorescence originated light intensity and phase modulations [18].

Commercial applications using fluorescence-based biosensors have shown up in the last years. For instance, Raptor (Research International, Monroe, WA) is a portable automated fiber-optic biosensor designed to detect biological threat agents. Its performance is quite quick (3 to 15 minutes) and its working principle is based on fluorescent sandwich immunoassays on the surface of short polystyrene optical probes for up to four target analytes simultaneously. The optical probes can be reused up to forty times, or until a positive result is obtained, reducing the logistical burden for field operations. More sophisticated versions of the same device are under development, being sponsored by the US Marine Corps. As an example of the applications, a solution assay for ricin toxin (via recognition of a substitute of its A-chain subunit) is worked out with this device [19]. Here, polyclonal anti-ricin antibodies are captured on the waveguide through incubation. Multiplexed assays are performed with four waveguides in one run using fluorescently labeled antibodies. Detection levels between 10 and 60 ng/ml of ricin A chain in deionized water and in tap water are detected respectively within 15

min. "Raptor" has been also applied to detect bacteria belonging to Enterococcus species in Florida Recreational Water. [20]. The detection method reduces to 2.5 hours the 24-hour standard method.

Other studies on fluorescent FOBs can be found in [21], where a sandwich immunoassay is performed on the surface of a tapered optical fiber to determine interleukin-6 (IL-6) in serum. The concentration of IL-6, directly related to the fluorescence intensity, can be detected at levels down to 5 pM (0.12 ng/mL), which reveals the high specificity and selectivity of the assay. A sandwich immunoassay was also performed by Valadez et al. for the detection of Salmonella in egg shell and chicken breast [22].

The utilization of quantum dots (QDs) as fluorescent labels is explored in [23] for human IgG detection using multiplexed immunoprobes with four QDs of different fluorescent colors.

Also, a wide variety of applications using this sort of FOBs have been reported. For instance, a reusable biosensor for small molecule (Hg^{2+}) detection based on fluorescent labeled DNA probes immobilized on an optical fiber is presented in [12]. A multi-target detection is performed by means of the utilization of oligonucleotide-functionalized nanospheres fabricated on etched nanofiber bundles [24]. Another application using fluorescently labeled aptamers immobilized onto the optical fiber surface is also described in literature for explosive TNT [25] and Bisphenol A [26] detection by means of competitive immunoassays. Finally, the utilization of enzymes in combination with oxygen sensing has been widely explored in FOBs for the detection of toluene in wastewater [27] or adrenaline [28].

BIOLUMINESCENCE-BASED FOBS

All the sensing techniques described above are related to fluorescent FOBs involving the immobilization of fluorescent labeled biosensing elements. Sometimes, the biosensing elements are luminescent in specific situations. Therefore, they can be detected without using any additional fluorophores.

These sensors are bioluminescence-based FOBs, which are used mainly for environmental monitoring of toxic chemicals, microorganisms, or bacteria [29]. Generally, they are based on substances called luciferins, which can emit light after an enzyme-catalyzed oxidation. Some studies claim that bioluminescence allows a much faster and more sensitive detection of the target analyte than fluorescence. This is because bioluminescence is normally used as an enzymatic activity

measurement, whereas fluorescence usually quantifies the presence of proteins. However, bacterial bioluminescence activity is relatively short-live and fluorescence techniques are more appropriate for long exposure and cumulative signal detection [30].

A fiber-optic biosensor based on bioluminescent bacteria is used for monitoring toxicity and pollutants [31-33]. However, a loss of functionality in the bacteria is observed after longer periods. Immobilized microalgae, another living species applied in bioluminescent biosensors, has been described for many applications in the detection of herbicides, such as simazine, atrazine, propazine, and linuron [34].

ABSORBANCE/REFLECTANCE-BASED FOBS

Absorbance and reflectance-based sensors rely on intensity modulations originated by refractive index or color modifications of the sensing material. These modifications produce a change in the optical power that can be measured.

This arrangement is the simplest but it also has some drawbacks. One of them, as it was described in section 4.1, is the need for a signal reference. Another issue is the lack of selectivity in this method. For instance, not only the target antigens but also some non-specific binding elements can change the refractive index. It is difficult to extract an accurate measurement if only absolute intensity measurement is taken. In order to avoid this problem, spectrometric arrangements have been proposed where the selectivity is sharply improved.

Concerning the changes in color, they can be associated to the detection of a chromophoric reaction product [35]. For instance, if an enzyme such as alkaline phosphatase is deposited at the end of optical fibers, then it is possible to detect p-nitrophenylphosphate. This is due to the strong absorption at 404 nm of the product p-nitrophenol of the catalyzed reaction indicated below [36]:

P-nitrophenylphosphate $\longrightarrow$ *P-nitrophenol + phosphate*
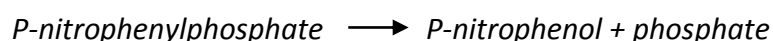
A different approach is presented in [37]. Here, celiac disease is detected through the formation of gliadin - anti-gliadin antibodies. Gliadin is first immobilized onto optical fiber tapered tips and changes in absorbance are monitored.

INTERFEROMETERS

A fiber-optic interferometer uses the interference between two or more beams that have propagated through different optical paths of a single fiber, several spliced fibers or thin-films deposited onto fibers. The working principle is based on combining at least two signals. One of them is the original signal and the other is a signal that has been altered by somehow actuating on it. Thus, when they recombine in the detection stage, the interferometric pattern will vary, providing the desired changes in the wavelength, phase, intensity, frequency, and else parameters. There are lots of ways to obtain an interferometer, although the most representative are commented in the following lines.

A wide extended strategy is to use Fabry-Perot (FP) nanocavities. This means, to deposit a few nanometers of a material that generates two mirrors of different refractive indices. As a result, the spectral difference between input (transmitted) and output (reflected) signals obtained using the set-up in Fig. 1.4 will be due to a change in the optical conditions with respect to the initial ones.

A defining example of this FP-based FOBs is a recent contribution depositing a nanocavity on the tip of an optical fiber, which uses proteins as bioreceptors [38]. The method is called Bio-Layer Interferometry®. The company ForteBio Inc. (Menlo Park, CA, USA) named it this way. Here, the deposited nanocavity is a streptavidin (protein) layer. Thus, for a specific optical fiber – bio-layer interferometer, a specific interferometry spectrum can be visualized in the detector. When the bioprobe is subjected to a solution where the specific analyte (biotinylated rh-Epo in this case) is present, the bioreaction is detected as a red shift in wavelength of the initial spectrum. By measuring this shift it is possible to know the corresponding concentration, since the biolayer thickness increases.

Another way to obtain interferometer-based FOBs is by using long period fiber gratings (LPFGs). This structure consists of a periodic perturbation of the waveguide properties, generally of the core refractive index. Consequently, several dips are created in the transmission spectrum at wavelengths where there is a coupling of optical power between the core and cladding modes in the optical structure. Moreover, one of the most important discoveries in LPFGs is the existence of the turn around point (TAP) or turn dispersion point (TDP) [39], which is good in terms of improving the sensitivity of these optical structures.

A recent application based on bringing the LPFG to the TAP has been also recently published, detecting IgG – anti-IgG complexes [40]. A comparison between a non-TAP-LPFG and a TAP-LPFG is done, in terms of sensitivity. The TAP-LPFG is more sensitive in wavelength than the non-TAP-LPFG, although only a nanometer

of improvement is registered. In spite of this, it is corroborated that working with a higher order mode permits to detect a lower limit, decreasing from 500 μg/ml to 100 μg/ml.
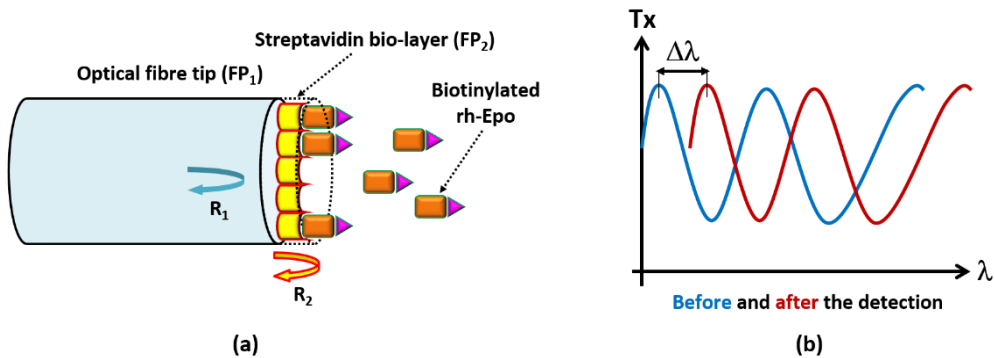
Fig. 1.4. *Bio-Layer Interferometry® as an interferometry-based FOB. The biological nanoFabry-Perot cavity (a) is in charge of shifting the interferometry shown in the spectrum (b) as the bioreactions take place [38].*

OTHER TECHNIQUES FOR FOBS

There are other various methods of fabricating FOBs that are also proposed in the literature. One of them is the utilization of non-adiabatic tapered single-mode optical fibers (T-SMFs) as evanescent field label-free FOBs. For instance, this structure is the chosen transducer for real-time monitoring of BSA with antibodies as bioreceptors [41]. The BSA detection limit is around 100 fg/mL. Also, the use of LPFGs as evanescent field-based FOBs is currently under exploration. For instance, antibodies are usually immobilized on the surface of the LPFG, which acts as a refractometric device [42]. In addition, a very recent FOB configuration is based on whispering gallery modes in dielectric microdisks, microtoroids or microspheres [43,44]. These disks or microspheres behave as resonant cavities that are very sensitive to the external refractive index, achieving single-molecule detection.

RESONANCE-BASED FOBS

This kind of sensors is the focus of this thesis. Although the fundamentals of these devices are going to be broadly studied in the following chapters, it is important to remark that most of the developed technology regarding FOBs is based on the surface plasmon resonance (SPR) phenomenon. In fact, SPR-based sensors consist of depositing gold onto the optical fiber, launch polarized light and

take a look at the spectrum to see a narrow attenuation band in the visible range. This dip is the product of the energy transfer from the inside optical fiber to the gold surface, which makes it disappear for a restricted wavelength range. Taking into account this phenomenon it is possible to see the wavelength shift as a function of the refractive index variations due to the biological reactions.

The utilization of gold or silver thin-films is very usual for the development of SPR-based biosensors. These metallic coatings enable the generation of SPR resonances and the subsequent target detection. Lin et al present a Cadmium (Cd(II)) sensor based on localized SPRs (LSPRs) [45]. The resonance is generated by a gold layer onto a 400 μm optical fiber. Phytochelatin is responsible of detecting the cadmium concentration. The low limit of detection of the sensor was 0.16 ppb. The work presented by Cao and coworkers is focused on the generation of the LSPR as a function of the gold nanoparticles shape [46]. The study was performed with nanospheres and nanorods deposited onto the optical fiber. The LSPR are located in a different spectral range. This configuration was used to detect anti-human IgG with a detection limit of 1.6 nM. One of the most recent contributions on SPRs is a sandwich technique being explored in [47]. Here, a sandwich aptamer-antibody assay is used to detect Ara h1 obtaining a detection limit improvement of 100 times.

However, a new type of resonance-based FOB is emerging in the last years based on lossy mode resonances (LMRs) technology. Along this thesis, an exhaustive description of some improvements when using this phenomenon is given, in order to design FOBs based on antigen-antibody complex reactions. Nevertheless, it is worth mentioning some of the most recent advances in LMR-based biosensors. They involve the utilization of aptamers immersed into a polymeric structure adhered to the optical fiber. Thrombin [48] and C-reactive protein (CRP) [49] sensors have been fabricated using indium tin oxide thin-films as the LMR supporting coating. The obtained results reach detection ranges of 2 mg/L for CRP.
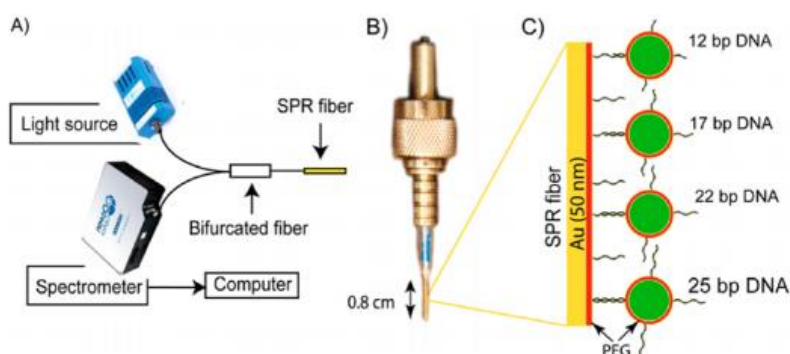

Fig. 1.5. *An example of a typical SPR-based biosensor. (a) Reflective configuration set-up. (b) Sensing head. (c) Biofunctionalization of the fiber-optic tip to achieve the bioprobe [36].*

1.4. Objectives

As it has been mentioned along this introduction, the main objective of this thesis is to study and characterize different fiber-optic-based platforms to be further used as biosensors. In this sense, several goals are proposed in the following lines, to be achieved along the development of this work.

a) Search of fiber-optic structures with a compact and cheap equipment, in order to monitor and try to optimize the behavior of resonant phenomena generated on them.
b) Thin-film deposition of low-cost and biocompatible materials that can be used not only to generate or enhance the properties of the corresponding resonant phenomena (LMRs), but also to maintain the bioreceptors in good conditions to achieve the biosensing applications.
c) Optical characterization of the developed sensors and biosensors, in order to determine functional ranges, detection limits, response times, etc.

Also, a study on the sensitivity of certain photonic microstructures (toroidal microring resonators) will be addressed, in order to enhance their properties by depositing thin-films and to corroborate if they can be used as potential candidates to detect bioreactions.

1.5. Bibliography

[1] G.L. Cote, R.M. Lec, M.V. Pishko, Emerging biomedical sensing technologies and their applications, Sensors Journal, IEEE. 3 (2003) 251-266.

[2] Y.H. Kwak, D.S. Choi, Y.N. Kim, H. Kim, D.H. Yoon, S. Ahn, J. Yang, W.S. Yang, S. Seo, Flexible glucose sensor using CVD-grown graphene-based field effect transistor, Biosensors and Bioelectronics. 37 (2012) 82-87.

[3] X. Guo, C.S. Lin, S.H. Chen, R. Ye, V.C. Wu, A piezoelectric immunosensor for specific capture and enrichment of viable pathogens by quartz crystal microbalance sensor, followed by detection with antibody-functionalized gold nanoparticles, Biosens. Bioelectron. 38 (2012) 177-183.

[4] B. Xie, B. Danielsson, Thermal Biosensor and Microbiosensor Techniques, in: Anonymous Handbook of Biosensors and Biochips, John Wiley & Sons, Ltd, 2008.

[5] Y. Lu, S. Peng, D. Luo, A. Lal, Low-concentration mechanical biosensor based on a photonic crystal nanowire array, Nat Commun. 2 (2011) 578.

[6] Y. Zhang, H. Shibru, K.L. Cooper, A. Wang, Miniature fiber-optic multicavity Fabry-Perot interferometric biosensor, Opt. Lett. 30 (2005) 1021-1023.

[7] R.F. Taylor, J.S. Schultz, Handbook of Chemical and Biological Sensors, CRC Press, 2010.

[8] A. Sassolas, L.J. Blum, B.D. Leca-Bouvier, Immobilization strategies to develop enzymatic biosensors, Biotechnol. Adv. 30 (2012) 489-511.

[9] H. Lau, Y. Lee, J. Kwon, Y. Sohn, J. Huh, J. Lim, Miniaturized Surface Plasmon Resonance Biosensor for Odorant and Pheromone Detection Using Odorant Binding Protein, Sensor Letters. 12 (2014) 961-966.

[10] R. Thusu, Strong growth predicted for biosensors market, Sens (Peterborough, NH). 27 (2010).

[11] D.W. Lubbers, N. Opitz, The pCO2-/pO2-optode: a new probe for measurement of pCO2 or pO in fluids and gases (authors transl), Z. Naturforsch. C. 30 (1975) 532-533.

[12] F. Long, C. Gao, H.C. Shi, M. He, A.N. Zhu, A.M. Klibanov, A.Z. Gu, Reusable evanescent wave DNA biosensor for rapid, highly sensitive, and selective detection of mercury ions, Biosens. Bioelectron. 26 (2011) 4018-4023.

[13] A. Barucci, S. Berneschi, F. Cosi, G. Nunzi Conti, S. Pelli, F. Quercioli, S. Soria, G.C. Righini, Fiber optic nanoprobes for biological sensing, Proc SPIE Int. Soc. Opt. Eng. 8011 (2011).

[14] O.S. Wolfbeis, Fiber-Optic Chemical Sensors and Biosensors, Anal. Chem. 76 (2004) 3269-3284.

[15] H.K. Hunt, C. Soteropulos, A.M. Armani, Bioconjugation Strategies for Microtoroidal Optical Resonators, Sensors. 10 (2010) 9317-9336.

[16] S. Song, L. Wang, J. Li, C. Fan, J. Zhao, Aptamer-based biosensors, TrAC Trends in Analytical Chemistry. 27 (2008) 108-117.

[17] A. Bossi, F. Bonini, A.P.F. Turner, S.A. Piletsky, Molecularly imprinted polymers for the recognition of proteins: The state of the art, Biosens. Bioelectron. 22 (2007) 1131-1137.

[18] V.C. Fernicola, Z.Y. Zhang, K.T.V. Grattan, Fiber optic thermometry based on Cr-fluorescence in olivine crystals, Rev. Sci. Instrum. 68 (1997) 2418-2421.

[19] J. Yue, L. Zhang, Z. Yang, Detection of ricin toxin in water using immunoassays, Int. J. Environ. Anal. Chem. 89 (2009) 821-833.

[20] S.D. Leskinen, V.J. Harwood, D.V. Lim, Rapid dead-end ultrafiltration concentration and biosensor detection of enterococci from beach waters of Southern California, Journal of Water and Health. 7 (2009) 674-684.

[21] R. Kapoor, C.-. Wang, Highly specific detection of interleukin-6 (IL-6) protein using combination tapered fiber-optic biosensor dip-probe, Biosens. Bioelectron. 24 (2009) 2696-2701.

[22] A.M. Valadez, C.A. Lana, S. Tu, M.T. Morgan, A.K. Bhunia, Evanescent wave fiber optic biosensor for Salmonella detection in food, Sensors. 9 (2009) 5810-5824.

[23] Y. Zhang, Q. Zeng, Y. Sun, X. Liu, L. Tu, X. Kong, W.J. Buma, H. Zhang, Multi-targeting single fiber-optic biosensor based on evanescent wave and quantum dots, Biosensors and Bioelectronics. 26 (2010) 149-154.

[24] J.M. Tam, L. Song, D.R. Walt, DNA detection on ultrahigh-density optical fiber-based nanoarrays, Biosens. Bioelectron. 24 (2009) 2488-2493.

[25] E. Ehrentreich-Förster, D. Orgel, A. Krause-Griep, B. Cech, V.A. Erdmann, F. Bier, F.W. Scheller, M. Rimmele, Biosensor-based on-site explosives detection using aptamers as recognition elements, Anal. Bioanal. Chem. 391 (2008) 1793-1800.

[26] N. Yildirim, F. Long, M. He, H.-. Shi, A.Z. Gu, A portable optic fiber aptasensor for sensitive, specific and rapid detection of bisphenol-A in water samples, Environ. Sci. Process. Impacts. 16 (2014) 1379-1386.

[27] Z. Zhong, M. Fritzsche, S.B. Pieper, T.K. Wood, K.L. Lear, D.S. Dandy, K.F. Reardon, Fiber optic monooxygenase biosensor for toluene concentration measurement in aqueous samples, Biosens. Bioelectron. 26 (2011) 2407-2412.

[28] J. Huang, H. Fang, C. Liu, E. Gu, D. Jiang, A novel fiber optic biosensor for the determination of adrenaline based on immobilized laccase catalysis, Anal. Lett. 41 (2008) 1430-1442.

[29] S. Belkin, Microbial whole-cell sensing systems of environmental pollutants, Curr. Opin. Microbiol. 6 (2003) 206-212.

[30] K. Hakkila, M. Maksimow, M. Karp, M. Virta, Reporter genes lucFF, luxCDABE, gfp, and dsred have different characteristics in whole-cell bacterial sensors, Anal. Biochem. 301 (2002) 235-242.

[31] K. Jia, E. Eltzov, R.S. Marks, R.E. Ionescu, Bioluminescence enhancement through an added washing protocol enabling a greater sensitivity to carbofuran toxicity, Ecotoxicol. Environ. Saf. 96 (2013) 61-66.

[32] E. Eltzov, V. Pavluchkov, M. Burstin, R.S. Marks, Creation of a fiber optic based biosensor for air toxicity monitoring, Sens Actuators, B Chem. 155 (2011) 859-867.

[33] E. Eltzov, R.S. Marks, Fiber-optic based cell sensors, Adv. Biochem. Eng. Biotechnol. 117 (2010) 131-154.

[34] E. Peña-Vázquez, E. Maneiro, C. Pérez-Conde, M.C. Moreno-Bondi, E. Costas, Microalgae fiber optic biosensors for herbicide monitoring using sol-gel technology, Biosensors and Bioelectronics. 24 (2009) 3538-3543.

[35] M.A. Arnold, Enzyme-based fiber optic sensor [4], Analytical Chemistry®. 57 (1985) 565-566.

[36] X. Wang, O.S. Wolfbeis, Fiber-Optic Chemical Sensors and Biosensors (2012), Anal. Chem. 85 (2013) 487-508.

[37] J.M. Corres, I.R. Matias, J. Bravo, F.J. Arregui, Tapered optical fiber biosensor for the detection of anti-gliadin antibodies, Sens Actuators, B Chem. 135 (2008) 166-171.

[38] J. Wallner, G. Lhota, D. Jeschek, A. Mader, K. Vorauer-Uhl, Application of Bio-Layer Interferometry for the analysis of protein/liposome interactions, J. Pharm. Biomed. Anal. 72 (2013) 150-154.

[39] S. Ramachandran, Z. Wang, M. Yan, Bandwidth control of long-period grating-based mode converters in few-mode fibers, Opt. Lett. 27 (2002) 698-700.

[40] F. Chiavaioli, P. Biswas, C. Trono, A. Giannetti, S. Tombelli, S. Bandyopadhyay, N. Basumallick, K. Dasgupta, F. Baldini, IgG/anti-IgG immunoassay based on a turn-around point long period grating, 8935 (2014) 89350V-89350V-6.

[41] M.I. Zibaii, A. Kazemi, H. Latifi, M.K. Azar, S.M. Hosseini, M.H. Ghezelaiagh, Measuring bacterial growth by refractive index tapered fiber optic biosensor, Journal of Photochemistry and Photobiology B: Biology. 101 (2010) 313-320.

[42] V. Mishra, N. Singh, U. Tiwari, P. Kapur, Fiber grating sensors in medicine: Current and emerging applications, Sens Actuators A Phys. 167 (2011) 279-290.

[43] R.M. Hawk, A.M. Armani, Label free detection of 5'hydroxymethylcytosine within CpG islands using optical sensors, Biosensors and Bioelectronics. 65 (2015) 198-203.

[44] M.D. Baaske, M.R. Foreman, F. Vollmer, Single-molecule nucleic acid interactions monitored on a label-free microcavity biosensor platform, Nat. Nanotechnol. (2014).

[45] T. Lin, M. Chung, Detection of cadmium by a fiber-optic biosensor based on localized surface plasmon resonance, Biosensors and Bioelectronics. 24 (2009) 1213-1218.

[46] J. Cao, M.H. Tu, T. Sun, K.T.V. Grattan, Wavelength-based localized surface plasmon resonance optical fiber biosensor, Sensors Actuators B: Chem. 181 (2013) 611-619.

[47] D.T. Tran, K. Knez, K.P. Janssen, J. Pollet, D. Spasic, J. Lammertyn, Selection of aptamers against Ara h 1 protein for FO-SPR biosensing of peanut allergens in food matrices, Biosensors and Bioelectronics. 43 (2013) 245-251.

[48] L. Razquin, C.R. Zamarreno, F.J. Munoz, I.R. Matias, F.J. Arregui, Thrombin detection by means of an aptamer based sensitive coating fabricated onto LMR-based optical fiber refractometer, Sensors, 2012 IEEE. (2012) 1-4.

[49] C.R. Zamarreno, I. Ardaiz, L. Ruete, F.J. Munoz, I. Matias, F.J. Arregui, C-reactive protein aptasensor for early sepsis diagnosis by means of an optical fiber device, SENSORS, 2013 IEEE. (2013) 1-4.

CHAPTER 2. Deposition of thin-films to generate resonant sensing phenomena

2.1. Introduction. Thin-films

Nothing in this work can be understood without the deposition of thin-films. As the name itself denotes, a thin-film can be defined as a nanometer sized layer of a material deposited on top of a surface, with the goal of obtaining a desired behavior in the resulting coated substrate [1,2].

Normally, the size of these thin-films range from nanometers to a few micrometers, depending on the application they are designed for [2]. To achieve this, there is a need for working with nanotechnology-based deposition techniques. Nanotechnology can be defined as the science of 'nano'. This means, working with sizes up to a billion times smaller than a meter. Nanotechnology could be defined as the study, design, creation, synthesis, manipulation and application of materials, equipment and functional systems by means of controlling the matter in the nanoscale, and also the exploitation of its phenomena and properties [3]. When working with these sizes, it has been discovered that matter behaves in a different way than it would in its natural state. Consequently, the interest in studying and trying to take advantage of these properties is increasing every day.

Among the advantages that working with nanotechnology offers, it is important to remark the considerable reduction in the size of the equipment, lower costs in materials, production, transportation, etc, all of them due to the fact of scaling to so small sizes. On the other hand, there are some issues to be solved, as the possible intoxications derived from working with substances that can be inhaled by the organism leading to a new kind of illnesses, or the possibility of using it for bad purposes. In this sense, there are many issues regarding nanotechnology, although it seems to be that side effects could be mostly avoided by taking the corresponding safety measurements.

During the last decades, a wide variety of nanotechnology-based deposition techniques has been developed. Some examples of this kind of methods are the three that are presented during this thesis: layer-by-layer assembly [4], sputtering [5] and spin-coating [6]. But there are also other methods to be taken into account, such as molecular beam epitaxy (MBE), electron beam evaporation, Langmuir-Blodgett [7], sol-gel method (dip-coating) [8], chemical/physical vapor deposition [9,10] and so on. In this sense, Fig. 2.1 reflects the wide spectrum of nanotechnology-based deposition techniques currently being developed.

From an engineering and industrial point of view, the development and improvement of thin-film deposition techniques has led to many applications. Currently, there is an interesting application of thin-films deposition in photovoltaics, in order to obtain higher efficiency solar cells that lead to accumulate and save energy [11]. Another current interesting application is the development of graphene/silicon nitride (and more) functionalized layers (essentially, atomic layers), in order to achieve electronical and flexible devices that people can use for communication, work and joy purposes [12]. But there are also daily applications, such as the design of self-cleaning surfaces [13] (see Fig. 2.2a) or hydrophobic/hydrophilic thin-films to avoid water drops when it is raining [14]. There are also biomedical applications, such as the development of anti-bacterial thin-films that prevent from tough illnesses [15] (see Fig. 2.2b), or the development of biocompatible prosthesis [16], so that the prosthesis inserted in the human body are even less aggressive when reacting with the biological tissues.
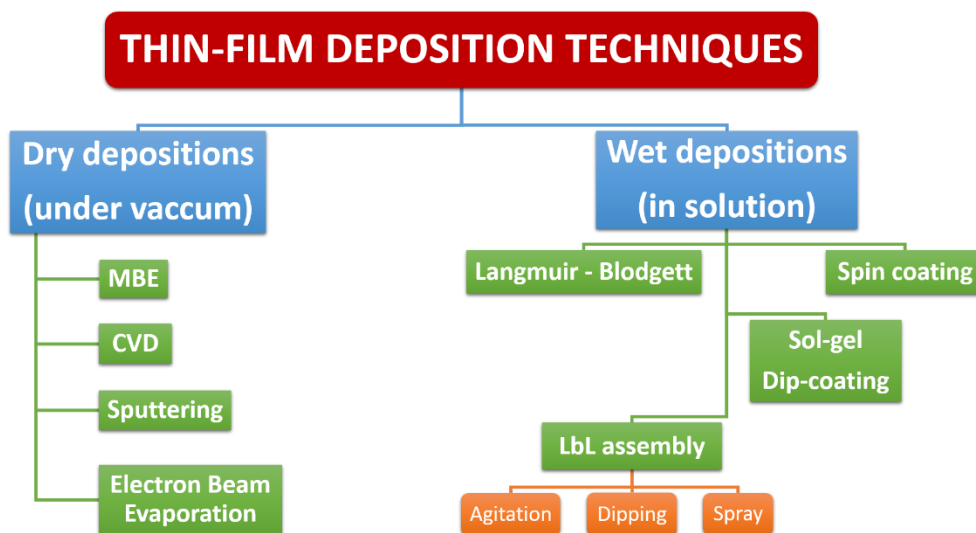
***Fig. 2.1.** Dry and wet methods to deposit thin-films using nanotechnology.*

Regarding the main use of thin-films in this thesis, their deposition on optical waveguides, there is an increasing interest in developing such devices, since they permit to obtain new sensing applications and other optical properties of interest. Thin-films can contribute to enhance the properties of these optical/photonic waveguides in order to obtain two main research fields: communications and sensors. Thus, thin-films can generate patterns that turn simple optical waveguides into tunable filters [17], but they also can be deposited

onto optical substrates to design sensors, giving specificity to a wide variety of physical/chemical/biological phenomena, such as solar radiation, moisture, pH, gases, refractive index or any type of illnesses [18-20].

In this sense, next section will show the main thin-film deposition techniques used during this thesis. For each method, the working principle will be presented first and some applications involving their use will be mentioned. Then, the use of thin-films to generate the sensing phenomena analyzed during this thesis: electromagnetic resonances, will be studied.
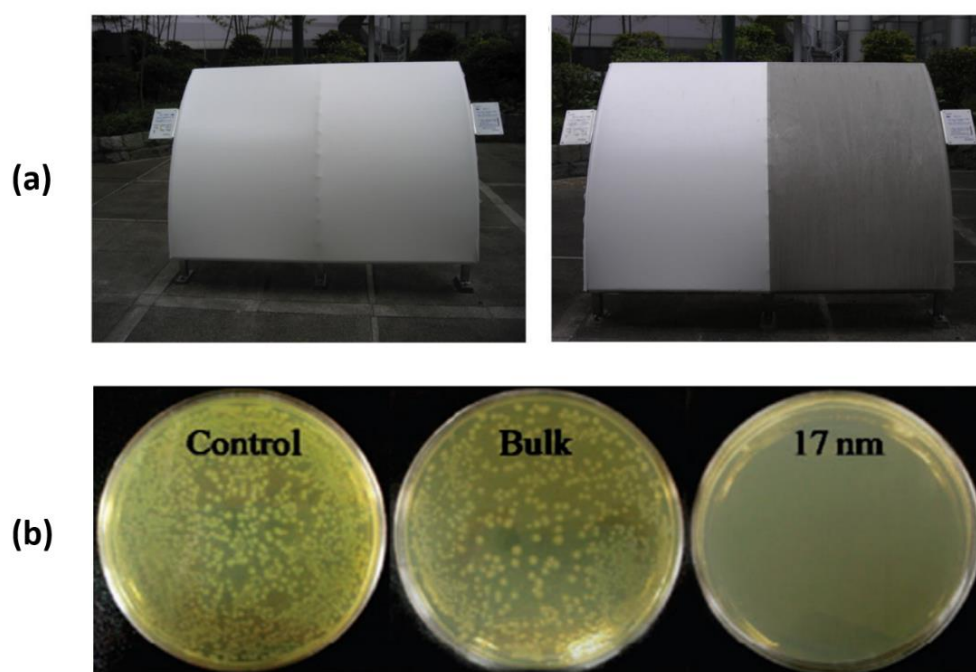
Fig. 2.2. *(a) Self-cleaning TiO$_2$-based thin-film on a tube to avoid environmental corrosion. After 4 years, the left side of the structure remains like the first day, whereas the right side has been affected [13]. (b) An antibacterial polymer-based thin-film to prevent E. coli growth [15]. No bacteria presence is observed after depositing 17 nm of thin-film, in comparison with bulk and control samples.*

2.2. Deposition of thin-films by means of nanotechnology techniques

Along this thesis, three main techniques have been used to deposit thin-films onto the desired substrates. The following lines try to briefly summarize the state of the art in every of them, in order to have an idea of their uses.

2.2.1. Layer-by-layer assembly

This deposition technique is also known as molecular self-assembly [21], electrostatic self-assembly (ESA) [15] or layer-by-layer (LbL) assembly [22], although, for the sake of simplicity, it will be called LbL-assembly henceforward. This method takes advantage of a property of the matter in these sizes called self-assembly. Certain type of molecules are able to orient and assemble spontaneously, forming complex structures, such as DNA, proteins and many biological and organic compounds. To address this, there is a need for a high purity degree in the substances. The attraction forces generated during the assembly is given by the nature of the binding between molecules and they will be stronger or weaker depending on whether these binds are covalent, ionic, hydrogen or Van der Waals bonding, etc.

LbL-assembly is produced due to electrostatic attraction forces between molecules. As a consequence, it is usual to use substances which may present some kind of charge when dissolved, leading to positive or negative compounds. Thus, several layers of positive and negative materials can be assembled, forming a thin-film in a nanometer scale onto the desired substrate. This characteristic is very interesting in terms of fabrication, since an accurate control of the process can be done, stopping the deposition when desired. The final results of the process will strongly depend on how the deposition is designed.

Among the advantages this technique gives, it is interesting to remark the versatility, not only in the materials to be deposited (polymers, biological substances, nanoparticles,…) but also in the substrates used and their size, since the deposition can be carried out in a high quality manner as long as the dipping recipient is large enough. In this sense, LbL-assembly can be performed onto a wide variety of substrates, such as ceramics, metals and polymers of different shapes and forms, including planar substrates, prisms, concave and convex lenses and even optical waveguides [23], as it will be shown during this thesis. However, it is important to know which compounds are susceptible to be deposited by this method, because not all the substances can be charged to be deposited. In particular, the main group of substances that can be used for LbL-assembling is that formed by polyelectrolytes.

The LbL-assembly technique involves different steps, which can be scaled to an industrial level due to their easiness to be carried out. In Fig. 2.3 this process is schematically described. First of all, the substrate is cleaned and treated to create a charged surface. After this step, the substrate is alternately dipped into solutions of cationic and anionic substances to create a multilayer thin-film. If the initial charge of the substrate is positive and the materials to deposit are polyelectrolytes,

the first monolayer will be a polyanion, whereas if it is negative, the first deposited monolayer will be a polycation. The result of a positive monolayer and a negative monolayer will be called "bilayer" henceforward. In this way, a multilayer structure is formed by electrostatic attraction between each bilayer and the bilayer previously deposited. After each polyelectrolyte immersion, the substrate is rinsed in ultrapure/deionized water (18.1 MΩ/cm) to remove the excess of material. At the end of the process, the molecular species of the anionic and the cationic components and the long-range physical order of the layers determine the resulting coating properties.
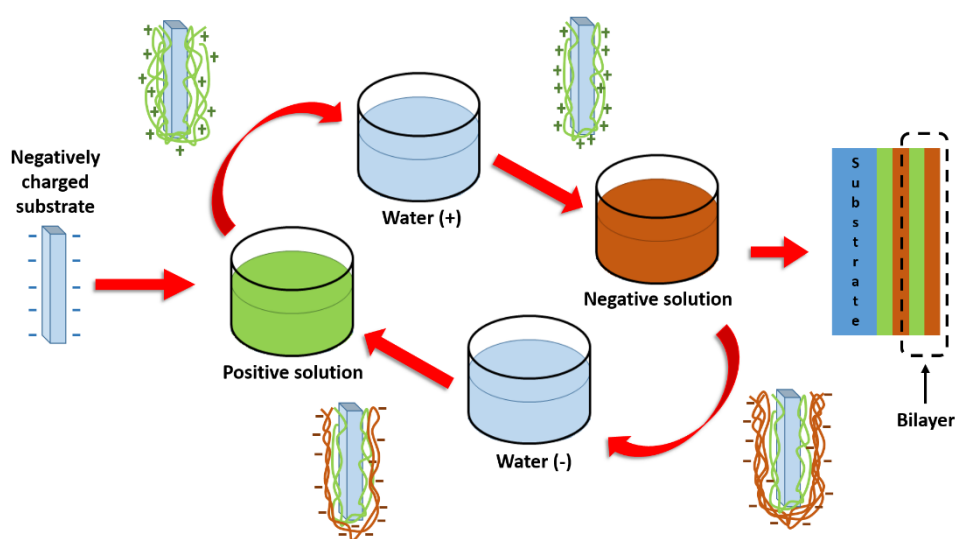
Fig. 2.3. *Schematic of a layer-by-layer assembly deposition technique.*

It is important to note that the polyanions and polycations overlap each other at molecular level, and this produces a homogeneous optical material. The composition and thickness of an individual bilayer can be controlled by adjusting the deposition parameters (concentration of solutions, pH, temperature, immersion times, etc).

To perform a classic LbL-assembly, the first approach is to prepare the positive and negative solutions and alternately immerse the substrate in them. However, there is an increasing interest in depositing using LbL-assembly but varying not only the deposition parameters but the way of depositing. In this sense, instead of just dipping, the polyelectrolytes can be sprayed, like in "spray-coating" [24] or stirred while depositing, like in agitating LbL-assembly [25]. The goal of spray-coating is to increase the smoothness of the thin-film by depositing little drops of material, what is an enhancement in comparison to just dipping the

substrate in the solution. A curious example of a thin-film deposited by LbL-spray-coating can be observed in Fig. 2.4 for a titanium oxide/silica matrix. In the case of stirring LbL-assembly, the goal is to obtain a more homogeneous solution at the same time the materials are deposited, so that the quality of the thin-film remains more constant than in a classic process.

Whichever the type of deposition desired, LbL-assembly is one of the most common utilized techniques to functionalize surfaces and obtain the desired behavior. In particular, there are LbL-assembly depositions to obtain organic LEDS [26], superhydrophobicity [27] or with application as anti-fog [28]. In the biomedical field, the majority of the applications are related to drug delivery structures [29], biocompatibility [30] and trying to adsorb bioreceptors with the objective of designing biosensors [31].

(a)   (b)   (c)
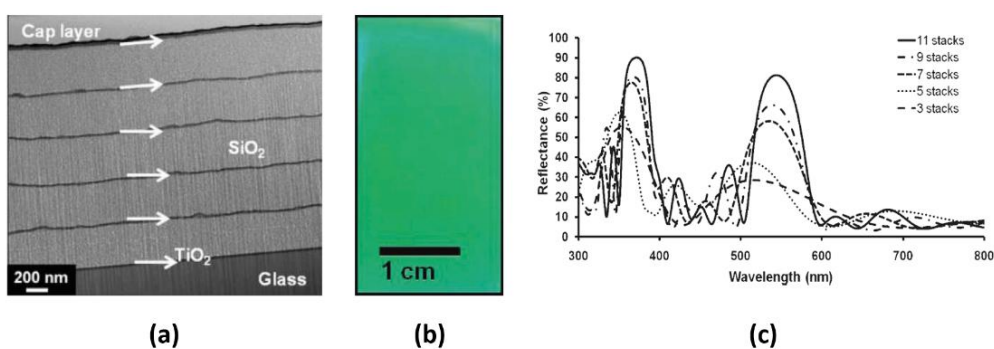
Fig. 2.4. TiO_2/SiO_2 *nanostructure deposited by LbL-spray-coating. The thinner layers are TiO_2 whereas the thicker layers are silica. (a) TEM image and (b) microscope image of the resulting thin-film. (c) Reflectance spectrum as a function of the increasing thickness [32].*

2.2.2. Sputtering

Sputtering is a phenomenon in which atoms are pulled out from a solid material (known as target) due to its bombardment by particles previously energized. It is commonly utilized for thin-films deposition, physical etching and analytical techniques [5]. There are several ways to deposit substrates by sputtering. Radiofrequency sputtering is one of them [33], although one of the most used from an easiness to handle and economic point of view (this work does) is that based on the application of a high voltage polarization between two electrodes, using an inert gas to carry out the deposition [34].

Fig. 2.5 presents a schematic of what happens during a sputtering process on a substrate by using the high voltage polarization method [34]. First, the substrate is cleaned in order to remove impurities and dirtiness from its surface. Then it is introduced in a vacuum chamber, between the target (acting as a cathode) and an anode connected to ground. When the deposition begins, the sputter equipment makes vacuum inside the chamber. Typically, a noble gas (i.e. Argon) is then released into the chamber increasing the pressure. The fact of introducing a noble gas corresponds to the need for developing the process in an inert atmosphere, so that both the target and the substrate are not contaminated by external agents. Moreover, Argon is chosen because in spite of being a noble gas and, therefore, difficult to alter, it is easy to ionize with high voltage.

Hence, after stabilizing the pressure and voltage conditions into the chamber, the deposition process begins. Due to the high voltage reached between the target and the ground, an electron current is generated, which ionizes the Argon. The electric field attracts the ionized Argon to the cathode starting a bombardment of the target and, consequently pulling out material from it. The released material follows the electric field created and is deposited onto the substrate. Moreover, during this process some of the ionized Argon atoms can recover electrons and become stable. When this happens, a recombination is produced and a photon is released. Consequently, a colored plasma can be observed into the chamber during the deposition. In addition to this, the free electrons can be accelerated, producing more collisions against other Argon atoms that permit to pull out more material from the target. Finally, the materials are deposited onto the substrate by condensation.
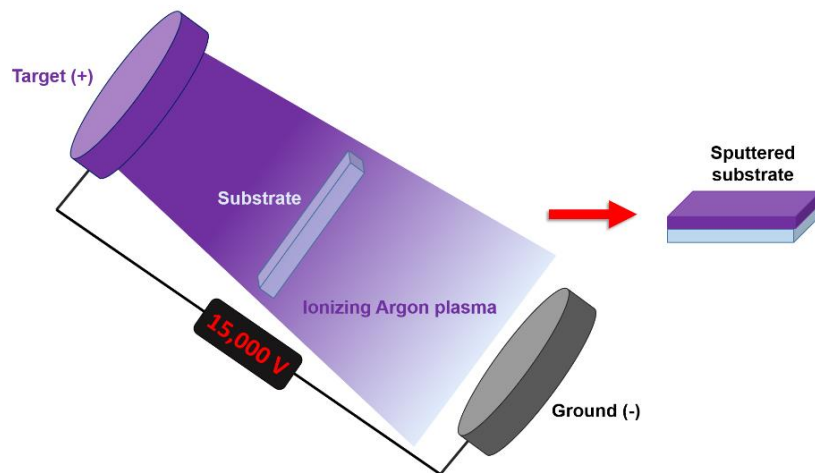

Fig. 2.5. *Schematic of a sputtering deposition technique.*

Depending on the parameters the sputter equipment has been scheduled with, different qualities and types of deposition can be obtained. Specifically, the average number of atoms pulled out from the target per incident ion depends on the ion incident angle, the ions energy, the ions masses, the target atoms and the surface binding energy of the target atoms.

This technique is commonly utilized in thin-film depositions for jewelry [35] and electronics, mainly, to fabricate transistors or PIN diodes on top of previously masked surfaces [36]. It is also frequent to deposit different materials on top of silicon wafers or glassy substrates. As a biomedical application, sputtering is used to produce layers that generate sensing phenomena. Once deposited and after depositing a sensitive biological element, they can be used to detect biological analytes [37].

2.2.3. Spin-coating

Similarly to sputtering, spin-coating is a procedure used to deposit uniform thin-films on flat substrates. But in this case, the equipment used for spin-coating is called a spin-coater, or simply, a spinner.

Fig. 2.6 shows a schematic of what happens when a substrate is deposited by spin-coating. Basically, a small amount of coating material is applied on the center of the substrate, which can be spinning at low speed or not spinning at all. The substrate is then rotated at high speed in order to spread the coating material by means of centrifugal force.

The effect of the spinning, essentially, centrifuge force, makes the coating material to spread to the edges of the substrate, at the same time the layer thickness decreases until desired. The applied solvent is usually volatile, and simultaneously evaporates, although it is acceptable to anneal after the spinning. In spin-coating technique, an increase in the angular velocity will lead to a thinner thin-film. The thickness of the film also depends on the viscosity and concentration of both the solution and the solvent.

Spin-coating is widely used in microfabrication of oxide layers using sol-gel precursors, where it can be used to create uniform thin-films with nanoscale thicknesses [38]. It is also used in photolithography, to deposit photoresist layers around 1 micron thick.

As occurs with sputtering, spin-coating is commonly deposited on any type of substrates to create electrodes or another class of thin structures on them. But because there is no need for inducing voltages or magnetic fields, it is also possible

to deposit polymer or metal oxide-based thin-films to achieve a broader range of applications.
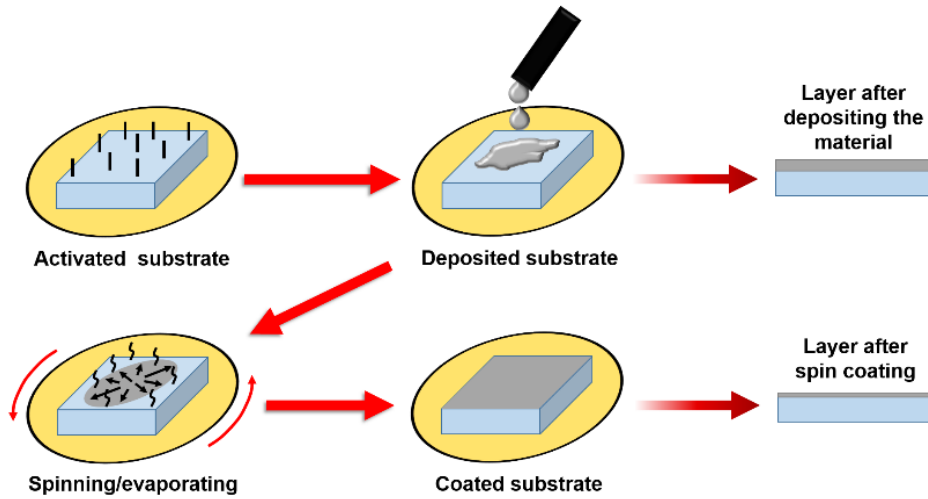
Fig. 2.6. *Schematic of a spin-coating deposition technique.*

2.3. Generation of electromagnetic resonances using thin-films

Before describing the light propagation in optical structures deposited with a thin-film, it is interesting to take a look at the properties of the thin-film itself.

First, it is important to take into account that each specific material owns intrinsic characteristics that make them propagate the light in different conditions. This characteristics can be modeled by the complex dielectric permittivity ($\hat{\varepsilon}$) [39]. Thus, for a generic material, its permittivity is given by Eq. (2.1):

$$\hat{\varepsilon} = \varepsilon' + \varepsilon''i \tag{2.1}$$

where ε' and ε'' are the real and imaginary parts of the medium's dielectric permittivity $\hat{\varepsilon}$ and both are frequency dependent. The former is related to the stored energy within the medium, whereas the latter is related to the loss of energy within the medium. In fact, $\hat{\varepsilon}$ is the well-known quotient between both displacement (D) and electric field (E) magnitudes, something widely explained in the fundamentals of electromagnetism.

The dielectric permittivity can also be expressed as a function of the refractive index and the absorption of the materials. The **refractive index (n)** is related to the inner molecular structure of the material, which makes the speed of light (denoted as v) be different than when propagating in vacuum (denoted as c). Thus, the refractive index is normally expressed as the ratio n = c/v. On the other hand, materials can absorb energy from the light. Such phenomenon is represented by the extinction coefficient or **absorption coefficient (k)**. Therefore, Eq. (2.1) can be also expressed as Eq. (2.2) [40]:

$$\hat{\varepsilon} = N^2 = (n + ki)^2 = n^2 - k^2 + 2nki \qquad (2.2)$$

where *N = n + ki* is known as the complex refractive index of the medium/material. By identifying Eqs. 2.1 and 2.2 it is possible to obtain the values for ε' and ε'', expressed in Eqs. 2.3 and 2.4.

$$\varepsilon' = n^2 - k^2 \qquad (2.3)$$

$$\varepsilon'' = 2nk \qquad (2.4)$$

Taking into account the previous considerations on the materials losses, it is important to highlight that every material not owning or owning negligible absorption properties (dielectric materials, generally) will have a null imaginary part and, therefore, both its permittivity and refractive index will be real magnitudes. On the other hand, pure metals, materials with metallic characteristics or similar will own an imaginary component due to these conductive characteristics since they absorb part of the light. Consequently, $\hat{\varepsilon}$ and *N* will be complex numbers in those cases. The relationships among *n, k,* ε' and ε'' are shown below, in Eqs. (2.5) and (2.6) by simply solving the system of equations formed by (2.3) and (2.4):

$$n = \sqrt{\frac{\sqrt{\varepsilon'^2 + \varepsilon''^2} + \varepsilon'}{2}} \qquad (2.5)$$

$$k = \sqrt{\frac{\sqrt{\varepsilon'^2 + \varepsilon''^2} - \varepsilon'}{2}} \qquad (2.6)$$

It is interesting to take into account the previous relationships, since depending on the different parameters, light will experiment the corresponding changes during its propagation within the materials. Nevertheless, there is also a need for reviewing the Snell's Law, since quite many of the light waveguides and, particularly, those in this thesis, use this phenomenon to propagate the light through them.

Thus, Fig. 2.7 represents a schematic typically used to describe the Snell's Law. From the ray theory point of view, when an incident beam strikes the interface between two media 1 and 2, in part is reflected and in part refracted with angles θ_3 and θ_2 respectively. Applying trigonometry to these considerations, it is simple to derive the Snell's Law. One of the most interesting conclusions is the possibility of calculating the necessary incident angle to reflect the light totally, known as "critical angle". For incident angles higher than the critical, light experiments the phenomenon of **"total internal reflection"** (TIR). This is the working principle of light propagation in optical fibers, the main optical substrate utilized in this thesis, and the same applies for most of the current light waveguides.

Once these concepts have been revised, it is possible to understand what happens when the light travels through a material and hits the interface between this material and another with different refractive index (i.e. an air – water interface). In particular, during this thesis the analysis will focus on the light propagation when a wave front faces the interface between a silica substrate (a dielectric material) and an absorbing thin-film made of a material deposited on it. In this sense, both permittivity and refractive index values will be real for the substrate, whereas depending on the thin-films deposited, the materials will present complex refractive indices.

$$n_1 \sin\theta_1 = n_2 \sin\theta_2$$

$$\theta_1 = \theta_3$$

Incidence critical angle for TIR regime

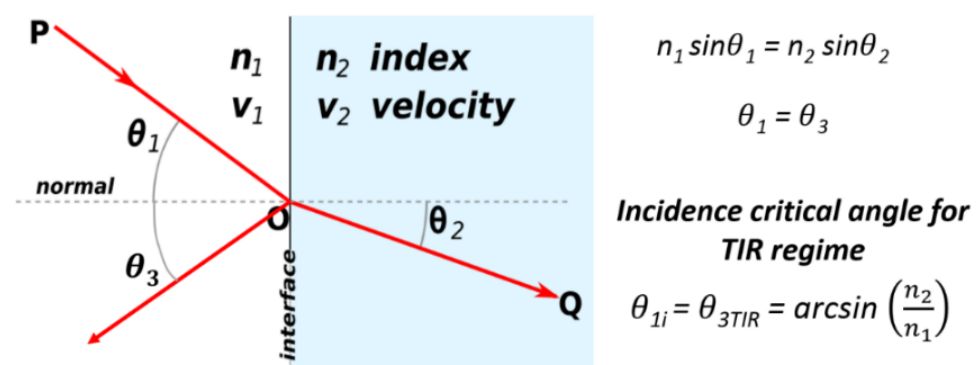$$\theta_{1i} = \theta_{3TIR} = arcsin\left(\frac{n_2}{n_1}\right)$$

Fig. 2.7. *Schematic of Snell's Law and conditions for TIR regime.*

The previous considerations have been extracted from a classic optics point of view, which means using the ray theory. However, since the substrates used during this thesis are light waveguides, it is better to explain what is happening from a mode theory point of view [41]. In this sense, it is already known that the interface between two media with different properties supposes a discontinuity when describing the light propagation. If an electromagnetic wave is propagating along a silica medium and suddenly finds another medium with different propagation conditions (i.e. air), it seems logical to establish some boundary conditions that ensure the electromagnetic field continuity when solving the Maxwell equations. Thus, assuming this continuity, the energy of those modes allowed to propagate has to be transferred somewhere following the energy conservation principle. Solving Maxwell equations is not the objective of this thesis, but the corresponding mathematical formulae can be found elsewhere [41] and, by following the development, it is possible to prove that there is a tiny region where the standing wave decays exponentially out of the waveguide. This standing wave is called **"evanescent field"**. Moreover, there is a penetration length/depth, d_p, which is defined as the distance where the evanescent field is reduced to 1/e. This distance can be calculated by evaluating Eq. (2.7) [42]:

$$d_p = \frac{\lambda}{2\pi\sqrt{n_1^2 sin^2\phi - n_2^2}} \qquad (2.7)$$

where λ is the free-space wavelength of incident light, n_1 and n_2 are the refractive indices of the materials involved in the light guidance and ϕ is the light incidence angle at the interface between both media.

The evanescent field can be taken in advantage for many applications, as shown in [43]. In fact, during this thesis, it will be shown how to use and modulate it by depositing thin-films onto optical substrates.

However, since light propagates as an electromagnetic field, what is obtained after solving the Maxwell equations is a combination of propagation modes. Each of this propagation modes generates its own evanescent field. Consequently, the evanescent field of the waveguide is actually a superposition of these propagation modes, each one contributing with its own evanescent field in a very short distance out of the waveguide.

Now, if a thin-film of a certain material is deposited onto the silica substrate, its behavior will be influenced by the evanescent field of the waveguide. Indeed, part of the energy propagated in these modes will be transferred to the

thin-film. Under these conditions, some wavelengths can suffer strong attenuation whereas the opposite is true for the rest. This leads to a resonant phenomenon called electromagnetic resonance (EMR).

Therefore, during this thesis, an **electromagnetic resonance (EMR)** will be defined as a physical phenomenon obtained by the coupling of light modes from a silica waveguide where they are initially propagating to the thin-film deposited on it. The idea is that those modes that have been coupled to the deposited thin-film are modulated by the thin-film's intrinsic characteristics, intimately related to its frequency dependent permittivity ($\hat{\varepsilon}$) and, therefore, to its refractive index and absorption. Moreover, this coupling of modes is produced in a restricted wavelength range and it is no longer returned to the original waveguide. So when observing the obtained spectrum in the output signal, a dip is obtained for that wavelength range. At the same time, both the substrate and the thin-film set the adequate conditions to modulate the coupling to the thin-film, which may lead to a wide variety of phenomena and applications [44].

An example of EMRs generation is presented in Fig. 2.8. Here, a glassy substrate (silica) with refractive index N_3 is coated with a thin-film of refractive index N_2, following the Krestchmann configuration [45]. Surrounding this structure, there is a thin-film of certain material as external medium, with refractive index N_1. Hence, when light tries to propagate either in 1-2 interface or in 2-3 interface, the refractive index differences will allow an energy transfer (coupling of light modes) from the silica substrate to the thin-film. Due to this, the corresponding EMRs will be generated. Consequently, a dip or attenuation band will show up in the optical spectrum, when looking at the detector placed on the other side of the set-up. Then, a further tracking or characterization of the EMR behavior can be done.

Where and how these EMRs are guided is something to be discussed in the following subsections. As it has been mentioned, EMRs can be generated and characterized by adsorbing thin-films onto optical waveguides [46]. Depending on the boundary conditions applied to the Maxwell equations in these waveguides, three main EMRs families can be distinguished after solving them: long-range exciton-polaritons (LRSEPs) [47], surface plasmon resonances (SPRs) [48], and lossy mode resonances (LMRs) [49]. There are several facts that make them distinguish one from another. They have been summarized in Table 2.1. Also, several examples of these 3 different types of resonances are given in Fig. 2.9.
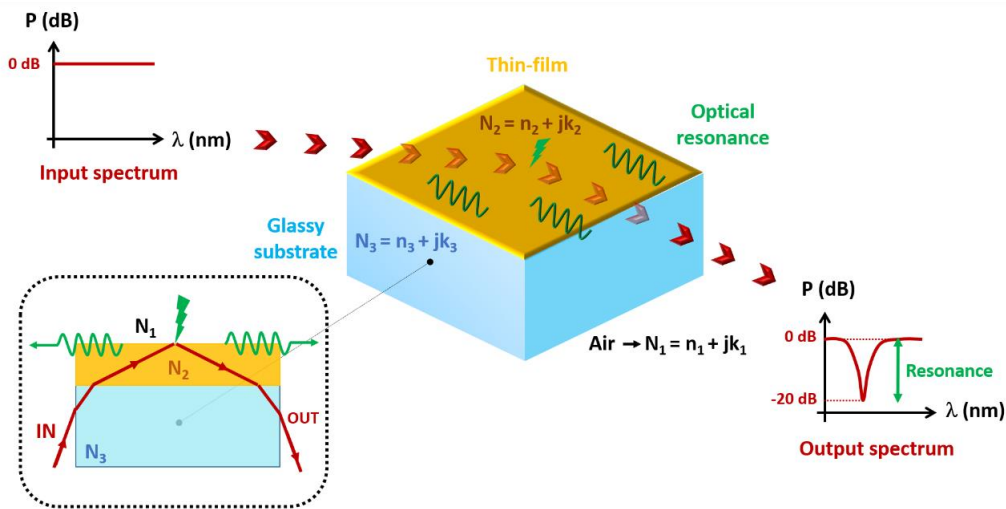
Fig. 2.8. *Krestchmann configuration to obtain electromagnetic resonances. Inset: cross-section of the set-up, to see the influence of the different media in the light.*

2.3.1. Long-range surface exciton-polaritons (LRSEPs)

Long-range surface exciton-polaritons are electromagnetic surface modes confined at the interface of a thin-film surrounded by a homogeneous dielectric (i.e. silica) [50]. The potential of this technology is still to be studied and maybe because of that they are receiving less attention by the scientific community. In order to propagate an LRSEP, it is necessary to have a very high imaginary part of the permittivity (which means high conductivity and, therefore, they are usually generated with metallic thin-films) and a very low real part, which means to have similar values in both *n* and *k* in magnitude (see Fig. 2.9a). However, the study of these resonances falls beyond the scope of this thesis, so they will no longer be analyzed.

2.3.2. Surface Plasmon Resonances (SPRs)

SPRs are generated when the real part of the thin-film permittivity is negative and higher in magnitude than both its own imaginary part and the real part of permittivity of the material surrounding the thin-film (i.e. the optical waveguide and the surrounding medium in contact with the thin-film), as summarized in Table 2.1 [46,48].

In accordance with the previous definition of EMR, the energy transfer (also known as coupling) occurs between the evanescent field of the light propagating

within the substrate and a surface plasmon on the thin-film surface. A surface plasmon is the particle for describing electron density waves in the thin-film surface. A photon is the particle for describing light waves. Thus, an incident light photon at a determined wavelength (optical frequency) will be converted into a plasmon in the thin-film and it will propagate parallel to the light direction of propagation. This energy is no longer returned to the substrate, so if this occurs for a determined number of wavelengths, this will be visualized as a dip in the optical spectrum when detecting. This dip is what is called surface plasmon resonance. A dip in transmission is the same as a rise in absorption, as represented in Fig. 2.9b.

Due to these metallic characteristics, it is usual to induce SPRs by fabricating a thin-film of sputtered noble metals such as gold, silver or copper but also with sodium, aluminum or indium. However, indium is too expensive, sodium too reactive, copper and aluminum provide broad SPRs and silver oxidizes easily. This reinforces gold as the most practical metal, due to its stability under many environmental conditions.

SPRs can be excited using the Krestchmann configuration proposed in Fig. 2.8. However, there is a need for launching monochromatic and TM-polarized (or p-polarized) light to excite the plasmonic waves. The reason for this is that an SPR can be understood as conductivity fluctuations of collective surface density charge oscillations. These charge densities have to be excited by an external electric field. TM-polarized light is the only polarization that contains an electric field component perpendicular to the silica - thin-film interface. Therefore, TM-polarizing is the only way to obtain these charge densities and, consequently, to excite the SPRs [51]. Thus, the light must be previously polarized, leading to an increase in the final device cost.

Additionally, as the thin-film increases, the metal absorption also increases and there is a hardly visible shift in wavelength. This phenomenon is produced because there is a pure metal thin-film over the substrate. A pure metal determines the plasmons oscillations at one frequency/wavelength predominantly. Consequently, only the photons with that precise energy are allowed to induce the resonance. Moreover, this situation remains as long as the thin-film thickness is in a range between 10 and 200 nm [52]. For thickness values higher than this, the evanescent wave is not able to reach the thin-film surface, so the plasmons cannot be excited and the whole system behaves as a new waveguide, making the resonance to disappear.

The fact of not being able to shift in wavelength while the resonance is generated supposes a drawback when designing SPR-based devices, since it is not possible to tune the resonances for a specific application. That is why, applications

based on the embedding of gold nanoparticles (nanospheres or nanorods, mainly) in a thin-film have been showing up lately [53,54] (see Fig. 2.9b). Working with nanoparticles instead of a plane and homogeneous thin-film makes the SPRs to be localized in the particles. The particles vibrations excite other particles and a localized SPR (LSPR) is obtained. The problem with LSPRs is that, since these particles are not always the same size, the width of the resonance broadens. However, depending on the application, the benefits allow to lose resolution in the phenomenon. Most of LSPRs are induced by gold nanospheres and are normally centered around 520 nm. In the case of gold nanorods, two LSPRs are generated at around 520 nm and 780 nm respectively. The second LSPR seems to be more sensitive to changes in refractive index, since the wavelength shift is higher than that presented by the LSPR at 520 nm. This is good in terms of improving the high sensitivity of SPRs, which can reach 57,000 nm/RIU [55] with a resolution limit of 10^{-7} RIU [56].

2.2.3. Lossy Mode Resonances (LMRs)

A review of the most recent updates for lossy mode resonances is done in the following lines.

LMRs are generated when the real part of the thin-film permittivity is positive and higher in magnitude than both its own imaginary part and the real part of the permittivity of the material surrounding the thin-film [57] (see Table 2.1). This kind of EMRs have received several names, such as long-range guided modes [46] or lossy modes [58]. The last term is used during this thesis, because there is a light coupling from a waveguide to a thin-film with complex refractive index. Consequently, modes guided in the core own a complex effective index, which is considered by some authors as a lossy mode [40,58]. This notation, lossy mode, is a specification of the group of guided modes. The phenomenon occurs when one of these lossy modes is near to cut-off in the thin-film [58]. Therefore, the corresponding resonances will be called "lossy mode resonances" or "LMRs" henceforward.

As it can be observed in Table 2.1, not only the conditions for the permittivities are shown, but also the corresponding conditions for the involved complex refractive indices. However, it may be difficult to have an idea of what they look like in a graphical representation. That is why Fig. 2.10 is plotted, so that these conditions can be distinguished at first sight. The horizontal axes represents the real part (n) whereas the vertical axes corresponds to the imaginary part (k). Given the conditions for the permittivities, the corresponding conditions for the refractive

index can be deduced. First, it is easy to notice that LRSEPs can be excited when the refractive index of the material is quite high. SPRs are excited when the imaginary part of the thin-film's refractive index is higher than 2.4 times its own real part and also than that of the substrate, something that typically happens for pure metals. Symmetrically, LMRs are excited when the real part of the thin-film's refractive index is higher than 2.4 times its own imaginary part and also than that of the substrate. These conditions are met typically by polymers and metal oxides, as it will be shown during this thesis. Along this whole document, the substrates are made of silica. The refractive index for silica is N = n = 1.45 and it does not vary so much between 400 and 2000 nm [59,60], so the approximation made by Table 2.1 and Fig. 2.10 can be assumable.

TYPE OF RESONANCE	$\hat{\varepsilon}$ CONDITIONS	n,k CONDITIONS $\forall\, n > 0, k > 0$
LRSEP Long Range Surface Exciton-Polariton	$\varepsilon_2' \approx 0$ $\varepsilon_2'' \gg 0$	$n_2 \approx k_2$ $n_2, k_2 \gg 0$
SPR Surface Plasmon Resonance	$\varepsilon_2' < 0$ $\|\varepsilon_2'\| > \|\varepsilon_2''\|$ $\|\varepsilon_2'\| > \|\varepsilon_3'\|$	$k_2 > (\sqrt{2} + 1)n_2$ $n_2^2 - k_2^2 > 1.45$
LMR Lossy Mode Resonance	$\varepsilon_2' > 0$ $\|\varepsilon_2'\| > \|\varepsilon_2''\|$ $\|\varepsilon_2'\| > \|\varepsilon_3'\|$	$k_2 < (\sqrt{2} - 1)n_2$ $n_2^2 - k_2^2 > 1.45$

Table 2.1. *Summary of the propagation conditions to generate electromagnetic resonances onto thin-film-deposited silica substrates.*

As examples of EMRs, LMRs also fulfill the boundary conditions that solve the Maxwell equations, in order to describe the coupling of modes from those modes propagating in the substrate to the thin-film. Hence, the conditions indicated in Table 2.1 are necessary and sufficient. In this sense, the explanation of the LMRs generation is summarized in the following lines.

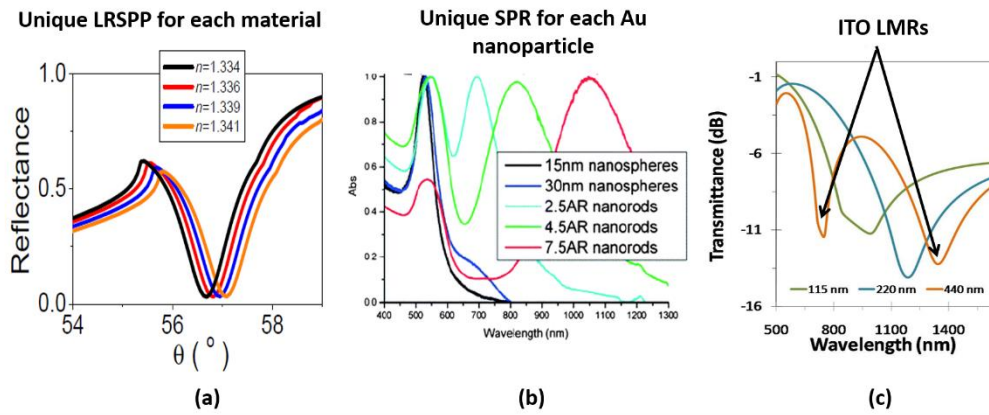***Fig. 2.9.*** *Different shapes of EMRs. (a) Refractive index sensor based on LRSEPs generated at 530 nm for p-polarized light [50]. (b) SPRs obtained depending on the nanoparticle shape [61]. (c) Generation of LMRs as a function of the increasing thin-film [62].*
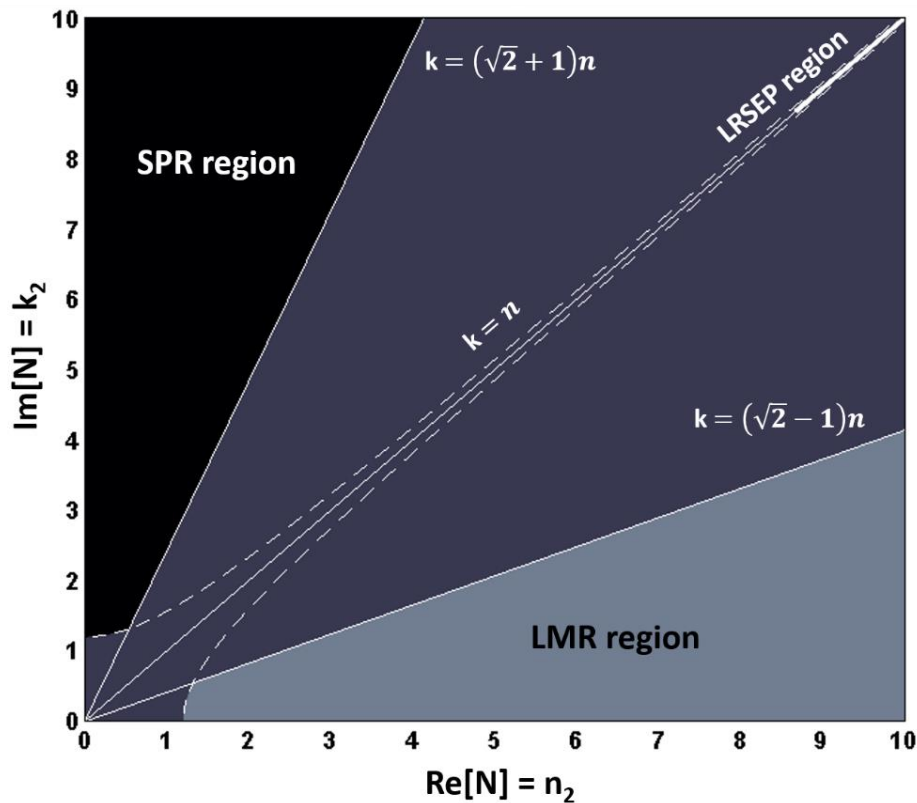

Fig. 2.10. *Representation of the n,k plane for the generation of electromagnetic resonances. The complex refractive index is defined as N=n+ki.*

The general idea underlying LMRs is that, as the thin-film thickness increases, a mode propagating in the waveguide starts to be guided in the thin-film. When this mode is near cut-off there is an important coupling of light from the waveguide to the thin film. The same idea observed as a function of thickness can be translated as a function of wavelength. For specific wavelength ranges there is a mode near cut-off. Consequently, there will be a lack of optical power at these wavelength ranges, which will be translated into dips in the optical spectrum. Fig. 2.9c shows an example of this kind of attenuation bands.

Moreover, in spite of the recent research to study the LMRs behavior under the Krestchmann configuration [63], most of the publications related to LMRs have been developed by depositing thin-films onto optical fibers. Therefore, the description of the light propagation for the LMRs during this thesis will be addressed from a fiber-optics point of view.

From the previous considerations, some important aspects concerning LMRs and SPRs must be addressed.

The first one is the kind of materials that can be deposited to generate them. By looking at both Table 2.1 and Fig. 2.10, as long as the real part of the thin-film permittivity is positive and the absorption coefficient (k) is low, many materials except pure metals (as in SPRs) can induce LMRs. For instance, several contributions using metal oxides [62,64] or polymer coatings [65] have successfully proved to produce LMRs so far. This is something to be continuously explored in the near future, in order to have an idea of what specific materials can induce LMRs.

The second consideration is the kind of modes propagated in the deposited optical fiber. It is important to notice that the structures analyzed during this thesis are cylindrically symmetric. Due to this kind of symmetry, it is known that the modes propagating in these structures are hybrid and present the form $HE_{1,n}$ or $EH_{1,n}$, which is more complicated to analyze than the planar substrates utilized for Krestchmann configuration. However, some assumptions can be made. Particularly, if the optical fiber owns a large diameter, then it is possible to approximate the geometry of the structure as planar. In this case, a simple method based on the attenuated total reflection (ATR) theory can be used (see Appendix 1 for more information on how to work with this method). Under this assumption, a planar geometry is considered, so the modes are not hybrid, but TE or TM modes. On the other hand, if the diameter of the optical fiber is reduced, the planar approximation is no longer valid, so a cylindrical geometry must be considered. This is the philosophy of FIMMWAVE® and CAMFR, simulators also used along this thesis and presented in Appendix 1. Thus, in spite of dealing with hybrid modes and for

the sake of simplicity, all the analyses during this thesis will consider the propagation of TE and TM modes.

This fact has some important implications when explaining the generation of SPRs and LMRs, since everything turns simpler. For instance, the generation of SPRs in optical fibers can be explained as a coupling of the TM-polarized light used in Krestchmann configuration to a predominantly TM-shaped mode in the optical fiber. This makes the SPRs show up in a deposited optical fiber when a white light spectrum is launched without the need of a polarizer or a polarization maintaining fiber [66]. In the LMRs case, these resonances can be excited by simply launching a white light spectrum, although it is also possible to polarize and take measurements with both polarizations since the LMRs are generated for TE and TM modes [67,68].

The third aspect is that unlike SPRs, in which only an increasing absorption resonance is generated as the material is deposited, LMRs have the capability of generating several resonances in the transmission spectrum as a function of the increasing thin-film thickness. Since the phenomenon occurs when the lossy mode is near cut-off, it is stated in [40] that there are mode cut-off thickness values that lead to attenuation maxima, as shown in Figs. 2.9c and 2.11. Each of these maxima corresponds with a new mode that is guided in the thin-film under near cut-off conditions. This idea can be extrapolated to the wavelength spectrum, where there are also attenuation bands caused by absorption maxima at specific wavelength values. Thus, as the material keeps on depositing, it is possible to tune the LMRs and locate them wherever desired in the optical spectrum by just controlling the amount of material deposited [64], as shown theoretically and experimentally in Fig. 2.11.

Additionally, some other characteristics can be extracted by deepening on the study of LMRs. Some of them are considered in this chapter, since they will be used along the different explanations in this thesis.

One of the most interesting is the influence of the deposited material in the resonance. Materials with high real part in the refractive index (n) generate more resonances than those with a low n. At the same time, materials with a high imaginary part in the refractive index (k) will absorb more light (as occurred in SPRs), so k will only influence in the depth of the resonances [64]. For instance, in Fig. 2.11 it can be observed that the [TiO_2/PSS] thin-film generates more resonances than in the [PAH/PAA] case. The reason is that the refractive index of [TiO_2/PSS] structure is higher than that of [PAH/PAA] (see Fig. 2.12a) and, hence, the [TiO_2/PSS] structure can support more lossy modes than the [PAH/PAA] structure under the same conditions.
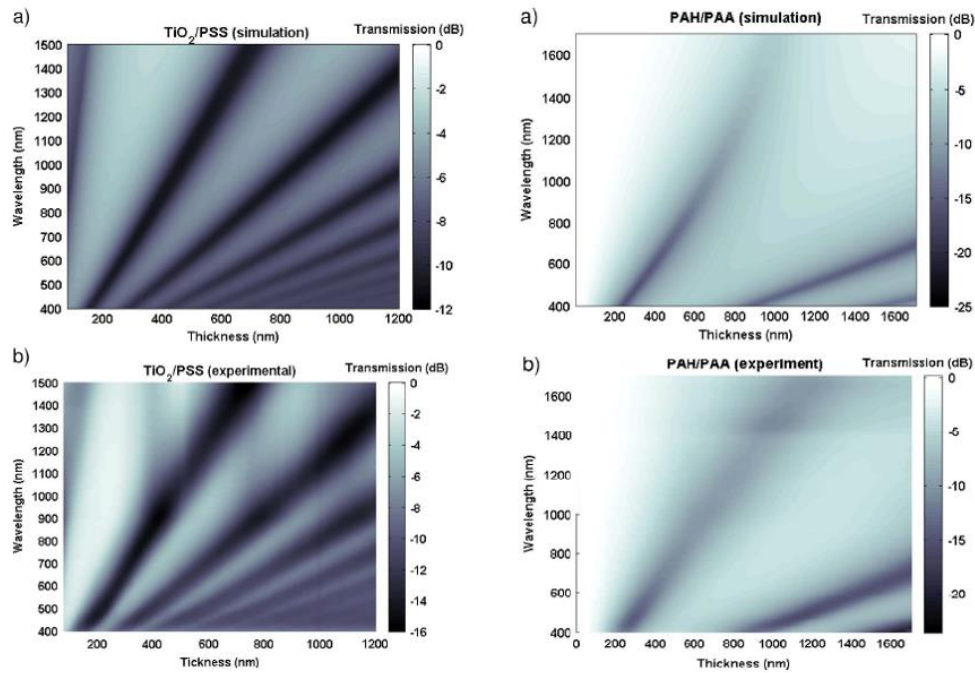
Fig. 2.11. *Spectral response obtained as a function of thickness for (left row) a high refractive index thin-film and (right row) a low refractive index thin-film deposited onto a cladding removed optical fiber (the surrounding medium refractive index is 1.321): (a) theoretical, (b) experimental [64].*

Moreover, it has been previously indicated that each of the LMRs corresponds with a mode near cut-off. Consequently, LMRs occur at specific wavelength values [62]. The generation process can be visualized in Fig. 2.13, for both ITO and In_2O_3 coatings for different thicknesses. At high wavelength values there is no guidance in the coating. As we move to lower wavelength values, a first mode is close to the cut-off condition, and an LMR is generated in the spectrum. This LMR is considered as the first LMR because it is caused by the first lossy mode guided in the coating. If moving to lower wavelength values, a second mode reaches the cut-off condition and is then guided. As a result another LMR is obtained in the spectrum. This LMR is considered as the second LMR because it is caused by the second lossy mode guided in the thin-film. The same explanation is valid for the subsequent LMRs showing up in the spectrum.

Another aspect to take into account is the different nature of the resonances obtained with different materials. It is easy to observe in Fig. 2.14a and b that the LMRs are more separated for an ITO thin-film than for an In_2O_3 thin-film. For instance, when a 220 nm ITO coating is deposited, there is an LMR at 1188 nm

but the second resonance is not yet visible (it is located below 500 nm). However, for an In_2O_3 coating of 49 nm, the first LMR, located at 986 nm, is already accompanied by a second LMR, located at 627 nm. The explanation is that both LMRs visible for a 49 nm In_2O_3 coated device are actually the LMRs associated to two different polarizations (we group them in Fig. 2.14c as dual-peak 'A'). The same is true for the 86 nm In_2O_3 coated device, so that is why we group them in Fig. 2.14c as dual-peak 'B'. In the case of ITO coating these resonances are closer to each other and they form just a single LMR (TE and TM polarizations are together).

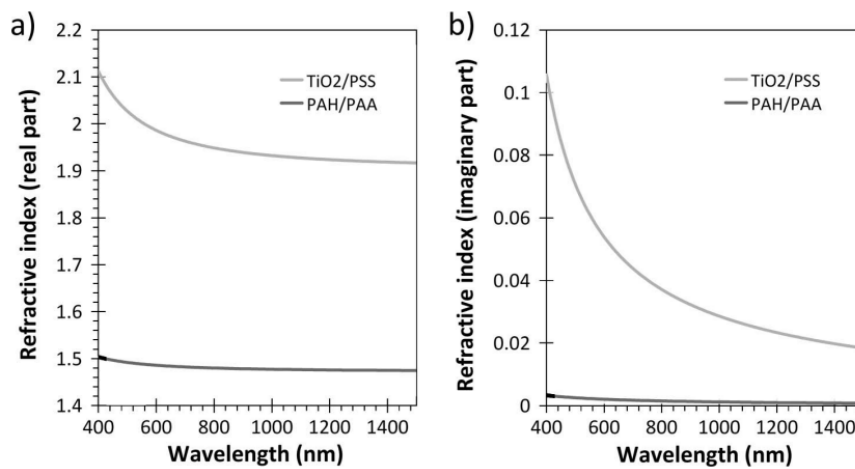**Fig. 2.12.** *Refractive index dispersion curves of [TiO$_2$/PSS] and [PAH/PAA]. (a) Refractive index real part (n). (b) Refractive index imaginary part (k) [64].*
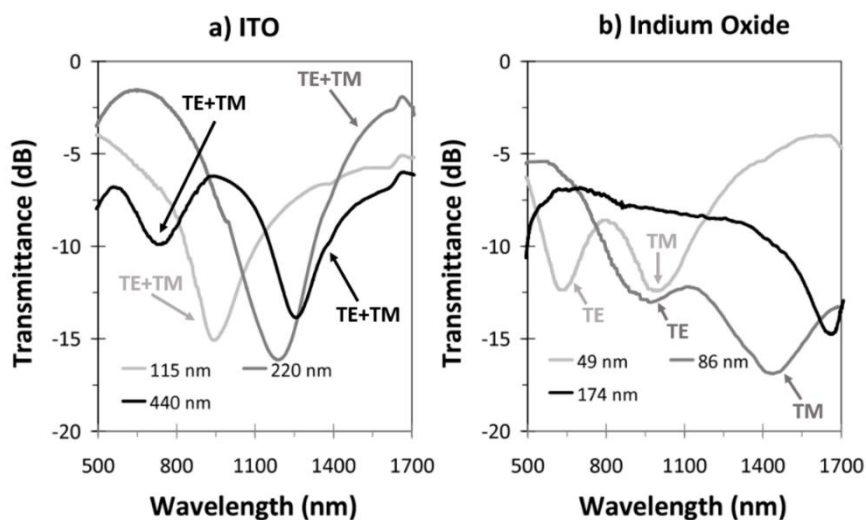

Fig. 2.13. *Experimental transmission spectra as a function of thickness for (a) ITO and (b) In$_2$O$_3$ deposited layers [62]. TE and TM modes are represented to indicate single-peak or dual-peak LMRs.*
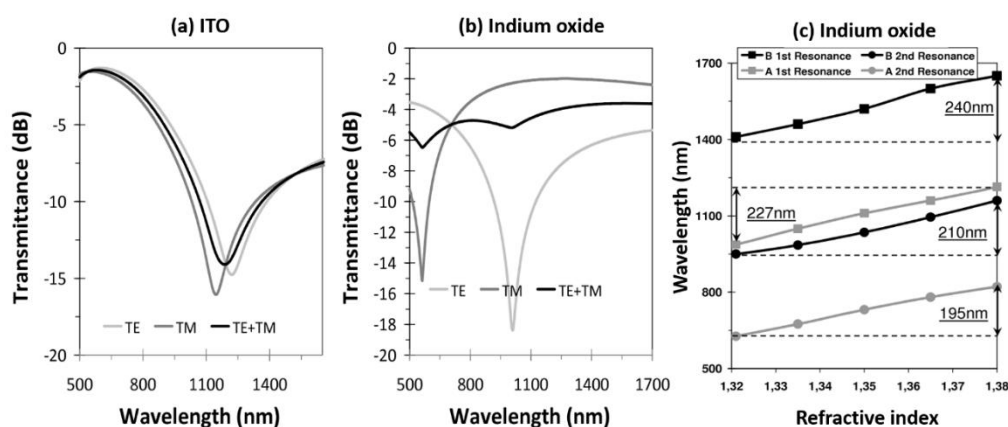
Fig. 2.14. *Simulated transmission spectra for three different polarizations: TE, TM and TE+TM. (a) 220 nm ITO deposited layer, (b) 86 nm In$_2$O$_3$ deposited layer. (c) Experimental results of resonance wavelengths as a function of the surrounding medium refractive index for dual-peak resonances obtained with In$_2$O$_3$ coatings (A indicates a 49 nm coating and B indicates a 86 nm coating) [62].*

In order to understand this question, in Fig. 2.14a and b the transmission spectra of two different devices (220 nm ITO coating and 49 nm In$_2$O$_3$ coating) for TE polarization, TM polarization and TE+TM polarization are presented. The evolution of the dual-peak LMRs obtained with indium oxide coatings is tracked in Fig. 2.14c as a function of the surrounding medium refractive index. Moreover, it has been previously indicated that the real part of the refractive index influences the number of LMRs propagated in the thin-film, whereas the imaginary part influences the depth of the resonance. In fact, is the k parameter what permits to observe this single or double peak in the LMRs. If *k* value is low, then the attenuation will not be so strong and it will be possible to see both TE and TM polarizations if they are sufficiently separated. The opposite will occur if k is higher [62].

Finally, a last consideration on the LMRs sensitivity is addressed. Taking a look to Fig. 2.11 it can be observed that the shifts of the resonances are different. For instance, focusing on the [TiO$_2$/PSS] case, less than a 200 nm-thick layer is enough to propagate the first resonance from 400 to 1700 nm. The second resonance can be tracked from 100 nm to 800 nm of layer thickness and so on. In the [PAH/PAA] case, the first LMR can be visualized from 200 to 1200 nm, whereas the second shows up at 900 nm and, due to its inclination, probably it will shift slowly, so more than 2 microns of thickness will be needed to make it shift over 1700 nm. In view of this, it seems obvious that the first resonance shifts in

wavelength faster than the others. Therefore, a good strategy to design LMR-based sensors is to deposit thin-films until the first LMR is obtained.

To finish this analysis on the state of the art for LMRs, it is compulsory to mention the achievements reached with this technology. In this sense, since the beginning of the studies on LMRs, their applications have spread to sensing devices, mainly. Thus, a wide variety of sensors have been shown, involving refractometers [69], humidity sensors [70], pH sensors [65] and biosensors [71], although their limit is still to be explored.

2.4. Conclusion

This second chapter has reviewed the state of the art in thin-film deposition techniques, trying to explain those methods utilized along this thesis. A high potential is predicted for the upcoming years when talking about the possibilities that thin-film depositions provide in terms of functionalizing surfaces to achieve novel properties in our daily life.

Also, as a particular application for the deposition of thin-films, the generation of electromagnetic resonances has been addressed. A special attention has been paid to describe the sensing phenomena used along this thesis: lossy mode resonances or LMRs. Such resonances have the potential of improving the results obtained with surface plasmon resonances (SPRs) when used as a sensing technology and this thesis tries to show how to improve their characteristics. But even if the resonant phenomenon is not required, the possibility of increasing the sensitivity of the device can be achieved by depositing thin-films of the same materials that generate the LMRs. Next chapters will show both phenomena and some sensing and biosensing applications as sensors will be shown.

2.5. Bibliography

[1] B.D. Gates, Q. Xu, M. Stewart, D. Ryan, C.G. Willson, G.M. Whitesides, New Approaches to Nanofabrication: Molding, Printing, and Other Techniques, Chemical Reviews. 105 (2005) 1171.

[2] P.M. Martin, Handbook of Deposition Technologies for Films and Coatings, Handbook of Deposition Technologies for Films and Coatings. (2010).

[3] R.P. Feynman, There's plenty of room at the bottom, Microelectromechanical Systems, Journal of. 1 (1992) 60-66.

[4] R.M. Iost, F.N. Crespilho, Layer-by-layer self-assembly and electrochemistry: Applications in biosensing and bioelectronics, Biosensors and Bioelectronics. 31 (2012) 1-10.

[5] R. Behrisch, Sputtering by Particle Bombardment I. Physical Sputtering of Single-Element Solids, (1981) 256.

[6] D.B. Hall, P. Underhill, J.M. Torkelson, Spin coating of thin and ultrathin polymer films, Polymer Engineering & Science. 38 (1998) 2039-2045.

[7] S. Acharya, J.P. Hill, K. Ariga, Soft Langmuir-Blodgett Technique for Hard Nanomaterials, Adv Mater. 21 (2009) 2959-2981.

[8] C.J. Brinker, A.J. Hurd, P.R. Schunk, G.C. Frye, C.S. Ashley, Review of sol-gel thin film formation, J. Non Cryst. Solids. 147–148 (1992) 424-436.

[9] A. Asatekin, M.C. Barr, S.H. Baxamusa, K.K.S. Lau, W. Tenhaeff, J. Xu, K.K. Gleason, Designing polymer surfaces via vapor deposition, Materials Today. 13 (2010) 26-33.

[10] J.E. Mahan, Physical Vapor Deposition of Thin Films, (2000) 340.

[11] M. Dhankhar, O. Pal Singh, V.N. Singh, Physical principles of losses in thin film solar cells and efficiency enhancement methods, Renewable and Sustainable Energy Reviews. 40 (2014) 214-223.

[12] Y. Lee, Graphene-based transparent conductive films, Nano. 8 (2013) 1330001.

[13] A. Fujishima, X. Zhang, D.A. Tryk, TiO_2 photocatalysis and related surface phenomena, Surface Science Reports. 63 (2008) 515-582.

[14] D. Chandler, Interfaces and the driving force of hydrophobic assembly, Nature. 437 (2005) 640-647.

[15] J. Song, Antimicrobial polymer nanostructures: Synthetic route, mechanism of action and perspective, Advances in Colloid and Interface Science. 203 (2014) 37-50-50.

[16] P. Kingshott, Surface modification and chemical surface analysis of biomaterials, Current Opinion in Chemical Biology. 15 (2011) 667-676-676.

[17] L.H. Domash, Thin films sing a new tune, Photonics Spectra. 38 (2004) 70-74.

[18] C. Cao, C. Hu, X. Wang, S. Wang, Y. Tian, H. Zhang, UV sensor based on TiO_2 nanorod arrays on FTO thin film, Sensors Actuators B: Chem. 156 (2011) 114-119.

[19] M.M. Rahman, A. Jamal, S.B. Khan, M. Faisal, Highly sensitive ethanol chemical sensor based on Ni-doped SnO_2 nanostructure materials, Biosensors and Bioelectronics. 28 (2011) 127-134.

[20] S.K. Arya, Recent advances in ZnO nanostructures and thin films for biosensor applications: Review, Analytica Chimica Acta. 737 (2012) 1-21-21.

[21] Y. Liu, A. Wang, R. Claus, Molecular Self-Assembly of TiO_2/Polymer Nanocomposite Films, J Phys Chem B. 101 (1997) 1385-1388.

[22] S. Renneckar, Nanoscale coatings on wood: Polyelectrolyte adsorption and layer-by-layer assembled film formation, Acs Applied Materials and Interfaces. 1 (2009) 559-566.

[23] I. Del Villar, I. Matias, F.J. Arregui, R.O. Claus, Fiber-optic nanorefractometer based on one-dimensional photonic-bandgap structures with two defects, Nanotechnology, IEEE Transactions on. 3 (2004) 293-299.

[24] P. Schaaf, Spray-assisted polyelectrolyte multilayer buildup: From step-by-step to single-step polyelectrolyte film constructions, Advanced Materials. 24 (2012) 1001-1016-1016.

[25] Y. Fu, Facile and efficient approach to speed up layer-by-layer assembly: Dipping in agitated solutions, Langmuir. 27 (2011) 672-677-677.

[26] J.E. Malinsky, Self-assembly processes for organic LED electrode passivation and charge injection balance, Advanced Materials. 11 (1999) 227-231.

[27] N.A. Kotov, Layer-by-layer self-assembly: The contribution of hydrophobic interactions, Nanostructured Materials. 12 (1999) 789-796.

[28] N. Nuraje, Durable antifog films from layer-by-layer molecularly blended hydrophilic polysaccharides, Langmuir. 27 (2011) 782-791-791.

[29] A.P.R. Johnston, Layer-by-layer engineered capsules and their applications, Current Opinion in Colloid and Interface Science. 11 (2006) 203-209.

[30] T. Xiang, R. Wang, H. Qin, H. Xiang, B.-. Su, C.-. Zhao, Excellent biocompatible polymeric membranes prepared via layer-by-layer self-assembly, J Appl Polym Sci. 132 (2015).

[31] H. Ai, S. Jones, Y. Lvov, Biomedical applications of electrostatic layer-by-layer nano-assembly of polymers, enzymes, and nanoparticles, Cell Biochem. Biophys. 39 (2003) 23-43.

[32] G.M. Nogueira, D. Banerjee, R.E. Cohen, M.F. Rubner, Spray-Layer-by-Layer Assembly Can More Rapidly Produce Optical-Quality Multistack Heterostructures, Langmuir 27(2011), 7860–7867.

[33] M. Kaur, N.S. Ramgir, U.K. Gautam, S.K. Ganapathi, S. Bhattacharya, N. Datta, V. Saxena, A.K. Debnath, D.K. Aswal, S.K. Gupta, H_2S sensors based on SnO_2 films: RGTO verses RF sputtering, Mater. Chem. Phys. 147 (2014) 707-714.

[34] C. Donley, Characterization of indium-tin oxide interfaces using X-ray photoelectron spectroscopy and redox processes of a chemisorbed probe molecule: Effect of surface pretreatment conditions, Langmuir. 18 (2002) 450-457.

[35] N. Chen, Antimicrobial copper-containing titanium nitride coatings Co-deposited by arc ion plating/magnetron sputtering for protective and decorative purposes, Surface and Coatings Technology (Formerly : Surface Technology). 253 (2014) 83-88-88.

[36] N.I. Cho, Fabrication of silicon PIN diode as proton energy detector, Current Applied Physics. 6 (2006) 239-242.

[37] S.P. Singh, Cholesterol biosensor based on rf sputtered zinc oxide nanoporous thin film, Applied Physics Letters. 91 (2007).

[38] M. Caglar, Influence of dopant concentration on the optical properties of ZnO: In films by sol-gel method, Thin Solid Films. 517 (2009) 5023-5028.

[39] F. Wooten, Optical Properties of Solids, Academic Press, 1972.

[40] T. Batchman, G.M. McWright, Mode coupling between dielectric and semiconductor planar waveguides, Microwave Theory and Techniques, IEEE Transactions on. 30 (1982) 628-634.

[41] A.W. Snyder, J. Love, Optical Waveguide Theory, Springer, 1983.

[42] F. Arregui, I. Matias, J. Goicoechea, I. Villar, Optical Fiber Sensors Based on Nanostructured Coatings, in: F.J. Arregui (Ed.), Springer US, 2009, pp. 275-301.

[43] L.M. Lechuga, Optical sensors based on evanescent field sensing Part II. Integrated optical sensors, (2000).

[44] K.V. Sreekanth, S. Zeng, J. Shang, K. Yong, T. Yu, Excitation of surface electromagnetic waves in a graphene-based Bragg grating, Sci. Rep. 2 (2012).

[45] A.K. Singh, S.C. Sharma, A fixed detector Kretschmann configuration optical system to study surface plasmon excitations, Optics & Laser Technology. 56 (2014) 256-262.

[46] F. Yang, J.R. Sambles, Determination of the optical permittivity and thickness of absorbing films using long range modes, Journal of Modern Optics. 44 (1997) 1155-1163.

[47] P. Berini, Long-range surface plasmon polaritons, Adv. Opt. Photon. 1 (2009) 484-588.

[48] J. Homola, Surface Plasmon Resonance Based Sensors, Springer, 2006.

[49] D. Razansky, P.D. Einziger, D.R. Adam, Broadband Absorption Spectroscopy via Excitation of Lossy Resonance Modes in Thin Films, Phys. Rev. Lett. 95 (2005) 018101.

[50] Y. Zhang, Long range surface polaritons in thin layers of absorbing materials, (2011).

[51] R.P.H. Kooyman, R.M. Corn, A. Wark, H.J. Lee, E. Gedig, G. Engbers, L. Walstrom, N. de Mol J., D.R. Hall, P. Yager, T. Chinowsky, E. Fu, K. Nelson, A. McWhirter, M.J.E. Fischer, A.M.C. Lokate, J.B. Beusink, G.J.M. Pruijn, W. Knoll, A. Kasry, J. Liu, T. Neumann, L. Niu, H. Park, H. Paulsen, R. Robelek, F. Yu, P. Schuck, R.B.M. Schasfoort, A.J. Tudos, Handbook of Surface Plasmon Resonance, The Royal Society of Chemistry, 2008.

[52] C. Rhodes, M. Cerruti, A. Efremenko, M. Losego, D.E. Aspnes, J. Maria, S. Franzen, Dependence of plasmon polaritons on the thickness of indium tin oxide thin films, Journal of Applied Physics. 103 (2008) 093108-093108-6.

[53] J. Cao, M.H. Tu, T. Sun, K.T.V. Grattan, Wavelength-based localized surface plasmon resonance optical fiber biosensor, Sensors Actuators B: Chem. 181 (2013) 611-619.

[54] M. Estevez, M.A. Otte, B. Sepulveda, L.M. Lechuga, Trends and challenges of refractometric nanoplasmonic biosensors: A review, Anal. Chim. Acta. 806 (2014) 55-73.

[55] R. Slavík, J. Homola, Ultrahigh resolution long range surface plasmon-based sensor, Sensors Actuators B: Chem. 123 (2007) 10-12.

[56] M. Piliarik, J. Homola, Surface plasmon resonance (SPR) sensors: approaching their limits? Opt. Express. 17 (2009) 16505-16517.

[57] M. Hernáez, I. Del Villar, C.R. Zamarreño, F.J. Arregui, I.R. Matias, Optical fiber refractometers based on lossy mode resonances supported by TiO2 coatings, Appl. Opt. 49 (2010) 3980-3985.

[58] M. Marciniak, J. Grzegorzewski, M. Szustakowski, Analysis of lossy mode cut-off conditions in planar waveguides with semiconductor guiding layer, Optoelectronics, IEE Proceedings J. 140 (1993) 247-252.

[59] G.P. Agrawal, Nonlinear Fiber Optics, Academic press, 2007.

[60] I. Udagedara, M. Premaratne, I.D. Rukhlenko, H.T. Hattori, G.P. Agrawal, Unified perfectly matched layer for finite-difference time-domain modeling of dispersive optical materials, Optics express. 17 (2009) 21179-21190.

[61] G. Walters, I.P. Parkin, The incorporation of noble metal nanoparticles into host matrix thin films: synthesis, characterisation and applications, J.Mater.Chem. The Royal Society of Chemistry, 19, 5, (2009) 574-590.

[62] I. Del Villar and C.R. Zamarreño and P. Sanchez and M. Hernaez and C.F. Valdivielso F.J. Arregui, I.R. Matias, Generation of lossy mode resonances by deposition of high-refractive-index coatings on uncladded multimode optical fibers, Journal of Optics. 12 (2010) 095503.

[63] D. Kaur, V.K. Sharma, A. Kapoor, High sensitivity lossy mode resonance sensors, Sensors Actuators B: Chem. 198 (2014) 366-376.

[64] I. Del Villar, M. Hernaez, C.R. Zamarreño, P. Sánchez, C. Fernández-Valdivielso, F.J. Arregui, I.R. Matias, Design rules for lossy mode resonance based sensors, Appl. Opt. 51 (2012) 4298-4307.

[65] C.R. Zamarreño, M. Hernáez, I. Del Villar, I.R. Matías, F.J. Arregui, Optical fiber pH sensor based on lossy-mode resonances by means of thin polymeric coatings, Sensors Actuators B: Chem. 155 (2011) 290-297.

[66] P.J. Rivero, M. Hernaez, J. Goicoechea I.R. Matias, F.J. Arregui, Optical fiber refractometers based on localized surface plasmon resonance (LSPR) and lossy mode resonance (LMR), Proc. of SPIE Vol. 9157, 91574T.

[67] C.R. Zamarreño, P. Zubiate, M. Sagües, I.R. Matias, F.J. Arregui, Experimental demonstration of lossy mode resonance generation for transverse-magnetic and transverse-electric polarizations, Optics Letters, 38, 14, (2013) 2481-2483.

[68] I. del Villar, C.R. Zamarreno, M. Hernaez, F.J. Arregui, I. Matias, Lossy Mode Resonance Generation With Indium-Tin-Oxide-Coated Optical Fibers for Sensing Applications, Lightwave Technology, Journal of. 28 (2010) 111-117.

[69] P. Sanchez, C.R. Zamarreño, M. Hernaez, I.R. Matias, F.J. Arregui, Optical fiber refractometers based on Lossy Mode Resonances by means of SnO_2 sputtered coatings, Sensors Actuators B: Chem. 202 (2014) 154-159.

[70] P.J. Rivero, A. Urrutia, J. Goicoechea, I.R. Matias, F.J. Arregui, A Lossy Mode Resonance optical sensor using silver nanoparticles-loaded films for monitoring human breathing, Sensors Actuators B: Chem. 187 (2013) 40-44.

[71] C.R. Zamarreno, I. Ardaiz, L. Ruete, F.J. Munoz, I. Matias, F.J. Arregui, C-reactive protein aptasensor for early sepsis diagnosis by means of an optical fiber device, SENSORS, 2013 IEEE. (2013) 1-4.

CHAPTER 3. Sensors based on lossy mode resonances by means of thin-films deposited on cladding removed optical fibers

3.1. Generation of lossy mode resonances in cladding removed multimode optical fibers (CRMMFs)

As mentioned in the previous chapters, the main optical structure used in this thesis is the optical fiber. In this sense, an adaption of Fig. 2.8 in chapter 2 can be done, substituting the generic substrate by a fused silica optical fiber waveguide. Fig. 3.1a shows a schematic of a typical optical fiber with the silica core and the cladding layers. Due to the differences between their refractive indices, light is propagated through the core by means of total internal reflection.

One of the simplest ways to modify the conditions for the light propagation in an optical fiber is accessing the core directly. In fact, there are some optical fibers with removable cladding made of polymer. Consequently, there is an actual possibility of modulating the light propagating in the core using this technique. In this chapter, a multimode cladding removable optical fiber is used. If this fiber is deposited with a thin-film, lossy mode resonances (LMRs) can be obtained. This is the easiest way to generate these resonances with optical fibers.

Hence, if a light source (for instance, a white light source) is connected on one side of the fiber and an adequate spectrometer is connected in the other side, it is possible to monitor LMRs as the optical silica – air waveguide is being deposited. Fig. 3.1b shows an example of an LMR wavelength shift as the fiber is deposited performing a layer-by-layer assembly (LbL-assembly) process.

Now, some key concepts must be defined before addressing the study of any LMRs during the following chapters. Essentially, the main parameters to consider when defining LMRs are three and they are also indicated in Fig. 3.1b.

The first one is the **resonance wavelength (λ_r),** defined as the value of the wavelength with maximum attenuation (or minimum transmission).

It is also interesting to analyze the spectral width of the resonance. To have an idea of the resolution given by this kind of resonances, it is good to define their **spectral width ($\Delta\lambda$)** as the wavelength range covered by the LMR at a transmission level 3 dB above the resonance minimum or at an absorption level 3 dB below the resonance maximum. In Fig. 3.1 this magnitude can be visualized as $\Delta\lambda$.
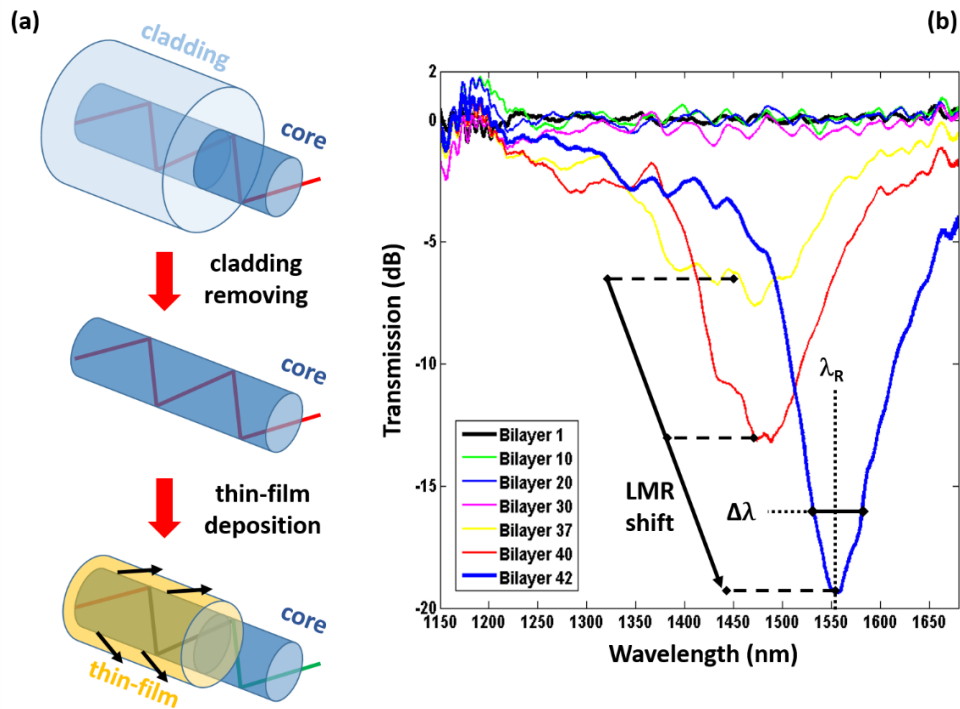
Fig. 3.1. *(a) Schematic of a thin-film deposition process for a cladding removable optical fiber. The light keeps on propagating through the core, although some light is coupled into the thin-film, generating the LMR. (b) A typical LMR shape as a function of the increasing thin-film thickness [1].*

Moreover, due to their capability of shifting in wavelength, the magnitude **"LMR shift"** denotes the number of nanometers the LMR shifts, either because of the thin-film deposition or during the detection process when used as a sensor.

The main goal of this chapter is to describe what happens with the light when guided into cladding removed optical fiber (CRMMF)-based structures when they are deposited with thin-films of materials that meet the permittivity conditions for the generation of LMRs. To this purpose, several configurations will be analyzed. Then, a review on the sensing devices fabricated during the development of such structures will be shown. Additionally, since this kind of multimode fibers can guide light in a broad spectral range, a characterization of the LMRs behavior will be presented from visible to infrared.

To sum up, two types of CRMMF structures will be analyzed in this chapter: non-tapered CRMMFs and tapered CRMMFs, which are fabricated by pulling CRMMFs. For the sake of simplicity, CRMMF will be the acronym utilized henceforward for referring to non-tapered cladding removed multimode optical

fibers, whereas T-CRMMF will be the acronym when talking about tapered cladding removed multimode optical fibers.

3.1.1. Theoretical study for non-tapered CRMMFs

First, some simulations extracted from FIMMWAVE® software are provided (see Appendix 1 for more information about the software). Fig. 3.2a shows a schematic of a CRMMF structure deposited with a thin-film to obtain the corresponding LMR. The waveguide is a cylindrical silica core of refractive index that of the silica (n = 1.45) and a diameter of 200 μm. The thin-film is a virtual material with refractive index 1.548 + 0.0105i and a thickness of 330 nm. These are the values estimated for a polymeric thin-film that will be presented afterwards in the experimental section, which are based on [2]. The sensitive or uncladded length is L_u = 40 mm, similarly to [2,3]. Light is launched into one end of the optical fiber with a white broadband source, which is modeled with a Gaussian source. After that, light passes through the sensitive region where the thin-film is deposited. Finally, it is received at the other end of the optical fiber. According to chapter 2, as the thin-film increases, some of the core modes will couple light to the thin-film (green arrows), leading to power losses in a restricted wavelength range and generating the corresponding LMRs. Moreover, in [4,5] it is indicated that the LMR will also red-shift until desired. In this case, the fact of simulating a thin-film thickness of 330 nm makes the LMR to be centered at around λ_r = 1425 nm [3], so the analysis is based on this assumption.

Figs. 3.2b and c show the electric field distribution in the longitudinal section of the optical fiber at 750 nm and 1425 nm respectively. The brighter colors indicate that the maximum electric field intensity is located in that position, whereas the cooler colors indicate the presence of a low intensity. In both cases, a spreading in the optical field is visualized just after coupling the light in the waveguide. This is due to the light mode arrangements that occur in the waveguide after entering it. Once the thin-film is deposited, the interaction of the different modes guided in the core with the thin-film – silica interface causes different transmission of light as a function of wavelength. Thus, for 750 nm, out of the LMR wavelength range, a better propagation of light can be observed in the output. However, for 1425 nm, since the LMR is centered there, it induces its maximum attenuation, so just a little amount of light can be received in the detection side.
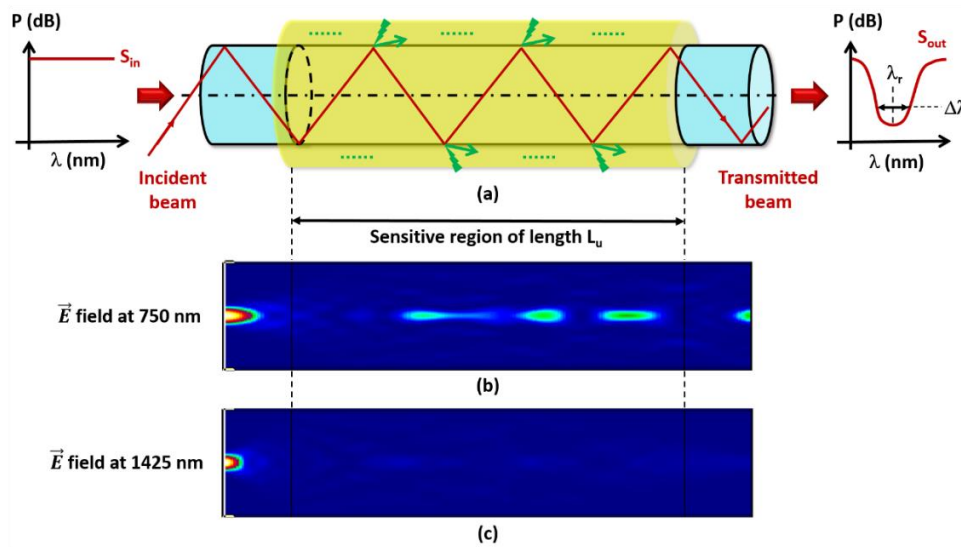
Fig. 3.2. *(a) Schematic of light propagation in a thin-film-deposited CRMMF, based on ray theory. Longitudinal electric field distribution along the sensitive area at (b) 750 nm and (c) 1425 nm, respectively, simulated by using mode theory in FIMMWAVE®.*

Now, focusing on the cross-sections in each stage of the propagation, an interesting analysis can be done. In Fig. 3.3, the electric field in the transversal section is plotted at different stages of the optical path, for the same wavelengths previously analyzed. In the beginning (a), a visible main beam can be observed, indicating that the light is totally guided inside the silica core. The side lobes correspond to the slight coupling of light to higher order modes propagating in the optical fiber when introducing the light in the beginning. In the center of the deposited area, the effect of the existing LMR can be visualized (b). The main lobe is partially attenuated for 750 nm, at the same time there is a coupling of light to the external part of the resulting waveguide, this means, to the thin-film. However, in the case of 1425 nm, most of the light is attenuated in the main lobe and only a little contribution of the electric field (just 0.015 V/µm) is propagated in the outer part of the waveguide. Here is where it can be observed that the light is being coupled to the thin-film.

Once the coated area is left behind, modes rearrange and fulfill the corresponding conditions to be propagated in the silica core. The main lobe is maintained for both wavelengths (c), although there are some differences. In the case of 750 nm, a remaining field contribution of 0.05 V/µm in the main lobe and around 0.02 V/µm in the side lobes still exist. This means that a considerable part

of the field is being propagated in the core at this wavelength. Moreover, the presence of side lobes indicates that there is also a considerable contribution of higher order modes due to the effect of passing through the thin-film deposited area. In the 1425 nm case, no relevant side lobes are highlighted, meaning that the light has been absorbed in the thin-film, and only a slight main lobe of 0.015 V/μm is detectable. This indicates that at 1425 nm the LMR induces its maximum attenuation and only a bit of light can be collected at this wavelength.
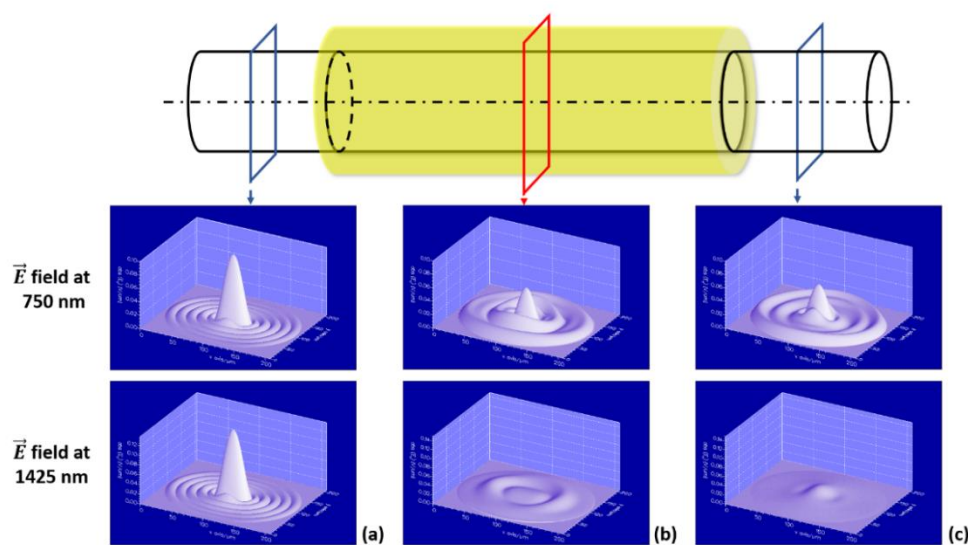

Fig. 3.3. *Numerical data obtained on the cross-section of the studied CRMMF (a) before entering the thin-film, (b) in the center of the deposited area, which means at $L = L_u/2 = 20$ mm and (c) before entering the detector, respectively. Simulations are obtained for 750 and 1425 nm in FIMMWAVE®.*

3.1.2. Theoretical study for tapered CRMMFs (T-CRMMFs)

Once the CRMMF has been studied, the next step is to try improving its properties. One of the best ways to access the evanescent field of the optical fibers is by tapering them [6], obtaining a T-CRMMF. A cladding removed optical fiber has been analyzed in section 3.1.1, accessing directly to the evanescent field by simply removing the polymer cladding. Now the fiber is tapered, so something different should happen due to the fact of decreasing its diameter.

It is not the main focus of this chapter to develop a theory on how the light propagates in a tapered fiber, because this is something to be fully developed in chapter 4. Nevertheless, it is worth keeping in mind that a tapered fiber is an optical fiber that has been pulled from both sides, at the same time the central area is

heated. This makes the fiber fuse and reduce its diameter. At the end of the process, there will be a central part with decreased diameter, known as "waist", which separates two decreasing diameter-regions called "transitions". The main advantage of fabricating tapers is that they have proved to increase the sensitive zone of the structure. Moreover, if this fiber is tapered, the diameter of the optical structure is reduced and, therefore, light goes out of the core, giving an increased evanescent field that has implications in the properties of LMRs obtained.

Thus, a T-CRMMF with 20 mm of waist length (L_w), 10 mm of transition length (L_t) and half the diameter of the CRMMF in section 3.1.1 is now simulated. These dimensions are chosen in view that with 10 mm of transition length, no oscillations showed up in the simulated spectrum. As it can be observed in Fig. 3.4a, the thin-film is also deposited on the optical fiber but now there is a transition region, where a decreasing slope reduces the diameter of the silica core to 100 μm. Consequently, less modes can be propagated into the silica waveguide. Indeed, some of these emerging modes will couple to the thin-film and generate an LMR. This should enhance the response in terms of reducing the number of modes involved when generating the LMR and, therefore, reducing the LMR spectral width.

In Fig. 3.4b and c, a schematic to describe the longitudinal electric field intensity distribution in the simulated T-CRMMF is presented. As it can be observed, there is also a spreading just after entering the optical waveguide, due to the mode rearrangements into the silica. The fact of tapering makes the electric field distribution be more chaotic in comparison to Fig. 3.2. There is a superposition of modes not only due to the thin-film deposition, but also to the fact of reducing the waveguide diameter. It is remarkable the high difference between the field intensities at 750 nm and that of the 1425 nm, but it is also interesting to notice that even for 750 nm, the field intensity between both CRMMF and T-CRMMF is different. This means that the power available to be detected after the T-CRMMF structure is reduced with respect to the CRMMF.

From a cross-section point of view, it is also interesting to analyze what happens in this deposited waveguide. Fig. 3.5 shows the electric field behavior in each one of the stages. At first sight, a drastic decrease in the electric field magnitude is noticeable from the input to the output in comparison to CRMMF case (see Fig. 3.3). Over 60% at 750 nm (from 0.1 to 0.04 V/μm) and almost 100% at 1425 nm. As it also happens in the CRMMF, the effect of the LMR at 750 nm is that a main beam surrounded by a coupling of light to peripheral modes is obtained at the end of the structure (see Fig. 3.5c). At the same time, for 1425 nm a hardly visible main lobe can be observed. Most of the light has been lost along the coated

waveguide (see Fig. 3.5b). Losses are so high that it is difficult to observe light propagation in the output side of the structure. This corroborates the longitudinal behavior simulated in Fig. 3.4.
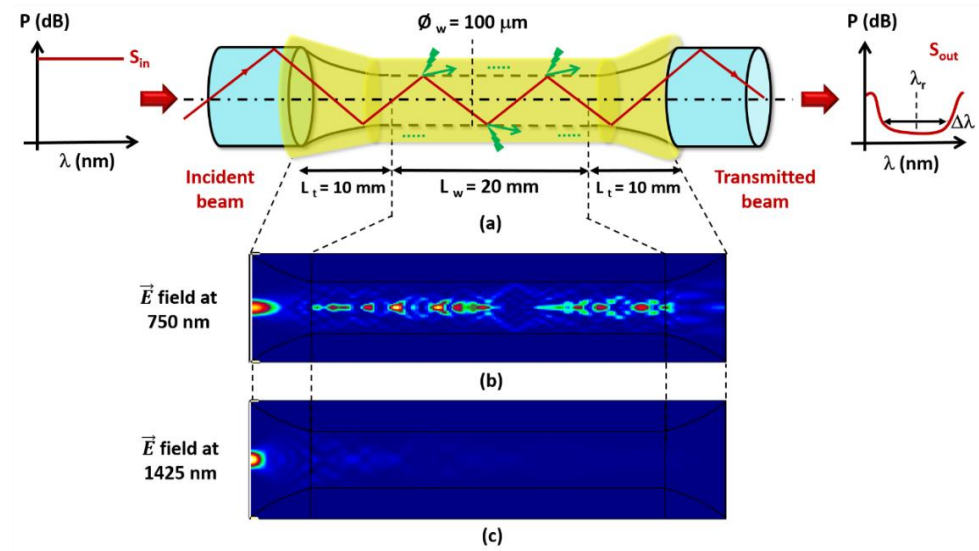
Fig. 3.4. *(a) Schematic of light propagation in a thin-film-deposited T-CRMMF. Longitudinal electric field intensity distribution along the sensitive area at (b) 750 nm and (c) 1425 nm, respectively, simulated by using mode theory in FIMMWAVE®.*

Fig. 3.5. *Numerical data obtained on the cross-section of the studied T-CRMMF (a) before entering the thin-film, (b) in the center of the deposited waist area and (c) before entering the detector, respectively. All the simulations have been obtained for 750 and 1425 nm in FIMMWAVE®.*

3.1.3. Experimental results

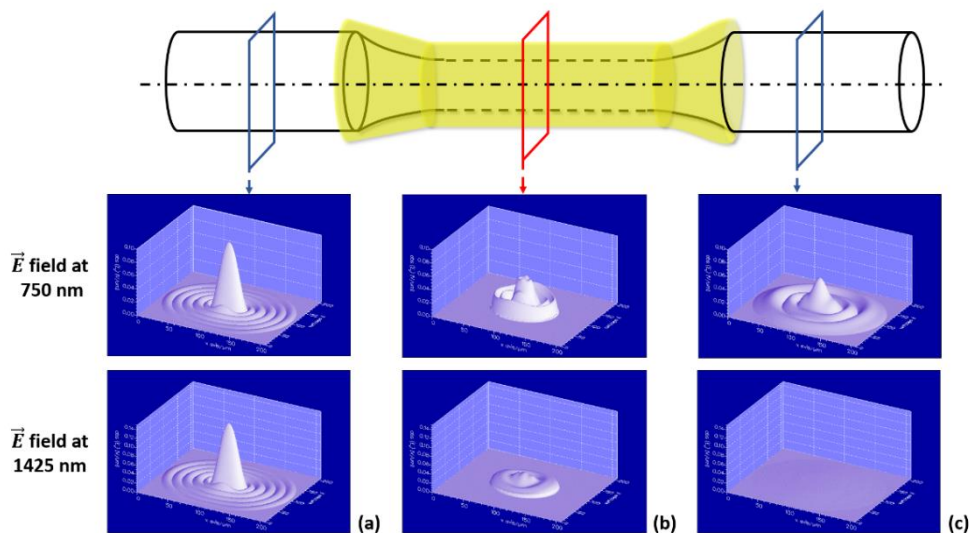In this subsection, an experimental corroboration for both CRMMF and T-CRMMF simulations is presented. To this purpose, two CRMMF structures were fabricated from a 200/250 µm (core/cladding diameter) cladding removable multimode optical fiber from Thorlabs Inc. (FT200EMT). They were stripped, uncladded until necessary and then cleaned with ethanol, in order to remove the undesired cladding. They were uncladded for 40 mm (similarly to that presented in Fig. 3.4a) and 20 mm respectively and named as C_1 and C_2, as it is summarized in Table 3.1.

Regarding the T-CRMMFs (named as T_{CRMMF}), a similar device to that presented in Fig. 3.5a was also fabricated, using a Nadetech Innovations S.L. tapering system (see Fig. 3.6). This equipment is capable of fabricating tapered structures by heating the optical fiber and pulling it from both sides until the desired structure is obtained. The software used to fabricate the tapers was based on the equations and theory suggested in [6]. The tapering system, consisted of a butane flux (1), two step-by-step motorized guides to pull the fibers (2), a third guide to move the heating flame side-by-side (3) and the corresponding digital electronics and power supply to control the tapering process ((4) and (5)). The software is based on a previous design of the desired taper and the corresponding controls to start, pause or stop the process.

To complete the optical set-up, a halogen light spectrum (AQ4303B, Anritsu Inc.) covering a wavelength range from 400 to 1800 nm, was launched into one end of the optical structures. The other end was connected through a bifurcated optical fiber (VIS-NIR with low OH content from Ocean Optics) to two spectrometers (a HR-4000 and a NIR-512), which permitted to monitor a total wavelength range from 400 to 1700 nm.

Optical structure	Initial diameter (µm)	Final diameter (µm)	Deposited length (mm)
CRMMF (C_1)	200	200	$L_u = 40$
CRMMF (C_2)	200	200	$L_u = 20$
T_{CRMMF}	200	100	$L_t = 10$ $L_w = 20$

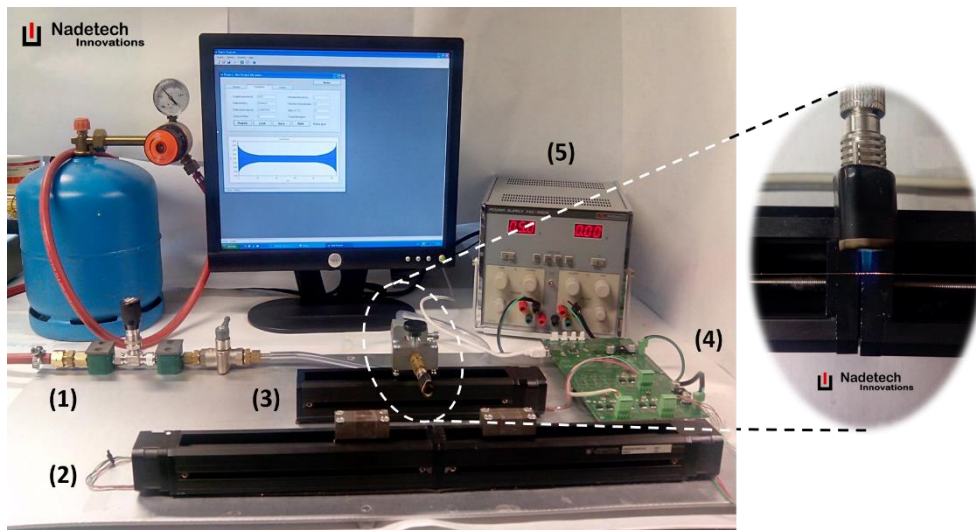***Table 3.1.*** *Summary of the CRMMFs and T_{CRMMF} dimensions.*

Fig. 3.6. *Nadetech Innovations S.L. tapering system prototype. The inset shows the butane flame and a fiber being pulled during a tapering process.*

In order to deposit the thin-film and induce the corresponding LMRs, an LbL-assembly process using aqueous solutions of poly (allylamine hydrochloride) (PAH) and poly (acrylic acid) (PAA) was performed, as depicted in Fig. 3.7. [PAH/PAA] matrix was deposited at pH 4.5. The progressive deposition of bilayers using the LbL-assembly technique permitted to monitor the spectral response of the devices for small thickness increments. All polyelectrolytes were used in 10 mM concentration, as indicated in [3].

The optical spectrum evolution as a function of the thin-film thickness is plotted in Fig. 3.8 for optical structures C_1 and T_{CRMMF}. Several attenuation bands, corresponding to the first, the second and the third LMRs can be observed as a function of thickness and wavelength [4]. The first aspect to take into account is the fact that the LMR attenuation is higher in the T_{CRMMF} case (down to -20 dB) than in C_1 case (down to -10 dB). The effect of tapering the optical fiber induces a higher light coupling from the modes propagating in the core to the thin-film. This is registered as a high optical power loss, what corroborates the results in the simulations obtained for the T_{CRMMF}.
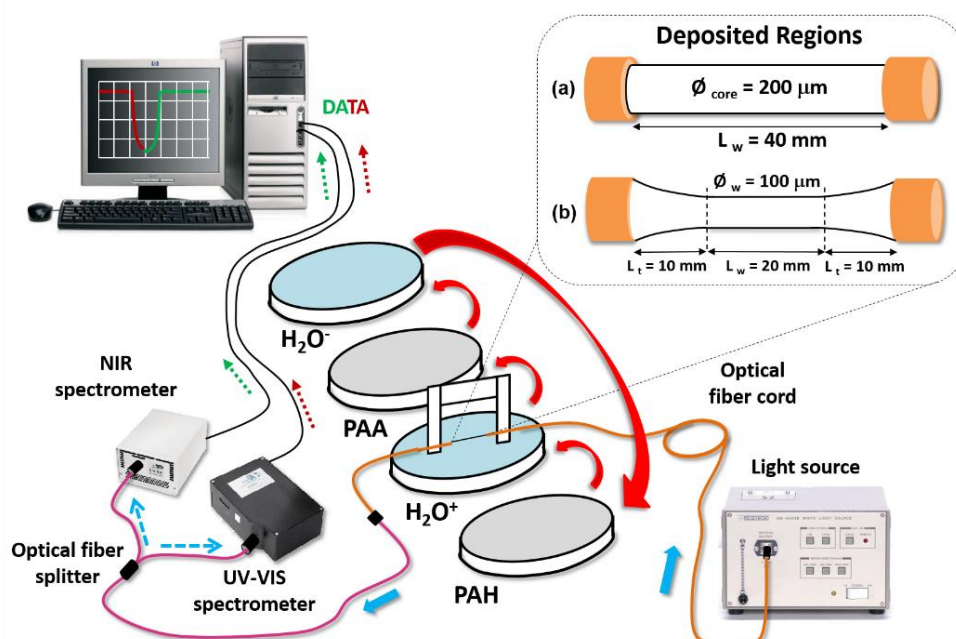
Fig. 3.7. *Set-up designed for the deposition and monitoring of the LMRs with multimode fibers.*

However, if the optical spectrum is plotted for a specific thin-film thickness of 200 nm (Fig. 3.9) it can be observed that the LMR spectral width is similar for both C_1 and T_{CRMMF} devices. Here, some more numerical data were taken. Concretely, for the multimode structures simulations (see Appendix 1 for more details), the finite difference mode solver was used and the waveguide was excited with a Gaussian source of full width at half maximum (FWHW) 20 μm. The optical power transmitted by the first 12 core modes was analyzed, because results started to converge for this number of modes. The integration order for the taper section was set to 1 because the optical structure was designed to avoid spectral oscillations. After fixing these parameters, several graphs were obtained for a [PAH/PAA] thickness of 200 nm, in order to compare and corroborate the hypotheses on the spectra behavior. These numerical data are depicted in Fig. 3.9a.

In Fig. 3.9b it can be observed that the LbL-assembly deposition corroborates the LMR spectral widths are quite similar for both devices. Additional experiments for T_{CRMMF} devices with lower diameter corroborated that the only remarkable change is an optical power decrease as a function of the decreasing diameter. Moreover, the optical losses are increased and consequently, the quality of the spectra is not good because the detection limit of the spectrometer is exceeded in some cases. In view of the presented results, it can be concluded that

there is no significant reduction in the spectral width of the LMRs by tapering a CRMMF.
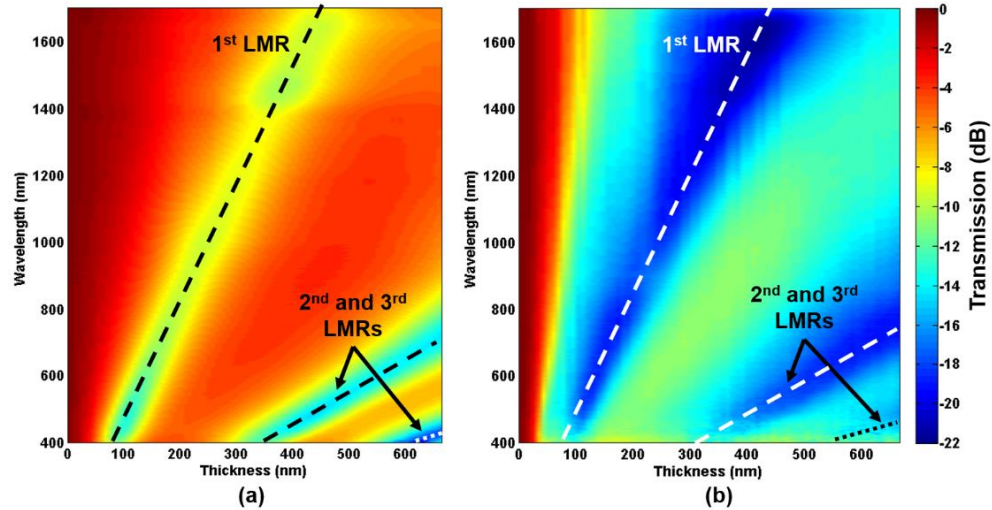

Fig. 3.8. *Comparison between the LMRs obtained with C_1 (a) and T_{CRMMF} (b) optical structures as a function of the [PAH/PAA] increasing thin-film thickness.*
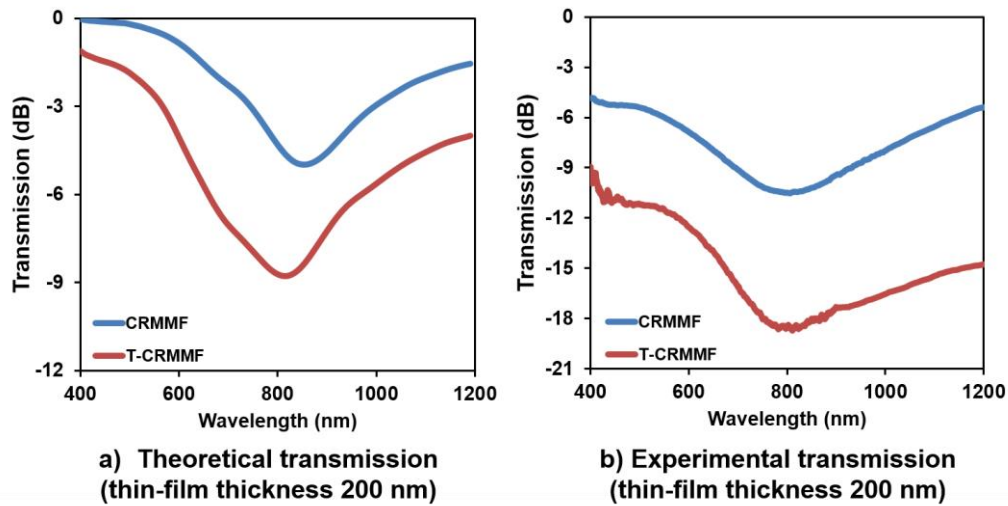

Fig. 3.9. *Transmission spectra for a thin-film thickness 200 nm both for C_1 and T_{CRMMF} devices: (a) simulation, (b) experimental data.*

3.2. Biosensors based on CRMMFs

In this section, the design and characterization of three biosensors, based on the generation of LMRs on tapered and non-tapered CRMMFs is detailed. The main goal is to extract some conclusions on the use of this technology as a potential platform to develop biosensors.

Prior to this, a brief review on the potential to detect changes in the surrounding medium refractive index (SMRI) is done, in order to have an idea of their behavior as refractometers. In this sense, since the publication of the first LMR contributions, most of the developed sensors have tried to detect changes in the SMRI. A first approach using CRMMFs was done in 2010, depositing a titanium oxide / 4-polystyrene sulfonate [TiO$_2$/PSS] thin-film by LbL-assembly. In this case, sensitivities up to 2872 nm/RIU were achieved [7]. Recently, by depositing tin oxide (SnO$_2$) thin-films onto CRMMFs, the sensitivity has been doubled, reaching 5390 nm/RIU [8]. This means that, by using metallic oxide, polymer/metallic oxide and, as it will be shown, polymer thin-films, it is possible to have enough sensitivity to detect small variations in the SMRI due to biological reactions. A biosensor based on a well-known ITO layer is shown along this chapter. Before that, a couple of contributions based on polymeric thin-films deposited by LbL-assembly are shown.

3.2.1. Immunosensor based on LMRs generated with a polymeric thin-film deposited on a CRMMF

To design this first sensor, an LbL-assembly based on a polymeric poly (allylamine chloride)/4-polystyrene sulfonate [PAH/PSS] matrix was performed [9]. Regarding the biological compounds, IgGs and anti- IgGs were extracted from goat serum. A PBS buffer solution at pH 7.4 was also used to dissolve the biological agents in order to maintain them in adequate environmental conditions.

Regarding the optical material, a 200/225 μm core/cladding diameter multimode cladding removable optical fiber was utilized. A white light source between 400 and 1700 nm launched the optical power into the fiber and an USB 2000-FLG spectrometer detected the optical output response.

<u>EXPERIMENTAL SET-UP</u>

In order to prepare a set-up to get information from the whole process, a reflective configuration was chosen, as described in Fig. 3.10. To monitor the behavior of the resonance, the reflection spectra of the CRMMF were captured at

all wavelengths between 400 and 1000 nm. This could be done by depositing a silver mirror on the sensor head using a sputtering process, as defined in chapter 2. In this way, the light emitted by the white light source and propagated along the fiber was totally reflected on the metallic mirror and returned to the spectrometer by an optical 2x1 coupler (splitter).

THIN-FILM DEPOSITION AND LMR GENERATION

The LbL-assembly was performed at room temperature and relative humidity conditions (T = 23°C and R.H. = 35%). In the first part of the deposition process, PAH was adjusted to pH 4.5 and PSS was adjusted to pH 7.4. According to [10] this combination between weak polyelectrolytes permits to form layers that generate an LMR.
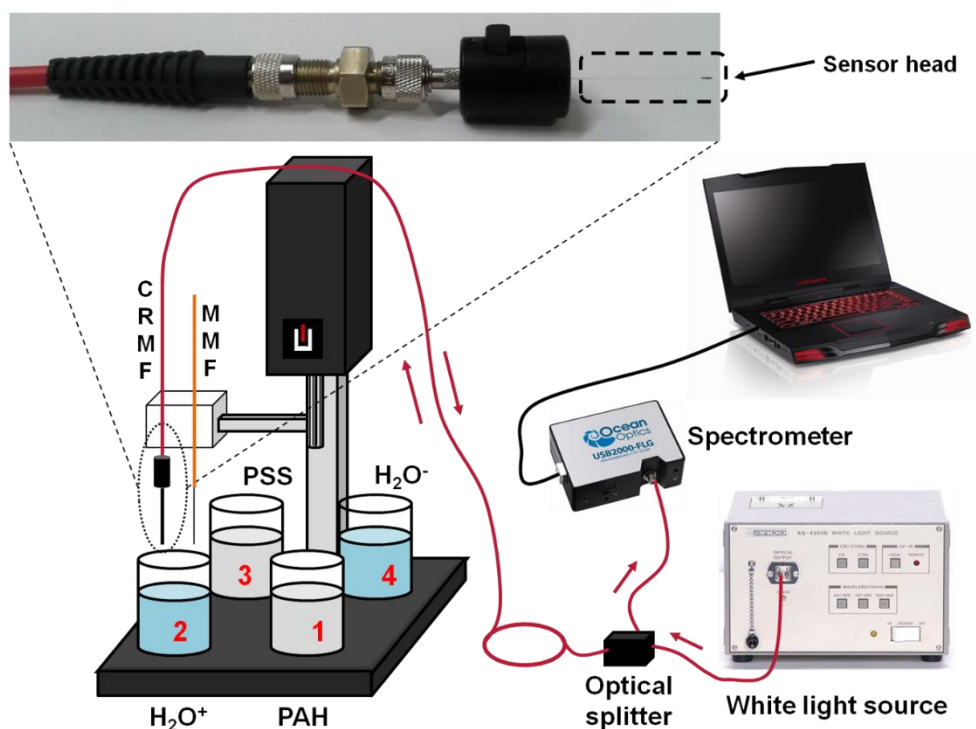

Fig. 3.10. *Set-up to take data from the thin-film, the construction of the sensor and the detection of the immunoreaction. The white light source ranges from 400 to 1700 nm, whereas the spectrometer analyzes from 400 to 1000 nm. Inset: An actual image of the sensor head is provided [9].*

Then, the second part of the nanocoating construction consisted of an LbL-assembly of 5 cycles. Here, the objective was to create an adequate medium so that the reaction between IgGs and anti-IgGs could occur at the optimal pH. To this purpose, both PAH and PSS pHs were adjusted to 7.4.

The method to get the evolution of the LMR is described in the following lines. During the construction, the reflected spectrum is captured at the end of every bilayer and referenced to the spectrum obtained when the sensor is immersed for the first time in the PAH solution. This result is called "LMR transmission spectrum". Therefore, the sequence formed by all the LMR transmission spectra obtained in the CRMMF along the deposition process is what it is called "evolution of the LMR". That is what is depicted in Fig. 3.11a and b, as a function of both the wavelength and the increasing number of bilayers. A typical behavior of an LMR can be observed here. No great transmission losses are registered until the LMR starts to be observable in the monitored spectral range at bilayer 25. As the thin-film thickness increases, the resonance presents a red shift in wavelength, while its spectral width spreads [5]. The maximum depth of the obtained resonance band reaches -10 dB.

At this point, if the nanocoating parameters vary, the characteristics of the LMR will change, since the new effective refractive index provided by the new thin-film affects to the modes that are being coupled into it. This is what happens in the second part of the deposition, when adsorbing the [PAH (pH 7.4) / PSS (pH 7.4)]$_5$ nanostructure onto the previous thin-film. The resonance changes its appearance, as it can be observed in Fig. 3.11b. Between bilayers 100 and 105 an increase of the optical power is registered along the whole spectrum, at the same time that it shifts slightly to higher wavelengths. Therefore, the LMR keeps on shifting to higher wavelengths, but following the new effective refractive index conditions. Finally, the resonance stops at bilayer 105 with its minimum located at around 720 nm.

IMMOBILIZATION OF THE ANTIBODIES (ANTI-IGGS)

At this point, the LMR generated by the polymeric thin-film was positioned in the center of the detection range and the outermost nanocoating was adsorbed in order to create an adequate environment so that the anti-IgGs were correctly attached. These steps are schematically represented in the upper right corner of Fig. 3.12a.
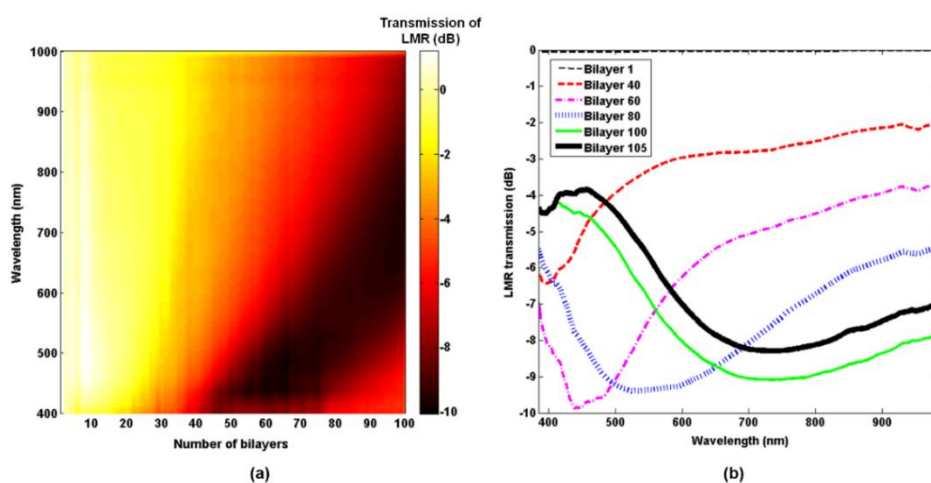
Fig. 3.11. *(a) Evolution of the LMR by means of the increasing polymeric thin-film. (b) Tracking of the LMR profile during the construction process. The construction finishes at bilayer 105 (black thicker spectrum) after a change of pH in the PAH solution [9].*

Once here, the immobilization of the biological detectors is addressed. To this purpose, a 5 µg/ml solution of anti-IgGs in PBS buffer at pH 7.4 was prepared at the same environmental conditions as in the previous experiments. Then, the substrate was immersed in the solution during 4 hours and the evolution of the LMR was monitored.

The tracking of the minimum of the LMR during the anti-IgGs deposition is plotted as a function of time in Fig. 3.12a. Since the resonance spectral width is approximately 600 nm (see Fig. 3.11), an algorithm based on the method of least squares was applied to locate accurately where the resonance wavelength was. It is remarkable that the resonance experiments an UV shift from 703 to 680 nm. Apart from that, a slight decay of around 1.2 dB is experimented by the spectrum during the process. The explanation to this behavior is that, due to the deposition of the anti-IgGs, the effective refractive indices inside and outside the nanocoating are modified. Consequently, the conditions for the LMR are different.

DETECTION RESULTS

Here, the detection of the IgGs is studied. To this purpose, a 50 µg/ml IgG solution in PBS buffer at pH 7.4 was prepared to be detected. The behavior of the optical fiber nanobiosensor designed in the previous lines was monitored with the same experimental set-up and at the same environmental conditions used for both the generation of the LMR and the immobilization of the anti-IgGs. Moreover, every

spectrum was captured by the spectrometer and processed, also by the method of least squares, to obtain the detection results presented in Fig. 3.12b. Here, the central wavelength of the LMR is plotted as a function of time once the sensor is introduced in the IgGs solution.

There are some aspects to be taken into account. The first question is that, unlike the immobilization process, there is a wavelength shift of the LMR to the red, ranging from 659 to 669 nm. At the same time, the optical power, which had decreased to almost -12.5 dB when immersing the biosensor into the IgGs solution, gets recovered until it reaches around -10 dB. In this case, as the solvent used to dissolve the IgGs is the same than that used in the immobilization of the anti-IgGs, the changes experimented by the LMR when immersing the sensor into the IgGs solution are due to the bindings between this biomolecules and the anti-IgGs film. Concretely, this phenomenon is produced due to the changes in the refractive indices between the thin-film and the anti-IgGs film when binding to the IgGs, which modify the LMR characteristics.

Finally, the response time of the sensor is obtained by measuring the time it takes to rise from the 10% to the 90% of the stabilization wavelength when detecting the IgGs. It can be observed in Fig. 3.12b that it takes around 12 minutes, which is comparable to other fiber-optic-based biosensors applied in clinical measurements [11]. Based on the results obtained, it can be affirmed that it is possible to detect an IgG – anti-IgG complex with a lossy mode resonance based optical fiber sensor. Moreover, the detection could be carried out by interrogating the LMR wavelength shift, which is something appropriate in terms of robustness. This means that this technology can be also taken into account in order to be developed for a further clinical application.
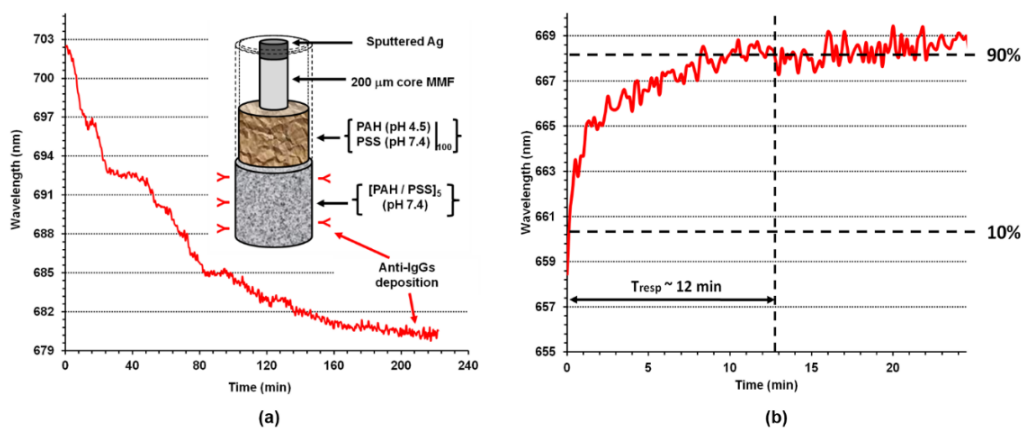

Fig. 3.12. *(a) Tracking of the anti-IgGs immobilization during the process. In the upper right corner, the different parts of the sensor are shown. (b) IgG detection curves. The LMR experiments a shift to higher wavelengths while the IgGs are binding to the anti-IgGs [9].*

3.2.2. Immunosensor based on LMRs generated with a polymeric thin-film deposited on a T-CRMMF

The previous sensor presented a main problem, which was that it took a hundred [PAH/PSS] layers to achieve a more or less well centered LMR in the middle of the spectral range. A novel approach to detect type G immunoglobulins (IgGs) was developed, based on two main principles. The first one, the fact that the poly (allylamine chloride) / poly (acrylic acid) [PAH/PAA] polymeric matrix generates a rapid LMR in quite a few layers if deposited at pH 4.5 [3]. The second one, the fact of tapering the optical fiber, which would permit a higher access to the evanescent field of the light propagating through the waveguide and to increase the detection surface.

To this purpose, and using the same kind of multimode fiber than in the previous sensor, a 30 mm uncladded segment was tapered using the tapering system by Nadetech Innovations S.L. until a waist diameter of 100 µm and a waist length of 10 mm were reached. This tapered uncladded multimode fiber (T-UMF, the same as T-CRMMF) was subjected to a sputtering process to deposit a silver mirror on its tip, so that a simple reflective set-up could be prepared, similar to Fig. 3.10.

Thus, the first step was to perform an LbL-assembly of 20 bilayers of [PAH/PAA] to locate the corresponding LMR in the desired wavelength. As it can be observed in Fig. 3.13a and b, the [PAH/PAA]$_{20}$ matrix located the LMR at 600 nm. Then, a [PAH/PSS]$_5$ polymeric matrix was deposited by LbL-assembly over the previous one, in order to create an adequate environment for the deposition of the anti-IgGs, according to [12]. The end of the construction finished when the LMR reached the center of the monitoring window, this means 700 nm (bilayer 25). The goal for doing this was to center the LMR in a position where the further displacements could be better monitored wherever the resonance shifted.

Then, both anti-IgGs and IgGs extracted from goat serum, were deposited and detected. In this sense, the next step was to register the LMR displacement when adsorbing the anti-IgGs layer and the further shifts when detecting the different IgG concentrations. Thus, Fig. 3.14 is depicted, where the mentioned biological processes are presented, as a wavelength shift while time passes. First, the substrate deposited by the previous paragraph was subjected to a 6 µg/ml solution of anti-goat IgG in PBS during 4 hours, so that the anti-IgGs were deposited onto the substrate at room temperature. As it is presented in Fig. 3.14, the LMR shifted around 14 nm to the right, from 735 to 749nm. Then, 3 different IgG concentrations were detected by immersing the resulting biosensor in 1.4, 4.2 and 12.5 µg/ml PBS-IgGs solutions, obtaining shifts to 747, 752 and 757 nm respectively.

The reason for this behavior is a change of the effective refractive index due to the adsorption of the biological compounds, which makes the LMR experiment a wavelength shift from one position to other.
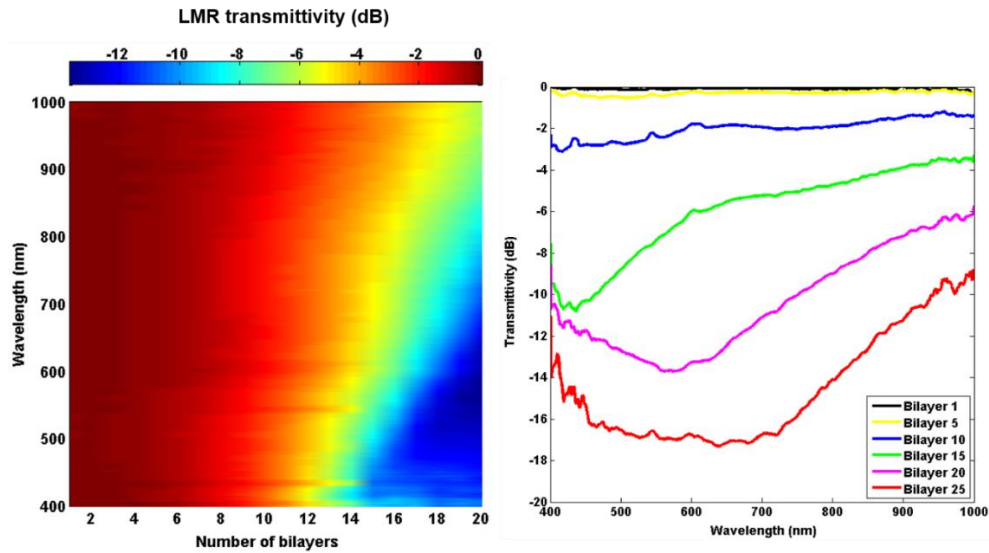

Fig. 3.13. *(a) LMR evolution as the thin-film thickness increases. (b) LMR at different bilayers [13].*
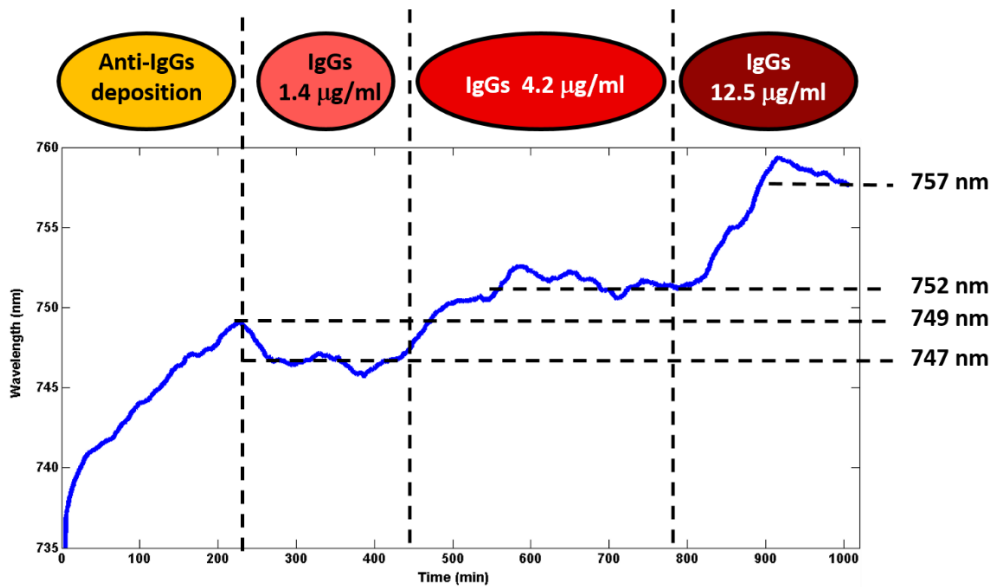

Fig. 3.14. *Tracking the minimum of the LMR during the anti-IgGs deposition and the IgGs detection. The vertical dashed lines indicate when the sensor is immersed into the next IgGs solution [13].*

3.2.3. Immunosensor based on LMRs generated with ITO thin-films and covalently attaching bioreceptors.

Among the materials that can induce LMRs by deposition onto optical fibers, one of the most utilized is indium tin oxide (ITO) [14,15] as mentioned at the beginning of this section. Particularly, ITO presents a higher refractive index than silica, what increases the sensitivity of the devices [4,5]. Moreover, when deposited, it usually provides a higher plane surface than by using polymer coatings, leading to a more effective way to adsorb bioreceptors on top of its surface [16]. In this sense, an ITO layer will be deposited on an optical fiber to generate the corresponding LMR. Then, a silane layer will be deposited on the ITO, in order to facilitate the IgGs adsorption. Finally, the detection of the anti-IgGs will be carried out, proving the presence of biological components in the biosensor.

LMR GENERATION AND OPTICAL MATERIALS

The first step to achieve the biosensor was to generate the sensing phenomenon, the LMR. To this purpose, several optical fiber segments from a 200/250 µm (core/cladding diameter) cladding removable multimode optical fiber (CRMMF) were obtained. They were stripped, uncladded and then immersed in detergent, deionized water (18.1 MΩ/cm), piranha solution (30% H_2O_2 + 70% H_2SO_4), again deionized water and acetone dry during 10 minute-time periods. The aim of these steps was to remove the undesired covers, clean the surface and prepare them for the ITO deposition [17].

A sputtering deposition using an ITO target was then performed over the fibers. To this purpose, a sputtering equipment was used with an Argon partial pressure of 9×10^{-2} mbar and a current intensity of 150 mA. Fibers were fixed to a rotating engine at 5 rps rotational speed and then located under the ITO target as indicated in the upper inset of Fig. 3.15. In order to make a study on the spectrum evolution as a function of the deposition process, sputtering times of 15, 30, 60, 120 and 180 seconds were programmed.

Once the substrates were fabricated, the set-up depicted in Fig. 3.15 was prepared. Basically, 30 mm-length segments of the ITO-coated fibers were cleaved at 90° and then spliced to two CRMMF pigtails. A broadband light source covering a wavelength range from 400 to 1800 nm, launched light into one end of the new created waveguide. The other end was connected through a bifurcated optical fiber (VIS-NIR with low OH content) to two spectrometers, which permitted to monitor a wavelength range from 400 to 1700 nm.

Regarding the optical data processing, as the different coatings were deposited, the corresponding transmission spectrum was captured and referenced to the spectrum obtained when the sensor was immersed for the first time in water solution. Additionally, in order to track the LMR shift in wavelength during the whole process, a real-time MATLAB® algorithm based on least squares was programmed.

SUBSTRATE BIOFUNCTIONALIZATION AND CHEMICAL MATERIALS

All the measurements were performed at constant temperature between 21 - 23°C and a relative humidity of 30%. To carry out this part of the fabrication, a common technique based on diluted 3-glycidopropyl-trimethoxysilane (GPTMS) was used [16,18]. The fabrication procedure is depicted in Fig. 3.16. Essentially, fibers were first immersed in 0.1 M potassium hydroxide (KOH) for 5 minutes and then rinsed in deionized water, in order to activate the ITO surface by hydroxylation.
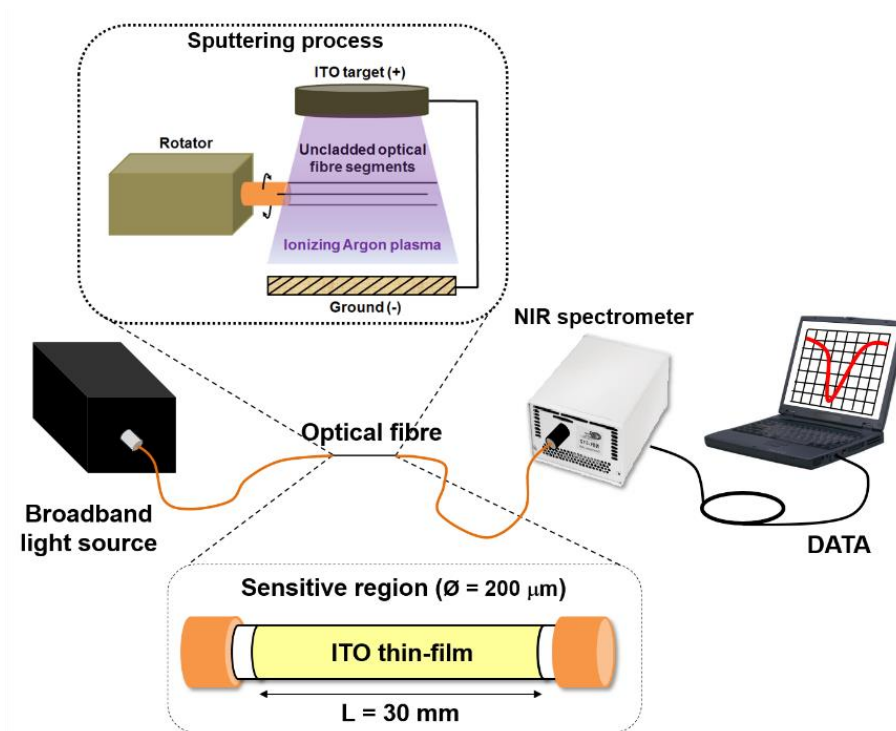

Fig. 3.15. *Optical set-up for monitoring the LMR evolution during the whole fabrication and detection process. The inset above is the sputtering process carried out to deposit the ITO onto de fibers. The inset below is the splicing of the ITO-coated fiber with both CRMMF pigtails, so that the transmission configuration is achieved.*

Then, the activated fibers were immersed in a solution containing 1% GPTMS in toluene. Here, 1 and 90 minutes of silanization were applied to the ITO-sputtered fibers, to be optically characterized afterwards. The objective was to check the influence of the silanization time when depositing biological compounds. After the silanization, fibers were gently rinsed in toluene, ethanol and finally, in ultrapure water, to remove the unattached silane molecules [16].

The goat IgGs adsorption was carried out afterwards. There are several methods describing how to bind IgGs to optical substrates [19]. A simple approach, like that used in [16] is presented here, since it is a simple technique where it is only necessary to immerse the silanized fibers in a PBS solution of IgGs. Moreover, due to the epoxy terminal ending the GPTMS carbohydrate chain, it is possible to attach IgGs more efficiently than by using other methods [20]. Particularly, the IgGs are mostly attached by their F_c chain and not by their F_{ab} part, what is interesting in terms of obtaining a more sensitive surface, as described in chapter 1.

In this case, as it can be observed in Fig. 3.16, GPTMS owns an epoxy terminal on top of the carbohydrate chain, which can be used to directly bind the goat IgGs by immersing the substrates in a 10 mM phosphate buffer saline solution (PBS) at pH 7.4 [16]. To this purpose, 200 µl from the stock IgGs solution in 12 mg/ml concentration were transferred to a 10 ml cuvette and fibers were then immersed for a maximum of 3 hours. At this point, the LMR evolution was continuously monitored, both for 1 minute and 90 minute-silane-deposited fibers, in order to see which of them was worth using to design the bioprobe. Once the IgGs were deposited, the bioprobes were rinsed in PBS solution for three times, to remove the excess of biomolecules that might not have bound.

Finally, the fabricated sensors were first immersed in 100 ml of 1 mM PBS adjusted at pH 7.4 during 90 minutes, to make the sensor get used to the environmental conditions. Then, a 2.2 mg/ml stock solution of anti-goat IgGs (anti-IgGs) was added step by step every periodically into the detection solution, increasing the anti-IgGs concentration. At the same time, a syringe pumped the whole detection solution to imitate a flowing environment. The LMR minimum was tracked during the whole process.

Although the work presented in this subsection is a label-free detection, the same process was also performed to several non-monitored fibers, in order to corroborate the anti-IgGs were adequately attached to the thin-film. To this purpose, a solution containing horseradish peroxidase (HRP)-conjugated goat anti-IgGs was used to bind the adsorbed IgGs. This solution also contains phosphate buffer saline (PBS pH 7.4) and 1% of bovine serum albumin (BSA). The presence of BSA is critical, as it prevents the adsorption of IgGs from binding with their non-

specific sites [21]. In addition to this, 3,3',5,5'-Tetramethylbenzidine (TMB) liquid substrate system was also used to corroborate the formation of IgG – anti-IgG complexes, as described in [22].

LMR AND ITO THIN-FILM CHARACTERIZATION

According to [14], several LMRs can be obtained with ITO-coated-based optical fibre sensors. Each of the LMRs is related to the guidance of a mode in the ITO thin-film. Consequently, as the thin-film thickness increases, the first mode is guided in the overlay (the first LMR is obtained in the optical spectrum), then the second mode is guided (a second LMR is visualized in the optical spectrum), and so on. The first LMR is the most sensitive among the different resonances showing up during the deposition of a thin-film on a substrate, and at the same requires to deposit less material than for the generation of the following LMRs [4]. In view of these good properties the generation and tracking of this first LMR will be the focus of the experiments.
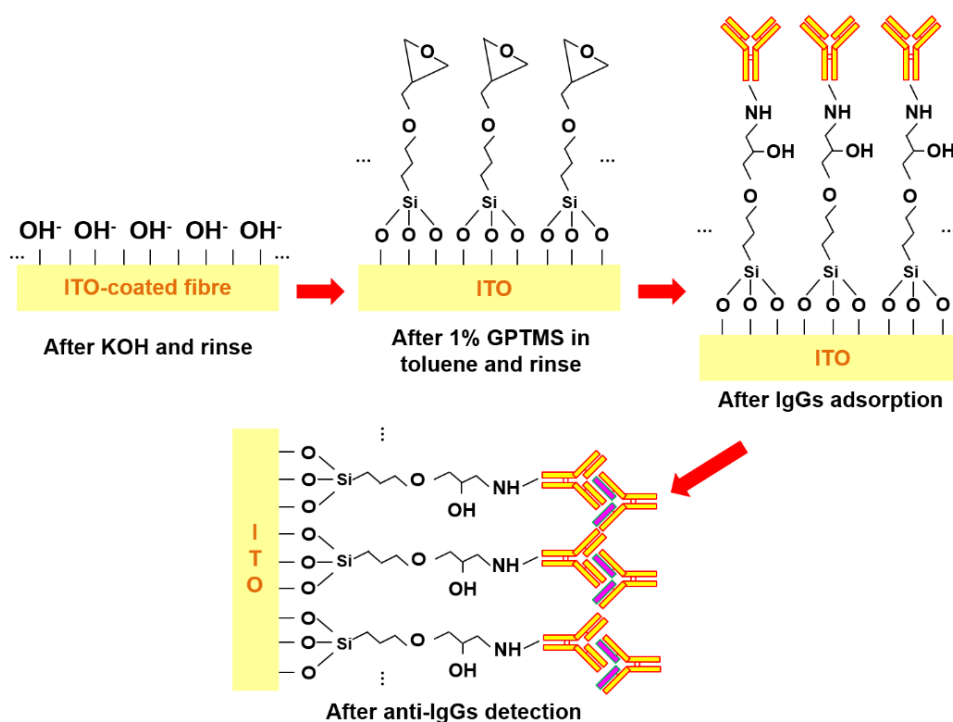

Fig. 3.16. *Schematic of the chemical steps followed to achieve the bioprobe.*

As an evidence of the above comments, Fig. 3.17 is shown, representing the evolution of the generated LMRs when the fibers are immersed in water (refractive index = 1.33). Here, the data provided by the spectrometers have been fused to show a total wavelength range from 400 to 1700 nm.

An LMR typical behavior can be observed here. After 15 seconds of ITO sputtering deposition, no LMRs appear. The thin-film continues increasing until 30 seconds, when the first LMR shows up and locates around 1200 nm. Then, after 60 seconds only the left shape of the first LMR is visible. It takes 2 minutes to have the second LMR located at around 520 nm and 3 minutes to see both second and third LMRs in the spectral range at 800 and 470 nm respectively. Therefore, a capacity of controlling the LMRs location as a function of the material thickness is demonstrated here.

It is also interesting to remark that the first LMR passes through the spectral range in a minute, whereas it takes the same time for the second LMR to shift less than 250 nm. This corroborates the hypothesis of the higher wavelength shift rate of the first LMR.
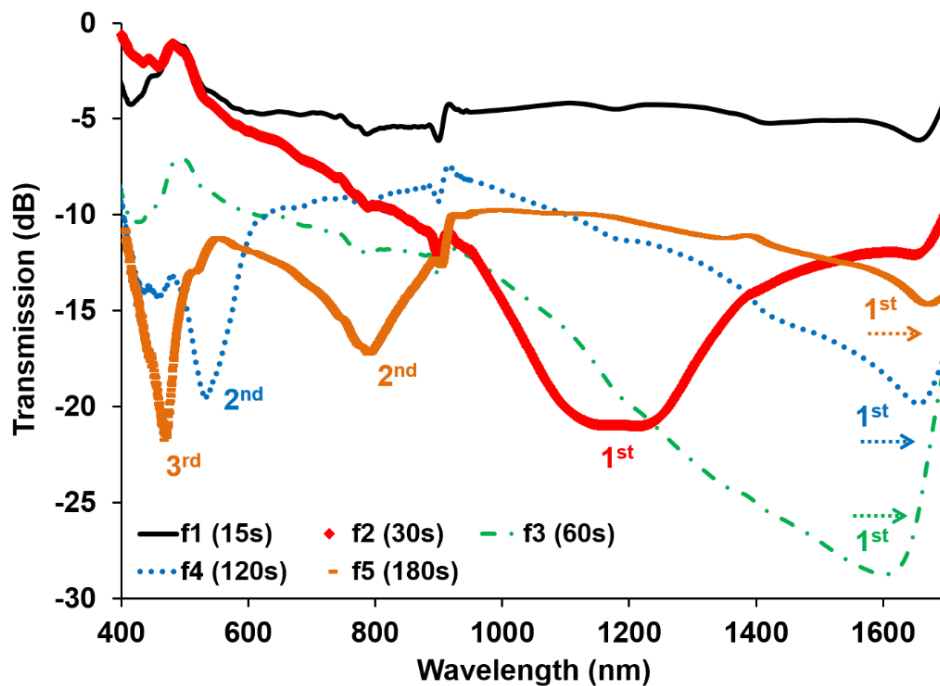

Fig. 3.17. *Fusion of the data provided by spectrometers XR1-FLG and NIR-512 in order to register the evolution of the different LMRs as a function of the sputtering deposition time when fibers are immersed in water (n_{H2O} = 1.33).*

In addition, after depositing ITO for 30 seconds on the optical fibers, a SEM characterization of this coating was performed, in order to know more about its properties. Then, several fibers were analyzed giving similar results to those presented in Fig. 3.18. It can be observed that the average thickness of the coating is 124 nm. Also, the plane and homogeneous surface as a result of the sputtering process can be noticed.

SILANIZATION AND ADSORPTION OF IGGS

After obtaining the LMR, the next step was to attach some molecules that permitted to bind the bioreceptors to the ITO thin-film covalently. The chemical silanization of GPTMS in toluene has been previously described in section 2.2 and [16]. In that contribution it is indicated that 90 minutes are enough to obtain a good bioreceptor attachment. Here, a 1 minute-silanization fiber was also deposited, to see if the silanization time influenced in the amount of bioreceptors adsorbed.

Thus, the 90-minute silanized fibers were tested by tracking the LMR minimum after immersing the bioprobe in the PBS solution containing goat IgGs. Here, after diluting the initial IgGs solution in PBS, the IgGs concentration in the cuvette was 232 μg/ml. Taking into account that the average molecular weight for a goat IgG is 144 kDal [23], this concentration can be expressed as 1.61 μM. Using high bioreceptor concentrations is a common technique to fill as much sensitive area as possible. In this way, a higher efficiency in the detection process is expected.
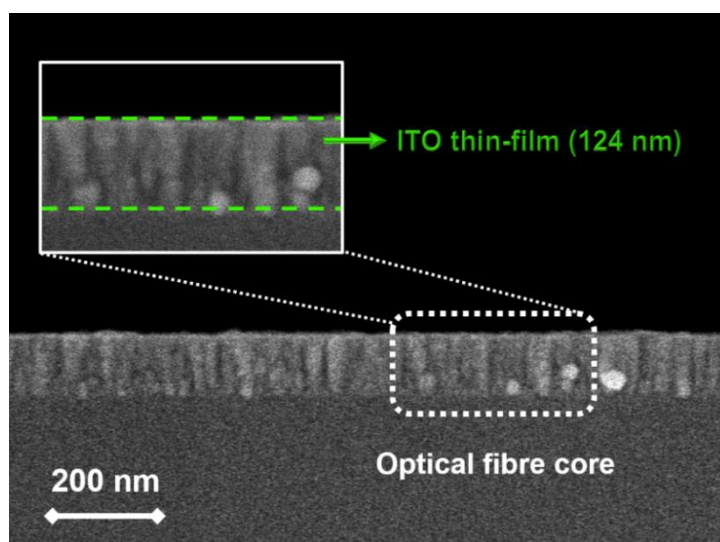

Fig. 3.18. *Characterization of the deposited 30 seconds ITO layer by SEM imaging. The average thickness is 124 nm and a nanostructured thin-film can be visualized.*

The results are depicted in Fig. 3.19. It is interesting to remark the different behavior in the IgGs adsorption rate depending on the silanization time. For example, when the silanization time is only 1 minute ($f_{1,1}$ and $f_{1,2}$), the antibodies adsorption lasts more than 2 hours to stabilize, whereas for a much longer silanization time, this means, 90 minutes ($f_{90,1}$ and $f_{90,2}$), the curves are stabilized in about an hour and a half. In addition to this, the LMR wavelength shift rates are higher in the 90 minutes case than in the 1 minute case. This difference in the shift rate is an indication of the success in the IgGs adsorption. A 90 minutes silanization permits to attach a high amount of IgGs to the optical fiber, which means to obtain a sensitive surface full of bioreceptors and, therefore, to improve the sensing efficiency. However, a 1 minute silanization process is not able to create a silane layer sufficiently consistent to adsorb as many IgGs as possible. Consequently, the 90 minutes silanization option is chosen to continue with the biodetection. Nevertheless, both types of fibers will be used to corroborate the IgGs attachment in the next paragraphs.

ANTI-IGGS DETECTION AND VERIFICATION

As it was indicated in previously, the bioprobe was cleaned and immersed in 1 mM PBS solution. Then, an increasing concentration of anti-IgGs was achieved by dropping a stock solution of 2.2 mg/ml IgGs (15.28 μM) in the PBS solution until the sensor stopped to respond adequately to the biological stimulus. During all this time, the LMR wavelength shift was monitored as in previous sections.

The three main parameters mentioned at the beginning of this chapter are analysed in in Fig. 3.20, where the evolution of the resonance wavelength can be observed as a function of the increasing anti-IgGs concentration. First, the biosensor was immersed in PBS for an hour to let it stabilize (see blue pointed spectrum). After stabilizing, the LMR was centered at around λ_r = 1430 nm, with a maximum attenuation of 35 dB and a spectral width of about 65 nm.

Then, some spectra are captured during the detection process as a function of the increasing anti-IgGs concentration. It can be observed that the LMR red-shifts as the amount of anti-IgGs increases. Consequently, the rise in the anti-IgGs concentration can be distinguished in a wavelength shift from 1430 nm to almost 1440 nm.

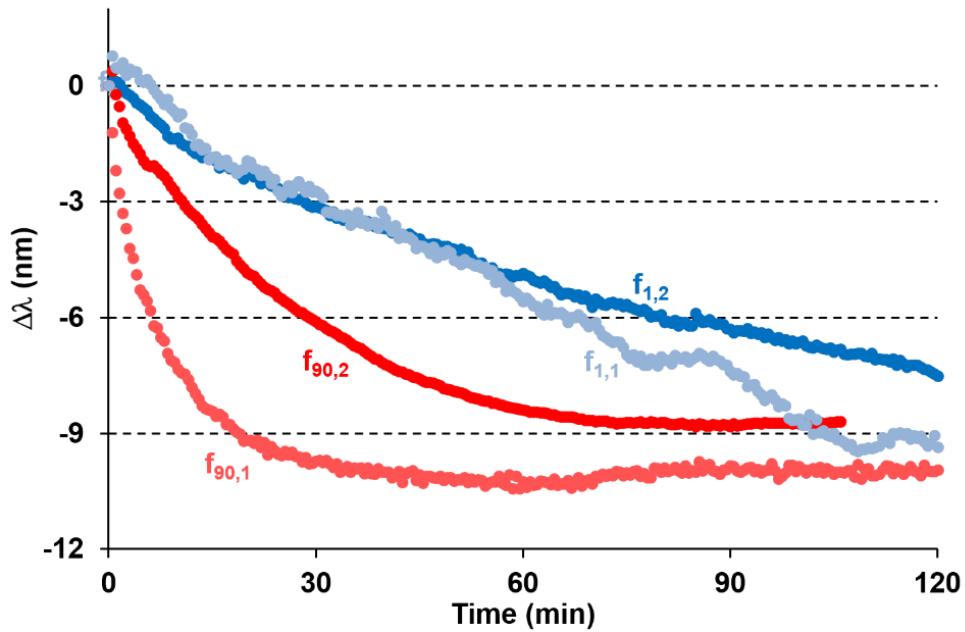**Fig. 3.19.** *Monitoring of the IgGs adsorption after 1 ($f_{1,1}$ and $f_{1,2}$) and 90 ($f_{90,1}$ and $f_{90,2}$) minutes of silanization. A faster adsorption can be observed after silanizing during 90 minutes.*
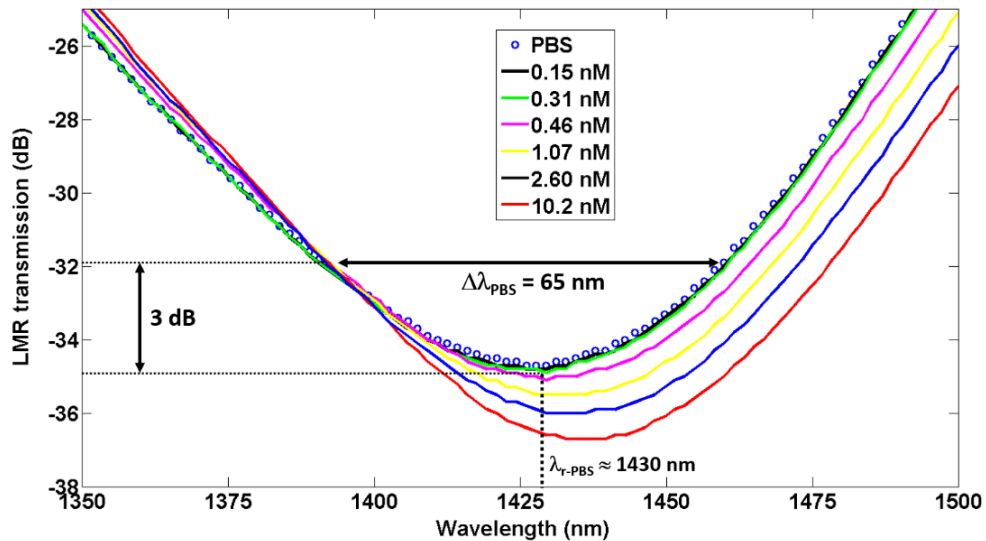

Fig. 3.20. *Tracking of the LMR at different moments during the anti-IgGs detection. There is a red-shift in wavelength as more IgGs are being accumulated in the sensitive area.*

In addition, Fig. 3.21 shows a change in the shift rate depending on the amount of anti-IgGs as they are accumulated during the detection. In order to corroborate this fact, each single slope is extracted and then referenced to its initial wavelength, (the moment after dropping more anti-IgGs solution). This permits to see the differences in the slopes, corresponding to the response of the bioprobe to the increasing IgGs concentration. It is clear that the slope of the sensor response rises as more IgGs are in the solution. Indeed, it can be observed that when the first 1 µl are dropped (0.15 nM concentration), the slope (shift rate) is 0.014 nm/min, it is 0.03 nm/min for 0.31 nM, 0.05 nm/min for 0.46 nM, 0.07 nm/min for 1.07 nM, 0.13 nm/min for 2.06 and 0.17 nm/min for 10.2 nM, the instant when the detection ends.

Analyzing the previous slope values, at lower concentrations the increment seems to be proportional to the anti-IgGs concentration. However, for the last two detectable increments (2.06 nM and 10.2 nM concentration respectively), the response is higher than the rest but it does not vary so much between them. In fact, it can be noticed that when detecting the highest concentration, (10.2 nM), the linear trend turns quadratic. This last condition can be observed when the sensitive surface is totally covered by the analyte (the anti-IgGs, in this case) [24]. This tendency is plotted in Fig. 3.22, where the wavelength shift rate is represented as a function of anti-IgGs concentration. As it can be observed, the previous description fits quite well to a logarithmic behavior.
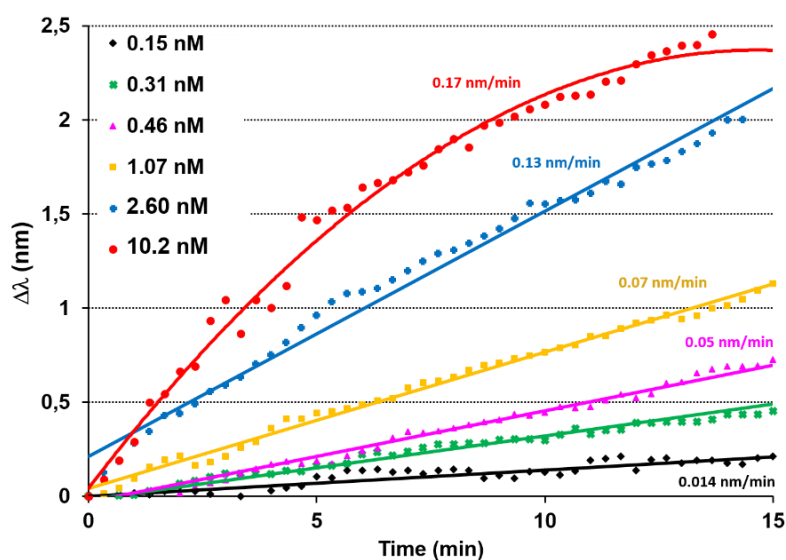

Fig. 3.21. *Different wavelength shift rates as a function of time for the different anti-IgGs concentrations tested. Each different slope is due to an increasing anti-IgGs concentration.*
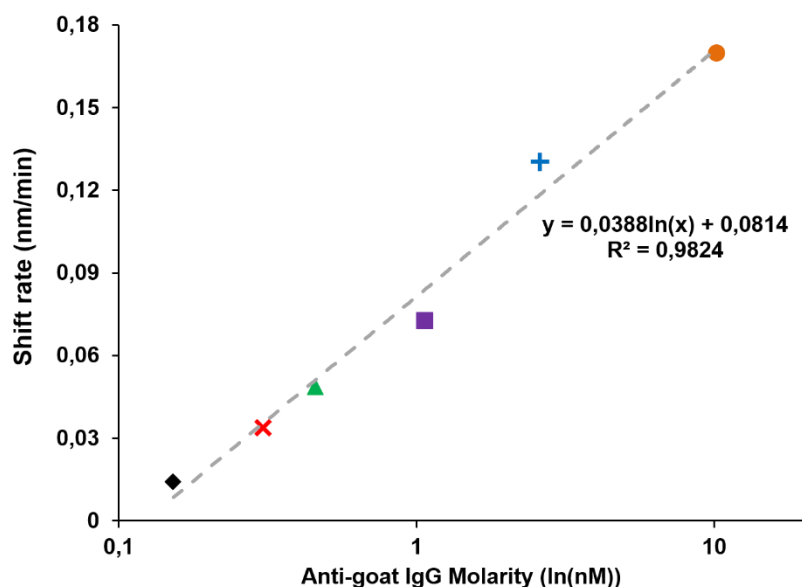
Fig. 3.22. *Sensitivity of the fabricated biosensor as a function of the anti-IgGs concentration. A linear trend (with horizontal axes in logarithmic scale) can be fitted for this LMR-based biosensor.*

Finally, some evidence of the anti-IgGs attachment to the bioprobes is provided. As it was indicated at the end of subsection 3.2, two 1 minute and 90 minutes silanized fibers were kept in order to prove the correct IgG attachment and further anti-IgG detection. The goal was to corroborate that with less silanization time the amount of anti-IgGs attached was lower than by silanizing for 90 minutes. To this purpose, a colorimetric reaction between 3,3',5,5'-Tetramethylbenzidine (TMB) and horseradish peroxidase (HRP) enzyme was induced, by adsorbing HRP-conjugated anti-IgGs over other biofunctionalized probes, once the IgGs were attached after the 1 minute and 90 minute silanizations. A color change from transparent to blue in the liquid substrate (TMB) indicates a correct attachment [1].

Thus, after attaching the IgGs to the bioprobe and rinsing it, the sensor was subjected to the same detection process presented previously, but using a PBS solution containing HRP-conjugated anti-IgGs this time. Then, once the detection was finished, the colorimetric reaction was carried out over a small white Teflon® tray. Basically, the bioprobes were rinsed in PBS and subjected to 1 ml TMB, carefully dropped over the sensitive area. As it can be observed in Fig. 3.23, with 1 minute of silanization it is hard to visualize an actual color change both in the liquid substrate and in the fiber after an hour of reaction. However, it is clearly visible a color change in the 90 minute silanization bioprobe after 20 minutes and not only

in the liquid but also in the fiber. This corroborates that the fact of silanizing more time is good in terms of attaching as many anti-IgGs as possible.

3.3. Conclusions

To sum up, the use of cladding removed multimode fiber-based structures (CRMMFs) is one of the simplest ways to increase and access the evanescent field of an optical fiber, since by only stripping the fiber polymer cladding it is possible to achieve this objective.

When adsorbing a high refractive index thin-film in order to generate lossy mode resonances, it is better to use the uncladded fiber itself. In fact, some biosensors based on LMRs generated on CRMMFs have been fabricated, even reaching nanomolar concentration. The sensitivity of the devices permits to achieve this kind of results, distinguishing between small changes in the properties of the thin-film or the surrounding medium refractive index as a function of the biological reactions. Tapering the fiber provokes higher attenuation and a broadening in the spectral width of the LMR, which is bad in terms of improving the LMRs parameters.

(a)   After 2 minutes   After 60 minutes   After 480 minutes

(b)   After 2 minutes   After 20 minutes   After 40 minutes

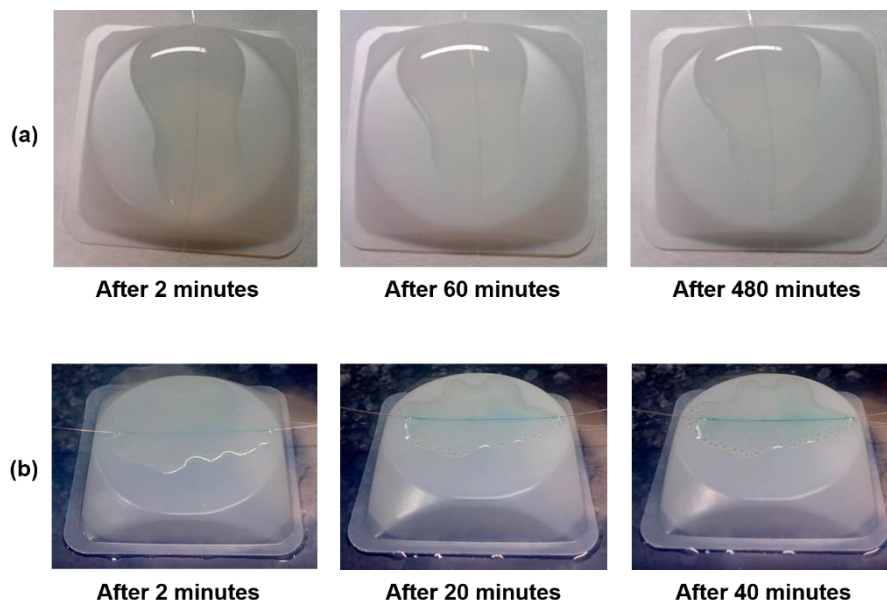*Fig. 3.23. Comparison of the TMB – HRP enzyme reaction when adsorbing 100 μl of TMB on two bioprobes deposited with 1 minute of silanization and 90 minutes of silanization respectively. The color change in the 90 minute silanization biosensor is enough to prove that by increasing the silanization time it is possible to attach more IgGs and, therefore, to obtain a better biosensor.*

Although the generated LMRs may be used for detection, they are quite broad, which reduces their measurement resolution. This means that their spectral width is not low and, consequently, there is a lack of resolution. This parameter is critical. If the application needs to detect small concentration variations, as it occurs in biology, it is better to use low spectral width and high sensitive phenomena, in order to distinguish small changes in the increasing concentration.

A concept that can help to describe this effect is a **figure of merit (FOM)** that relates the sensitivity in wavelength with the resolution of the obtained resonances. Based on [25], this FOM is described as indicated in Eq. 3.1:

$$FOM = \frac{S\,[nm/RIU]}{\Delta\lambda|_{-3dB}\,[nm]}$$

(3.1)

where S is the wavelength shift over the refractive index variation. This means the sensitivity of the device calculated after subjecting it to refractive index changes. $\Delta\lambda$ is a magnitude indicating line width. For instance, the commonly used Full Width at Half Maximum (FWHM) can fit this equation.

At the end of each chapter, an analysis of the FOM for each specific structure will be done, in order to compare their sensitivity to refractive index variations based on [TiO$_2$/PSS] deposited thin-films. The comparison will be done in the near infrared range, where all the analyzed resonances of interest coincide.

Thus, the sensitivity calculated for CRMMFs is 2872 nm/RIU [7]. Taking into account that the full width at half maximum is FWHM $\approx$ 400 nm and evaluating in Eq. 3.1 it is obtained:

$$FOM_{CRMMF} = \frac{S[nm/RIU]}{FWHM\,[nm]} = \frac{2872}{400} = 7.18 \approx 7.2\,RIU^{-1}$$

In spite of the high sensitivity, this is a quite reduced value for this device, since the resonance FWHM is too large. In the following chapters the corresponding FOMs will be measured, in order to compare with the obtained here and to extract some conclusions on this magnitude.

3.4. Bibliography

[1] A.B. Socorro, J.M. Corres, I. Del Villar, I.R. Matias, F.J. Arregui, Celiac disease biodetection using lossy-mode resonances generated in tapered single-mode optical fibers, Proceedings of SPIE - The International Society for Optical Engineering. 9157 (2014).

[2] I. Del Villar, I. Matias, F.J. Arregui, R.O. Claus, Fiber-optic hydrogen peroxide nanosensor, Sensors Journal, IEEE. 5 (2005) 365-371.

[3] C.R. Zamarreño, M. Hernáez, I. Del Villar, I.R. Matías, F.J. Arregui, Optical fiber pH sensor based on lossy-mode resonances by means of thin polymeric coatings, Sensors Actuators B: Chem. 155 (2011) 290-297.

[4] I. Del Villar, M. Hernaez, C.R. Zamarreño, P. Sánchez, C. Fernández-Valdivielso, F.J. Arregui, I.R. Matias, Design rules for lossy mode resonance based sensors, Appl. Opt. 51 (2012) 4298-4307.

[5] I. Del Villar, C.R. Zamarreño, P. Sanchez, M. Hernaez, C.F. Valdivielso, F.J. Arregui, I.R. Matias, Generation of lossy mode resonances by deposition of high-refractive-index coatings on uncladded multimode optical fibers, Journal of Optics. 12 (2010) 095503.

[6] T.A. Birks, Y.W. Li, The shape of fiber tapers, Lightwave Technology, Journal of. 10 (1992) 432-438.

[7] M. Hernáez, I. Del Villar, C.R. Zamarreño, F.J. Arregui, I.R. Matias, Optical fiber refractometers based on lossy mode resonances supported by TiO_2 coatings, Appl. Opt. 49 (2010) 3980-3985.

[8] P. Sanchez, C.R. Zamarreño, M. Hernaez, I.R. Matias, F.J. Arregui, Optical fiber refractometers based on Lossy Mode Resonances by means of SnO_2 sputtered coatings, Sensors Actuators B: Chem. 202 (2014) 154-159.

[9] A.B. Socorro, J.M. Corres, I. Del Villar, F.J. Arregui, I.R. Matias, Fiber-optic biosensor based on lossy mode resonances, Sensors Actuators B: Chem. 174 (2012) 263-269.

[10] S.S. Shiratori, M.F. Rubner, pH-Dependent Thickness Behavior of Sequentially Adsorbed Layers of Weak Polyelectrolytes, Macromolecules. 33 (2000) 4213-4219.

[11] C.M. Hanbury, W.G. Miller, R.B. Harris, Fiber-optic immunosensor for measurement of myoglobin, Clin. Chem. 43 (1997) 2128-2136.

[12] Z. Feldoto, I. Varga, E. Blomberg, Influence of Salt and Rinsing Protocol on the Structure of PAH/PSS Polyelectrolyte Multilayers, Langmuir. 26 (2010) 17048-17057.

[13] A.B. Socorro, J.M. Corres, I. Del Villar, F.J. Arregui, I.R. Matias, Immunoglobulin G sensor by means of lossy mode resonances induced by a nanostructured polymeric thin-film deposited on a tapered optical fiber, (2012).

[14] I. del Villar, C.R. Zamarreno, M. Hernaez, F.J. Arregui, I. Matias, Lossy Mode Resonance Generation With Indium-Tin-Oxide-Coated Optical Fibers for Sensing Applications, Lightwave Technology, Journal of. 28 (2010) 111-117.

[15] P. Sanchez, C.R. Zamarreño, M. Hernaez, I. Del Villar, C. Fernandez-Valdivielso, I.R.Matias, F.J. Arregui, Lossy mode resonances toward the fabrication of optical fiber humidity sensors, Measurement Science and Technology. 23 (2012) 014002.

[16] D. Guo, M. Zhuo, X. Zhang, C. Xu, J. Jiang, F. Gao, Q. Wan, Q. Li, T. Wang, Indium-tin-oxide thin film transistor biosensors for label-free detection of avian influenza virus H_5N_1, Anal. Chim. Acta. 773 (2013) 83-88.

[17] R. Ota, S. Seki, M. Ogawa, T. Nishide, A. Shida, M. Ide, Y. Sawada, Fabrication of indium–tin-oxide films by dip coating process using ethanol solution of chlorides and surfactants, Thin Solid Films. 411 (2002) 42-45.

[18] C.D. Corso, A. Dickherber, W.D. Hunt, An investigation of antibody immobilization methods employing organosilanes on planar ZnO surfaces for biosensor applications, Biosensors and Bioelectronics. 24 (2008) 805-811.

[19] M.E. Bosch, A.J.R. Sánchez, F.S. Rojas, C.B. Ojeda, Recent development in optical fiber biosensors, Sensors. 7 (2007) 797-859.

[20] H.K. Hunt, A. Armani, Bioconjugation Strategies for Label-Free Optical Microcavity Sensors, Selected Topics in Quantum Electronics, IEEE Journal of. 20 (2014) 121-133.

[21] H. Niu, R. Yuan, Y. Chai, L. Mao, Y. Yuan, Y. Zhuo, S. Yuan, X. Yang, Electrochemiluminescence of peroxydisulfate enhanced by l-cysteine film for sensitive immunoassay, Biosensors and Bioelectronics. 26 (2011) 3175-3180.

[22] G. Volpe, R. Draisci, G. Palleschi, D. Compagnone, 3,3',5,5'-Tetramethylbenzidine as electrochemical substrate for horseradish peroxidase based enzyme immunoassays. A comparative study, Analyst. 123 (1998) 1303-1307.

[23] D. Givol, E. Hurwitz, Goat immunoglobin G. Peptide chains and terminal residues, Biochem. J. 115 (1969) 371-375.

[24] M. Piliarik, J. Homola, Surface plasmon resonance (SPR) sensors: approaching their limits? Opt. Express. 17 (2009) 16505-16517.

[25] A. Cattoni, P. Ghenuche, A. Haghiri-Gosnet, D. Decanini, J. Chen, J. Pelouard, S. Collin, $\lambda_3/1000$ plasmonic nanocavities for biosensing fabricated by soft UV nanoimprint lithography, Nano letters. 11 (2011) 3557-3563.

CHAPTER 4. Sensors based on lossy mode resonances by means of thin-films deposited on tapered single-mode optical fibers

According to what has been explained in previous chapters, LMRs depend on parameters such as the surrounding medium refractive index (SMRI) [1] and the thin-film thickness and refractive index [2], similarly to SPRs. However, depending on the experimental set-up, sometimes LMRs present a broad attenuation band, which leads to a reduction in the resolution of the measurements. In this sense, chapter 3 has shown that by utilizing cladding removed multimode optical fibers (CRMMFs), the obtained LMRs present spectral widths on the order of cents of nanometers and lose too much power. Moreover, it has been proved that these results are worse if a tapered CRMMF is used. Even with the sensitivities provided by such devices, their capability to detect small concentration variations like those required for designing biosensors is quite reduced.

The fact of such large width can be explained due to two reasons. First, for unpolarized light, there is a coupling to both TE and TM lossy guided modes in the thin-film, and the maximum coupling to both TE and TM modes is achieved at different wavelengths [3]. Thus, for unpolarized light, the resulting spectral response is a combination of coupling to these two modes [2].

Secondly, if the refractive index of the thin-film is increased, the LMR presents a wavelength shift to the red and at the same time its spectral width is increased [3]. Since most of the optical equipment is designed to work in the third optical communications window, this is a drawback when using LMRs as a sensing technology. Therefore, there is a need for narrower LMRs, especially when using the devices for detecting small wavelength variations due to small changes in a specific biological variable.

Hence, it seems clear that if the optical fiber is designed to propagate several modes, the obtained LMRs do not fulfill the required conditions to become good biosensing platforms. That is why it was decided to work with standard monomode or single-mode fibers. In addition, since a standard single-mode fiber itself does not permit to access its evanescent field directly due to the existence of a 125 micron-diameter cladding over a 8 micron-diameter core, it was decided to work with tapered single-mode fibers (T-SMFs). To this purpose, a study on the LMRs generation in T-SMFs will be first done. Some sensors and biosensors based on this structure will be presented afterwards.

4.1. Optimization of T-SMF parameters to generate LMRs

Because standard optical fibers were originally designed for low loss communications, the penetration depth (d_p – see chapter 2 for more details on this magnitude) is really small in comparison to the cladding thickness, so there is a null interaction between the surrounding medium and the fiber evanescent field. Additionally, in standard optical fibers the cladding cannot be removed, since it is also made of fused silica, so there is no way to access the fiber evanescent field unless the fiber diameter is gently reduced. Thus, tapering a fiber helps to have this evanescent field accessible.

A tapered single-mode optical fiber (T-SMF) is usually fabricated by pulling an SMF fiber from both sides at the same speed while it is heated to its softening temperature, reducing the diameter until desired. A design of a taper puller prototype by Nadetech Innovations S.L. can be visualized in Fig. 3.6 on chapter 3. As a result, every T-SMF consists of three regions: a waist segment with length L_w and reduced and uniform diameter $\emptyset_w$, and two conical transition regions with gradually varied diameter and length L_t. A typical T-SMF is plotted in Fig. 4.1a, where the profile and shape of a reconstructed T-SMF is observed. This image has been obtained after applying an edge detection algorithm, in order to check that the T-SMF dimensions are correctly achieved. Concretely for this case, the waist length is 10 mm and the transition region lengths are 5 mm each, whereas the radius of the structure has been reduced from 62.5 to 15 μm. Thus the T-SMF waist diameter is 30 μm [4]. The idea is that, once the necessary T-SMF diameter is achieved, its evanescent field is accessible, since some wavelengths will not be able to propagate adequately into the core and will start to be propagated in the cladding. Consequently, it will be possible to couple light from the waveguide to the deposited thin-film and thus generate the LMRs. However, there is a need for keep on studying the issues showing up when dealing with T-SMFs, since the main goal of this chapter is to optimize the generation of LMRs using these structures.

First of all, the shape of the T-SMF is a key point to obtain the desired results. In accordance with both the literature and the experiments done in the laboratory, there are two main groups of tapers: adiabatic and non-adiabatic [4-6]. Fig. 4.1b shows two transitions for an adiabatic and a non-adiabatic T-SMF respectively [7]. In the first group, due to a softer diameter decrease in the transition region, the fundamental mode (HE_{11}) is propagated with losses lower than 1 dB, preserving the input spectrum. Consequently, the evanescent field is accessible and there are no remarkable changes in the spectrum. On the opposite, non-adiabatic tapers present higher losses and oscillations in the transmission spectrum, proving that there is an interferometry phenomenon in the optical

structure. In fact, despite both structures permit to access their evanescent field, they can be used for different purposes. Non-adiabatic tapers are normally used as interferometer-based optical filters, whereas adiabatic T-SMFs can be used as simple waveguides with an accessible evanescent field [8]. Moreover, the fact of choosing minimum length tapers is quite good in terms of reducing the sensor size at the same time the propagation losses are reduced. In view of this, and taking into account the possible attenuation values induced by the LMRs when induced, quasi-adiabatic tapers of minimum length are chosen in this chapter to be studied and used as biosensing platforms.

As mentioned, the fact of dealing with single-mode fibers permits to reduce the number of modes propagated in the optical structure. However, it is necessary to introduce a crucial parameter: the V parameter. This magnitude can be only used to describe the propagation of light modes in standard optical fibers as long as the light propagation is carried out under weak guidance conditions. This means that the working wavelength is much lower than the core diameter and that both core and cladding refractive indices are quite similar. Under this situation, the V parameter sets the conditions to propagate several modes inside the fiber, according to the well-known equation (4.1):

$$V = \frac{2\pi r}{\lambda} \sqrt{\mathrm{n}_{co}^2 - \mathrm{n}_{cl}^2} \qquad\qquad (4.1)$$
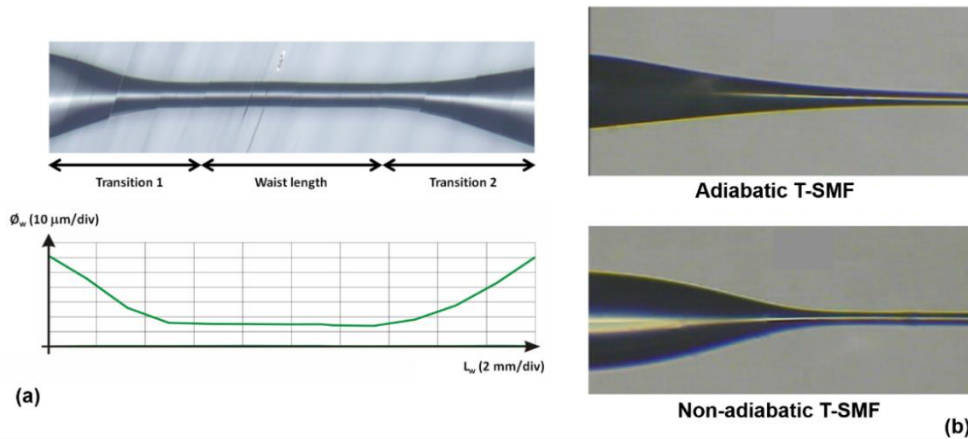

Fig. 4.1. *(a) T-SMF shape and profile, obtained by applying an edge detection algorithm to define the contour of the structure [4]. (b) Examples of adiabatic and non-adiabatic transitions in a T-SMF [7].*

where *r* is the SMF radius, λ is the free space studied wavelength and the squared root term is called numerical aperture (*NA*), which gives an idea of how much light can be coupled in the optical cable just after introducing it (see Fig. 4.2a for more details).

Taking the previous equation, and doing the necessary calculations, the well-known V-b curve represented in Fig. 4.2b can be drawn. This graph indicates how many modes are propagated in a standard optical fiber as a function on the *V* value [9]. More specifically, if the fiber to be used is monomode, just by substituting the values of *r* (4 μm), *λ* and the corresponding refractive indices for a standard SMF fiber, it can be obtained that the necessary *V* value to propagate only one mode is *V* = 2.405. From another point of view, this means that any other modes that may be propagated are under cut-off conditions, so no more modes are allowed to propagate within the optical fiber.

However, after tapering a single-mode fiber, the previous values are not exactly the same, because if the tapering process is done properly, there is a proportional reduction of both core and cladding diameters, which leads to new guidance conditions. Due to this proportionality, the necessary *V* values to guide only one mode keeps on ranging in 1 ≤ V < 2.405, but due to the changes in the diameters, the cut-off conditions are limited to new wavelengths.

Considering the previous assumptions, q is defined as the quotient between cladding and core diameters. According to [10], the limit to propagate an only mode in a SMF fiber is given by equation (4.2):

$$V_{cc} = \sqrt{\frac{2}{\ln(q)}} = \sqrt{\frac{2}{\ln(\frac{125}{8})}}) = 0.853 \qquad (4.2)$$

which is close to 1, the minimum value considered as the limit to completely propagate the fundamental mode in the SMF. Thus, the actual range for propagating only one mode in the SMF fiber would be V_{cc} = 0.853 < *V* < 2.405.

Assuming that, when tapering the fiber, the obtained structure is symmetric, both the cladding and the core will be reduced in the same factor. Therefore, as long as *V* remains in the previous interval, only one mode will be propagated in the core of the fiber. However, the V value varies as a function of the position in the taper. Assuming a linear transition region, Fig. 4.3 shows this variation in a T-SMF core.
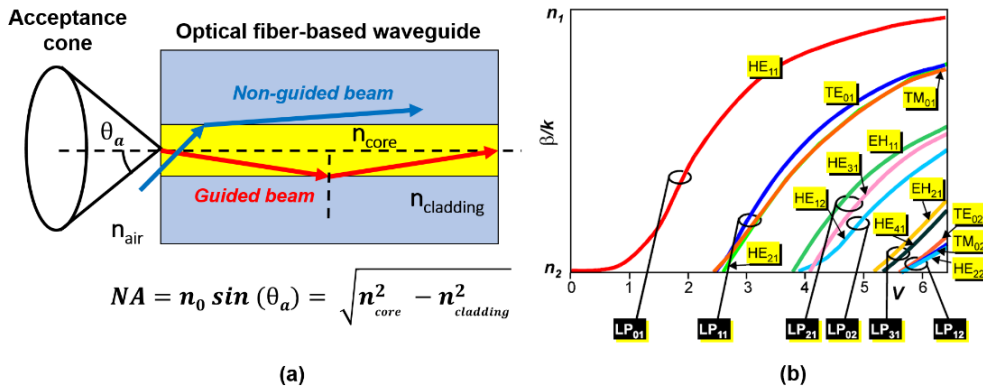
Figure 4.2. *(a) Concept of numerical aperture, necessary to propagate modes properly in a standard optical fiber. (b) V-b curve for standard optical fibers [9]. Hybrid and LP modes are represented. For single-mode fibers, the V value is 2.405.*

A simple analysis can be done by just taking a look at the core diameter. It is clear that, before the tapered region, the core diameter is the usual for a SMF fiber (8 microns), so *V* remains at 2.405. If the cladding diameter is reduced down to 50 μm, then the core diameter will be 3.2 μm, which means 0.4 times its initial value. Consequently, *V* will also be reduced by this factor, so now *V* = 0.962. Since *V* > V_{cc}, then the fundamental mode of the fiber would be still propagated by the reduced core. However, if the cladding diameter is reduced to 30 microns, the core diameter would be 1.92 and *V* = 0.58 < V_{cc}. In this case, the fundamental mode of the SMF fiber would be also under cut-off conditions, so it would not be propagated inside the fiber core. Some other core and taper waist cladding diameters with their corresponding values are presented in Table 4.1, where it can be observed that the necessary cladding diameter to start losing the only mode propagated is 44.33 μm. This means that, if the taper waist diameter is less than 44.33 μm, then the fundamental mode of the fiber will fulfill the cut-off conditions and will be progressively coupling out of the core, this means, to the cladding, as an evanescent field of the optical structure.

As it was mentioned before, the fact of reducing the diameters to guide the fundamental mode does not influence the conditions for *V* to propagate only one mode (assuming a proportional reduction and symmetry in the whole structure). However, this do influence in the wavelengths that this fundamental mode starts to be under cut-off conditions. Fig. 4.4 shows the inversely proportional dependence on the cut-off wavelengths as a function of the V parameter in the T-SMF for different taper waist cladding diameters. Thus, when the cladding diameter is the standard of an SMF fiber, this means 125 μm, the cut-off wavelength (λ_c) is

really high. Considering that standard SMFs are designed to efficiently propagate their fundamental mode at 1550 nm (third communications window) there are no transmission problems. The same occurs for $\lambda < 1252$ nm, if the taper waist cladding diameter is 50 μm; for $\lambda < 1002$ nm, if the taper waist cladding diameter is 40 μm and for $\lambda < 751.5$ nm, if the taper waist cladding diameter is 30 μm.
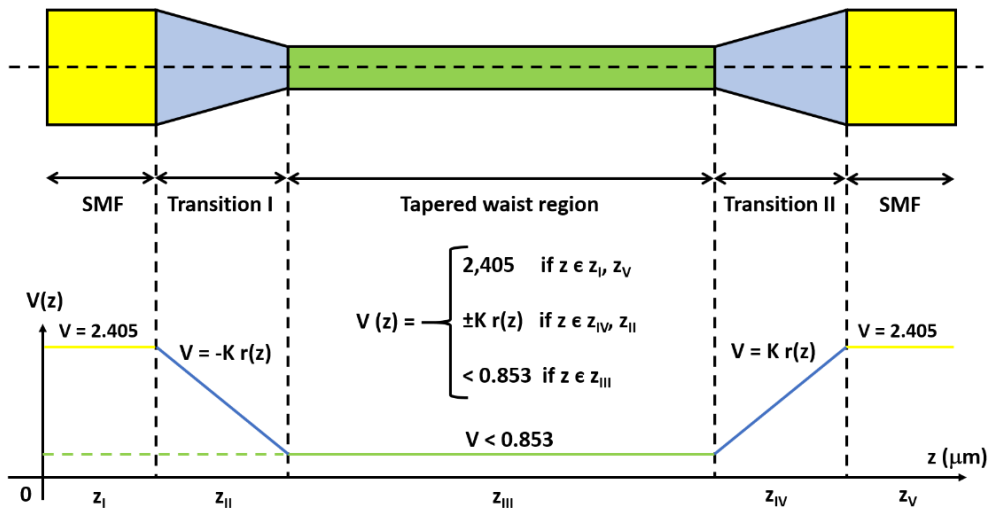
Fig. 4.3. Schematic of the T-SMF core with the corresponding evolution of the V parameter as a function of the diameter and position along the structure. K corresponds to the constant product $2\pi NA/\lambda$, whereas the taper radius (r) is linearly dependent on the position.

Cladding diameter (μm)	Core diameter (μm)	V	Evanescent field?
125	8	2.405	No
50	3.2	0.962	No
44.33	2.84	0.853	Yes (minimum)
40	2.56	0.7696	Yes
30	1.92	0.58	Yes
20	1.28	0.3848	Yes

Table 4.1. Access to the evanescent field of a T-SMF as a function of V in waist area (z_{III}).

The previous considerations suggest that, as the taper waist diameter decreases, the cut-off wavelength also decreases. This means that in low-diameter T-SMFs the light is not propagated by the T-SMF core, but it couples to the cladding. This means that the outermost medium of the structure is more accessible if the waist diameter is lower, so this is good in terms of depositing thin-films onto the T-SMFs, as there will be a coupling of light to the thin-film that will generate LMRs.
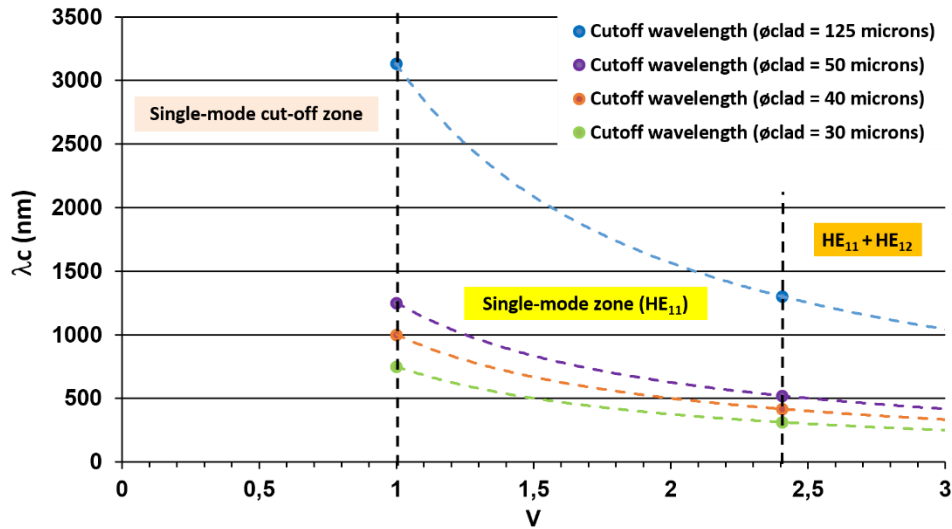

Figure 4.4. *Cut-off wavelengths and propagated modes as a function of the taper waist cladding diameter for a T-SMF structure.*

To prove this, a pair of experiments based on the deposition of a [PAH+NR/PAA] thin-film (where NR is Neutral Red) by LbL-assembly were performed [4]. Here, NR is used to make sure that the fiber is correctly deposited because of the purple color it dyes the substrate, although it does not affect the generation of the LMR [4]. Two T-SMF structures were fabricated from a SMF-28 single-mode optical fiber from Telnet Inc. Their transition lengths were L_t = 3 mm, their waist lengths were L_w = 10 mm and their waist diameters were around 50 and 40 μm respectively. They were stripped and cleaned with ethanol before subjecting them to the tapering machine designed by Nadetech Innovations S.L. and obtaining the corresponding T-SMFs.

To complete the optical set-up, Fig. 4.5 plots a schematic of the fabrication. Basically, the idea was the same than the rest of deposition processes presented so far, but changing the optical equipment to get results in the third optical communications window, since SMF fibers are optimized to work in this range.

Thus, a superluminescent light emitting diode (SLED) broadband light source (83437A, Agilent Technologies) was connected to the fibers on one side and the spectral response was monitored by an optical spectrum analyzer (OSA - 86140B, Agilent technologies) in the other. The detection wavelength range covered from 1150 to 1680 nm.
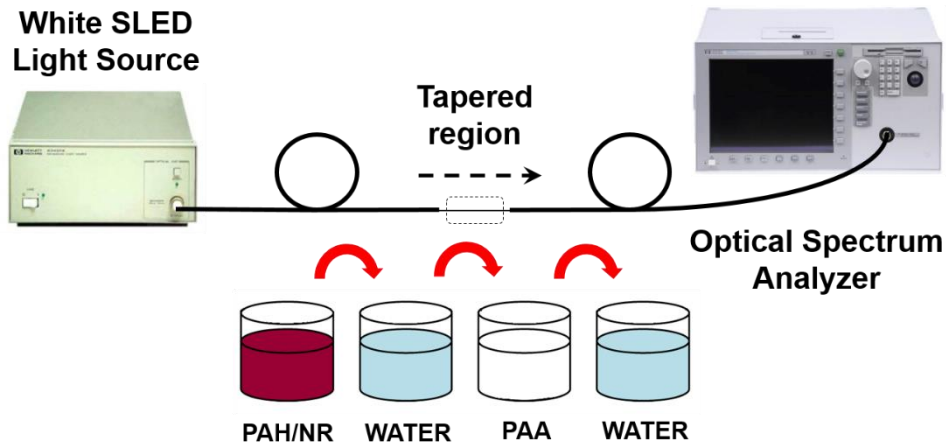
Fig. 4.5. *Set-up designed for the deposition and monitoring of these first preliminary experiments with T-SMFs [4].*
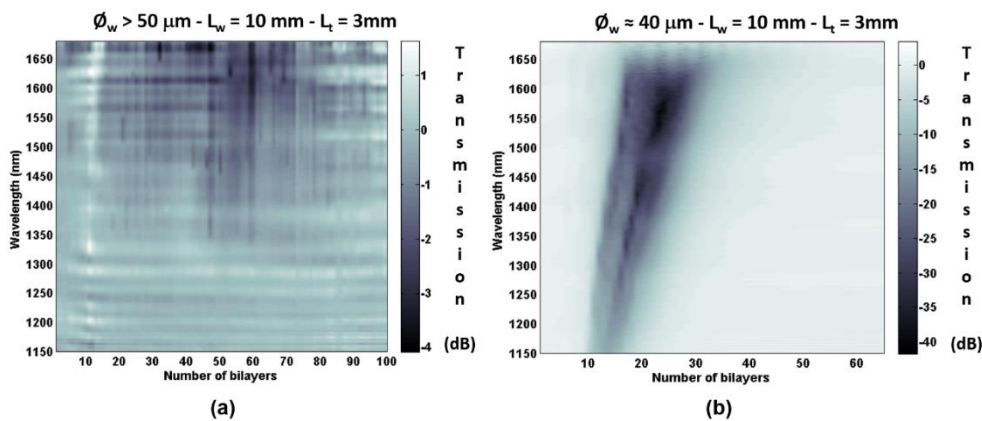
Fig. 4.6. *LbL-assembly deposition of a [PAH+NR/PAA] thin-film on two T-SMFs for taper waist diameters of (a) 50 μm and (b) 40 μm respectively. Dimensions are indicated in the upper part. No LMRs show up in the 50 μm case whereas an LMR shows up from bilayer 10 in the 40 μm case.*

After analyzing the data, Fig. 4.6 can be plotted. Here, the difference in the obtained spectra as a function of the increasing thin-film thickness for both T-SMFs is shown. It can be observed that, for the 50 microns case, there is a slight oscillation

in the spectrum. This is due of the slight non-adiabatic behavior of the T-SMF. There are some points in which the spectrum presents sudden rise and falls, but the overall response remains constant. The opposite can be observed for the 40 microns case, where there is a clear attenuation band of more than 40 dB between layers 10 and 30, showing the LMRs capacity of inducing optical power losses. In view of these data, a study on the influence of both T-SMFs diameter and length was done, in order to optimize the LMRs parameters for achieving better sensing applications.

LMR DEPENDENCE ON THE T-SMF's PARAMETERS

A study on the influence of the T-SMF parameters is shown in the following lines, in order to determine the most adequate characteristics to generate LMRs in these structures [4].

First, the influence of the waist diameter is studied. To this purpose, several groups of four tapers with waist diameters of 20, 30, 40 and 50 μm and transition regions with L_t = 3 mm were prepared. The parameters of the different analyzed tapers are summarized in Table 4.2, from T_1 to T_4. Fig. 4.7a is an experimental and theoretical representation of the LMR minimum evolution as a function of the number of bilayers at 1310 nm, when the diameter is varied. Simulations are obtained with CAMFR software [11], (see Appendix 1) which is based on the three-dimensional eigenmode expansion technique with perfectly matched layers [12].

By comparing the three tapers with diameters below 42 μm, it can be observed that the depth of the LMR decreases as a function of the waist diameter. The relationship between the depth and the diameter of the LMR has been also analyzed theoretically, showing a non-linear behavior. The red dots indicate the resonance depth for the T-SMFs previously mentioned. The simulation reaches T-SMF diameters of 10 μm, where the accumulated losses are approximately 50 dB (undetectable for the OSA used). From this point on, diameters below 10 μm present disadvantages such as fragility and the dependence of the properties of the LMR on other external phenomena, like vibrations, so this has been set as the lower limit for this study.

Another conclusion that can be extracted from these theoretical and experimental results, is that LMRs occur at the same range of bilayers for all the tapers analyzed. Consequently, this property does not actually depend on the waist diameter of the T-SMF.

The analysis of the taper waist length is also addressed. To this purpose, three T-SMFs were studied with the dimensions also shown in Table 4.2, from T_5 to T_7. Here, it is important to highlight that the three tapers had a fixed waist diameter and transition region of 40 μm and 3 mm respectively. This decision was based on the results obtained for Fig. 4.6, where it was proved that a taper waist diameter of 40 μm was enough to generate an LMR. The waist lengths were varied between 5 and 20 mm, in order to study the effect of this magnitude on the characteristics of the LMR.

Taper	Waist length L_w (mm)	Waist diameter $\varnothing_w$ (μm)
T_1	5	20
T_2	5	30
T_3	5	40
T_4	5	50
T_5	5	40
T_6	10	40
T_7	20	40

Table 4.2. *Parameters used to study the influence of the T-SMF waist diameter and length*

In Fig. 4.7b, the evolution of the LMR minimum is presented as a function of the number of bilayers at λ = 1310 nm. The experimental results obtained in the laboratory and the theoretical simulations for the three tapers considered, also obtained with CAMFR software, are shown. As in the previous section, the aim is to study the evolution of the attenuation band generated by the LMR as the taper waist length increases.

First of all, it can be observed that every LMR minimum occurs at the same range of bilayers (or thickness). Consequently it does not depend on the waist length of the T-SMF either. In addition, Fig. 4.7b shows that the minimum value for taper T_5 decays to almost −14 dB at bilayer 40. The next taper, T_6, falls down to −26 dB, which implies 12 dB deeper than T_5 and, finally, T_7 decays to −40 dB (27 dB deeper than T_5). Moreover, these data are also confirmed theoretically. In view of

these results, it can be affirmed that the LMR is deeper when the taper is longer. This phenomenon can be explained as an effect of the taper length, since there is a longer region where the cladding modes couple to the thin-film. This means that having a longer waist length permits to couple more power from the cladding to the thin-film along the sensitive region and that the losses registered are higher. This is confirmed in Fig. 4.7b, where the power losses experimented by the taper are represented as a function of the waist length. Apart from that, the sensitivity of the OSA is not enough to detect where the minimum of T_7 data is located, so this results in a difference between experimental and theoretical data in the case of T_7. As a consequence, there is a little distortion in the detection of the minimum value.

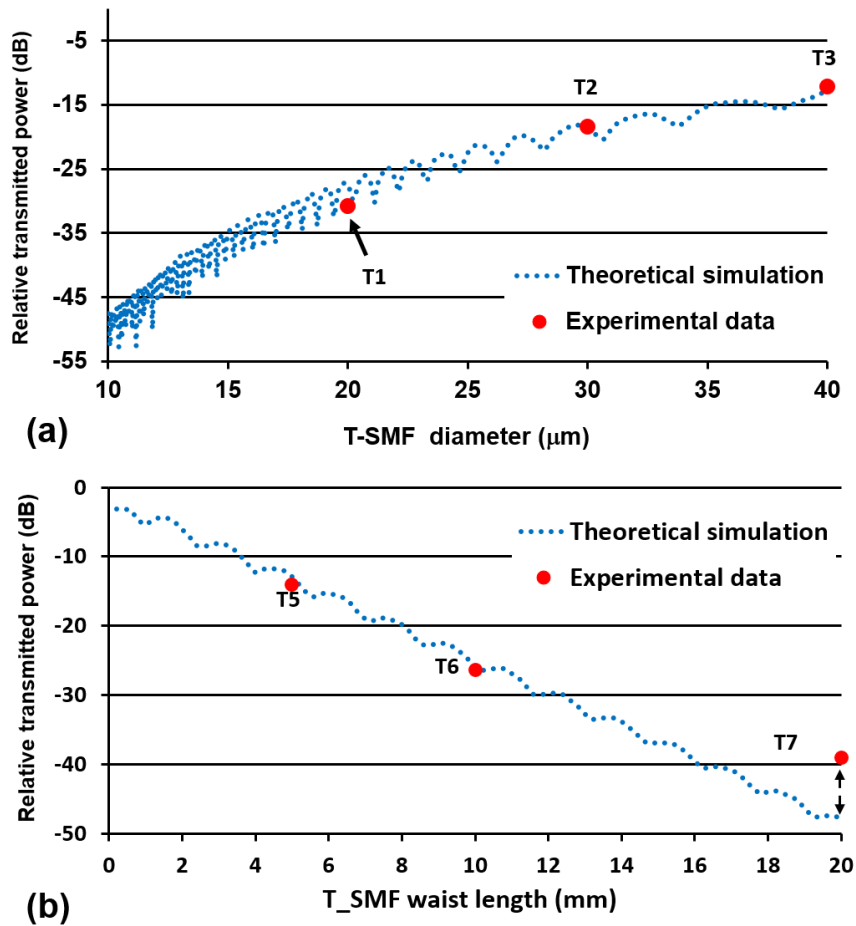*Fig. 4.7. Theoretical and experimental evolution of the LMR minimum as the deposited thin-film thickness increases at λ = 1310 nm. Results are obtained by varying (a) the taper waist diameter maintaining L_w = 5 mm and (b) the taper waist length maintaining $Ø_w$ = 40 μm [4].*

Finally, the study of the effect of a T-SMF dimensions on the formation of LMRs is concluded with a sensitivity analysis. To this purpose, the parameter "rate of change" (ROC), given in dB/bilayer, indicates the maximum relative power loss in dB per bilayer deposited at a determined wavelength. This is depicted in Fig. 4.8a, where ROC is the maximum slope of the plot, representing the relative power loss in dB versus the nanocoating thickness (given in bilayers) at a fixed wavelength. Another parameter is the "aspect ratio". This is defined as the quotient between the length and the diameter of a T-SMF, given in microns of length divided by microns of diameter. Since this magnitude can be too large due to the values used in this work, it is better to normalize it to its maximum value, so that it can be included in the [0,1] interval. Thus, the aspect ratio turns into "normalized aspect ratio" or NAR, which expression is given in equation (4.3):

$$NAR = \frac{AR}{AR|_{max}} = \frac{\frac{L_w}{\phi_w}}{\frac{L_w}{\phi_w}|_{max}} \tag{4.3}$$

According to this, NAR = 0 involves no tapering process. This means L_w = 0. In fact, for diameters higher than 44.33 μm, no LMRs can be produced when depositing the [PAH+NR/PAA] thin-film, as it is depicted in Fig. 4.8. This situation can be observed in the results obtained for T_4. Here, the rate of change is null, as has been mentioned previously, so the sensitivity is also null.

For diameters below 44.33 μm and with a certain waist length, the evanescent field is accessible, since part of the fundamental core mode is propagated in the cladding. Then, the thin-film deposited makes the LMRs to show up. The depth of the LMR increases as the taper waist is longer and thinner, as confirmed in Fig. 4.8b, with T_7 dimensions. As a result, the ROC decays as a function of the NAR. These considerations are interesting in terms of optimizing the sensitivity of the LMR, although the latter dimensions are not appropriate to work with them due to the fragility of the structure.

Therefore, a compromise solution is required. This means that, from a practical point of view, by having the diameter reduced, the length of the structure can be shortened too. Losses will not be high, although it can be affordable as long as the LMR induces enough attenuation. In this way, the device can be miniaturized and, thus integrated as a part of a whole sensor system.
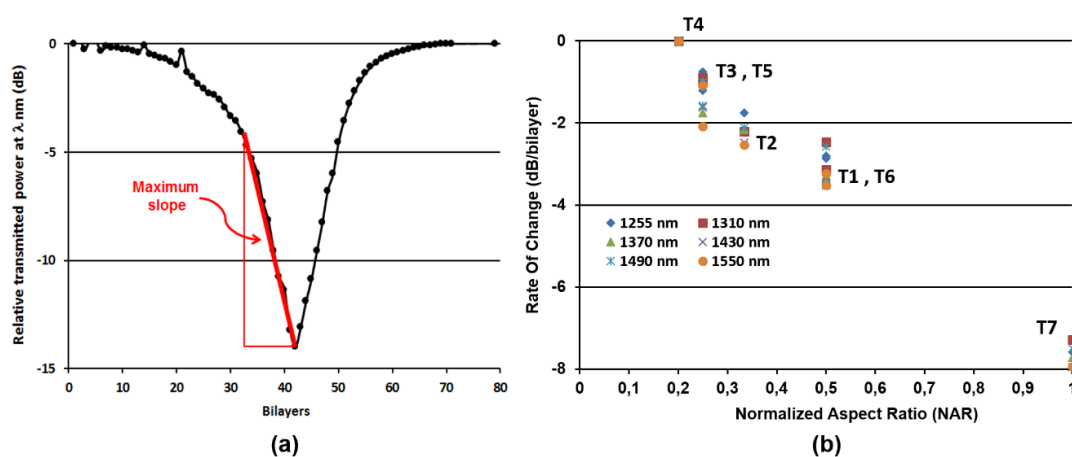
Fig. 4.8. *(a) Graphical explanation of the concept "rate of change" in an LMR. (b) ROC versus normalized aspect ratio (NAR) graph, to observe the evolution of the sensitivity of a T-SMF as a function of the NAR parameter [4].*

4.2. Generation of LMRs on tapered single-mode optical fibers

As a theoretical example of what is happening under the previous conditions when an LMR is being generated on a T-SMF, some simulations similar to the CRMMF structures case have been performed, but now using FIMMWAVE® software (see Appendix 1 for more information about this software). The reason for this change is that due to the fact of working with an input waveguide range for single-mode operation, only the fundamental mode of the core is analyzed. Moreover, since the thin-film deposited again is [PAH/PAA], the same refractive index and thickness for the thin-film deposited onto the CRMMFs is simulated (parameters N = 1.548 + 0.0105i and thickness = 330 nm). As demonstrated in chapter 3, under these conditions the LMR is located at 1425 nm. The only difference in the parameterization is the light source, which has been changed by a fundamental mode Gaussian source. In addition, due to the previous conclusions, a tapered SMF with reduced dimensions is simulated, with parameters $\emptyset_w$ = 40 μm, L_t = 3 mm and L_w = 11 mm. Fig. 4.9 shows the numerical data.

First, the longitudinal section of the electric field intensity is analyzed, for 1150 and 1425 nm, which is the spectrometer wavelength range. Thus, in Figs. 4.9b and c it can be observed the light propagation into the fiber core and not expanding to the cladding. It is also remarkable that, as the fiber core is reduced, there is an actual field confinement. However, the colors are less bright and they even almost disappear, indicating that there are losses in the electric field intensity along the deposited area that cannot recover in the detection side. Moreover, the

simulations show certain guidance for 1150 nm which is quite higher in comparison to that of 1425 nm, so it is clear that the effect of the LMR attenuation is higher at 1425 nm.
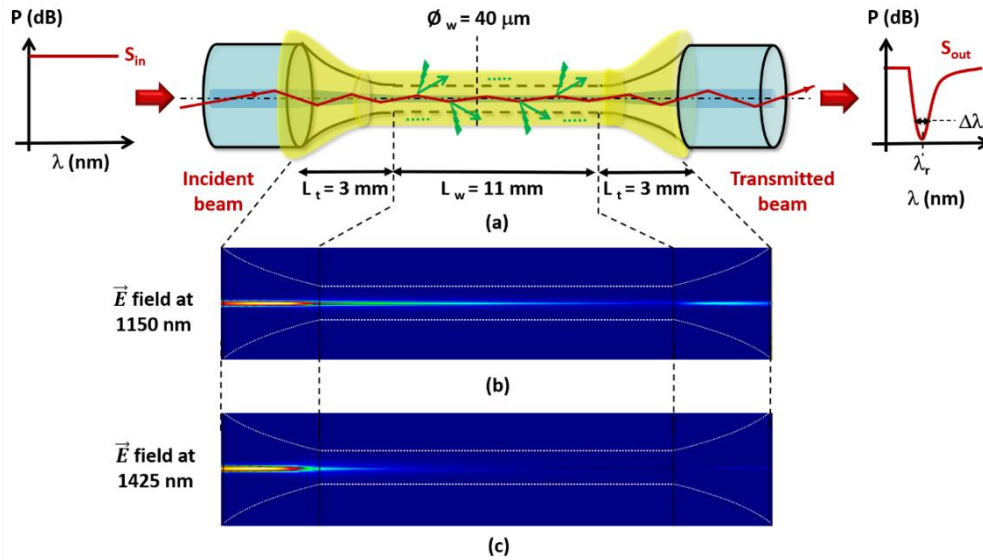

Fig. 4.9. *(a) Schematic of light propagation in a thin-film-deposited T-SMF, based on ray theory. Longitudinal power distribution along the sensitive area at (b) 1150 nm and (c) 1425 nm, respectively, simulated by using mode theory in FIMMWAVE®.*

Regarding the cross-section, there are some differences with respect to the multimode structures. First, due to the SMF conditions before the deposited zone, only the $HE_{1,1}$ mode can be propagated inside the fiber core (see Fig. 4.10a for both field contributions at 1150 and 1425 nm). Thus, the main beam (lobe) is quite clear, reaching 2.5 V/μm, and being totally confined in the core without side lobes. It is remarkable the fact that the electric field values obtained during the whole structure are higher in the single-mode case than in the multimode case, as a consequence of the better guidance obtained.

The effect of the LMR can be observed for 1150 and 1425 nm cases in the deposited zone. For 1150 nm, a slight field contribution in the main lobe, this means, in the fundamental mode of the core ($HE_{1,1}$) still exists in the center of the structure (see Fig. 4.10b). The sharp shape obtained means that the electric field is hardly propagated inside the fiber core, estimated to be 2.8 μm thick. However, the intensity decreases from 2.5 to 1.5 V/μm and a portion of the electric field is transferred to the cladding (around 0.1 V/μm in magnitude). This makes the field be less confined in comparison to its shape before the deposited zone. The key

point of this transfer is that with that core size, the $HE_{1,1}$ mode is under cut-off conditions, according to what was explained in Fig. 4.4. Consequently, the electric field expands while it is being guided in the new waveguide formed by the 40-micron-fiber and the thin-film. Additionally, it is important to notice that there are no side lobes, something that did not happen in the CRMMF case. This means that the T-SMF transition is adiabatic, so no modes are interfering in the new created waveguide. In the case of CRMMFs, these little oscillations were due to the mode beatings when propagating in the sensitive area.

When analyzing what happens for 1425 nm, the shape of the electric field is the same than for the 1150 nm case, indicating that the fundamental mode of the core is cut-off. In fact, there is also a field contribution out of the silica waveguide that still remains propagating with 0.1 V/μm. The difference here is that the main beam is strongly attenuated to less than 0.5 V/μm. This corroborates the high attenuation effect of the LMR, centered at that wavelength and shows the coupling from the fundamental mode of the core to the thin-film, where it is lost.

Finally, when the core diameter returns to 8 microns after the second transition region, the obtained electric field is quite attenuated although it seems logical to obtain more electric field contribution in the 1150 nm case than in the 1425 nm case (see Fig. 4.10c). It is also interesting to highlight that due to the characteristics of the single-mode fiber, all the light received in the detection side is propagated with the same shape that before entering the sensitive area, this means, a main beam without side lobes and more confined than in the sensitive zone. This indicates that the transition is again adiabatic and, because of the propagation of only one mode ($HE_{1,1}$), this should lead to a reduction in the spectral width of the LMRs produced.

In order to corroborate the numerical data presented above, the same experiments prepared for the CRMMF structures were performed, but now using CRMMFs and T-SMFs, with the objective of comparing the obtained results. To this purpose, two CRMMFs and four T-SMFs from several standard single-mode optical fiber segments were prepared. The dimensions and names given to all these optical structures are summarized in Table 4.3. The optical set-up was the same described in Fig. 4.5 and the chemicals were the same used for the CRMMF depositions, this means, a [PAH/PAA] polymer matrix. To support the T-SMF data obtained experimentally, some additional simulations were also run.

When analyzing the data, it is important to compare in the same wavelength range. Since the FT200EMT fiber is intended mainly for VIS-NIR applications, the multimode structures were compared in that spectral window (from 400 to 1200 nm) in chapter 3. However, SMFs are normally used in the second

and third telecommunications windows. Therefore, the multimode structures will also be compared in the OSA spectral region, ranging from 1150 to 1680 nm.
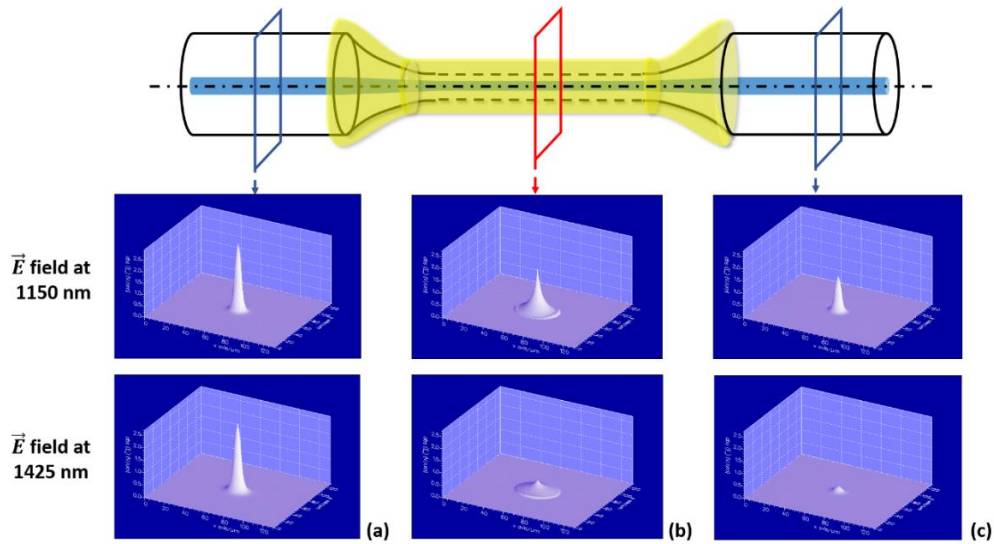
Fig. 4.10. *FIMMWAVE® simulations for the cross-section of the studied T-SMF (a) before entering the thin-film, (b) in the center of the deposited area and (c) before entering the detector, respectively. Data for 1150 and 1425 nm.*

Optical structure	Initial diameter (μm)	Final diameter (μm)	L_t (mm)	L_w (mm)
C_1	200	200	0	40
C_2	200	200	0	20
T_1	125	40	3	20
T_2	125	40	3	15
T_3	125	40	3	13
T_4	125	40	3	11

Table 4.3. *Summary of both the CRMMFs and T-SMFs dimensions utilized to prove the spectral width reduction of the LMRs.*

Fig. 4.11. *LMR evolution registered by C_1 (a) and T_1 (b) as a function of [PAH/PAA] increasing thin-film thickness. Higher attenuation values are obtained in T_1 case [13].*

In Fig. 4.11, the spectra of structures C_1 and T_1 are represented as a function of the increasing thin-film thickness. It can be observed that the LMR attenuation is higher in T_1 case (more than 40 dB) than in C_1 case (around 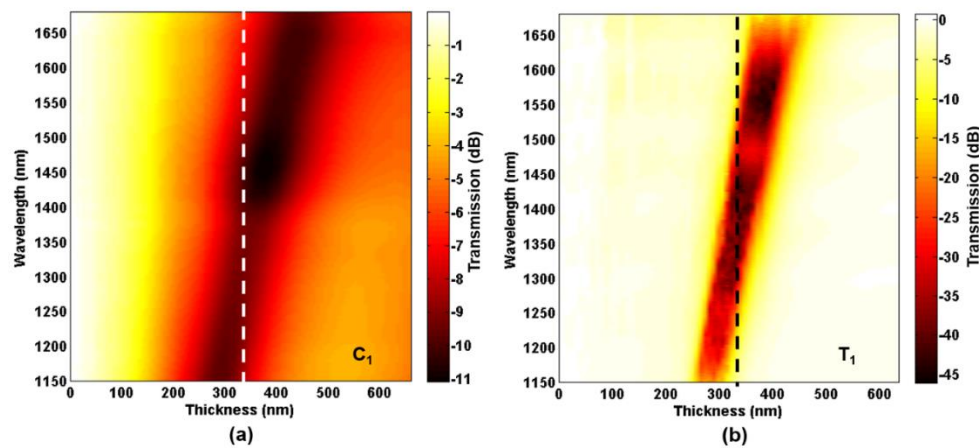10 dB). Thus, the first conclusion is that a lower length T-SMF device permits to obtain higher attenuation values in the generated LMR than those obtained with both CRMMF devices.

In this sense, Fig. 4.12 shows the theoretical and experimental optical spectra for all the analyzed devices. Here, the white and black dotted lines highlighted in Fig. 4.11 are the corresponding spectra to C_1 and T_1 structures, respectively. As it can be observed, experimental results agree well with their corresponding simulations and reveal two interesting facts. The first one is that by increasing the length of a CRMMF the LMR attenuation is higher. The second, and most important, is that the LMRs obtained with T-SMFs are narrower.

Moreover, it is important to highlight that the attenuation of the generated LMRs is not the same as a function of the sensitive region length. This is the same phenomenon shown in CRMMF devices. However, as it can be observed by comparing the experimental results in Figs. 4.12b and d, the attenuation values given by T-SMFs with less sensitive region than the CRMMF cases are higher. To verify this phenomenon, in Fig. 4.13 it is theoretically compared the optical spectrum of T_4 with CRMMF devices with different lengths. The results obtained prove that more length is needed in the CRMMFs case to achieve the T-SMFs attenuation values. Moreover, even for the same attenuation value there is net reduction of the LMR spectral width with T-SMF devices.
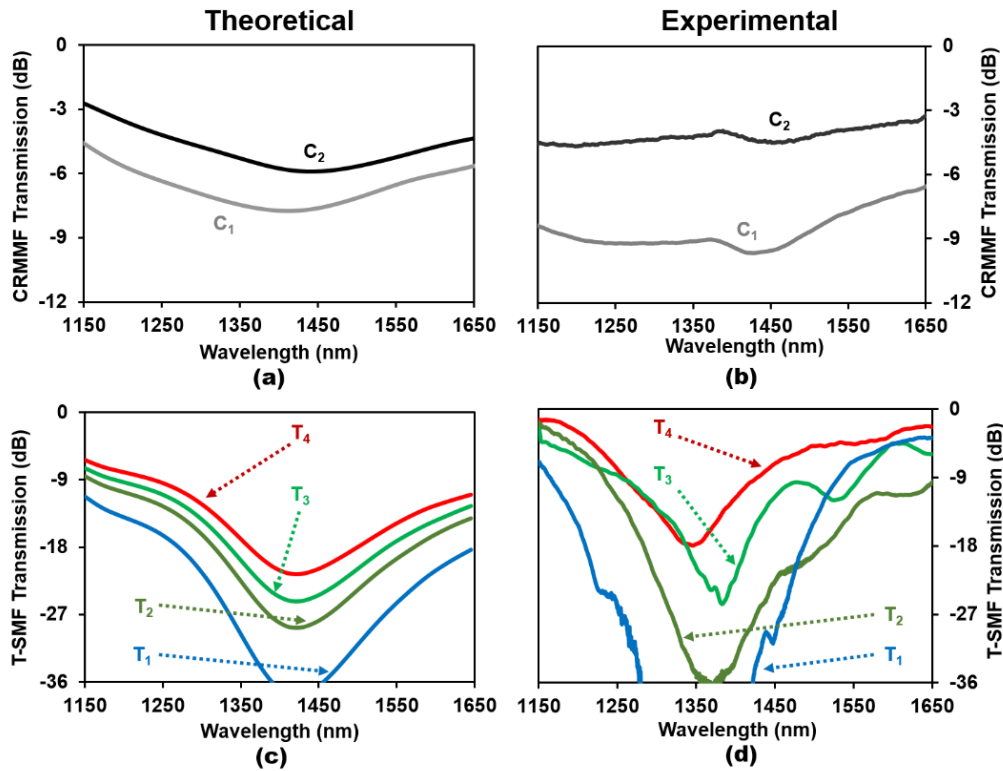
Fig. 4.12. *Transmission spectra with thin-film thickness 330 nm. (a) and (b) Numerical and experimental results for C_1 and C_2 devices. (c) and (d) Numerical and experimental results for T_1 to T_4 devices [13].*

Taking a look to Fig. 4.13a, it can be observed that the spectral width of the LMR is $\Delta\lambda|_{CRMMF}$ = 110 nm for the 40 mm-length CRMMF, whereas in the T_4 case, it is $\Delta\lambda|_{T4}$ = 50 nm. This is more than a two-fold improvement, obtained with a device thirty times shorter. Moreover, the two minima obtained with CRMMF devices are reduced to one minimum for the T-SMF. This can be also corroborated by comparing Figs. 4.12b and d, where the difference is even higher, presenting more than 500 nm in the CRMMFs case and between 30 and 150 nm in the T-SMFs case. Thus, there is a visible reduction in the spectral width by using a T-SMF.

At this point it is crucial to somehow confirm that T-SMF provided a better spectral width than T_{CRMMF}. In view that the experiments only suggest a drastic decrease in the optical power, a theoretical study of different T_{CRMMF} diameters is provided, to see what would happen if such structure reduced its diameter. T_{CRMMF} diameters are varied between 100 and 60 μm. As a result, Fig. 4.13b is presented,

corroborating optical power losses as the main obtained effect and null reduction in the spectral width of the LMRs.

The reason for the high Δλ in multimode structures can be explained by considering the condition for maximum coupling from a core mode to the thin-film. Due to the different effective refractive index of each core mode, the maximum coupling is obtained at a different wavelength in each case. As a result, the final attenuation band consists of the sum of the attenuation bands for each specific core mode coupled to the thin-film lossy-mode, what leads to a higher dispersion [14]. Thus, the LMR broadens.

However, due to the adiabaticity of the used T-SMFs, the fundamental core mode couples predominantly to the fundamental mode of the new 40-micron-thick waveguide [6]. Consequently, the light coupled in the thin-film is due mainly to this fundamental mode, and not due to a set of modes like in the multimode structures. As a result, light coupling occurs in a narrower wavelength interval and so, the spectral width of the obtained LMR is reduced.
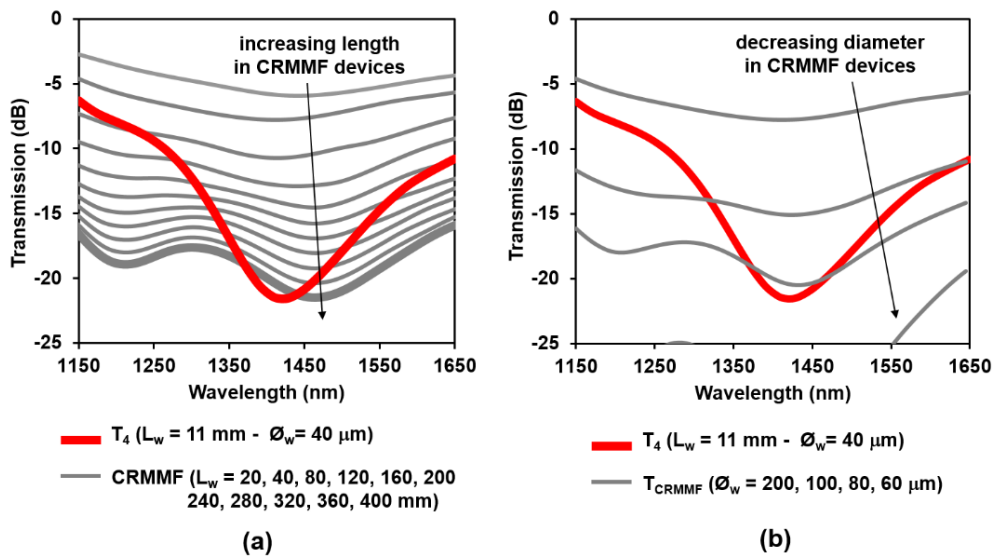

Fig. 4.13. *Simulated transmission spectra with a thin-film thickness of 330 nm for T_4 and CRMMFs with different lengths (a) and T-CRMMFs with different waist diameters (b). The LMR maintains narrower in the T-SMF case [13].*

Therefore, it has been demonstrated that there is a net reduction in the spectral width of the LMRs propagated in a T-SMF structure, if compared with

CRMMFs or T-CRMMFs. Moreover, even more attenuation has been obtained by reducing the length of the fabricated devices. As a consequence, the resolution capacity of the LMRs has been improved and this can be taken into account to address a better detection of the different magnitudes. Consequently, when addressing the biodetection, it should be possible to distinguish small concentration increments, which is good in terms of designing LMR-based biosensors.

4.3. Sensors based on LMRs generated on T-SMFs

In this section, different examples of sensors are provided, based on the generation of LMRs with T-SMFs. The main goal is to extract some conclusions on the use of this technology as a potential platform to develop biosensors.

4.3.1. pH sensor depositing polymer thin-films

A pH sensor based on a [PAH/PAA] polymer thin-film deposited by LbL-assembly is presented [15]. The swelling property of this matrix permits to expand or contract its thickness depending on the amount of water molecules accumulated (then, a moisture sensor can be designed) or the ionic force of the solution. Consequently, the corresponding LMR will shift as a function of this thickness variation.

First, the LMR evolution as a function of the increasing thin-film thickness is plotted in Fig. 4.14a. Here, the arrows indicate that the LMR experiments an increase in wavelength displacement and depth. Moreover, there is one more aspect to observe: the double peak presented by the resonance during its generation. This phenomenon corresponds to the separation of the two different polarizations that form a typical LMR: TE and TM. In fact, the resonance obtained is the contribution of both modes as it is described in [3].

Once located in the optimal position, the pH detection is shown. In this sense, five PBS solutions with pH values 4.0, 4.5, 5.0, 5.5 and 6.0 were used. The experimental set-up was the same as that shown in Fig. 4.5. The experiment involved subjecting the sensor to several cycles between pH 6.0 and 4.0 in order to study its repeatability and response time.

Regarding the characterization of the LMR, the results obtained are graphically described in Fig. 4.14b. Here, the different wavelengths at which the sensor stops after immersing in every pH solution are presented. At the beginning

of the experiment, the sensor is immersed in the pH 6.0 PBS buffer solution, which causes a wavelength shift from 1410 to 1375 nm without any considerable movement in the transmission of the LMR, stabilized at −34 dB. The explanation of this is that when the $[PAH/PAA]_{30}$ assembled structure reaches this pH value, both polymers are oppositely charged. However, while PAH chains are fully ionized, PAA ones are close to fully ionized, which provokes a strong adhesion between molecules. As a result, there is a compression in the polymeric structure due to a deswelling process [16,17]. This induces a change in the thickness and the refractive index of the thin-film and, therefore, the resonance shifts to lower wavelengths.
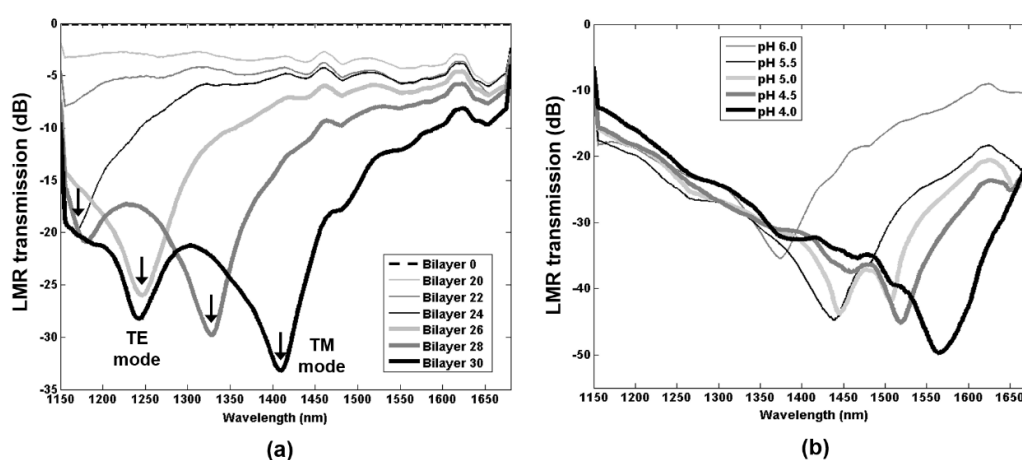
Fig. 4.14. *(a) Evolution of the LMR while the construction takes place (b) pH detection for the sensor proposed. The resonance shifts to higher wavelengths when pH decreases from 6.0 to 4.0 [15].*

In addition to this, a single peak is observed when detecting pH, instead of the dual peak observed at the end of the fabrication process. This is not a problem for the purpose of this study, since the surrounding medium outside the detector is different to air or water (PBS) and, due to the changes in the refractive index, the re-organization of the coupling modes makes TE and TM modes propagate together.

From this point on, the resonance experiments a progressive wavelength shift to the red as a function of pH Fig. 4.14b and Fig. 4.15a. The explanation is that below pH 6.0, the polymeric matrix experiments a great swelling effect due to the quick loss of the weak bonds between PAH and PAA [16,17]. As a result, the thin-film expands, reaching its highest values. This induces a change in the refractive index and, consequently, both a red-shift and an increase in the resonance depth.

Concretely, when pH equals 5.5, the LMR locates around 1435 nm with almost −46 dB of transmission. A similar magnitude is obtained at pH 4.5, but the resonance is located at 1515 nm. When the LMR reaches 1560 nm with −50 dB of transmission, this is an indication of pH 4.0. Finally, for pH 5.0 a dual peak centered at 1470 nm can be observed in Fig. 4.14b. This is caused by a lack of sensitivity of the OSA at this wavelength range. In this situation, the transmission of the LMR decays below the sensitivity limit of the OSA, so it is difficult for an electronical device to detect where the real peak of the resonance is. That is why, in the following lines, an algorithm to estimate accurately the resonance wavelength as a function of pH is proposed.

To finish the sensor characterization, the response time of the sensor when detecting pH is studied. Focusing on the second cycle of the detection shown in Fig. 4.15a, which by the way shows the sensor repeatability, the response time for every change of pH can be estimated. In view of the similarity in the response time for every pH step, Fig. 4.15 shows the response time to a variation from pH 6.0 to pH 5.5. Here, the horizontal axis is expressed in seconds to see the performance in a better way. As it can be observed, the response time is around 60 seconds. In this case, the [PAH/PAA] polymeric matrix experiments a great swelling effect, which provokes a refractive index change that makes the resonance wavelength rise from 1375 to 1435 nm, as has been mentioned PAA [16,17].
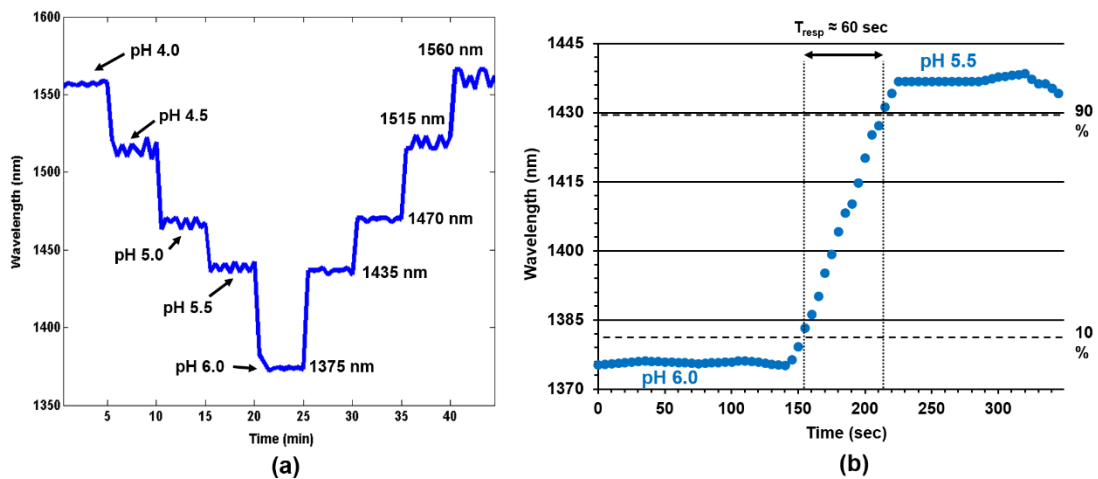

Fig. 4.15. *(a) Tracking of the minimum of every spectrum after processing (a) with the algorithm proposed. (b) Response time of the sensor. The time separation between samples is 5s, which is the time needed by the OSA to acquire each piece of information [15].*

4.3.2. Celiac disease biosensor based on polymer thin-films

In this work, LMRs are generated in thin-film coated T-SMFs to develop an optical fiber biosensor to detect anti-gliadin antibodies (AGAs). These biological compounds are fabricated in the human body when it suffers from celiac disease, which supposes one of the most prevalent affections in the current society. Concretely, the critical values considered to develop celiac disease are 8-10 ppm [18]. There are some contributions reporting how to solve this issue [18,19], although this is the first time, to our knowledge, that the detection is achieved by using LMRs developed in T-SMF structures.

To this purpose, the T-SMF was subjected to an LbL-assembly deposition of [PAH/PAA] as indicated in Fig. 4.16. As it can be observed, a first LMR was observed in the transmission spectrum after 30 bilayers, presenting a wavelength shift to the red as more bilayers were deposited. At the same time, the attenuation was increased, as it was expected for an LMR generated in an optical waveguide [20,21]. Then, a [PAH/PSS]$_3$ thin-film was adsorbed onto the previous one. This permitted to create an adequate environment for the deposition of the biological substances and to prevent the adsorbed nanostructure from allowing the diffusion of the antigens/antibodies [22]. Finally, a {[gliadin/PSS]$_2$ + gliadin} film was deposited to embed the antigen into the bioprobe. At this point, the LMR was centered in 1550 nm presenting a spectral width (3 dB above the LMR minimum) of around 50 nm and 20 dB of attenuation.
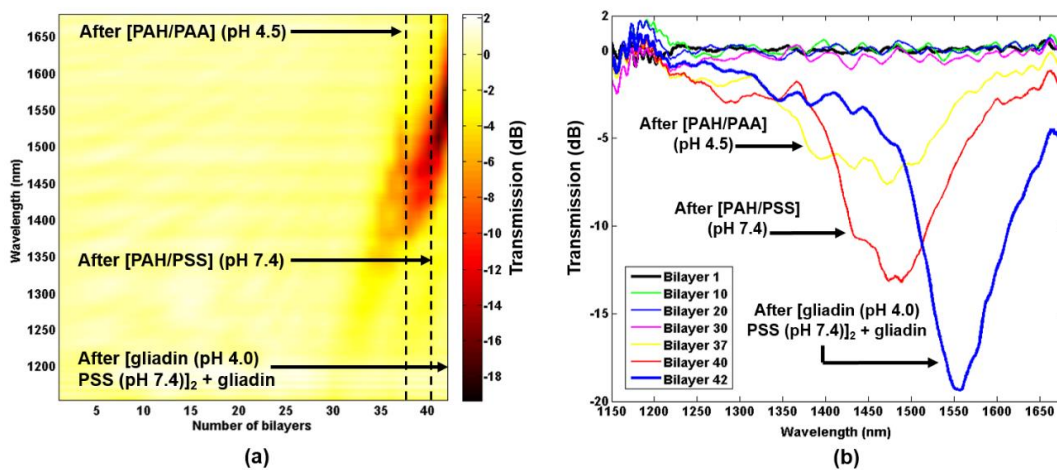

Fig. 4.16. *(a) Power evolution during the sensor fabrication. (b) LMR profile as a function of the increasing thin-film [23].*

Thus, the biosensor was prepared to adsorb the AGAs. To this purpose, it was first immersed in a cuvette containing 50% v/v aqueous diluted PBS at pH 7.4 for an hour and the optical spectrum during this process was monitored. Then, the AGAs solution was added to the cuvette and the same procedure was followed for monitoring the LMR behavior. So it is presented in Fig. 4.17a. The depicted spectra correspond to the first immersion in the PBS solution (the beginning of the experiment), after an hour (end of the stabilization in the PBS solution) and at the end of the AGAs binding process [23].

Moreover, in view of the possibility of tracking the LMR shifts, a simple algorithm based on least squares was programmed in MATLAB® to estimate the LMR minimum at any time. The results are presented in Fig. 4.17b.

First, the evolution of the resonance wavelength when immersing the biosensor in PBS can be observed, obtaining an LMR minimum shift from 1500 to almost 1565 nm due to a refractive index change in the thin-film. Then, after adding the AGAs, LMR shows another wavelength shift from 1565 to 1585 nm. As it has been mentioned along this thesis, the presence of BSA avoids the adsorption of AGAs by binding with their non-specific sites [24]. Therefore, the wavelength shift is due to a change in the thin-film optical properties, as a consequence of the generation of gliadin – AGAs complexes. Another interesting point is that the detected concentration (5 ppm) is lower than that currently considered a cut-off when diagnosing celiac patients, this means, 8-10 ppm [18]. This could be an improvement in terms of early diagnosis.
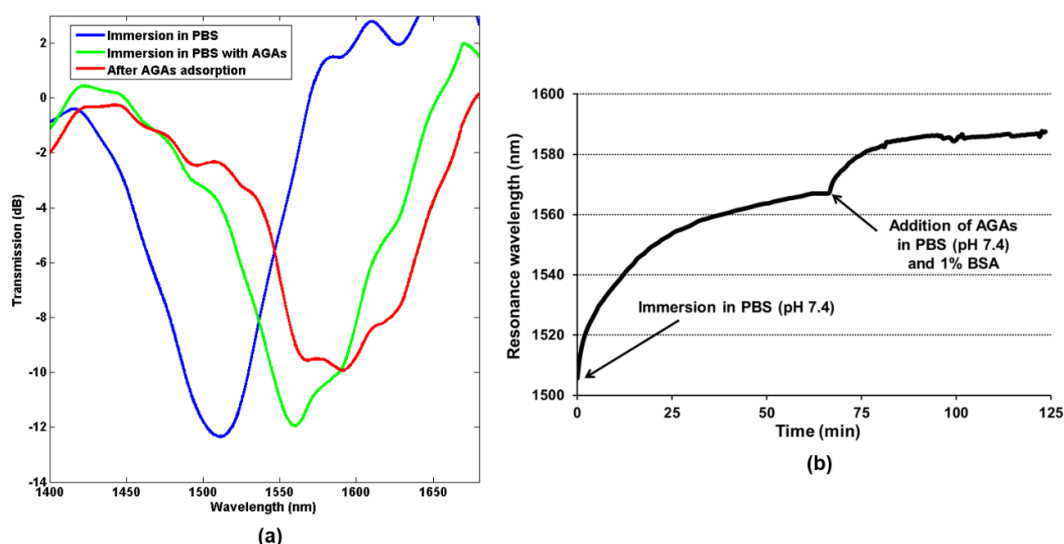

Fig. 4.17. *Shapes (a) and tracking of the LMR minimum (b) during the AGAs detection process [13].*

Finally, in order to corroborate the presence of AGAs in the biosensor once the detection process ended, the device was washed three times in PBS in order to remove the not correctly bounded AGAs. Then, the sensor was positioned over a little Teflon® tray and 100 µl of TMB substrate were dropped over the whole sensitive region to see whether the TMB-HRP enzyme reaction produced hydrogen peroxide. This usually leads to the TMB oxidation, showing a color change in the resulting medium [25]. This is shown in Fig. 4.18, where some of the process pictures are presented as a function of time. It can be observed that, during one hour, the color of the TMB substrate changed from transparent to blue, indicating the presence of conjugated AGAs in the medium. Moreover, the sensitive region of the T-SMF itself showed the same color, confirming that the conjugated AGAs were adsorbed onto the biologic thin-film and, therefore, to the optical fiber.

Fig. 4.18. *Presence of AGAs in the T-SMF proved by using the TMB - HRP enzyme method [23].*

4.4. Conclusions

All in all, the use of tapered single-mode optical fibers (T-SMFs) supposes an enhancement of the LMR properties when generated by polymeric thin-films deposited onto optical fiber-based structures. They provide more interaction with the evanescent field of the optical structure and permit to improve the spectral width and the attenuation of the LMRs generated with a reduction in the devices dimensions. If compared to CRMMFs, the LMRs spectral widths are quite reduced and the attenuation is gently improved. This permits to detect small increasing concentrations of biological compounds with a better resolution in the measurements. Therefore, T-SMFs are good candidates to address a biodetection.

In order to check this affirmation, a figure of merit (FOM) like that defined in chapter 3 can be calculated. It has been shown along this chapter that the optical structure does not influence the LMRs sensitivity. In fact, the simulations locate the LMRs in the same position for the same parameters. Therefore, in order to obtain the FOM for the T-SMF structure, the same sensitivity of the CRMMF structure, this

means, 2872 nm/RIU, will be used, considering that a [TiO$_2$/PSS] thin-film is deposited. Regarding the spectral width of the resonances, this parameter has been quite reduced, since the optical structures chosen permit a limited access to the evanescent field and, moreover, the collected light in the detection side is single-mode. So in case there are modes that are not allowed to be propagated in the fiber, they are just filtered. In this sense, the best LMRs produced in this chapter have been obtained in the celiac biodetection on section 4.3.2, where the spectral width was around 50 nm. However, in order to compare the values of the FOM, the FWHM must be taken to evaluate the formula. In this case, considering that the LMR centered at 1550 nm (before the biodetection) is visible down to -5 dB in transmission, then FWHM ≈ 120 nm. Therefore, the FOM for T-SMFs will be:

$$FOM_{T-SMF} = \frac{S[nm/RIU]}{FWHM\ [nm]} = \frac{2872\ nm/RIU}{120\ nm} = 23.93 \sim 24\ RIU^{-1}$$

which implies more than a 3-fold improvement if compared to CRMMFs, although still low. In spite of that, a clear enhancement has been obtained in comparison to CRMMFs, which is encouraging to keep on improving the results by using this kind of structures.

4.5. Bibliography

[1] M. Hernáez, I. Del Villar, C.R. Zamarreño, F.J. Arregui, I.R. Matias, Optical fiber refractometers based on lossy mode resonances supported by TiO2 coatings, Appl. Opt. 49 (2010) 3980-3985.

[2] I. Del Villar, M. Hernaez, C.R. Zamarreño, P. Sánchez, C. Fernández-Valdivielso, F.J. Arregui, I.R. Matias, Design rules for lossy mode resonance based sensors, Appl. Opt. 51 (2012) 4298-4307.

[3] I. Del Villar, C.R. Zamarreño, P. Sanchez, M. Hernaez, C.F. Valdivielso, F.J. Arregui, I.R. Matias, Generation of lossy mode resonances by deposition of high-refractive-index coatings on uncladded multimode optical fibers, Journal of Optics. 12 (2010) 095503.

[4] A.B. Socorro, I. Del Villar, J.M. Corres, I.R. Matias, F.J. Arregui, Lossy mode resonances dependence on the geometry of a tapered monomode optical fiber, Sensors and Actuators A: Physical. 180 (2012) 25-31.

[5] T.A. Birks, Y.W. Li, The shape of fiber tapers, Lightwave Technology, Journal of. 10 (1992) 432-438.

[6] J.D. Love, W.M. Henry, W.J. Stewart, R.J. Black, S. Lacroix, F. Gonthier, Tapered single-mode fibres and devices. I. Adiabaticity criteria, Optoelectronics, IEE Proceedings J. 138 (1991) 343-354.

[7] H. Latifi, M. Zibaii, S. Hosseini, P. Jorge, Nonadiabatic tapered optical fiber for biosensor applications, Photonic Sensors. 2 (2012) 340-356.

[8] M. Quintela, A. Quintela, N. Becue, J. Lázaro, F. Anabitarte, J.M. Lopez-Higuera, Tunable fiber laser using concatenated non-adiabatic single-mode fiber tapers, (2008) 700453-700453-4.

[9] I. Gomez-Castellanos, R.M. Rodriguez-Dagnino, Intensity distributions and cutoff frequencies of linearly polarized modes for a step-index elliptical optical fiber, Optical Engineering. 46 (2007) 045003-045003-11.

[10] R.J. Black, R. Bourbonnais, Core-mode cutoff for finite-cladding lightguides, 133 (December 1986) 377-384.

[11] P. Bienstman, CAMFR Software, from University of Ghen, Belgium, (2007).

[12] I. Udagedara, M. Premaratne, I.D. Rukhlenko, H.T. Hattori, G.P. Agrawal, Unified perfectly matched layer for finite-difference time-domain modeling of dispersive optical materials, Optics express. 17 (2009) 21179-21190.

[13] A.B. Socorro, I. Del Villar, J.M. Corres, F.J. Arregui, I.R. Matias, Spectral width reduction in lossy mode resonance-based sensors by means of tapered optical fibre structures, Sensors and Actuators, B: Chemical. 200 (2014) 53-60.

[14] M. Marciniak, J. Grzegorzewski, M. Szustakowski, Analysis of lossy mode cut-off conditions in planar waveguides with semiconductor guiding layer, Optoelectronics, IEE Proceedings J. 140 (1993) 247-252.

[15] A.B. Socorro, I. del Villar, J.M. Corres, F.J. Arregui, I.R. Matias, Tapered Single-Mode Optical Fiber pH Sensor Based on Lossy Mode Resonances Generated by a Polymeric Thin-Film, Sensors Journal, IEEE. 12 (2012) 2598-2603.

[16] S.S. Shiratori, M.F. Rubner, pH-Dependent Thickness Behavior of Sequentially Adsorbed Layers of Weak Polyelectrolytes, Macromolecules. 33 (2000) 4213-4219.

[17] C.S. Kumar, Nanostructured Thin Films and Surfaces, John Wiley & Sons, 2010.

[18] J.M. Corres, J. Bravo, I.R. Matias, F.J. Arregui, Tapered Optical Fiber Biosensor for the Detection of Anti-Gliadin Antibodies, Sensors, 2007 IEEE. (2007) 608-611.

[19] N. Cennamo, A. Varriale, A. Pennacchio, M. Staiano, D. Massarotti, L. Zeni, S. D'Auria, An innovative plastic optical fiber-based biosensor for new bio/applications. The case of celiac disease, Sensors Actuators B: Chem. 176 (2013) 1008-1014.

[20] A.B. Socorro, J.M. Corres, I. Del Villar, F.J. Arregui, I.R. Matias, Immunoglobulin G sensor by means of lossy mode resonances induced by a nanostructured polymeric thin-film deposited on a tapered optical fiber, (2012).

[21] A.B. Socorro, J.M. Corres, I. Del Villar, F.J. Arregui, I.R. Matias, Fiber-optic biosensor based on lossy mode resonances, Sensors Actuators B: Chem. 174 (2012) 263-269.

[22] F. Caruso, K. Niikura, D.N. Furlong, Y. Okahata, 2. Assembly of Alternating Polyelectrolyte and Protein Multilayer Films for Immunosensing, Langmuir. 13 (1997) 3427-3433.

[23] A.B. Socorro, J.M. Corres, I. Del Villar, I.R. Matias, F.J. Arregui, Celiac disease biodetection using lossy-mode resonances generated in tapered single-mode optical fibers, Proceedings of SPIE - The International Society for Optical Engineering. 9157 (2014).

[24] H. Niu, R. Yuan, Y. Chai, L. Mao, Y. Yuan, Y. Zhuo, S. Yuan, X. Yang, Electrochemiluminescence of peroxydisulfate enhanced by l-cysteine film for sensitive immunoassay, Biosensors and Bioelectronics. 26 (2011) 3175-3180.

[25] G. Volpe, R. Draisci, G. Palleschi, D. Compagnone, 3, 3', 5, 5'-Tetramethylbenzidine as electrochemical substrate for horseradish peroxidase based enzyme immunoassays. A comparative study, Analyst. 123 (1998) 1303-1307.

CHAPTER 5. Sensors based on high refractive index thin-films deposited on single-mode – multimode – single-mode optical structures

So far, a process followed to reduce the spectral width of the LMRs has been presented. In this sense, a considerable reduction has been obtained by using adiabatic tapered single-mode optical fibers (T-SMFs). This has been good in terms of enhancing the resolution of the measurements at the same time a high sensitivity is maintained.

From this point on, a different approach is carried out. As mentioned in chapter 2, thin-films can be also used to increase the effective refractive index of the whole optical structure and thus make it more sensitive to surrounding medium refractive index (SMRI) variations. In this sense, a less studied method for the detection of biomolecular species is multimode interference (MMI). The fact of dealing with interferences involves to control the behavior of the sensing phenomena in a different way, since there are different parameters to take into account for each specific structure.

It seems to be that most of the MMI-based sensors are not extensively studied because their sensitivity is low in comparison to other optical structures. However, there are many applications (physical applications, mainly) involving the use of MMI to create sensors, as mentioned in chapter 1. In fact, one of the most developed due to its low-cost and easiness to fabricate is the single-mode – multimode – single-mode structure or SMS. Trying to improve the SMS structure characteristics and potential response will be the main focus of this chapter.

5.1. Light propagation in SMS structures

The SMS structure is used in important fields such as optical communications and sensors. In optical communications, interesting devices such as wavelength filters have been developed [1,2], whereas in the optical sensors field it has been possible to measure magnitudes such as displacement, strain, pressure, temperature or refractive index [2-8].

An SMS optical fiber-based structure is formed by two standard single-mode fiber pigtails spliced on both sides of a length-varying multimode no-core fiber of the same diameter (see Fig. 5.1 inset). As a result, the total diameter of the

structure is 125 microns, although the SMF fiber has a core diameter of 8 microns and the MMF segment core is 125 microns thick. Here, it is important to point out the nomenclature. It is widely accepted that the MMF segment is called no-core (or coreless) fiber. However, it is a silica core without cladding actually, so the light is all the time propagating into the core of the resulting structure.

The basic physical principle of the device is that light transmitted through the fundamental mode of the input SMF pigtail is coupled to several modes into the MMF segment and then recoupled to the fundamental mode of the output SMF [8]. Due to MMI phenomenon, both transmission and attenuation bands are obtained in the optical spectrum. Particularly, the transmission bands obtained by the self-imaging effect exhibit minimum losses [9], and its central wavelength can be controlled as a function of the MMF segment dimensions, mainly by the MMF segment length and diameter [8].
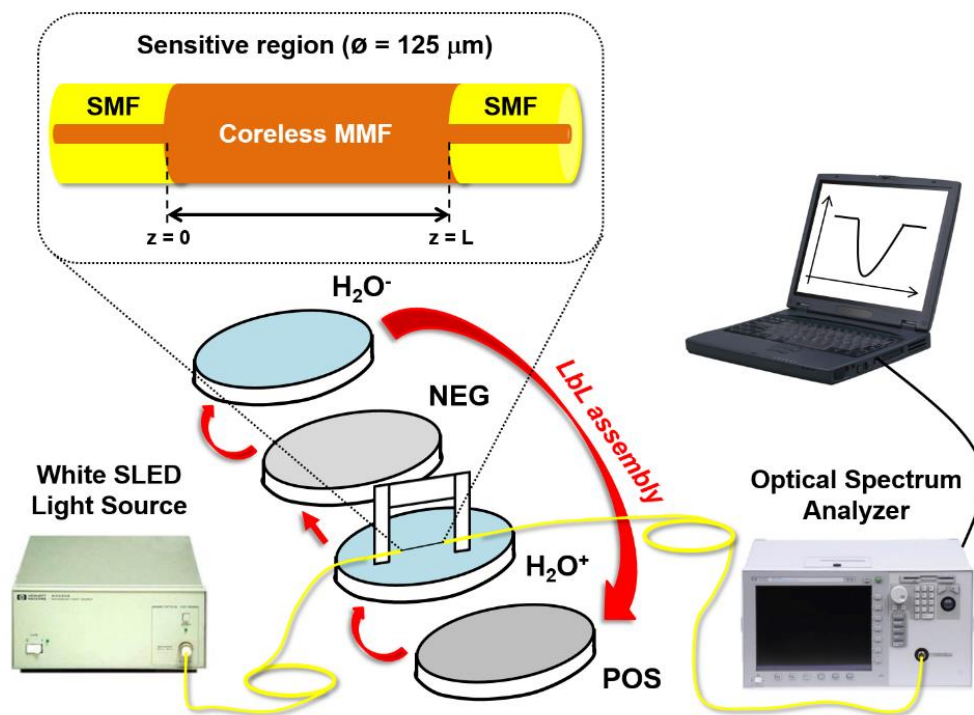

Fig. 5.1. *Optical set-up prepared to measure the spectrum behavior when increasing the coreless MMF length L, and to see its evolution during a thin-film deposition process. The inset represents an SMS optical structure [10].*

In this sense, by simply connecting an SMS to a white light source and to an optical spectrum analyzer (OSA), covering the third optical communications window, as shown in Fig. 5.1, it is possible to track the spectrum evolution as a function of the MMF segment length [10].

Thus, Fig. 5.2 is presented, showing the theoretical and experimental results of varying the MMF segment length, for length values of 5, 10, 15, 20, 25, 30, 35, 40, 45, 50 and 58 mm. There is a good agreement between theoretical and experimental data when comparing the output spectrum when the MMF segment length increases. Different transmission and attenuation bands can be observed in the optical spectrum for all cases.

These bands are caused by multimodal interferometry, which can be constructive or destructive. If the interferometry is constructive, it may be caused by a fractional constructive interference or by a light field condensation between several guided modes in a particular plane [11]. The last spectrum permits to obtain a higher transmission band than in the rest of cases, known as the self-imaging band. Consequently, most of the following designs will be focused on monitoring the evolution of the band produced by the self-imaging effect. In this sense, the design can be simplified in a great manner by using the analytical expression that approximates the length of the MMF section that is adequate for positioning the band at a specific wavelength:

$$Z_i = \frac{4D^2 n}{\lambda} \tag{5.1}$$

where *D* and n are the MMF diameter and refractive index, respectively, and λ is the operational wavelength. In the presented SMS structure, *D* is 125 µm. Consequently, just by fixing the refractive index and the operational wavelength, the length of MMF segment can be determined. In view of the wavelength range that is monitored with the experimental set-up of Fig. 5.1, a good option is to fix the transmission band at the third optical communications window, centered at 1550 nm. At this wavelength the refractive index of silica is N = n = 1.444 [12], which can be applied to Eq. 5.1. So the length of the MMF segment should be 58 mm.

Moreover, the MMF segment diameter is also responsible for the sensitivity of the device. In [5,8,9] it has been proved that, by reducing the diameter, an improved sensitivity to refractive index can be obtained. However, there are additional issues to address, such as fiber misalignment and inadequate splicing to the SMF fiber. That is why in [11] it has been proposed a tapered SMS. Nevertheless, the MMF segment diameter will be analyzed later on.
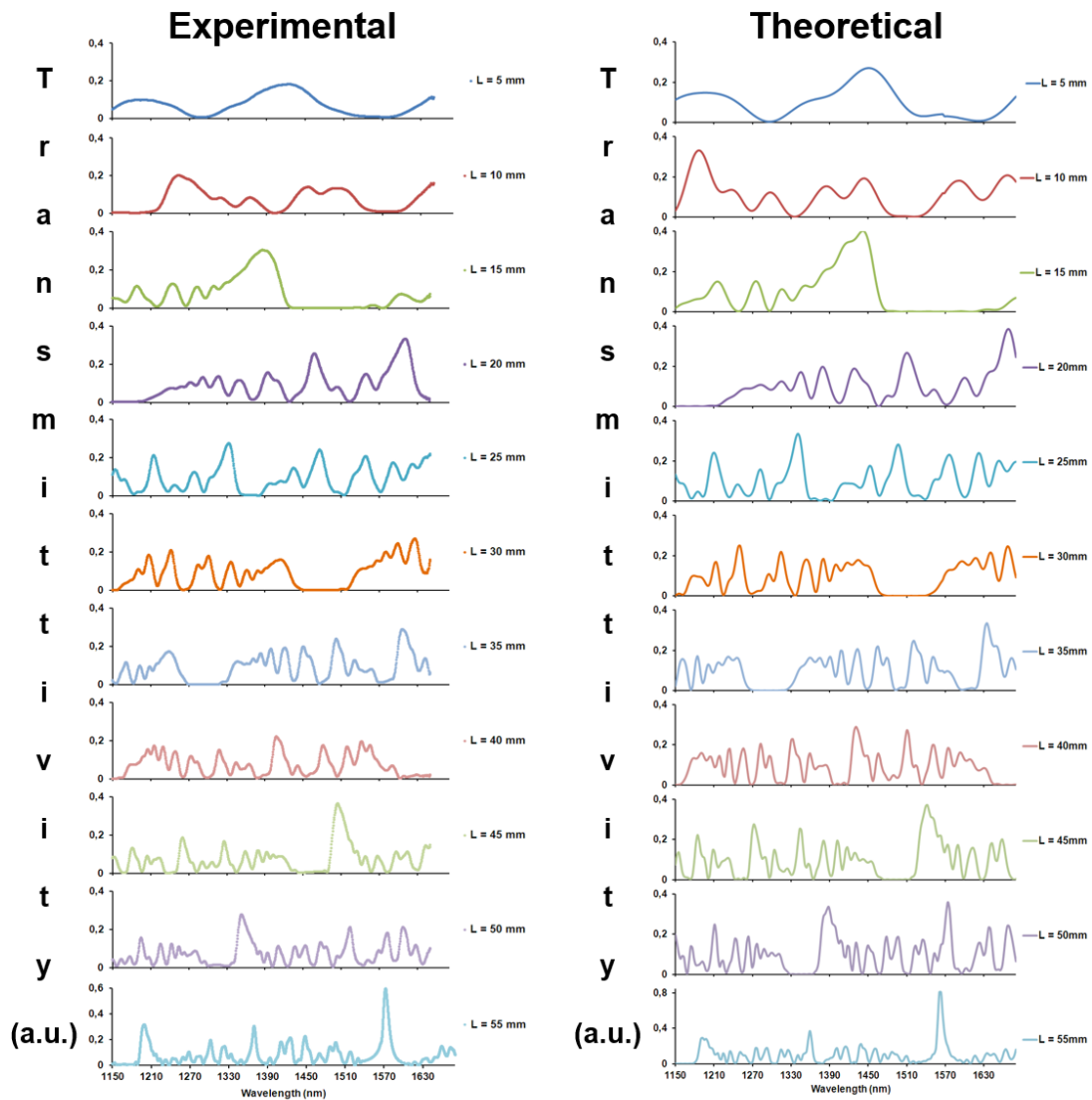
Fig. 5.2. *Experimental and theoretical spectra of uncoated SMS structure for different MMF section lengths: 5, 10, 15, 20, 25, 30, 35, 40, 45, 50 and 58 mm [10].*

Additionally, there is also an increasing interest in developing structures coated with thin-films. Two reasons justify the application of an additional coating. The first one is the ability to improve the performance of the same devices without coating [13]. As an example it has been possible to obtain a 10-fold increase in long-period fiber grating refractometers [14]. The second reason is the possibility of

using thin-films that are sensitive to humidity, a specific gas [15], pH [16], a chemical species [17], or a biological species [18], which permits to increase the number of applications of these devices in a great manner.

In view of the previous success in combining thin-films with optical structures that are inherently sensitive to the surrounding medium, the application of a thin-film to an SMS structure should lead to interesting results. So far, this idea has been studied theoretically in [19], showing promising results such as the improvement, as a function of coating thickness, of the sensitivity of one of the resonances created in the optical spectrum.

In addition to this, simulation data obtained with the transfer-matrix-method (see Appendix 1) permit to understand the influence of losses in the thin-film in terms of visibility of the interferences obtained in the optical spectrum. The phenomenon owns similarities with thin-film-coated LPFGs, where there is a progressive blue wavelength shift of the resonances as a function of the thin-film thickness [20]. The phenomenon is caused by a modification of the effective index of cladding modes induced by the thin-film, which in some works is called "mode transition" [13,14]. In the SMS there is also a wavelength shift caused by the modification of the effective index of cladding modes. Contrary to LPFGs there is a wavelength shift to the red, which will be explained later. In addition to this, the results obtained for different MMF section lengths permit to obtain important conclusions that can be applied for the miniaturization of these devices.

In order to check the spectrum evolution as a function of a high refractive index material deposition, a layer-by-layer assembly process (LbL-assembly) is performed, with the set-up presented in Fig. 5.1. Each bilayer of the coating is obtained by immersing the substrate in two solutions of poly (allylamine hydrochloride) (PAH) and poly (acrylic acid) (PAA), both of them in 10 mM concentration and adjusted to pH 4.5. According to the previous indications, the optical spectrum evolution is represented in Fig. 5.3 as a function of the number of bilayers of the [PAH/PAA] thin-film. A wavelength shift to the red is observed for all bands, which indicates that Eq. (5.1) is no longer valid if a thin-film is deposited on the MMF section.

By comparing the experimental results in Fig. 5.3a with numerical data in Fig. 5.3b and c, it is easy to observe the similarity in the evolution of the transmission bands. However, there is an important difference in terms of fading of the transmission bands. In the region between 450 and 650 nm the experimental data show a null transmission, a phenomenon that has been observed in thin-film coated long-period fiber gratings (LPFGs) [21,22], in thin-film coated cladding removed multimode optical fibers [16], and in thin-film coated tapered fibers [23].

This phenomenon is caused by coupling of light to a mode guided in a thin-film that presents losses and it is not considered in Fig. 3.20b. According to previous estimations [22], the refractive index of [PAH/PAA] at 1310 nm was 1.5 + 0.0025i. The real part of this value was used for obtaining the numerical results of Fig. 5.3b. However, if the complex refractive index is considered, the theoretical results obtained in Fig. 5.3c fit better with those of Fig. 5.3a.

In Fig. 5.4, the central wavelength of the transmission bands and its maximum power is represented both theoretically and experimentally, confirming the similarity between the model and the experimental data. Also, it is interesting to observe the shape of plots in Figs. 5.3 and 5.4. Both resemble to those plots obtained with deposition of thin-films on LPFGs [13,14]. However, instead of a blue wavelength shift, transmission bands experiment a wavelength shift to the red.
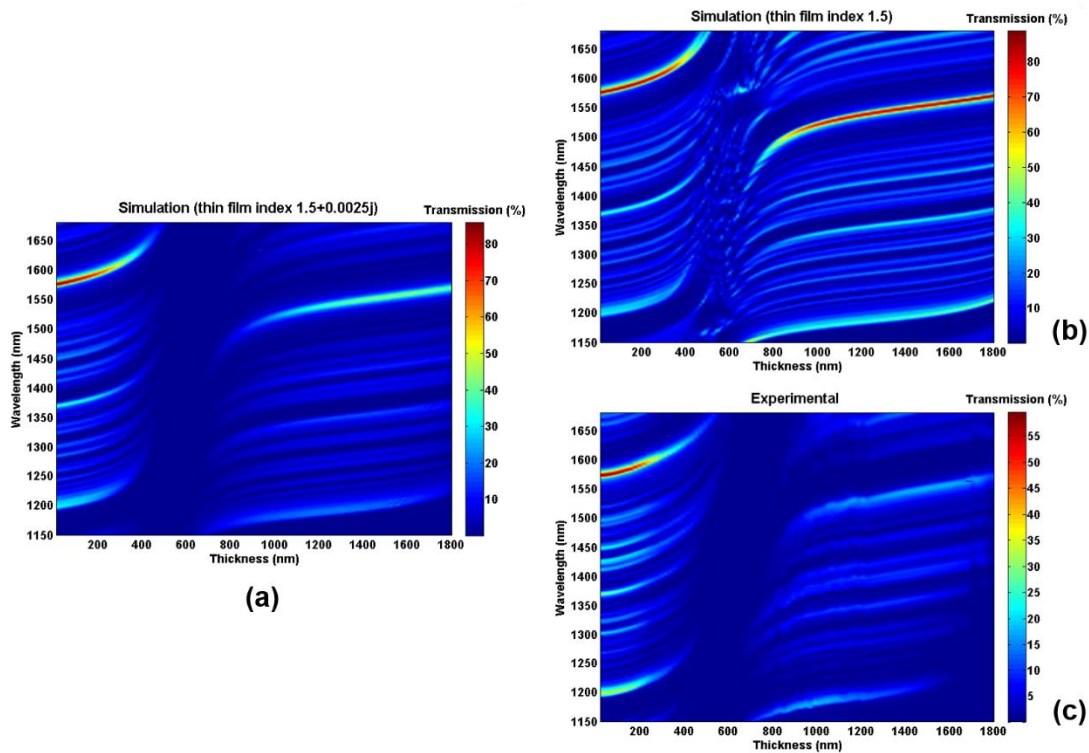

Fig. 5.3. *Evolution of the spectrum as a function of thickness for an SMS structure of 58 mm-length MMF segment. (a) Experimental results, (b) Theoretical results assuming thin-film RI = 1.5 and (c) Theoretical results assuming thin-film RI = 1.5+0.0025i [10].*
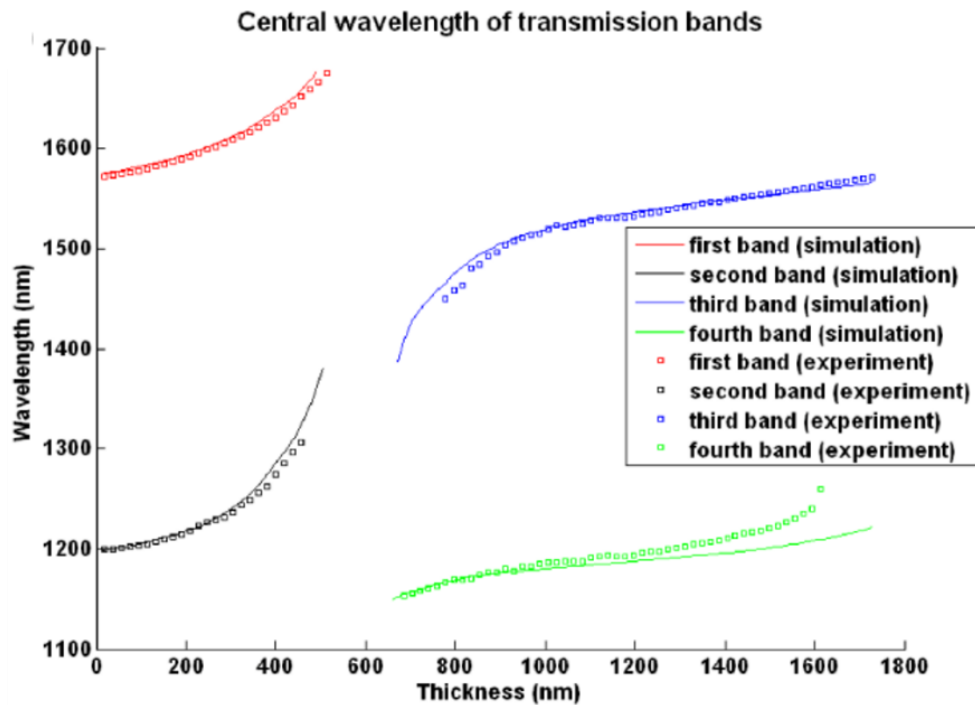
Fig. 5.4. *Evolution of the spectrum as a function of the central wavelength of two transmission bands obtained with an SMS structure of 58 mm [10].*

Now, it is important to take a look at the evolution of the mode effective refractive index as a function of the increasing thin-film thickness (see Fig. 5.5). It is easy to observe that in the fading region there is a double step mode transition (the $HE_{1,7}$ mode becomes de $HE_{1,5}$ mode, the $EH_{1,6}$ becomes the $EH_{1,4}$, and so on), exactly like cladding modes in LPFGs [13].

In LPFGs each resonance is caused by coupling of light from the core mode to a cladding mode. The attenuation bands caused by coupling to cladding modes of higher order are located at higher wavelengths whereas the opposite is true for bands induced by coupling to lower order modes. Consequently, the same transition of the effective indices of cladding modes is observed for the attenuation bands (the band of the $HE_{1,7}$ mode experiments a blue shift to the band of the $HE_{1,5}$ mode, the band of the $EH_{1,6}$ experiments a blue shift to the band of the $EH_{1,4}$ mode and so on) [13].

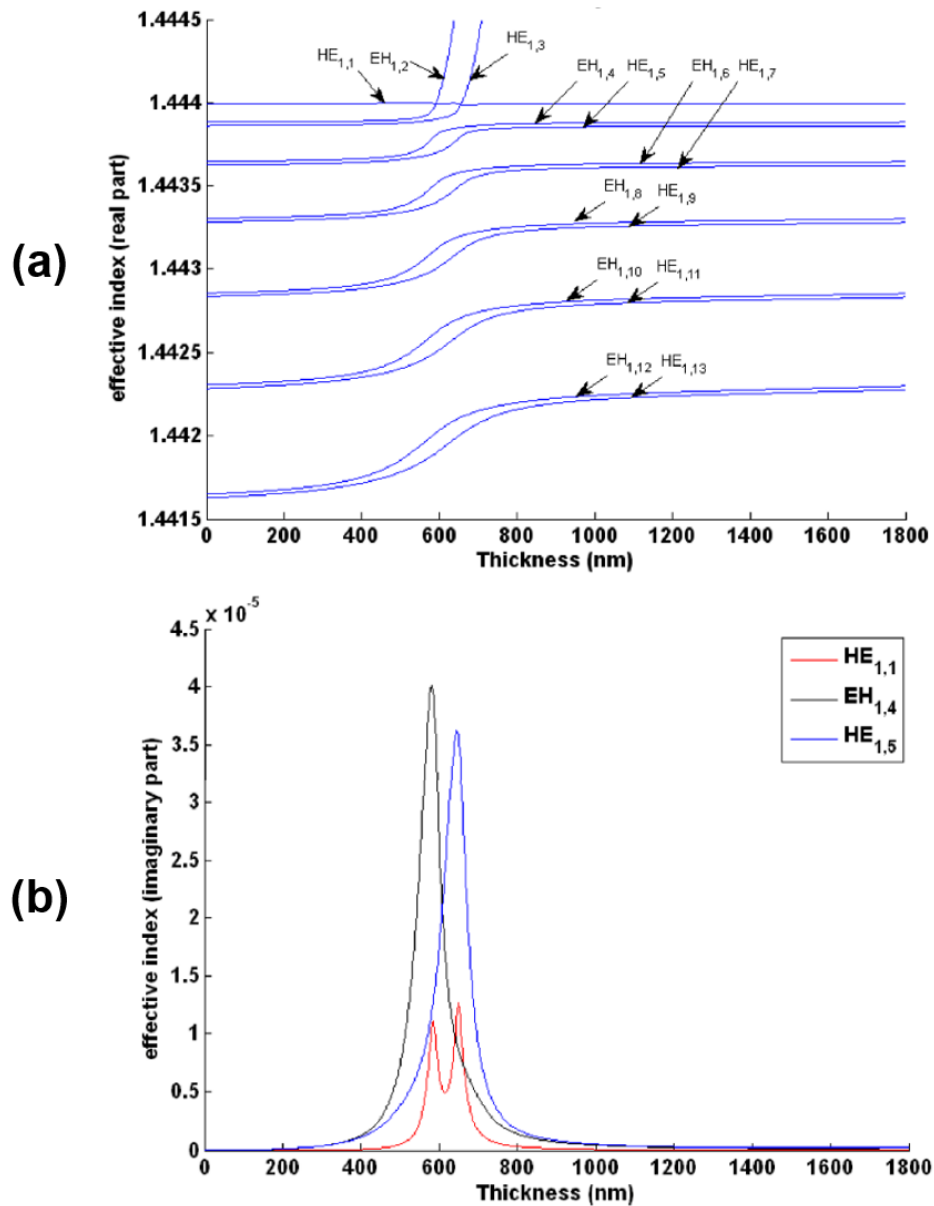**Fig. 5.5.** *Evolution of the spectrum as a function of thickness of the effective index of modes in the MMF segment of an SMS structure (incident wavelength 1550 nm) [10].*

In an SMS structure there is also a transition of modes as can be deducted by associating Figs. 5.4 and 5.5. Unlike in LPFGs, attenuation and transmission bands are produced by constructive and destructive interference among several

modes. Focusing on constructive interference, this phenomenon occurs if the difference between the phases of modes is a multiple of 2π. The phase is directly proportional to the separation between the effective indices of the modes guided in the MMF section and to the length of the MMF section, and inversely proportional to the incident wavelength. By considering Fig. 5.5a, higher order modes experiment a higher effective index increase than lower order modes. In addition to this, the phase of higher order modes exceeds that of lower order modes. Consequently, the phase difference between the modes is increased. In view of the fact that the difference in phase is inversely proportional to the incidence wavelength, this last parameter must be increased in order to continue satisfying the condition for constructive interference. In other words, there is a wavelength shift to the red, which also occurs for bands with destructive interference, following the same explanation but for a phase difference of an uneven multiple of π.

By analyzing Fig. 5.6a, the constructive interference points between $HE_{1,1}$ and $HE_{1,3}$ modes in the MMF segment, it is easy to visualize the two main bands of Figs. 5.3a, b and c. They experiment a wavelength shift to the red because the effective index of $HE_{1,1}$ increases more slowly as a function of the thin-film thickness than that of $HE_{1,3}$ (see Fig. 5.5a).

The reason why the constructive interference between the two first even modes coincides exactly with the main bands can be understood in Fig. 5.6b, where the normalized coupling factor between the fundamental mode guided in the core of the SMF section and the modes guided in the MMF section is plotted. Out of the fading region observed in Fig. 5.3b there is a maximum coupling to uneven modes. Consequently, interference among uneven modes is the predominant. Since among the group of uneven modes, $HE_{1,1}$ and $HE_{1,3}$ are the ones with a lowest separation in effective index, the wavelengths where constructive interference occurs are more separated than for the rest of modes.

However, it is obvious that each band may obey to constructive interference among several modes. In fact the band located at the third optical communications window is where the self-imaging effect occurs. Consequently, it is obvious that there are other constructive interferences concurrent at that position. In this sense, the uniform evolution of the transmission bands indicates that the evolution of the difference between the effective indices of all modes is proportional. The increase in the effective index of $HE_{1,1}$ is lower than that of $HE_{1,3}$, the increase of $HE_{1,3}$ is lower than that of $HE_{1,5}$, and so on. Only in the transition region the original bands disappear and new ones are created if the thin-film presents no losses (see Fig. 5.3b). This is due to the abrupt change in the coupling

conditions between the fundamental mode of the SMF section and the modes in the MMF section as it can be observed in Fig. 5.6b.

However, if the thin-film presents losses there is an increase in the imaginary part of the modes effective index (see Fig. 5.5b), which causes a reduction of the optical transmission (see Fig. 5.3), something that occurred also for LPFGs.
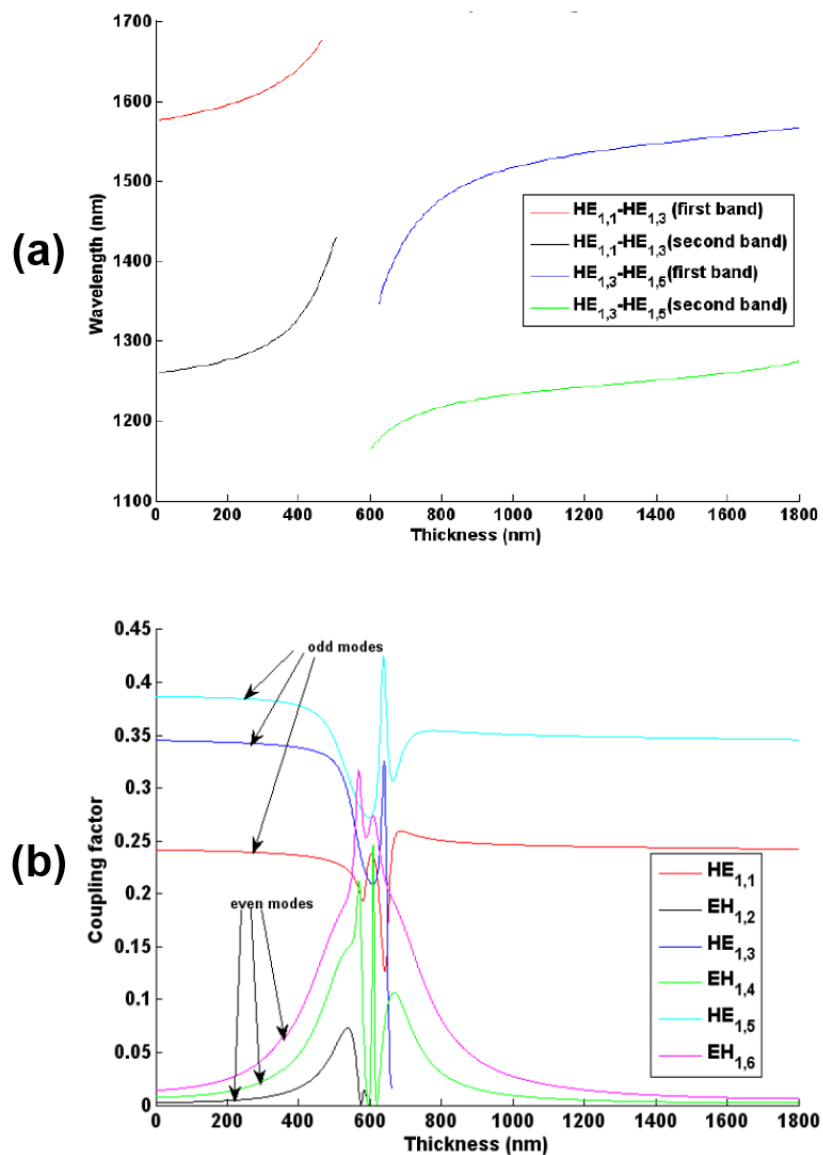

Fig. 5.6. *Evolution as a function of thickness of (a) the constructive interference wavelengths of mode $HE_{1,1}$ and $HE_{1,3}$ and (b) the coupling between the fundamental mode of the SMF section and the modes in the MMF section in an SMS structure (incidence wavelength 1550 nm)* [10].

5.2. Optimization of sensitivity in SMS structures

As has been mentioned, there are two main parameters that can be modified in SMS structures, in order to obtain a better sensitivity: The MMF segment length and diameter. However, in view of the potential of the materials deposited as thin-films presented along this thesis, it is possible that their intrinsic characteristics may also influence the behavior of the final device. Therefore, the main goal of this section will be trying to improve the SMS sensitivity by varying these parameters and extract some conclusions on the evidence.

5.2.1. Influence of the MMF segment length

By simply depositing the same [PAH/PAA] thin-film previously used for the 58 mm-length MMF segment to an MMF segment of 20 mm it can be observed that there are no differences when the evolution of the spectrum as a function of the thin-film thickness is compared to a 58 mm MMF segment length SMS. Fig. 5.7 shows several attenuation and transmission bands (brighter and cooler colors, respectively) corresponding to fourth and last spectra plotted in Fig. 5.2. It is easy to observe that the wavelength shift rate is similar with independence on the length of the structure [24].

Therefore, the main conclusion is that the MMF segment length is not a key factor on the sensitivity of the device, although it is crucial to obtain a self-image band and, therefore, a maximum in transmission. In view of this, as long as there are attenuation bands that can be used to track a further wavelength detection, it seems logical to use shorter length devices. This will lead to more miniaturized structures without sensitivity losses.

5.2.2. Influence of the deposited material

To make a study on this, several theoretical and experimental results are provided. They are based on the deposition of high refractive index thin-films of polymeric [PAH/PAA] and [TiO_2/PSS] metal oxide/polymer matrixes onto 20 mm-length MMF segments on SMS structures. The results are shown in Fig. 5.8.

The selection of a material with a refractive index that approximates that of the substrate increases the wavelength shift. As an example, the self-image band moves from 1521 to 1613.7 nm with [PAH/PAA] and from 1521 to 1568.6 nm with [TiO_2/PSS]. However, the scale of the x-axis is different for [PAH/PAA] and [TiO_2/PSS]. By calculating the sensitivity to variations in the nanocoating thickness

as the wavelength shift divided by nanocoating thickness range, this parameter is lower with [PAH/PAA] (92.7/504 nm = 0.184) than with the higher refractive index matrix [TiO$_2$/PSS] (47.6/132 nm = 0.361). However, the wavelength shift is nonlinear. Consequently, a better knowledge of the sensitivity can be obtained with the derivative of the wavelength as a function of thickness. The maximum derivative is obtained in the proximity of the fading region and it is 0.383 and 0.690, respectively, for both [PAH/PAA] and [TiO$_2$/PSS] thin-films.

The reason why the deposition of a thin-film with a higher refractive index leads to a higher sensitivity can be explained by the phenomenon of modal transition [10,25]. As it has been previously indicated, this basically consists of the guidance of a mode in the thin-film, which induces a reorganization of the effective indices of the modes in the MMF section. With a higher refractive index in the thin-film the transition region is achieved for a lower thickness and it is more abrupt, which causes and increase in the wavelength shift induced by variation in the thin-film refractive index.
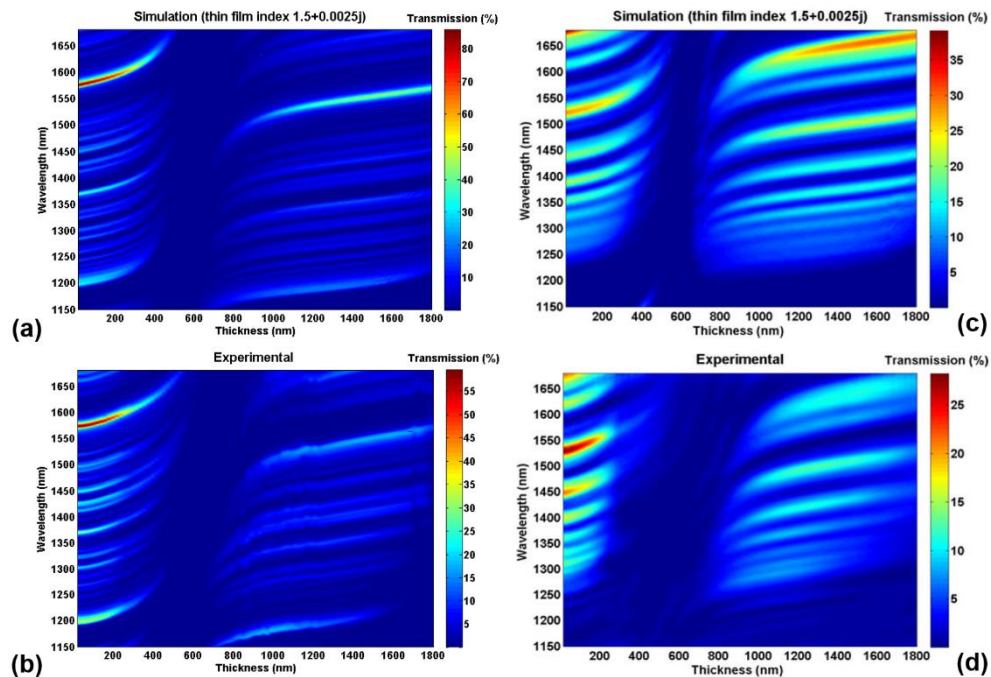

Fig. 5.7. *Evolution of the spectrum as a function of thickness for an SMS structure of (a and b) 58 mm and (c and d) 20 mm of MMF segment length. On the bottom, the experimental results. Above, the theoretical results assuming thin-film RI = 1.5+0.0025i [24].*
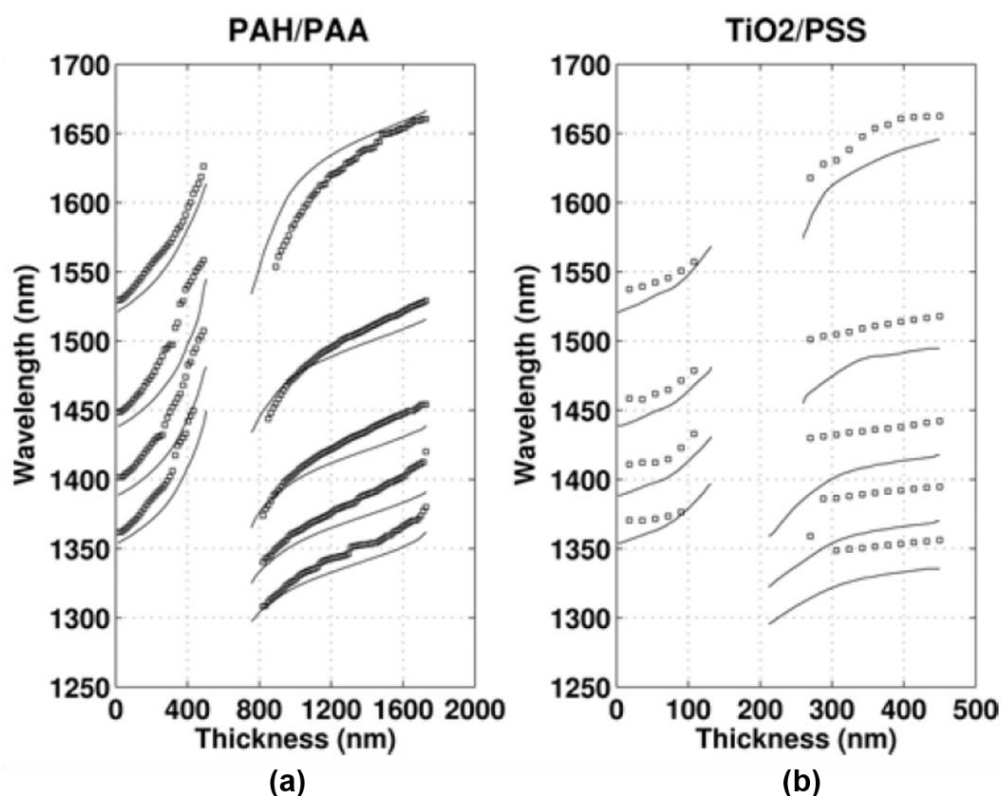
Fig. 5.8. *Evolution as a function of thickness of the central wavelength of transmission bands obtained with an SMS structure of 20 mm. Simulation data, continuous line; experimental data, squares. (a) Deposition of [PAH/PAA] assuming RI = 1.5+0.0025i; (b) Deposition of [TiO$_2$/PSS] assuming RI from 1.749+0.01i to 1.737+0.007i [23].*

5.2.3. Influence of the MMF segment diameter

Once it has been observed that the depositing a material with a higher refractive index than that of the substrate is a better option in terms of sensitivity, the diameter of the MMF segment is analyzed from now on. The expectations, as mentioned in section 5.1 are that the sensitivity is increased if the MMF segment diameter is reduced.

Following this idea, an SMS structure with an MMF segment diameter of 61.5 microns was deposited and coated with [PAH/PAA]. The length of the device was 15 mm, which permits to visualize the self-image band in the optical spectrum.

As expected, theoretical and experimental results in Figs. 5.9 prove that the total wavelength shift is increased by a factor that approximates the ratio between the diameters of the optical fibers analyzed: 125 /61.5 μm. By comparing in Figs.

5.9a and b, the central wavelength of the transmission bands of the 58 mm-length SMS with diameter 125 μm and the 15 mm-length SMS with diameter 61.5 μm as a function of the nanocoating thickness. For example, in Fig. 5.9a the band located at 1574nm for a nanocoating thickness of 420 nm experiments a wavelength shift of 89.6 nm if a nanocoating of 468 nm is deposited, whereas in Fig. 5.9b, the band located at 1494.5 nm for a nanocoating of thickness 420 nm experiments a wavelength shift of 172.3 nm if a nanocoating of 420 nm is deposited. This behavior can be explained by considering the results obtained in [10,25], where it is proved that the resonance wavelength shift is caused by changes in the difference between the effective indices of modes $HE_{1,1}$ and $HE_{1,3}$ in the MMF section. Since the separation between the effective indices of $HE_{1,1}$ and $HE_{1,3}$ modes in the MMF section of an uncoated SMS structure with a lower diameter is increased, the wavelength shift is higher as the nanocoating is progressively deposited on the structure.
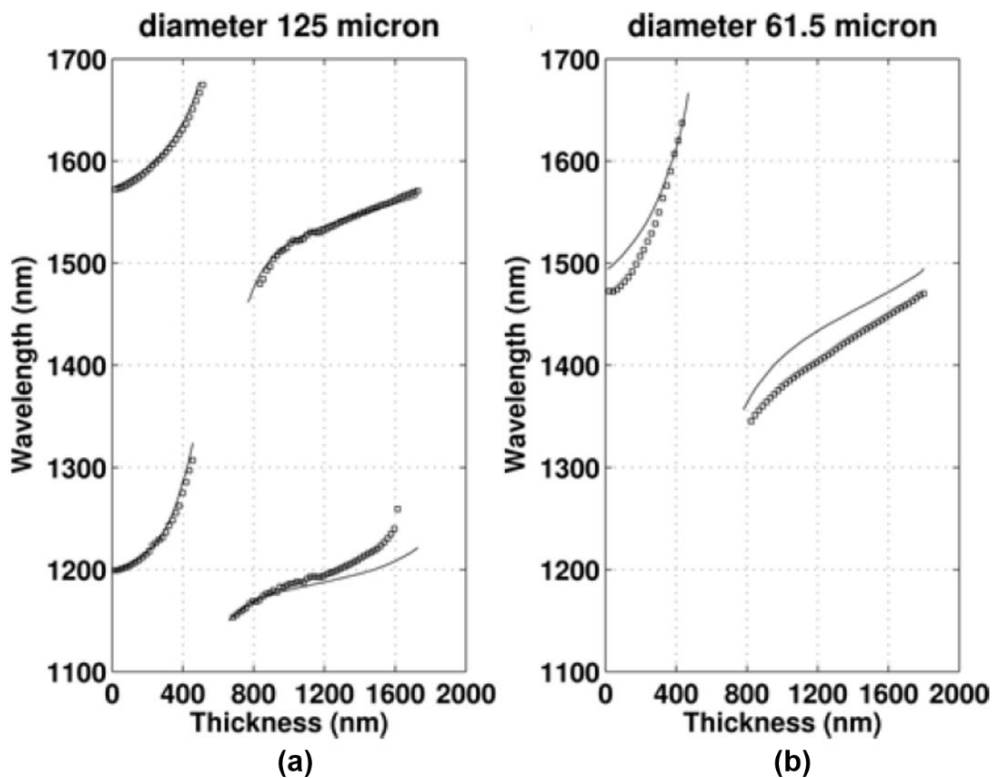

Fig. 5.9. *Evolution as a function of thickness of the central wavelength of transmission bands obtained with an SMS structure where a [PAH/PAA] thin-film is deposited. Simulation data, continuous line; experimental data, squares. (a) MMF segment diameter 125 μm and length 58 mm (b) MMF segment diameter 61.5 μm and length 15 mm. [23].*

5.3. Sensors based on thin-film-deposited SMS structures

In this section, a pair of sensing applications are presented using thin-films onto SMS structures. The goal is to check experimentally the influence of the previous mentioned parameters in the sensitivity of these devices.

5.3.1. pH sensor

To fabricate this sensor, the same set-up depicted in Fig. 5.1 was prepared [26]. Two 58 mm-MMF-length SMS devices were fabricated and deposited with 9 and 18 [PAH/PAA] bilayers respectively. The self-image transmission bands shifted 25 nm from 1570 to 1595 nm in the first case (S_1) and 40 nm from 1560 to 1600 nm in the second case (S_2). According to Fig. 5.7b, the sensitivity of S_2 should be higher than in the case of S_1, since the wavelength shift of the self-image transmission band in S_2 is higher.

To prove this fact, both sensors were subjected to a roundtrip cycle between pH 4.0 and 7.0. Thus, each sensor was immersed in the corresponding pH buffer solution until the self-image transmission band stabilized at some wavelength into the third communications window. After that, the sensors were vigorously rinsed in ultrapure water and then immersed in the next pH buffer solution and so on during the whole process.

Fig. 5.10 shows the spectra obtained as a function of the pH value, focusing on the third optical communications window. It can be observed that the self-image transmission bands shift to higher wavelengths as a function of the decreasing pH value for both S_1 and S_2. The difference is that S_2 shifts in a higher magnitude. This is confirmed in Fig. 5.11, where the tracking of the self-image transmission band maximum is represented as a function of time for both sensors when immersing them in the corresponding pH solutions. Here, the sudden fallings and risings correspond to detections made along the cleaning processes, consisting of several dippings with ultrapure water during a minute. In the case of S_1, the maximum wavelength shift is 7 nm (from 1589 to 1596), whereas this value is 14 nm (from 1565 to 1579) for S_2. This implies to double and, in any case, to increase the values obtained for S_1, what is interesting in terms of improving the sensitivity of the device.

As far as time measurements is concerned, the average response time (t_r) is defined as the average of the time passed to reach from the 10% to the 90% of the stabilization wavelength at every pH values. By calculating this, $t_{r1} = 42$ s, whereas $t_{r2} = 90$ s.
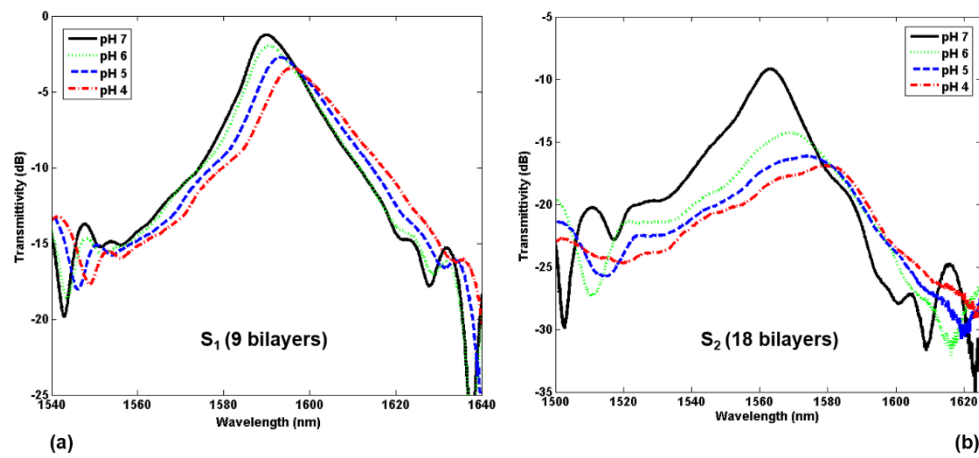
Fig. 5.10. *Obtained spectra during the pH detecting process for S_1 (a) and S_2 (b), focusing on the self-image transmission band, centered in the third optical communications window. The legends match the spectra with their corresponding pH values [26].*
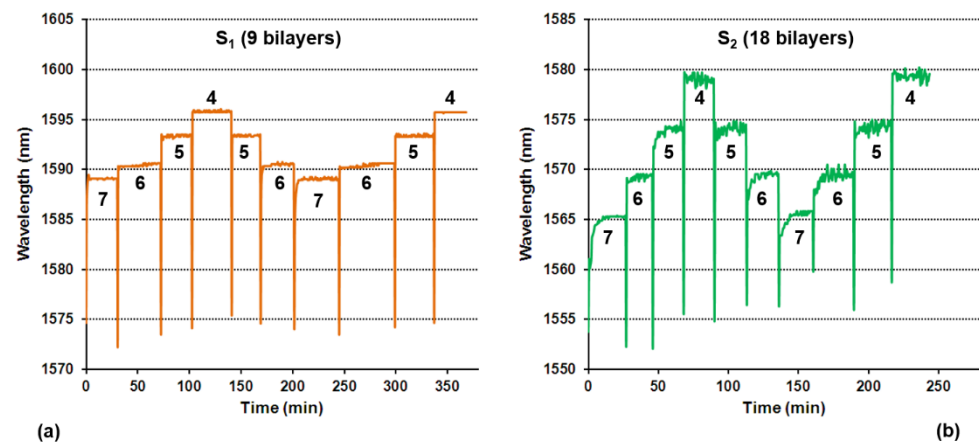
Fig. 5.11. *Tracking of the self-image transmission band displacement during the pH detection process for S_1 (a) and S_2 (b) [26].*

Finally, the stabilization wavelengths obtained during the pH detection process are presented in Fig. 5.12, where it can be observed the sensitivity improvement mentioned before when detecting with S_1 and S_2. Concretely, for the same pH range (4–7), S_1 (the sensor with 9 bilayers) shifts 6.5 nm (i.e. sensitivity 2.17 nm/pH unit) whereas S_2 (the sensor with 18 bilayers) shifts 14 nm (i.e. sensitivity 4.67 nm/pH unit). This means around a 2-fold improvement, what proves the sensitivity enhancement by locating the self-image band near the fading region.
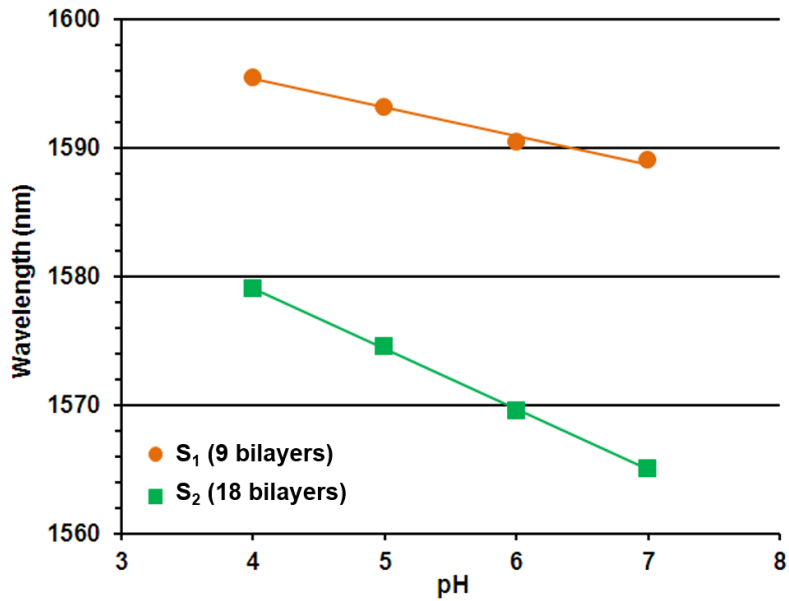
Fig. 5.12. *Stabilization wavelengths for S_1 and S_2 for every pH value detected. The slope of the tendency line is higher for S_2 than for S_1 case, indicating the sensitivity improvement [26].*

5.3.2. Refractometers

In this case, in order to reduce the size of the final device, a simpler reflection configuration based on the use of an optical 2 by 2 coupler was used. In particular, the MMF segment was only spliced to one single-mode segment, as shown in Fig. 5.13 inset. Though there are some previous works of multimode interference in SMS structures in reflection configuration this is the first time to our knowledge that thin-film SMS coated devices in a reflection configuration are explored [27].

The expression for calculating the self-image position of an SMS structure in reflection configuration can be obtained just by dividing Eq. 5.1 by 2, thus obtaining Eq. 5.2:

$$Z_i = \frac{2D^2 n}{\lambda} \qquad\qquad (5.2)$$

However, in order to obtain the same response with the reflection configuration a mirror is required, although this can be avoided at the cost of a power loss [28,29]. In this sense, Fig. 5.14 shows the theoretical and experimental results for both transmission and reflection spectra.
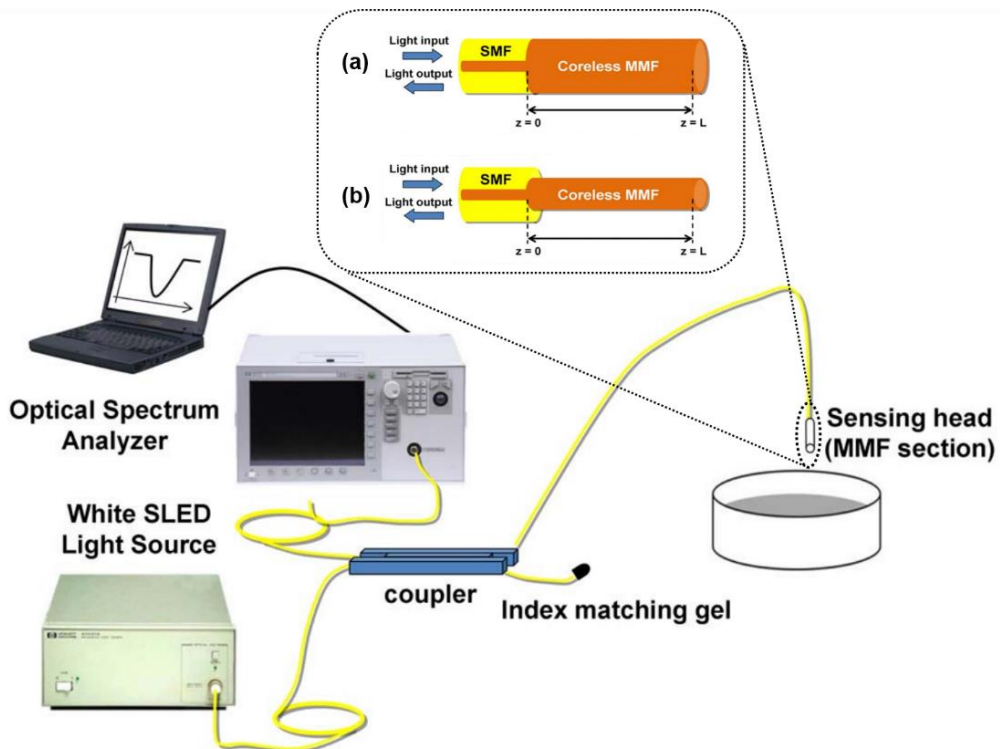
Fig. 5.13. *Experimental setup in reflection configuration for monitoring of the spectral variations during the deposition process and upon introducing the sensor in different refractive index solutions. The inset shows the SMS-based structures utilized during this work [26].*
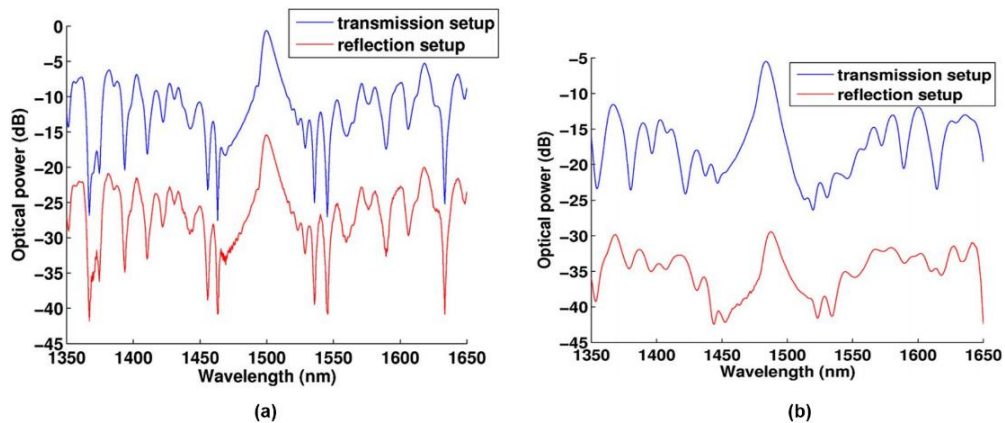
Fig. 5.14. *Experimental results: optical power transmitted and reflected, respectively, with a transmission configuration setup (60 mm long MMF section) and with a reflection configuration setup (30 mm long MMF section) [26].*

In order to make a comparison on the SMS behavior by varying the MMF segment diameter, two SMS structures in reflection configuration were fabricated by splicing a segment of coreless MMF to a standard SMF pigtail. In one of the structures, the diameter of the MMF section was 125 µm and the length, 30 mm (see the setup of Fig. 5.13a), whereas in the other one the diameter was 61.5 µm and the length 15 mm (see the setup of Fig. 5.13b). These values were selected to satisfy the requirement that the central wavelength of the self-image band was located approximately at 1500 nm.

Also, a thin-film sensitive to refractive index was deposited, based on an LbL-assembly of [TiO_2/PSS], as reported in previous sections. This process is repeated up to two bilayers and five bilayers for the SMS structures with MMF section of diameter 125 µm and up to five bilayers for the SMS structures with MMF section of diameter 61.5 µm. When simulating, the refractive index dispersion model can be found in [30], where the values from 1150 to 1680 nm range from 1.749+0.011i to 1.737+0.005i. The bilayer thickness is estimated to be 17 nm.

After the fabrication of the sensor, the same setup was used to characterize the device when it is subjected to changes in the external refractive index. In order to observe the wavelength shift of the self-imaging band, the sensitive fragment is immersed in different glycerol in water solutions: 0%, 10%, 20%, 30%, 40%, 50%, and 60%, which respectively correspond to refractive index values 1.321, 1.336, 1.352, 1.367, 1.382, 1.397, and 1.413 [31,32].

In Fig. 5.15, the evolution of the central wavelength of the self-imaging band is represented both numerically and experimentally as a function of the refractive index for the structures mentioned structures and for the same structures without deposition. The results reveal the improvement of the sensitivity if more bilayers are deposited (five bilayers versus two bilayers) and if the diameter of the MMF section is reduced (125 versus 61.5 µm). This first question is explained in [23], whereas the second question is detailed in [8], where it is indicated that SMS structures with lower MMF section diameter are more sensitive to refractive index variations because the interaction between the modes guided in the MMF segment and the external medium is increased.

In order to have a more precise idea of the improvement, in Table 5.1 the sensitivity (wavelength shift versus a refractive index range from 1.321 to 1.382) is indicated for both structures with and without thin-film. In the experimental results, a 3.9-factor increase is obtained with the five-bilayers thin-film deposited SMS structure with MMF segment diameter 125 µm compared with the same structure without thin-film. This value is exactly the same as that obtained when the five-bilayer thin-film coated SMS structure with MMF segment diameter 61.5

µm is compared with the same structure without thin-film. However, if the sensitivities of structures with MMF segment diameter 61.5 µm are compared to those with MMF segment diameter 125µm, an improvement factor of 1.9 is obtained. In other words, if these two factors are multiplied, the structure with the best performance (the five-bilayer thin-film coated SMS structure with MMF segment diameter 61.5µm) with the structure with the worst performance (the uncoated SMS structure with MMF segment diameter 125 µm), an improvement factor of 7.4 is obtained.

Finally, in order to prove the long-term repeatability of the devices developed in this refractometer, the response after two months of the SMS device with MMF section of length 30 mm, diameter 125 µm, and coated with five bilayers was again checked, obtaining a good agreement and thus corroborating the repeatability of the measurements (see Fig. 5.16).
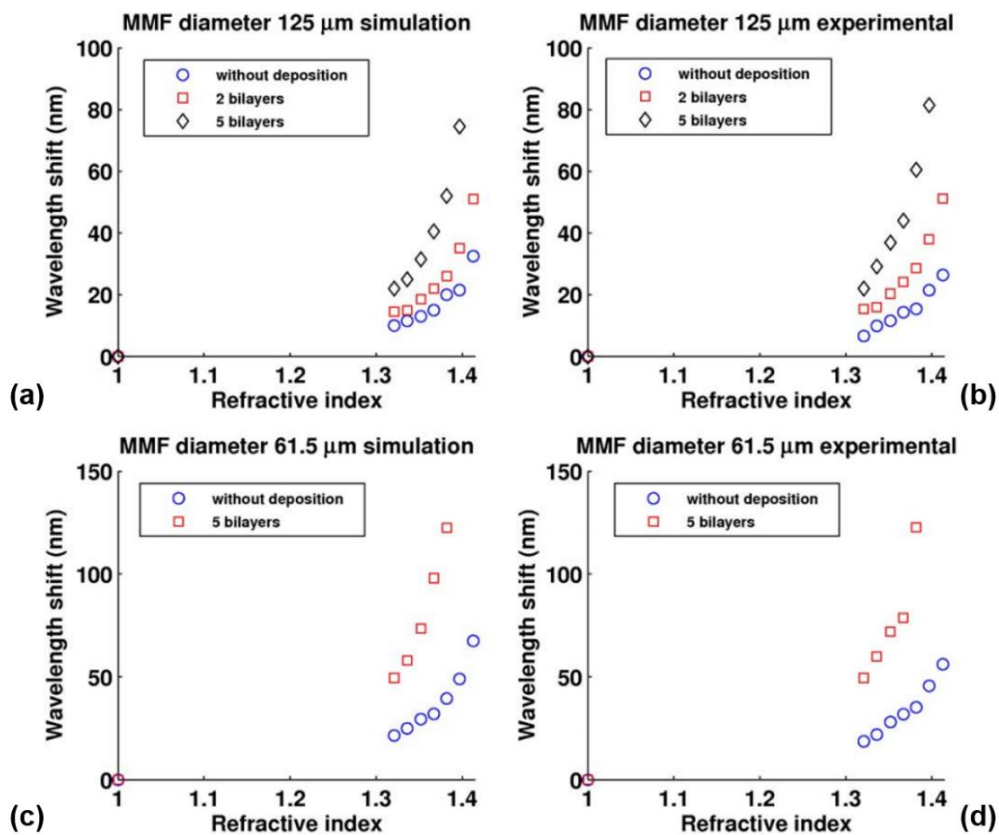
Fig. 5.15. *Theoretical and experimental wavelength shift of the central wavelength of the self-imaging band for different SRIs [26].*

Characteristics of the SMS-based structure	Theory (nm/refractive index unit)	Experiment (nm/refractive index unit)
Diameter 125 μm and no thin film	163.93	162.30
Diameter 125 μm and thin film (two bilayers)	188.52	216.39
Diameter 125 μm and thin film (five bilayers)	491.80	631.15
Diameter 61.5 μm and no thin film	295.08	306.56
Diameter 61.5 μm and thin film (five bilayers)	1196.72	1199.18

Table 5.1. *Sensitivity (wavelength shift in nanometers versus refractive index variation from 1.321 to 1.382 in nm/refractive index unit) for the different SMS structures analyzed [26].*
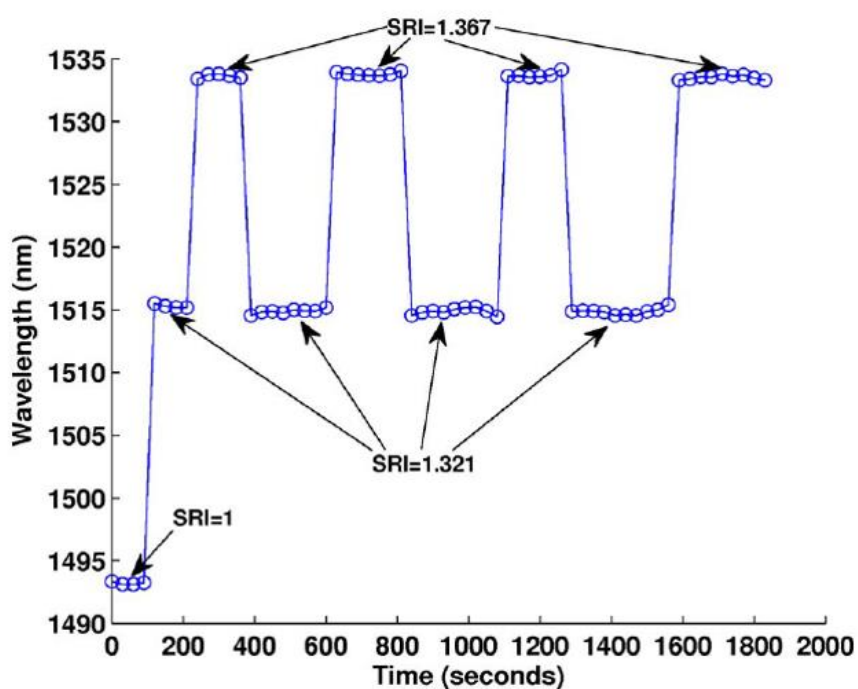
Fig. 5.16. *Response of an SMS device with an MMF section of length 30 mm, diameter 125 μm, and coated with five bilayers two months after the fabrication of the sensor [26].*

5.4. Conclusions

To conclude this fifth chapter, a study on the parameters of the single-mode – multimode – single-mode (SMS) fiber-optic-based structure has been made, also developing sensing applications based on the deposition of a thin-film on the multimode fiber (MMF) segment and the optimization of the parameters of the structure.

It has been observed that depending on the MMF segment length the interferometry pattern is different although, when deposited with a thin-film the spectrum tends to shift in wavelength at the same time. Also depending on the deposited thin-film, several fading regions can show up, corresponding to the LMRs shown along this thesis and also in a similar way that occurs in long period fiber gratings (LPFGs).

Regarding sensitivity, it has been proved that the length of the multimode-segment plays no role in the sensitivity of the bands obtained in the optical spectrum. However, the diameter of the multimode-segment is a very important parameter, which permits to increase the sensitivity of the device. Additionally, the thin-film thickness is another important parameter, since it permits to set the attenuation bands in the optical spectrum in three different regions. In the middle region, the attenuation bands fade, whereas for the other two regions, setting the coating thickness in the proximity of the fading region leads to a higher sensitivity. The thin-film refractive index plays also a role in the sensitivity of SMS coated devices, since the higher is the magnitude, the higher is the wavelength shift as a function of the surrounding refractive index variations.

As applications to check all these parameters, a pH sensor and a refractometer have been developed, corroborating the previous hypotheses. A reflective configuration has been used when detecting refractive index, showing an interesting possibility of using this optical structure as a size-reduced sensor.

At this point, the figure of merit (FOM) is calculated, for this structure. To this purpose, the best results obtained with an SMS of 61.5 microns of MMF segment diameter and 30 mm of length deposited with a [TiO$_2$/PSS] nanostructure is chosen. Thus, its sensitivity is S = 1200 nm/RIU. Additionally, focusing on the self-image band obtained in the SMS structure of length 30 mm (reflection configuration), its FWHM ≈ 30 nm. Thus: the FOM can be now calculated, by evaluating the already known expression:

$$FOM_{SMS} = \frac{S[nm/RIU]}{FWHM\,[nm]} = \frac{1200\,nm/RIU}{30\,nm} = 40\,RIU^{-1}$$

which implies to almost double the values obtained for the T-SMF and a 5.5-fold if compared to the CRMMF results. It is easy to observe that, in spite of the lower sensitivity, what actually increases the FOM value is the reduced FWHM of the self-imaging band.

Finally, the use of SMS-based structures to detect bioreaction is commented. As a bioprobe, the multimode interference phenomenon presented in SMS structures generates quite narrow attenuation/transmission bands that could be used to qualitatively improve the resolution of the measurements when detecting small concentrations of biological analytes. However, due to the low sensitivity presented by the SMS structure even when deposited with a high refractive index thin-film, this structure has not been considered in this thesis to develop a biosensing application.

5.5. Bibliography

[1] W.S. Mohammed, P.W.E. Smith, X. Gu, All-fiber multimode interference bandpass filter, Opt. Lett. 31 (2006) 2547-2549.

[2] J. Antonio-Lopez, A. Castillo-Guzman, D. May-Arrioja, R. Selvas-Aguilar, P. LiKamWa, Tunable multimode-interference bandpass fiber filter, Opt. Lett. 35 (2010) 324-326.

[3] A. Mehta, W. Mohammed, E.G. Johnson, Multimode interference-based fiber-optic displacement sensor, Photonics Technology Letters, IEEE. 15 (2003) 1129-1131.

[4] Q. Wu, Experimental demonstration of a simple displacement sensor based on a bent single-mode–multimode–single-mode fiber structure, Measurement Science and Technology. 22 (2011) 025203.

[5] Q. Wu, Y. Semenova, P. Wang, G. Farrell, High sensitivity SMS fiber structure based refractometer?analysis and experiment, Opt. Express. 19 (2011) 7937-7944.

[6] Q. Wu, Y. Semenova, A.M. Hatta, P. Wang, G. Farrell, Single-mode-multimode-single-mode fiber structures for simultaneous measurement of strain and temperature, Microwave Opt Technol Lett. 53 (2011) 2181-2185.

[7] V.I. Ruiz-Perez, M.A. Basurto-Pensado, P. LiKamWa, J.J. Sanchez-Mondragon, D.A. May, Fiber Optic Pressure Sensor using Multimode Interference, Journal of Physics: Conference Series. 274 (2011) 012025.

[8] S. Silva, E.G.P. Pachon, M.A.R. Franco, J.G. Hayashi, F.X. Malcata, O. Frazão, P. Jorge, C.M.B. Cordeiro, Ultrahigh-sensitivity temperature fiber sensor based on multimode interference, Appl. Opt. 51 (2012) 3236-3242.

[9] L.B. Soldano, E.C.M. Pennings, Optical multi-mode interference devices based on self-imaging: principles and applications, Lightwave Technology, Journal of. 13 (1995) 615-627.

[10] A.B. Socorro, I. Del Villar, J.M. Corres, F.J. Arregui, I.R. Matias, Mode transition in complex refractive index coated single-mode–multimode–single-mode structure, Opt. Express. 21 (2013) 12668-12682.

[11] C.R. Biazoli, S. Silva, M.A.R. Franco, O. Frazão, C.M.B. Cordeiro, Multimode interference tapered fiber refractive index sensors, Appl. Opt. 51 (2012) 5941-5945.

[12] G.P. Agrawal, Nonlinear Fiber Optics, Academic press, 2007.

[13] I.D. Villar, I.R. Matías, F.J. Arregui, P. Lalanne, Optimization of sensitivity in Long Period Fiber Gratings with overlay deposition, Opt. Express. 13 (2005) 56-69.

[14] A. Cusano, A. Iadicicco, P. Pilla, L. Contessa, S. Campopiano, A. Cutolo, M. Giordano, Mode transition in high refractive index coated long period gratings, Opt. Express. 14 (2006) 19-34.

[15] Z. Gu, Y. Xu, K. Gao, Optical fiber long-period grating with solgel coating for gas sensor, Opt. Lett. 31 (2006) 2405-2407.

[16] C.R. Zamarreño, M. Hernáez, I. Del Villar, I.R. Matías, F.J. Arregui, Optical fiber pH sensor based on lossy-mode resonances by means of thin polymeric coatings, Sensors Actuators B: Chem. 155 (2011) 290-297.

[17] P. Pilla, A. Iadicicco, L. Contessa, S. Campopiano, A. Cutolo, M. Giordano, G. Guerra, A. Cusano, Optical chemo-sensor based on long period gratings coated with δ form syndiotactic polystyrene, Photonics Technology Letters, IEEE. 17 (2005) 1713-1715.

[18] D.W. Kim, Y. Zhang, K.L. Cooper, A. Wang, Fibre-optic interferometric immuno-sensor using long period grating, Electronics Letters. 42 (2006) 324-325.

[19] Lin-Lin Xue, Li Yang, Sensitivity enhancement of RI sensor based on SMS fiber structure with high refractive index overlay, Lightwave Technology, Journal of. 30 (2012) 1463-1469.

[20] G.W. Chern, L.A. Wang, Transfer-matrix method based on perturbation expansion for periodic and quasi-periodic binary long-period gratings, J. Opt. Soc. Am. A. 16 (1999) 2675-2689.

[21] N.D. Rees, S.W. James, R.P. Tatam, G.J. Ashwell, Optical fiber long-period gratings with Langmuir?Blodgett thin-film overlays, Opt. Lett. 27 (2002) 686-688.

[22] I. Del Villar, I. Matias, F.J. Arregui, R.O. Claus, Fiber-optic hydrogen peroxide nanosensor, Sensors Journal, IEEE. 5 (2005) 365-371.

[23] A.B. Socorro, I. Del Villar, J.M. Corres, I.R. Matias, F.J. Arregui, Lossy mode resonances dependence on the geometry of a tapered monomode optical fiber, Sensors and Actuators A: Physical. 180 (2012) 25-31.

[24] I. Del Villar, A.B. Socorro, J.M. Corres, F.J. Arregui, I.R. Matias, Optimization of Sensors Based on Multimode Interference in Single-Mode–Multimode–Single-Mode Structure, Lightwave Technology, Journal of. 31 (2013) 3460-3468.

[25] M. Giordano, M. Russo, A. Cusano, G. Mensitieri, G. Guerra, Syndiotactic polystyrene thin-film as sensitive layer for an optoelectronic chemical sensing device, Sensors Actuators B: Chem. 109 (2005) 177-184.

[26] A. Socorro, I. Del Villar, J. Corres, F. Arregui, I. Matias, Sensitivity enhancement in a multimode interference-based SMS fibre structure coated with a thin-film: Theoretical and experimental study, Sensors Actuators B: Chem. 190 (2014) 363-369.

[27] I. Del Villar, A.B. Socorro, J.M. Corres, F.J. Arregui, I.R. Matias, Refractometric sensors based on multimode interference in a thin-film coated single-mode–multimode–single-mode structure with reflection configuration,.

[28] O. Frazão, S.O. Silva, J. Viegas, L.A. Ferreira, F.M. Araújo, J.L. Santos, Optical fiber refractometry based on multimode interference, Appl. Opt. 50 (2011) E184-E188.

[29] E. Li, X. Wang, C. Zhang, Fiber-optic temperature sensor based on interference of selective higher-order modes, Appl. Phys. Lett. 89 (2006) 091119-091119-3.

[30] M. Hernáez, I. Del Villar, C.R. Zamarreño, F.J. Arregui, I.R. Matias, Optical fiber refractometers based on lossy mode resonances supported by TiO_2 coatings, Appl. Opt. 49 (2010) 3980-3985.

[31] P.R. Cooper, Refractive-index measurements of liquids used in conjunction with optical fibers, Appl. Opt. 22 (1983) 3070-3072.

[32] M. Daimon, A. Masumura, Measurement of the refractive index of distilled water from the near-infrared region to the ultraviolet region, Appl. Opt. 46 (2007) 3811-3820.

CHAPTER 6. Sensitivity enhancement based on high refractive index thin-films deposited on toroidal microring resonators

During this chapter, an optical structure called toroidal microring resonator (toroid henceforward) is analyzed. Unlike the previous chapters, where the spectral width of the treated resonances was on the order of nanometers, the deal now is with only a few picometers. In this sense, the resolution of the measurements can be gently enhanced, so it seems possible to detect very small variations in the analytes concentration. Consequently, toroids are good candidates to achieve biosensing applications.

6.1. Whispering gallery modes in toroidal microring resonators

Whispering gallery waves were originally discovered as acoustic phenomena. In adequate designed cavities, as occurs in St. Peter's Cathedral (Vatican), St Paul's Cathedral (London) or Grand Central Station (New York), sound waves can propagate from one side to another, being easy to have a conversation by simply speaking at a normal volume. Lord Rayleigh, who first discovered this phenomenon in St. Paul's Cathedral in 1878, indicated that whispers could be heard across the dome (see Fig. 6.1a). The sound would decay inversely proportional to the distance, instead to the squared distance (as usual in acoustics/radiation). This would permit the possibility of hearing sounds from sources split some meters. The phenomenon was explained as reflections of the sound waves across circular galleries, not straight ones.

What happens in "macro" dimensions with sound waves also happens in "micro" dimensions with light. Fortunately, the fabrication methods permitted to start the optical resonators research from the 1990's on. Analogically to sound, light can also generate whispering gallery modes (WGMs) by propagating in micro-glass spheres and, more specifically, in dielectric spheres, as shown in Fig. 6.1b. Regarding their applications, they can be used for microlasers fabrication, narrow filters, optical switching, ultrafine sensing, displacement measurements, high resolution spectroscopy, Raman sources and studies of non-linear optical effects.

As long as the structure keeps round-shaped, it is possible to generate light WGMs. Some of the structures normally utilized as WGM resonators are depicted in Fig. 6.2. They can be **microspheres**, **microdisks**, **microrings** or **microtoroids** (the

main focus of this thesis chapter), among others [1]. Microspheres are probably the best structures to develop optical resonators due to their high quality resonances. However, they are less used because it is difficult to integrate them on a chip obtaining the same response and because their spectral response is too noisy due to the presence of the high interferometry occurring inside them. The same occurs when dealing with microdisks, since in spite of presenting a quite clean spectral response, the quality of the resonances decreases considerably, something that also happens with microrings. Toroids are in the middle. They combine relatively high quality resonances with a quite clean spectral shape. Whenever they are adequately fabricated, it is possible to use toroids with good results. That is why this structure is chosen for this part of the thesis.

Several optical waveguides are normally utilized to introduce the light in the resonators. This process is carried out by coupling the light using the evanescent field of the waveguide. In this sense, adiabatic tapered single-mode optical fibers (T-SMFs) are the most common [1], since they are the easiest way to transfer and collect the evanescent field to and from the resonating structures. But it is also possible to use side-polished (D-shape) fibers [2] or even prisms [3] when coupling the light into the resonators.
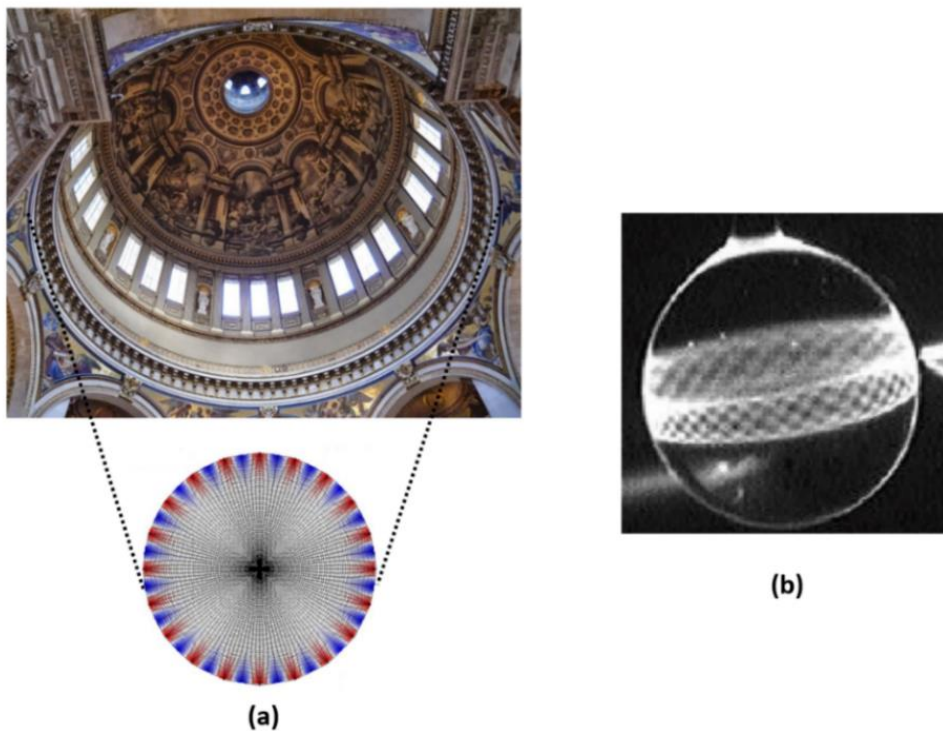

Fig. 6.1. *(a) Whispering gallery sound waves pattern in St. Paul's Cathedral (London) at 69 Hz [4]. (b) Fluorescence imaging of WGMs circulating around a sphere equator [5].*
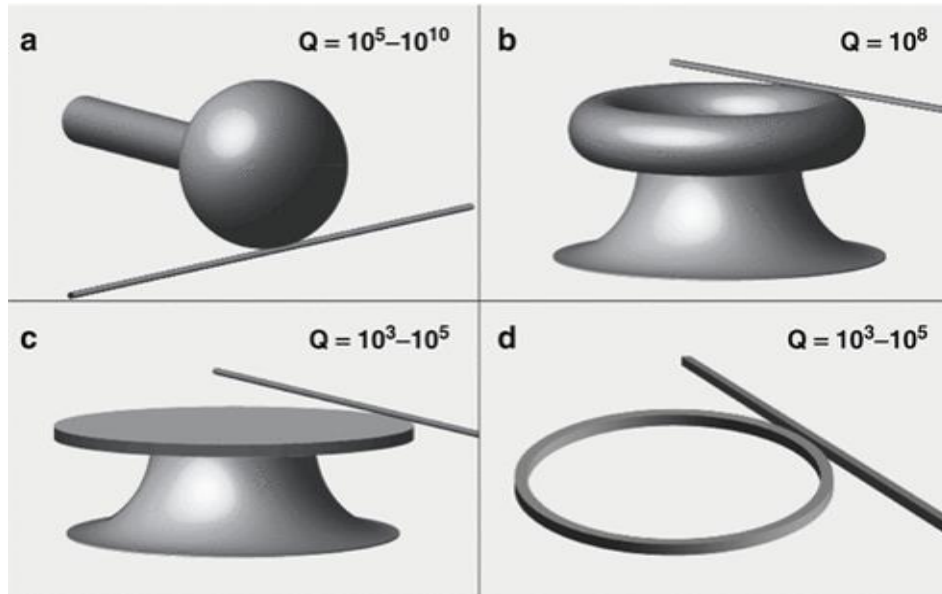
Fig. 6.2. *Different resonating devices with quality factor (Q) values. (a) Microspheres, (b) microtoroids, (c) microdisks and (d) microrings [6].*

The working principle of the light guidance in every microresonator is similar, although this chapter will focus on the toroids. As mentioned, an almost tangent waveguide (a tapered SMF, for example) is in charge of coupling the light into the toroids by means of evanescent field transfer. In this sense, the taper must be thin enough to couple as much evanescent field as possible in the toroid.

After entering the toroid, light propagates following the total internal reflection rules as it occurs in the optical fiber. Here, the condition in Eq. 6.1 must be satisfied to obtain the desired resonance phenomenon.

$$2\pi nR = m\lambda_0 \tag{6.1}$$

where *n* is the refractive index of the toroid fabrication material, *R* is the toroid radius, λ_0 is the resonance wavelength and m is the resonant mode. Essentially, under these conditions, circulating light of different cycles in the toroid interfere constructively with each other and build up resonance modes. As the resonance occurs, the coupled light is trapped in the toroid and the optical power of these resonance wavelengths is minimized when returning to the waveguide. Consequently, a strong attenuation covering a really narrow wavelength band is registered in the optical spectrum. Moreover, since this condition can be fulfilled several times in a broad wavelength range (λ_0 multiples), several peaks can be

observed if zooming out the spectral span, as shown in Fig. 6.3. Each one of these peaks corresponds to a resonating mode, as described in Eq. 6.1.

Now some concepts have to be introduced, in order to characterize the light propagation in these structures. They are summarized in the following lines and indicated in Fig. 6.3 where the typical broadband spectral response of a toroid, is depicted.

a) **Free Spectral Range (FSR)**: it is defined as the wavelength separation between two resonance peaks and it is closely related to the toroid dimensions. In particular, it is mathematically described as Eq. 6.2:

$$FSR = \frac{\lambda^2}{4\pi n R} \qquad (6.2)$$

where λ is the free space wavelength, *n* is the fabrication material of the toroid and *R* is the toroid radius.

b) **Full Width at Half Maximum (FWHM)**: focusing on a resonance, it is the wavelength range where the attenuation is higher than half the signal's power.

c) **Quality Factor (Q):** as occurs in filters, this magnitude is an idea of how narrow is the resonance in comparison to λ_0 and it is calculated as follows in Eq. 6.3:

$$Q = \frac{\lambda_0}{FWHM} \qquad (6.3)$$

d) **Mode volume:** it is defined as the ratio of the total energy stored inside the resonator in that mode and the maximum energy density of that mode. It seems obvious that the objective is to have a lower mode volume, since this means that most of the field is confined in a small cross-section area. This will increase the Q and the resolution of the further measurements.

However, it is not so easy to couple the light into the toroids and to obtain good results from the beginning. Some parameters must be considered. First, it is almost impossible to obtain a 100% coupling due to an effect called "tunneling ray attenuation" [7]. Like in fiber-optics, when working with WGMs it is said that a leaky or tunneling ray is a ray that would be totally reflected at the interface between two media (core-cladding in fiber-optics and silica-air in WGMs) but, however, it loses power due to the curvature of the interface. Moreover, when approaching the T-SMF or the coupling substrate to the resonators, there are sudden variations

due to the attraction between both structures that make the coupling vary from time to time. It is very important to maintain a minimum power coupling to avoid errors in the measurements.
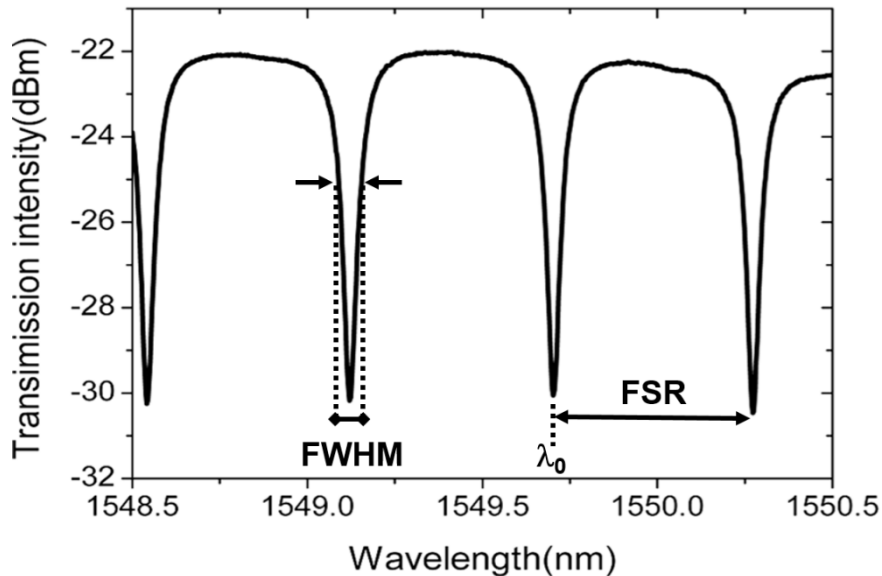
Fig. 6.3. *Spectral parameters defining a typical optical spectrum of a WGM resonator. Two similar samples are represented, showing that the fabrication process is repeatable [8].*

Additionally, obtaining a high Q involves perfection in the fabrication of the devices. Any variation in the device fabrication, any anti-symmetry, any inhomogeneity in the thin-films can be definitely bad for the Q value. In fact, it is stated that Q is the inverse sum of several contributions, such as the thin-film material and its thickness, the surface absorption, the scattering or the tunneling ray attenuation itself [7]. But the external medium can also actuate on the Q, reducing its quality. So, in general, it is better to work with good quality devices from the beginning, because the following steps to reach the application are going to impoverish the results.

Thus, taking into account the previous aspects, it makes sense to say that working with toroids is suitable for detection and, more specifically, for biodetection. The fact of dealing with high Q values permits to work with high resolution in the measurements, so it is possible to distinguish between small variations in an analyte concentration. However, in order to improve the properties of the devices it is difficult to go forward, because the main problem of this technology is the sensitivity. When subjected to refractive index variations, the

sensitivities only reach cents of nanometers per RIU in the best cases [9,10]. In spite of this, it is possible to detect concentration variations, but it would be better to improve the sensitivity characteristics. As an example of this improvement, the next section will show how it is possible to increase the sensitivity of a toroid to temperature. This can be taken into account to develop further work and thus improving the toroids sensitivity to surrounding refractive index variations.

6.2. Sensitivity enhancement to temperature by depositing high refractive index thin-films on toroidal microring resonators

Assuming that no imperfections are induced to bare silica toroids, it is possible to obtain Q values up to 10^8. As it has been mentioned along the whole thesis, a simple and, apparently, unique way to improve the sensitivity of the toroids can be by depositing thin-films of materials that permit to enhance the desired properties. In the case of resonators (and toroids in particular), the goal is to compare the characteristics of the hybrid structures with those achieved by bare structures.

As a first example of this enhancement, an easily affordable polymer like polystyrene (PS) can be deposited by spin-coating on the toroids to improve their sensitivity up to 3 times if compared to a bare toroid itself [11]. The fact of choosing PS is because its refractive index is higher than that of the silica, what provokes an overlap of the optical field from the silica to the PS. This makes the field to be confined more in the outer part of the hybrid optical structure, what enhances the sensitivity to variations in the surrounding medium refractive index due to temperature changes.

A second option is to use near metal oxides, as indium tin oxide (ITO), as shown in [12]. This material has already been analyzed in some contributions along this thesis with considerable results. The goal was to apply the same substance to toroids and try to characterize this new hybrid structure with a near to metallic layer on it. In general, polymer-based systems face numerous limitations, particularly in the field of temperature detection. The explanation to this relies on the fact that the glass transition temperature of the polymer limits the ultimate working range of the device. Near metal oxides are better temperature conductors, so it is expectable to obtain better results than by using either bare silica or polymer-coated toroids.

Thus, in order to deposit the ITO onto the toroids, an ITO-based sol-gel solution was first made, following the recipe indicated in [13]. Throughout the process, the solution was maintained at 25°C and vortexed several times, to

minimize the formation of aggregates. Regarding the silica toroidal cavities, they were fabricated in three steps on silicon wafers as indicated in [14]. After preparing the wafer surface using an oxygen plasma to increase the hydrophilicity, the ITO was deposited twice on the SiO_2/Si wafer using spin-coating to form a uniform thin-film and then annealed at 500°C for 20 minutes in an ambient environment. The samples were immediately removed from the furnace after the first annealing, whereas in the second annealing the furnace was programmed to decrease from 500°C to room temperature at a rate of 1°C/min. This gradual decrease allowed producing smooth and defect-free films. As can be observed in Fig. 6.4a, the ITO coating seems homogeneous and defect-free.

To measure the quality factor, the deposited toroid was coupled to a narrow linewidth tunable laser centered at 765 nm using a T-SMF. The waveguide was aligned with the cavity using top and side view cameras and a 3-axis nano-positioning stage, as shown in Fig. 6.4b. The output from the waveguide was sent to a photodetector, and the signal was monitored on an integrated digitizer/oscilloscope. By scanning across a series of wavelengths, a resonant wavelength (λ_0) could be identified and recorded. The spectrum was then fit to a Lorentzian shape, and the cavity Q was determined according to: $Q=\lambda_0/\Delta\lambda$, where $\Delta\lambda$ is the linewidth. The scan range, scan frequency and input power were optimized to minimize any thermal distortion of the resonant linewidth [15].

To characterize the thermal response of the device, a temperature control stage with a thermo-couple controlled feedback loop was integrated into the previously described set-up (see Fig. 6.4b). Using this stage, the device was able to be heated in 0.5°C steps with minimal overshoot.

The analysis of this device was done theoretically and experimentally. Fig. 6.5 shows the theoretical results obtained by using finite element method (FEM) to simulate the described structure in COMSOL Multiphysics [7] with an analyzed wavelength of 780 nm.

A pair of simulations is shown in Fig. 6.5a and b. In the first simulation, the film has the same properties as the silica toroid. As a result, the film simply increases the diameter of the device and the optical field is not perturbed or changed by the presence of the film. In contrast, in the second simulation, an ITO film is used. By comparing these two simulations, it becomes evident that several significant changes occur.
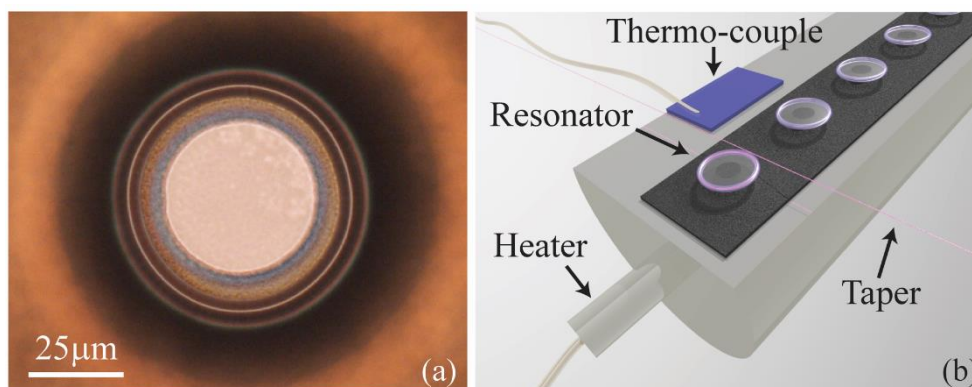
Fig. 6.4. *(a) An optical micrograph of an ITO-coated silica toroidal cavity. The toroid major and minor diameters were found to be 60 microns and 7 microns, respectively. (b) A schematic of the testing set-up, with the key components of the temperature control stage [12].*

First, due to the large refractive index contrast between the coating and the resonator, the mode is split when the ITO film is included. While the majority of the optical mode pushed back into the resonator, a small optical lobe appears inside the coating. This effect is apparent in Fig. 6.5c. This small, secondary field lobe changes how the optical field interacts with the coating.

As mentioned in the previous section, there are many factors contributing to the degradation of the cavity Q, most notably surface scattering and material loss. In sol-gel coated hybrid cavities, it is critical to optimize the annealing of the sol-gel film, as small cracks in the film will give rise to large scattering losses. Indeed, it can be observed in Fig. 6.6a that a Lorentzian fit (dashed red line) of loaded $Q = 2.61 \times 10^5$ is obtained. This indicates that the Q is ITO-dependent in this case.

The so fabricated device was subjected to temperature sensing. As can be observed in Fig. 6.6b, the resonant wavelength increases in direct response to each 0.5°C temperature increase.

The sensor response can be more explicitly evaluated if the wavelength shift versus temperature increment is plotted. Fig. 6.6c shows the results from both measurement methods: 1) wavelength tracking in real-time (ITO-SiO$_{2,RT}$) and 2) measuring the spectra at discrete time points (ITO-SiO$_{2,Q}$). Most importantly, the results are clearly self-consistent. For comparison, the baseline noise level and the theoretically predicted shift from a pure SiO$_2$ device have been also plotted. The change in resonant wavelength in the ITO-SiO$_2$ hybrid cavity is significantly larger than the SiO$_2$ device. This improvement in device performance is directly related to

the increase in the effective thermo-optic coefficient of the cavity, which varies from 1.2×10^{-5} °C^{-1} to 1.712×10^{-5} °C^{-1} due to the presence of the ITO thin-film. This increase is worth being remarkable, given the relative distribution of the optical field in the SiO$_2$ and the ITO, and also indicates that the ITO has a very large, positive thermo-optic response.

By combining the simulated and spectroscopic ellipsometry results, the thermo-optic coefficient of ITO equals 2.229×10^{-4} °C^{-1}. This value is around 18 times larger than the thermo-optic coefficient of silica (1.2×10^{-5} °C^{-1}). Unfortunately, there is minimal previous work studying the dn/dT of ITO for comparison, so more research is still to come in order to discover the potential of the ITO-coated devices.
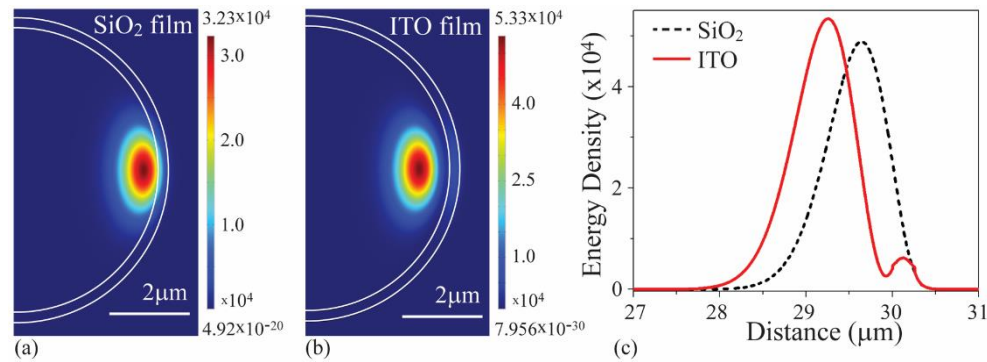
Fig. 6.5. *Optical field distribution based on FEM modeling results for a 260nm thick layer for a) a SiO$_2$ film and b) an ITO film. c) Modal energy density distribution cross-section in the device with both films. The periphery of the device or silica-film interface occurs at 30μm [12].*
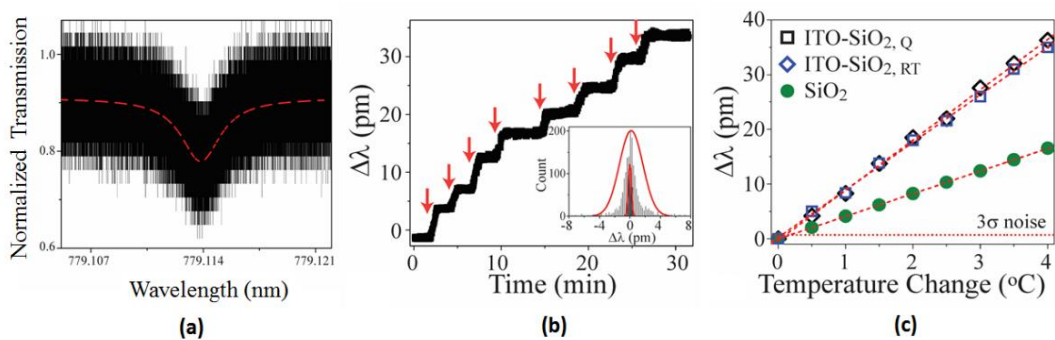
Fig. 6.6. *(a) Loaded Q obtained in the ITO-coated device. (b) Temperature sensing in real-time with noise. Inset: Gaussian fit of the histograms for the noise distributions. c) Comparison between a bare silica toroid and an ITO-coated toroid in real-time and discrete point measurements [12].*

6.3. Conclusions

In conclusion, an ITO-coated silica toroidal microcavity temperature sensor has been fabricated and characterized. After optimizing the ITO coating method to reduce defects in the ITO film, material limited quality factors higher than 10^5 are achieved. Additionally, the dn/dT of ITO is nearly 20-fold larger than the underlying silica device. As a result of this increase, the thermal response of the hybrid ITO-SiO$_2$ sensor is more than doubled. Given the high thermal and chemical stability of both silica and ITO, this hybrid device could be used in many applications requiring high precision temperature detection, such as temperature monitoring in harsh environments. Additionally, the general device architecture is translatable to other refractometric-based sensor platforms, including microrings, waveguides and lasers.

The current research in resonators (toroids included) seems to focus on achieving better Q values [14] and reducing the signal-to-noise ratio (SNR) [16], so that the resolution of the measurements is better. So far, the sensitivities as a function of refractive index changes in the surrounding medium have been reported on microspheres [9,10] and microdisks [17], mainly, obtaining values of 30 nm/RIU and near 300 nm/RIU respectively. Given that the FWHMs reached in the reported applications are 2×10^{-4} nm and 0.1 nm, respectively, the figure of merit equals FOM$_S \approx 150,000$ for the microspheres and FOM$_D \approx 3,000$ for the microdisks. Such FOM values suggest that spheres are better when addressing a sensing application. However, this is not so obvious in view that the wavelength shift in disks may afford a more distinguishable change as a function of refractive index variations.

In the case of toroids, no FOMs have been found, since in spite of getting Qs near 10^7, no applications have been found showing sensitivity as a function of surrounding medium refractive index variations. However, an approximation can be done based on the temperature detection achieved in this work. First, if the loaded Q obtained is 2.61×10^5, then the FWHM is around 3 pm (0.003 nanometers). Now, taking into account that the thermo-optic coefficient of ITO, dn/dT, is 2.229×10^{-4} °C^{-1} it is possible to multiply this value by the temperature range tested in the application, obtaining refractive index units. In this case, for 4°C change, 8.916×10^{-4} RIU is obtained. Moreover, during the testing, the total wavelength shift was 35 pm, the sensitivity could be calculated by dividing this two values, obtaining 39.26 nm/RIU $\approx$ 39 nm/RIU. Now, the FOM can be calculated as usual:

$$FOM_{TOROID} = \frac{S\,[nm/RIU]}{FWHM\,[nm]} \approx \frac{39}{0.003} = 13000\ RIU^{-1}$$

which, of course, is lower than the FOMs obtained for microspheres and higher than estimated for microdisks. The interesting thing is that this is the highest FOM obtained among the different devices studied in this thesis. Indeed, the sensitivity is really low if compared to LMRs, but the key point is the Q. The temperature sensor presented in this thesis is not the best Q that can be achieved for a coated toroid, possibly. However, the fact of dealing with this line width quality makes these devices very attractive when designing sensors based on them.

Nevertheless, by depositing high refractive index thin-films onto the resonators it is possible to fabricate hybrid structures that permit to increase the resonators sensitivity, at the same time the quality of the Qs is almost maintained. Moreover, depending on the deposited materials, Qs could even increase, as shown in [18]. This will probably lead to challenging objectives in the future when addressing biodetection, since a combination between high quality factors and increased sensitivity is strongly required to address such measurements.

6.4. Bibliography

[1] J. Knight, G. Cheung, F. Jacques, T. Birks, Phase-matched excitation of whispering-gallery-mode resonances by a fiber taper, Opt. Lett. 22 (1997) 1129-1131.

[2] S. Shibata, T. Yano, Spherical cavity glass lasers for multiwavelength emission, International Journal of Applied Ceramic Technology. 8 (2011) 1010-1016.

[3] A. Mazzei, S. Götzinger, L.d.S. Menezes, V. Sandoghdar, O. Benson, Optimization of prism coupling to high-Q modes in a microsphere resonator using a near-field probe, Opt. Commun. 250 (2005) 428-433.

[4] O. Wright, Physics World. 25 (2) (2012) 31.

[5] A. Matsko, V. Iltchenko, D. Strekalov, A. Savchenkov, L. Maleki, Delaying Trains of Short Light Pulses in WGM Resonators, NASA Tech Briefs. NPO-44956 (2008).

[6] K. Wilson, F. Vollmer, Whispering Gallery Mode Resonator Biosensors, in: B. Bhushan (Ed.), Springer Netherlands, 2012, pp. 2837-2849.

[8] H.S. Choi, X. Zhang, A.M. Armani, Hybrid silica-polymer ultra-high-Q microresonators, Opt. Lett. 35 (2010) 459-461.

[7] H.S. Choi, X. Zhang, A.M. Armani, Hybrid silica-polymer ultra-high-Q microresonators, Opt. Lett. 35 (2010) 459-461.

[8] X. Han, J. Zhang, L. Wang, Y. Gu, M. Wang, J. Teng, J. Wang, X. Jian, G. Morthier, M. Zhao, Quasi-single-sideband radio over fiber transmission with a polymer-based waveguide microring resonator, Optical Engineering. 50 (2011) 124601-124601-7.

[9] N.M. Hanumegowda, C.J. Stica, B.C. Patel, I. White, X. Fan, Refractometric sensors based on microsphere resonators, Appl. Phys. Lett. 87 (2005).

[10] F. Xu, P. Horak, G. Brambilla, Optical microfiber coil resonator refractometric sensor, Opt. Express. 15 (2007) 7888-7893.

[11] H.S. Choi, S. Ismail, A.M. Armani, Studying polymer thin films with hybrid optical microcavities, Opt. Lett. 36 (2011) 2152-2154.

[12] A.B. Socorro, S. Soltani, I. Del Villar, J.M. Corres, A.M. Armani, Temperature sensor based on a hybrid ITO-silica resonant cavity, Optics Express. (in press) (2014).

[13] R. Ota, S. Seki, M. Ogawa, T. Nishide, A. Shida, M. Ide, Y. Sawada, Fabrication of indium–tin-oxide films by dip coating process using ethanol solution of chlorides and surfactants, Thin Solid Films. 411 (2002) 42-45.

[14] D.K. Armani, T.J. Kippenberg, S.M. Spillane, K.J. Vahala, Ultra-high-Q toroid microcavity on a chip, Nature. 421 (2003) 925-928.

[15] H.S. Choi, A.M. Armani, Thermal nonlinear effects in hybrid optical microresonators, Appl. Phys. Lett. 97 (2010).

[16] M.I. Cheema, Ce Shi, A.M. Armani, A.G. Kirk, Optimizing the Signal to Noise Ratio of Microcavity Sensors, Photonics Technology Letters, IEEE. 26 (2014) 2023-2026.

[17] G. Kim, G. Son, H. Lee, K. Kim, S. Lee, Refractometric sensor utilizing a vertically coupled polymeric microdisk resonator incorporating a high refractive index overlay, Opt. Lett. 34 (2009) 1048-1050.

[18] C. Shi, S. Soltani, A.M. Armani, Gold Nanorod Plasmonic Upconversion Microlaser, Nano Lett. 13 (2013) 5827-5831.

CHAPTER 7. Conclusions and future research lines

7.1. Conclusions

After the development of this thesis some interesting conclusions can be extracted for each of the chapters addressed. They are reviewed in the following lines.

First, a state of the art in fiber-optic biosensors has been presented. There are many techniques to detect bioreactions, although it seems that those based on resonance wavelength tracking are the most commonly utilized. In this sense, some widely known techniques such as surface plasmon resonances (SPR), interferometry or even resonances based on taking advantage of the evanescent field of the optical structure (like in single-mode tapers or long-period fiber gratings) are the most common in the scientific community.

One of the best options to enhance the performance of the optical devices is by depositing thin-films that induce the desired effect and lead to improved parameters. Among the different methods globally used to deposit thin-films onto optical substrates, sputtering, spin-coating and LbL-assembly have been chosen to deposit materials along this thesis.

These thin-films have been used for a double purpose. On the one hand, they can generate the corresponding detection phenomena: an increase in the effective refractive index of the whole structure or the generation of a kind of electromagnetic resonances called lossy mode resonances (LMRs). On the other, these thin-films have been used as precursors and/or biocompatible substrates to be deposited with a biological layer made of proteins o antibodies afterwards. In this sense, the use of materials that permit to obtain a homogeneous and effective biological surface is a key point when biofunctionalizing a surface. According to the consulted bibliography, LbL-assembly is not a bad idea, although it is better to use flat surfaces deposited by other methods and try to covalently attach the bioreceptors on the substrates. At this moment, this is the only way to "ensure" that the biology is adequately attached to the devices.

Several optical/photonic devices have been analyzed in this thesis, based on different phenomena. First, the generation of LMRs has permitted to deal with cladding removed multimode optical fibers (CRMMFs) and tapered single-mode optical fibers (T-SMFs). Working with CRMMFs is easier probably, since by just stripping the fibers it is possible to access the evanescent field of the structure and deposit thin-films that generate LMRs. In the T-SMFs case, there is a need for

tapering the fibers in order to extract the evanescent field, which can be modulated by the LMRs afterwards. It has been observed that both structures present the same sensitivity. Once the optical structure is done, only the type of material is in charge of generating as many LMRs as possible and the material itself will tell how sensitive the induced LMR will be. The key point is the number of modes propagating within the structure. Due to the fact of propagating only one mode, the spectral width of the LMRs in T-SMFs is lower than in CRMMFs if an adequate T-SMF is designed. This has opened a new research field on how to continue improving the parameters of the LMRs.

Regarding the single-mode – multimode – single-mode structure (SMS), the sensitivity of this device is lower than those obtained with CRMMFs and T-SMFs. The reason is that the interferometry in charge of generating the self-image band cannot resist the strong attenuation of the LMRs generated, so it is necessary to stop the deposition before the fading region (LMR) shows up. On the opposite, the spectral width of the self-image band is quite reduced, so this partially compensates the lack of sensitivity. If a well-defined self-image band is obtained, it is possible to resolve little changes in refractive index due to small changes in the measurand.

Finally, a brief study on a more complicated photonic structure called toroidal microring resonator or microtoroid has been done. The key point of this interferometry-based structure (as occurs in microspheres or microdisks) is the high resolution of the resonances that it generates. Due to its high Q values, the spectral widths (FWHM) that it provides are really low, so it is possible to distinguish tiny changes in the measurand translated into wavelength shifts. However, the sensitivity of the devices is really low, unless it is slightly improved by depositing thin-films of high refractive index materials. Among others, indium tin oxide (ITO) has proved to enhance the sensitivity of these devices, although there is still a long way to achieve the optimal conditions.

When facing a biosensing application, there is a need for high resolution measurements and also high sensitivity, since the biological magnitudes vary in a very small range and this should be distinguishable by appropriately separating the resonances between changes. This is the main issue of the biosensing field, without taking into account that the size of the detector should be as smaller as possible, in order to detect the anomalies in a reduced quantity.

Therefore, as it has been suggested along this explanation and the whole thesis, the main conclusion is that a **compromise solution** is required at this moment, for the studied devices. The optical fiber-based structures presented are quite sensitive to surrounding medium refractive indices, although their spectral widths are high. The opposite occurs for the photonic resonating structures and,

particularly, for toroids. A magnitude analyzed during this thesis that helps to understand this concept is the figure of merit (FOM), which divides the sensitivity of the device by its spectral width. Based on this magnitude, it could be thought that the best structure among those presented in this thesis is the toroidal resonator, due to its high FOM values (see Table 7.1). However, depending on the application requirements, maybe it is not the best solution.

Therefore, in spite of their lower resolution, the use of optical fiber-based structures and, more specifically, the use of tapered single-mode fibers deposited with high refractive index thin-films that generate LMRs could be the best options to use. Moreover, their performance when subjecting them to detect biological reactions has been quite good. This shows the possibilities of LMRs to compete against a well-established technology like SPRs.

Optical structure	Sensitivity (nm/RIU)	Spectral width (nm)	FOM (RIU^{-1})
CRMMF	2872	400	7.2
T-SMF	2872	120	24
SMS	1200	30	40
Resonators			
- Microdisks	300	0.1	3000
- Microspheres	30	0.0002	100000
- Microtoroids	40	0.003	13300

Table 7.1. Comparative study on the FOM for each of the structures analyzed along this thesis.

7.2. Future research lines

Based on the results obtained in this thesis, some future open research lines are suggested in the following lines.

Firstly, the sensing platforms are analyzed. When designing biosensors based on wavelength detection of resonances, it is crucial to get a good sensitivity and a good resolution. If an LMR-based biodetection is addressed, then the objective is working with monomode structures that permit the access to their evanescent field avoiding the interference of added modes. This thesis has shown the results for tapered single-mode fibers, but they present the added difficulty of tapering the fibers before depositing anything. In this sense, the use of uncladded

thin-core monomode fibers, to propagate only one mode in visible wavelengths could be a good solution, as well as the use of polished (or d-shaped) fibers. The access to the evanescent field of the structure is direct and the only key point would be to deposit adequate materials. A good point to keep on decreasing the line width of the resonances is to polarize the light. The LMRs obtained with the structures studied in this thesis can propagate both of them because they are radially symmetric and can be excited without polarized light, what is determinant to obtain broad resonances in the spectral response. By filtering one of them and somehow maintaining the polarization, it would be possible to have narrower resonances.

Another possibility could be the use of long period fiber gratings specifically designed for reaching the turn dispersion point (TDP-LPFGs). In chapter 1 it could be seen that their sensitivity is really high in spite of their low quality factor (Q) values. The same applies for the SMS structures, since their working principle is quite similar when deposited with higher refractive index materials.

The fact of dealing with photonic resonant cavities such as microspheres, disks or toroids has led to open a new research line, since these devices own very high resolution. By depositing thin-films of adequate materials it is also possible to increase their sensitivity and thus obtain an interesting technology to be developed in the future. Its capability of detecting minimum changes in the molecules makes it suitable for designing biosensors based on it.

Secondly, the deposition of thin-films has proved to give many benefits to the optical structures, since it is possible to increase their sensitivity to chemical reactions (even biological) and even improve their performance. However, not every thin-film should be considered when designing biosensors. It is true that polymers deposited by LbL-assembly increase the effective refractive index of the structure and makes it more sensitive. However, the biofunctionalization should be done in terms of biocompatibility and effectiveness in the sensitive surface. In this way, planar thin-films are recommended when generating resonant phenomena, in order to better attach the bioreceptors afterwards as it is done in the SPRs-based cases. Besides, there is a need for materials with very high refractive index. Indium tin oxide or titanium oxide have proved to work in this sense, so maybe the use of other kind of metal oxides or even other metals or semiconductors could enhance the performance of the thin-films.

Also, the best way to ensure a correct attachment of the biological part is to take advantage of covalent bonds. Trying to deposit or embed biological molecules by ionic attraction or weak bonds, in general, seems to be not reliable to obtain an efficient sensitive area in the biosensors. Moreover, the fact of working with aggressive media similar to blood plasma forces to avoid weak bonds and try

to focus only in the biological attachment and not in whether the rest of the biosensor is correctly designed.

To sum up, the use of resonant phenomena-based optical devices that combine high resolution and sensitivity with a good attachment of the bioreceptors will be very helpful when detecting minimum changes due to the presence of the biological targets. It is important to notice that the only presence of a few molecules is enough to trigger disease symptoms, so it is important to design devices that permit the clinicians to obtain an accurate early diagnosis. This thesis has tried to contribute to this objective from different points of view by somehow enhancing the state of the art in these devices. Fortunately, further research must be done in order to reach an optimal biosensor.

APPENDICES

APPENDIX 1: THEORETICAL SIMULATIONS

There is not a method that serves for simulating all optical waveguides. Depending on the parameters of the waveguide, especially on the dimensions and the geometry, there are some methods more adequate than others. In this section the methods for simulating optical waveguides used in this thesis will be presented.

Ap.1.1. Method based on attenuated total reflection (ATR method) for simulation of cladding removed multimode optical fibers in transmission configuration

For the simulation of the experimental setup of Fig. Ap.1.1, where light is transmitted through a thin-film coated cladding removed multimode optical fiber of high diameter (≥200 μm), a theoretical method was developed based on that reported in other works focused on SPR phenomenon [1,2].
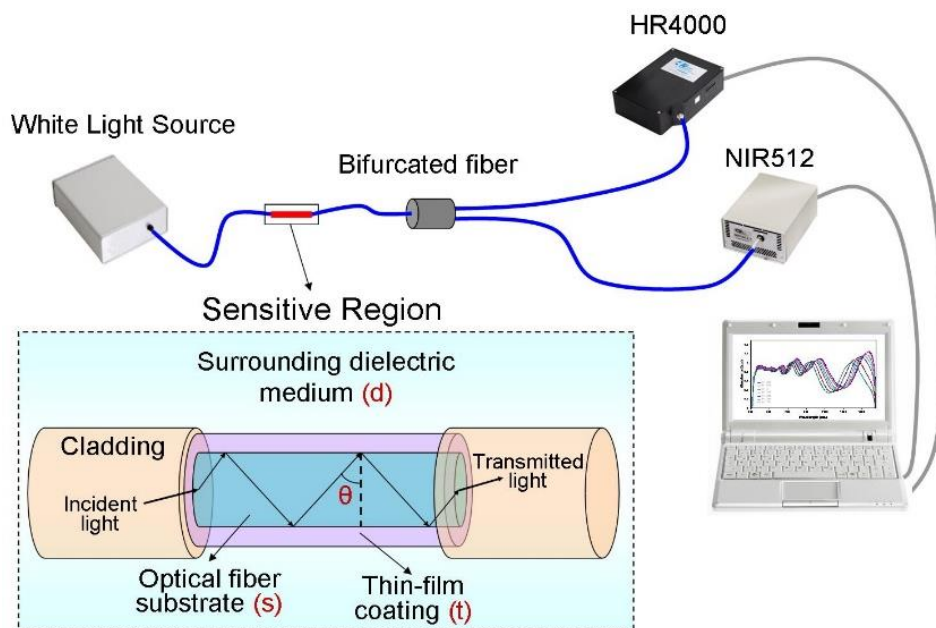

Fig. Ap.1.1. *Optical transmission setup of a thin-film coated cladding removed multimode optical fiber (CRMOF).*

In order to obtain the transmitted optical power in the structure depicted in Fig. Ap.1.1 it is important to apply first the attenuated total reflection (ATR) method with a Kretschmann configuration [3]. With this method the reflectivity as a function of wavelength and incidence angle is obtained at the ITO - fiber core interface R(θ,λ) [1,2] under the assumption that the structure is planar. Consequently, two cases are considered: the TE and TM polarization of the incidence light. For a more exact analysis that considers the cylindrical geometry of the fiber, hybrid modes must be used. It is also important to highlight that the method can only be applied for specific core diameter dimensions. Typically the limit value is 400 µm [4]. However, in [5] the adequateness of the method is proved for diameters of 100 µm.

Depending on the length of the metal-coated region and on the incidence angle the number of reflections N at the ITO - fiber core interface is obtained:

$$N(\theta) = \frac{L}{d \tan \theta} \tag{1}$$

where *L* is the length of the metal coated region, *d* is the diameter of the optical fiber core and θ the angle of incidence.

The final step is to calculate de transmitted power. According to [2], depending on the sensor's application, the propagation of light can be analyzed considering remote sensing or non-remote sensing. Since the dimension of the fiber used in these experiments is short, it will be considered the non-remote case. The transmitted power can be calculated numerically with the following integral [1,2]:

$$T(\lambda) = \frac{\int_{\theta_c}^{90°} p(\theta) R^{N(\theta)}(\theta, \lambda) d\theta}{\int_{\theta_c}^{90°} p(\theta)} \tag{2}$$

where θc is the critical angle.

The main issue now is to select an adequate equivalent of the light source power distribution p(θ). Since a broadband light source is used in the experiments, the power distribution is expressed as [1,6]:

$$p(\theta) \propto n_{co}^2 \sin \theta \cos \theta \tag{3}$$

where θ is the angle represented in Fig. Ap.1.1.

It is also important to mention that since the light introduced in the optical fiber is unpolarized, $R_{N(\theta)}(\theta,\lambda)$ can be replaced in Eq. (2) with the following expression, which considers the reflected light as a combination of the reflected power in TE and TM mode polarization [2]:

$$R^{N(\theta)}(\theta,\lambda) = \frac{R_{TM}^{N(\theta)}(\theta,\lambda) + R_{TE}^{N(\theta)}(\theta,\lambda)}{2} \tag{4}$$

Both TE and TM components of $R_{N(\theta)}(\theta,\lambda)$ in Eq. (4) are expressed as [3]:

$$R_{TM}^{N(\theta)}(\theta,\lambda) = \left| \frac{r_{st}^{TM} + r_{td}^{TM} \exp(2ik_{tz}q)}{1 + r_{st}^{TM} r_{td}^{TM} \exp(2ik_{tz}q)} \right|^2 \tag{5}$$

$$R_{TE}^{N(\theta)}(\theta,\lambda) = \left| \frac{r_{st}^{TE} + r_{td}^{TE} \exp(2ik_{tz}q)}{1 + r_{st}^{TE} r_{td}^{TE} \exp(2ik_{tz}q)} \right|^2 \tag{6}$$

where

$$k_{iz} = \sqrt{\left(\frac{2\pi}{\lambda}\right)^2 \varepsilon_i - k_x^2} \tag{7}$$

$$r_{ij}^{TM} = \frac{\varepsilon_j k_{iz} - \varepsilon_i k_{jz}}{\varepsilon_j k_{iz} + \varepsilon_i k_{jz}} \tag{8}$$

$$r_{ij}^{TE} = \frac{k_{iz} - k_{jz}}{k_{iz} + k_{jz}} \tag{9}$$

$$k_x = \left(\frac{2\pi}{\lambda}\right) n_s \sin(\theta) \tag{10}$$

and where subscripts i and j are s (optical fiber substrate), t (thin-film coating), or d (surrounding dielectric medium), according to Fig. Ap.1.1.

Ap.1.2. Vectorial method for simulation of single-mode – multimode – single-mode (SMS) structures in transmission configuration

In order to obtain the optical transmission through the SMS structure of Fig. Ap.1.2, a simulation tool is developed based on the transfer matrix method [7]. The procedure for obtaining the transmission as a function of wavelength is based on three steps:
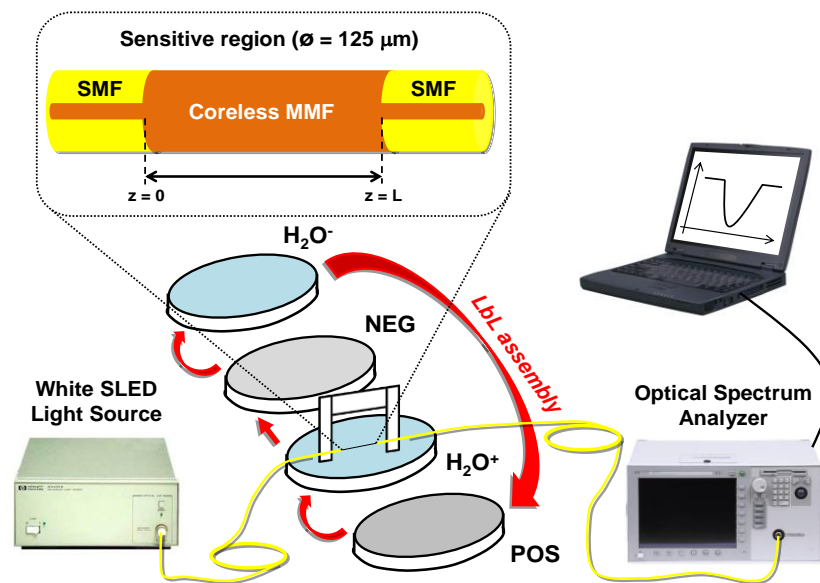

***Fig. Ap.1.2.** Optical transmission setup of a thin-film coated single mode-multimode-single mode (SMS) optical fiber [8].*

1. Calculation of the propagation constants

The application of the transfer matrix method presented in [9], permits to calculate the propagation constants of the modes in a cylindrical waveguide by expressing their fields in terms of radial and azimuthal vector components. In the SMS structure of Fig. Ap.1.2 there are two different waveguides, whose propagation constants are calculated. In view of the azimuthal symmetry of the waveguides, only modes with azimuthal order $v = 1$ are considered for the analysis [10]. Consequently, the notation for modes will be of the type '1,j' (the first subindex representing the azimuthal order, and the second subindex indicating the jth mode).

2. Derivation of the transmission and reflection coefficients

Considering in Fig. Ap.1.2 the SMF on the left side of the SMS structure as waveguide 'a', the coreless MMF as waveguide 'b', and the SMF on the right side as waveguide 'c', the transmission and reflection coefficients can be obtained with the general equation Eq. 11:

$$
\begin{pmatrix} A_{11}^{(c)} \\ B_{11}^{(c)} \\ A_{12}^{(c)} \\ B_{12}^{(c)} \\ \vdots \\ A_{1N}^{(c)} \\ B_{1N}^{(c)} \end{pmatrix} = H_{cb} \cdot F \cdot H_{ba} \begin{pmatrix} A_{11}^{(a)} \\ B_{11}^{(a)} \\ A_{12}^{(a)} \\ B_{12}^{(a)} \\ \vdots \\ A_{1N}^{(a)} \\ B_{1N}^{(a)} \end{pmatrix}
\tag{11}
$$

where $A_{1j}(a)$ is the normalized forward amplitude of the j mode in waveguide 'a', $A_{1j}(c)$ is the normalized forward amplitude of the j mode in waveguide 'c', $B_{1j}(a)$ is the normalized backward amplitude of the j mode in waveguide 'a', and $B_{1j}(c)$ is the normalized backward amplitude of the j mode in waveguide 'c'.

H_{ba} and H_{cb} are the matrices that relate the amplitudes of the modes at both sides of the interface between waveguide 'b' and 'a', and between waveguide 'c' and 'b' respectively. As an example of both expressions, according to [7], matrix H_{cb}, which relates the amplitude of the modes at both sides of the interface between waveguide c and b, can be expressed as indicated in Eq. 12:

$$
\begin{pmatrix} A_{11}^{(c)} \\ B_{11}^{(c)} \\ A_{12}^{(c)} \\ B_{12}^{(c)} \\ \vdots \\ A_{0N}^{(c)} \\ B_{1N}^{(c)} \end{pmatrix} = \begin{pmatrix}
\frac{1}{2}(I_{11,11}+J_{11,11}) & \frac{1}{2}(I_{11,11}-J_{11,11}) & \frac{1}{2}(I_{11,12}+J_{11,12}) & \frac{1}{2}(I_{11,12}-J_{11,12}) & \cdots & \frac{1}{2}(I_{11,1N}+J_{11,1N}) & \frac{1}{2}(I_{11,1N}-J_{11,1N}) \\
\frac{1}{2}(I_{11,11}-J_{11,11}) & \frac{1}{2}(I_{11,11}+J_{11,11}) & \frac{1}{2}(I_{11,12}-J_{11,12}) & \frac{1}{2}(I_{11,12}+J_{11,12}) & \cdots & \frac{1}{2}(I_{11,1N}+J_{11,1N}) & \frac{1}{2}(I_{11,1N}+J_{11,1N}) \\
\frac{1}{2}(I_{12,11}+J_{12,11}) & \frac{1}{2}(I_{12,11}-J_{12,11}) & \frac{1}{2}(I_{12,12}+J_{12,12}) & \frac{1}{2}(I_{12,12}-J_{12,12}) & \cdots & \frac{1}{2}(I_{12,1N}+J_{12,1N}) & \frac{1}{2}(I_{12,1N}+J_{12,1N}) \\
\frac{1}{2}(I_{12,11}-J_{12,11}) & \frac{1}{2}(I_{12,11}+J_{12,11}) & \frac{1}{2}(I_{12,12}-J_{12,12}) & \frac{1}{2}(I_{12,12}+J_{12,12}) & \cdots & \frac{1}{2}(I_{12,1N}+J_{12,1N}) & \frac{1}{2}(I_{12,1N}+J_{12,1N}) \\
\vdots & \vdots & \vdots & \vdots & \ddots & \vdots & \vdots \\
\frac{1}{2}(I_{1N,11}+J_{1N,11}) & \frac{1}{2}(I_{1N,11}-J_{1N,11}) & \frac{1}{2}(I_{1N,12}+J_{1N,12}) & \frac{1}{2}(I_{1N,12}-J_{1N,12}) & \cdots & \frac{1}{2}(I_{1N,1N}+J_{1N,1N}) & \frac{1}{2}(I_{1N,1N}+J_{1N,1N}) \\
\frac{1}{2}(I_{1N,11}-J_{1N,11}) & \frac{1}{2}(I_{1N,11}+J_{1N,11}) & \frac{1}{2}(I_{1N,12}-J_{1N,12}) & \frac{1}{2}(I_{1N,12}+J_{1N,12}) & \cdots & \frac{1}{2}(I_{1N,1N}+J_{1N,1N}) & \frac{1}{2}(I_{1N,1N}+J_{1N,1N})
\end{pmatrix} \begin{pmatrix} A_{11}^{(b)} \\ B_{11}^{(b)} \\ A_{12}^{(b)} \\ B_{12}^{(b)} \\ \vdots \\ A_{1N}^{(b)} \\ A_{1N}^{(b)} \end{pmatrix}
\tag{12}
$$

where $I_{1j,1k}$ and $J_{1j,1k}$ are the following expressions:

$$
I_{1k,1j} = \sqrt{P_{1j}^{-1}P_{1k}^{-1}} \frac{1}{2} \operatorname{Re} \int_{\phi=0}^{2\pi} d\phi \int_{r=0}^{\infty} \left[E_{1,j-r}^{b}(r) H_{1,k-\phi}^{a}(r)^{*} - H_{1,k-r}^{a}(r)^{*} E_{1,j-\phi}^{b}(r) \right] \cdot r dr
\tag{13}
$$

$$J_{1k,1j} = \sqrt{P_{1j}^{-1}P_{1k}^{-1}} \, \frac{1}{2} \mathrm{Re} \int_{\phi=0}^{2\pi} d\phi \int_{r=0}^{\infty} \left[E_{1,j-r}^{a}(r)^{*} H_{1,k-\phi}^{b}(r) - H_{1,k-r}^{b}(r) E_{1,j-\phi}^{a}(r)^{*} \right] \cdot r dr$$

(14)

In Eqs. (13) and (14) $E_{1,j-r}$ is the radial electric field of mode$_{1,j}$, $E_{1,j-\phi}$ is the azimuthal electric field of mode$_{1,j}$, $H_{1,j-r}$ is the radial magnetic field of mode$_{1,j}$, $H_{1,j-\phi}$ is the azimuthal magnetic field of mode$_{1,j}$, and $P_{1,j}$ is the normalized power of the same mode.

The expression for matrix F, which is the free propagation matrix over the MMF region of length L is:

$$F = \begin{pmatrix} \exp(-j\beta_{11}L) & 0 & 0 & 0 & \cdots & 0 & 0 \\ 0 & \exp(j\beta_{11}L) & 0 & 0 & \cdots & 0 & 0 \\ 0 & 0 & \exp(-j\beta_{12}L) & 0 & \cdots & 0 & 0 \\ 0 & 0 & 0 & \exp(j\beta_{12}L) & \cdots & 0 & 0 \\ \vdots & \vdots & \vdots & \vdots & \ddots & \vdots & \vdots \\ 0 & 0 & 0 & 0 & \cdots & \exp(-j\beta_{1N}L) & 0 \\ 0 & 0 & 0 & 0 & \cdots & 0 & \exp(j\beta_{1N}L) \end{pmatrix}$$ (15)

where β_{1j} is the propagation constant of mode$_{1,j}$.

3. Derivation of the transmission and reflection coefficients

The transmission can be found by assuming in Eq. 11 that only one mode is incident ($A^{(a)}_{1,1} = 1$ and $A^{(a)}_{1,2} = \ldots = A^{(a)}_{1,N} = 0$) and that there is no backward reflection in waveguide 'c' ($B^{(c)}_{1,1} = B^{(c)}_{1,2} = \ldots = B^{(c)}_{1,N} = 0$), and solving the equation. After that, the transmission power can be expressed as Eq. 16:

$$T = \left| A_{11}^{c} \right|^{2}$$

(16)

Ap.1.3. Commercial software

The numerical methods presented in sections 3.1 and 3.2 own the limitation that they have only been developed for structures in transmission configuration. As well as the complexity of the structures analyzed during the thesis increased (thin-film coated optical fibers in reflective configuration and tapered optical fibers), it was necessary to consider the acquisition of a commercial software. Initially CAMFR [11] permitted to solve the transmission trough tapered structures in one publication [12]. However, this software shows some errors for specific parameterizations. Consequently, a more powerful tool was acquired: FIMMWAVE. This last software permitted to analyze all the structures not simulated with the other three methods.
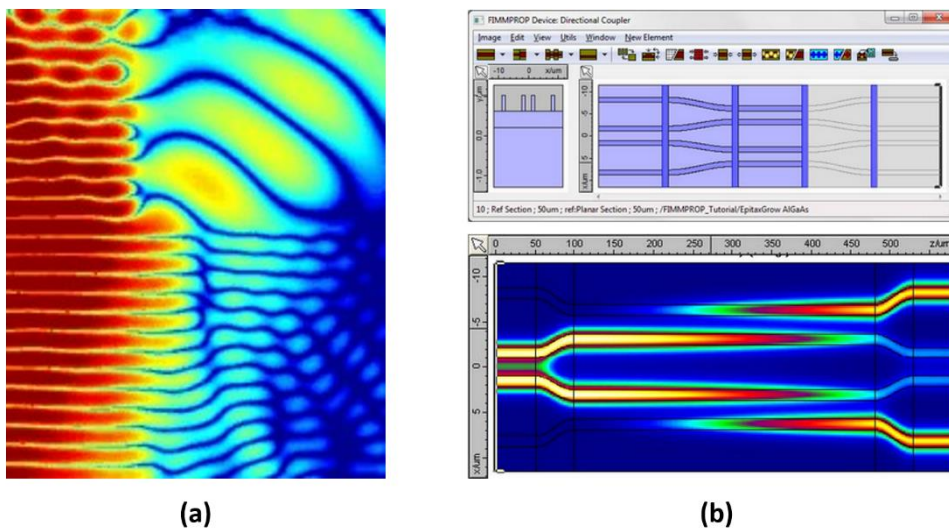

(a)   **(b)**

Fig. Ap.1.3. *(a) Photogram of a Vertical Cavity Surface Emitting Laser (VCSEL) simulated in CMFR. (b) Programming a directional coupler in FIMMWAVE®.*

Ap.1.4. Dispersion models for the materials used in the thin-films

For the modelization of the complex dielectric function of the complex materials used in the thesis, some dispersion models have been used:

1. Sellmeier equation for fused silica:

$$n^2(\omega) = 1 + \sum_{j=1}^{m} \frac{B_j \omega_j^2}{\omega_j^2 - \omega^2}$$

(17)

with parameters: B_1=0.691663, B_2=0.4079426, B_3=0.8974794, λ_1=0.0684043 μm, λ_2= 0.1162414, and λ_3= 9.896161, where λ_j=2πc/ω_j and c is the speed of light in vacuum [13].

2. Lorentz model for [TiO_2/PSS] [14]:

$$\varepsilon(E) = \varepsilon_\infty + \sum_k \frac{A_k}{E_k^2 - E^2 - iB_k E} \tag{18}$$

where A_k, B_k and E_k are respectively the amplitude, the center energy and the broadening of the kth oscillator, E is the photon-energy and ε_∞ is an offset that indicates the permittivity at high frequency. For the sake of simplicity a single oscillator is used in expression (18). The parameters that lead to a best fit with experimental results developed by deposition of [TiO_2/PSS] on optical fiber are: B_k=0.5 eV, A_k=61 eV^2 and E_k=5.55 eV. They were calculated by computing numerically the global error between the experimental and the theoretical transmission spectra for different coating thicknesses [15].

Ap.1.5. Bibliography

[1] Y. Xu, N.B. Jones, J.C. Fothergill, C.D. Hanning, Analytical estimates of the characteristics of surface plasmon resonance fibre-optic sensors, Journal of Modern Optics. 47 (2000) 1099-1110.

[2] A.K. Sharma, B.D. Gupta, On the sensitivity and signal to noise ratio of a step-index fiber optic surface plasmon resonance sensor with bimetallic layers, Opt. Commun. 245 (2005) 159-169.

[3] J. Homola, Surface Plasmon Resonance Based Sensors, Springer, 2006.

[4] A. Messica, A. Greenstein, A. Katzir, Theory of fiber-optic, evanescent-wave spectroscopy andsensors, Appl. Opt. 35 (1996) 2274-2284.

[5] A.K. Sharma, B.D. Gupta, Absorption-based fiber optic surface plasmon resonance sensor: a theoretical evaluation, Sensors Actuators B: Chem. 100 (2004) 423-431.

[6] B. Gupta, C. Singh, Evanescent-absorption coefficient for diffuse source illumination: uniform-and tapered-fiber sensors, Appl. Opt. 33 (1994) 2737-2742.

[7] P. Yeh, A. Yariv, E. Marom, Theory of Bragg fiber, J. Opt. Soc. Am. 68 (1978) 1196-1201.

[8] A.B. Socorro, I. Del Villar, J.M. Corres, F.J. Arregui, I.R. Matias, Mode transition in complex refractive index coated single-mode–multimode–single-mode structure, Opt. Express. 21 (2013) 12668-12682.

[9] T. Erdogan, Cladding-mode resonances in short-and long-period fiber grating filters, JOSA A. 14 (1997) 1760-1773.

[10] G. Decher, Fuzzy nanoassemblies: toward layered polymeric multicomposites, Science. 277 (1997) 1232-1237.

[11] P. Bienstman, CAMFR Software, from University of Ghen, Belgium, (2007).

[12] A.B. Socorro, I. del Villar, J.M. Corres, F.J. Arregui, I.R. Matias, Tapered Single-Mode Optical Fiber pH Sensor Based on Lossy Mode Resonances Generated by a Polymeric Thin-Film, Sensors Journal, IEEE. 12 (2012) 2598-2603.

[13] G.P. Agrawal, Nonlinear Fiber Optics, Academic press, 2007.

[14] R. Synowicki, Spectroscopic ellipsometry characterization of indium tin oxide film microstructure and optical constants, Thin Solid Films. 313 (1998) 394-397.

[15] M. Hernáez, I. Del Villar, C.R. Zamarreño, F.J. Arregui, I.R. Matias, Optical fiber refractometers based on lossy mode resonances supported by TiO_2 coatings, Appl. Opt. 49 (2010) 3980-3985.

APPENDIX 2: SCIENTIFIC PUBLICATIONS

Ap.2.1. INTERNATIONAL JOURNALS

1. "Influence of waist length in lossy mode resonances generated with coated tapered single mode optical fibers". A.B. Socorro, I. Del Villar, J.M. Corres, F.J. Arregui, I.R. Matias. **Photonics Technology Letters** Vol. 23, No 21 (2011), pp. 1579 – 1581.

2. "Lossy mode resonances dependence on the geometry of a tapered monomode optical fiber", A. B. Socorro, I. Del Villar, J.M. Corres, F.J. Arregui, I.R. Matias. **Sensors and Actuators A: Physical** 180 (2012), pp. 25 – 31.

3. "Tapered single-mode optical fiber pH sensor based on lossy mode resonances generated by a polymeric thin-film". A.B. Socorro, I. Del Villar, J.M. Corres, F.J. Arregui, I.R. Matias. **IEEE Sensors Journal**, Vol. 12, No 8 (2012), pp. 2598 – 2603.

4. "Fiber-optic biosensor based on lossy mode resonances", A.B. Socorro, J.M. Corres, I. Del Villar, I.R. Matias, F.J. Arregui, **Sensors and Actuators B: Chemical**, Vol. 174 (2012), pp. 263-269.

5. "Mode transition in complex refractive index coated single-mode–multimode–single-mode structure", A.B. Socorro, I. Del Villar, J.M. Corres, F.J. Arregui, I.R. Matias, **Optics Express** Vol. 21 (10) (2013), pp. 12668–12682.

6. "Optimization of sensors based on multimode interference in single-mode–multimode–single-mode structure", I. Del Villar, A.B. Socorro, J.M. Corres, F.J. Arregui, I.R. Matias, **Journal of Lightwave Technology** Vol. 31, No. 22 (2013), pp. 3460-3468.

7. "Sensitivity enhancement in a multimode interference-based SMS fibre structure coated with a thin-film: theoretical and experimental study", A.B. Socorro, I. Del Villar, J.M. Corres, F.J. Arregui, I.R. Matias, **Sensors and Actuators B: Chemical** Vol. 190 (2014), pp. 363–369.

8. "Spectral width reduction in lossy mode resonance-based sensors by means of tapered optical fibre structures", A.B. Socorro, I. Del Villar, J.M. Corres, F.J. Arregui, I.R. Matias, **Sensors and Actuators B: Chemical** Vol. 200 (2014), pp. 53–60.

9. "Refractometric sensors based on multimode interference in a thin-film coated single-mode – multimode - single-mode structure with reflection configuration", I. Del Villar, A.B. Socorro, J.M. Corres, F.J. Arregui, I.R. Matias, **Applied Optics** Vol. 53, No. 18 (2014), pp. 3913-3919.

10. "Temperature sensor based on a hybrid ITO-silica resonant cavity", A.B. Socorro, S. Soltani, I. Del Villar, J.M. Corres, A.M. Armani, **Optics Express** (in press).

Ap.2.2. INTERNATIONAL CONFERENCES

1. Poster: "Study of sensitivity as a function of waist length in nanocoated tapered optical fibers", A.B. Socorro, I. Del Villar, J.M. Corres. **IMAGINENANO 2011 – NanoSpain Conference**. Bilbao Exhibition Centre – Bilbao (Spain), Apr. 11 – 14, 2011.

2. Oral contribution: "Lossy Mode Resonances in Nanocoated Optical Fibers", I. Del Villar, A.B. Socorro, J.M. Corres, C.R. Zamarreño, M. Hernáez, I.R. Matías, F.J. Arregui. **Nanoelectronic Devices for Defense & Security (Nano-DDS) Conference 2011**. Brooklyn – Nueva York (USA), Aug. 29 – Sep. 1, 2011.

3. Oral contribution: "Lossy Mode Resonance-based pH Sensor Using a Tapered Single Mode Optical Fiber Coated with a Polymeric Nanostructure". A.B. Socorro, I. Del Villar, J.M. Corres, F.J. Arregui, I.R. Matías. **IEEE Sensors Conference 2011**. Limerick (Ireland), Oct. 28 – 31, 2011. IEEE CATALOG NUMBER: CFP11SEN-CDR, ISBN: 978-1-4244-9288-6, pp. 238-241.

4. Poster: "Immunoglobin G sensor by means of lossy mode resonances induced by a nanostructured polymeric thin-film deposited on a tapered optical fiber". A.B. Socorro, J.M. Corres, I. Del Villar, F.J. Arregui, I.R. Matías. **Trends in Nanotechnology (TNT) 2012**. Madrid (Spain), Sep. 10 – 14, 2012. Legal dep.: BI-1480/2012. Edited by Phantoms Foundation.

5. Poster and oral contribution: "Optical fiber sensors based on lossy mode resonances" F.J. Arregui, I.R. Matías, J.M. Corres, I. Del Villar, J. Goicoechea, C. Ruiz-Zamarreño, C. Elosúa, M. Hernáez, P.J. Rivero, A. Urrutia, A.B. Socorro, P. Sánchez-Zabal, I. Vidondo, L. Razquin, J. Ascorbe. **6èmes Journées Franco-Espagnoles IBERNAM - CMC2 "Micro and nano Sensors and Microsystems".** Marseille (France), Nov. 22 – 23, 2012.

6. Oral contribution: "Celiac disease biodetection using lossy mode resonances generated in tapered single-mode optical fibers", A.B. Socorro, J.M. Corres, I. Del Villar, I.R. Matías, F.J. Arregui. **23rd International Conference on Optical Fiber Sensors (OFS) 2014**. Santander (Spain), Jun. 2 – 6, 2014.

7. Plenary conference: "Fiber-Optic Lossy Mode Resonance Sensors", Francisco J. Arregui, Ignacio Del Villar, Jesus M. Corres, Javier Goicoechea, Carlos R. Zamarreño, Cesar Elosua, Miguel Hernaez, Pedro J. Rivero, Abian B. Socorro, Aitor Urrutia, Pedro Sanchez, Pablo Zubiate, Diego Lopez, Nerea De Acha, Ignacio R. Matias, **28th EUROSENSORS 2014**. Brescia (Italy), Sep. 7 – 10, 2014.

8. Invited conference: "Optimization of thin-film coated optical fiber sensors without gratings", Ignacio Del Villar, Abian B. Socorro, Miguel Hernaez, Jesús M. Corres, Carlos R. Zamarreño, Pedro Sanchez, Francisco J. Arregui, Ignacio R. Matias, **20th IMEKO TC4 International Symposium**. Benevento (Italy), Sep. 15 – 17, 2014.